176 5-6-77

Drawer 989

GENERAL ATOMIC

GA-A14298
UC-77

HTGR FUELS AND CORE DEVELOPMENT PROGRAM

QUARTERLY PROGRESS REPORT FOR THE PERIOD ENDING FEBRUARY 28, 1977

Prepared under
Contract EY-76-C-03-0167
Project Agreement No. 17
for the San Francisco Operations Office
U.S. Energy Research and Development Administration

DATE PUBLISHED: MARCH 1977

Printed in the United States of America
Available from
National Technical Information Service
U.S. Department of Commerce
5285 Port Royal Road
Springfield, Virginia 22161
Price: Printed Copy $9.00; Microfiche $3.00

DISCLAIMER

DISCLAIMER

GENERAL ATOMIC

GA-A14298
UC-77

HTGR FUELS AND CORE DEVELOPMENT PROGRAM

QUARTERLY PROGRESS REPORT FOR THE PERIOD ENDING FEBRUARY 28, 1977

Prepared under
Contract EY-76-C-03-0167
Project Agreement No. 17
for the San Francisco Operations Office
U.S. Energy Research and Development Administration

GENERAL ATOMIC PROJECT 3224

DATE PUBLISHED: MARCH 1977

QUARTERLY REPORT SERIES

GA-4072-December, 1962, through February, 1963
GA-4350-March, 1963, through May, 1963
GA-4569-June, 1963, through August, 1963
GA-4937-September, 1963, through November, 1963
GA-5104-December, 1963, through February, 1964
GA-5366-March, 1964, through May, 1964
GA-5618-June, 1964, through August, 1964
GA-5866-September, 1964, through November, 1964
GA-6113-December, 1964, through February, 1965
GA-6418-March, 1965, through May, 1965
GA-6671-June, 1965, through August, 1965
GA-6869-September, 1965, through November, 1965
GA-7010-December, 1965, through February, 1966
GA-7181-March, 1966, through May, 1966
GA-7396-June, 1966, through August, 1966
GA-7553-September, 1966, through November, 1966
GA-7801-December, 1966, through February, 1967
GA-7981-March, 1967, through May, 1967
GA-8200-June, 1967, through August, 1967
GA-8356-September, 1967, through November, 1967
GA-8530-December, 1967, through February, 1968
GA-8662-March, 1968, through May, 1968
GA-8860-June, 1968, through August, 1968
GA-9090-September, 1968, through November, 1968
GA-9227-December, 1968, through February, 1969
GA-9372-March, 1969, through May, 1969
GA-9660-June, 1969, through August, 1969
GA-9815-September, 1969, through November, 1969
GA-9944-December, 1969, through February, 1970
GA-10088-March, 1970, through May, 1970
GA-10288-June, 1970, through August, 1970
GA-10399-September, 1970, through November, 1970
GA-10501-December, 1970, through February, 1971
GA-10661-March, 1971, through May, 1971
Gulf-GA-A10784-June, 1971, through August, 1971
Gulf-GA-A10930-September, 1971, through November, 1971
Gulf-GA-A10999-December, 1971, through February, 1972
Gulf-GA-A12150-March, 1972, through May, 1972
Gulf-GA-A12222-June, 1972, through August, 1972
Gulf-GA-A12422-September, 1972, through November, 1972
Gulf-GA-A12515-December, 1972, through February, 1973
Gulf-GA-12599-March, 1973, through May, 1973
Gulf-GA-A12725-June, 1973, through August, 1973
Gulf-GA-A12818-September, 1973, through November, 1973
GA-A12916-December, 1973, through February, 1974
GA-A13030-March, 1974, through May, 1974
GA-A13126-June, 1974, through August, 1974
GA-A13253-September, 1974, through November, 1974
GA-A13353-December, 1974, through February, 1975
GA-A13444-March, 1975, through May, 1975
GA-A13592-June, 1975, through August, 1975
GA-A13737-September, 1975, through November, 1975
GA-A13804-December, 1975, through February, 1976
GA-A13941-March, 1976, through May, 1976
GA-A14046-June, 1976, through August, 1976
GA-A14180-September, 1976, through November, 1976

ABSTRACT

This publication continues the quarterly report series on the HTGR Fuels and Core Development Program. The Program covers items of the base technology of the High-Temperature Gas-Cooled Reactor (HTGR) system. The development of the HTGR system will, in part, meet the greater national objective of more effective and efficient utilization of our national resources. The work reported here includes studies of reactions between core materials and coolant impurities, basic fission product transport mechanisms, core graphite development and testing, the development and testing of recyclable fuel systems, and physics and fuel management studies. Materials studies include irradiation capsule tests of both fuel and graphite. Experimental procedures and results are discussed and, where appropriate, the data are presented in tables, graphs, and photographs. More detailed descriptions of experimental work are presented in topical reports; these are listed at the end of the report.

INTRODUCTION

This report covers the work performed by the General Atomic Company under U.S. Energy Research and Development Administration Contract EY-76-C-03-0167, Project Agreement No. 17. This Project Agreement calls for support of basic technology associated with the fuels and core of the gas-cooled, nuclear power reactor systems. The program is based on the concept of the High-Temperature Gas-Cooled Reactor (HTGR) developed by the General Atomic Company.

Characteristics of advanced large HTGR designs include:

1. A single-phase gas coolant allowing generation of high-temperature, high-pressure steam with consequent high-efficiency energy conversion and low thermal discharge.

2. A prestressed concrete reactor vessel (PCRV) offering advantages in field construction, primary system integrity, and stressed member inspectability.

3. Graphite core material assuring high-temperature structural strength, large temperature safety margins, and good neutron economy.

4. Thorium fuel cycle leading to U-233 fuel which allows good utilization of nuclear resources and minimum demands on separative work.

These basic features are incorporated into the 330-MW(e) prototype Fort St. Vrain reactor which is currently undergoing prestartup testing.

CONTENTS

FIGURES

FIGURES (Continued)

FIGURES (Continued)

TABLES

TABLES (Continued)

TABLES (Continued)

4. HTGR FISSION PRODUCT MECHANISMS
189a NO. 00549

TASK 100: FISSION PRODUCT TRANSPORT

Subtask 140: Diffusion of Fission Product Metals in Graphite

Diffusion of Cesium in Graphite

Introduction and Summary. The work reported here concludes the reporting on a study of cesium transport through H-451 graphite using a permeation method. This study was discontinued in September 1976 due to lack of funds. The main purpose of this study was to reduce the uncertainty of data relating to cesium diffusivity in graphite. The AIPA study (Ref. 4-1) found that uncertainty in cesium diffusivity in graphite was the largest contributor to the uncertainty in cesium release predictions.

The work reported here covers mainly the analysis of an in-pile experiment conducted under conditions which permitted close comparison with out-of-pile results. The analysis shows that much less cesium left the source under irradiation that would have out-of-pile and that much more of what left the source was stopped in the H-451 graphite sleeve, with the result that the amount reaching the sink was drastically reduced. These results can be best understood in terms of other (out-of-pile) findings of this study showing that the presence and level of oxidizing impurities is a primary determinant of the rate at which cesium permeates through graphite. Presumably, these impurities displace the cesium from highly active adsorption centers (traps) on the surface and permit it to diffuse rapidly over the less active surface of pores and defects. Under irradiation conditions many such centers are formed which in the absence of impurities are very effective in immobilizing the cesium. Thus permeation under in-pile conditions was found to be 100 times slower than in the laboratory when air is carefully excluded and at least 1000 times slower than when oxidizing impurities are present in minute amounts.

The work reported here also includes an extended experiment on highly sorptive char-loaded graphite.

In-Pile (Capsule) Experiment. One purpose of out-of-pile experiments, the results of which are described in previous quarterly reports (Refs. 4-2 through 4-5) was to provide a basis for meaningful in-pile experiments and their evaluation. An opportunity presented itself to prepare a capsule sample just at the time when the need for the "sterile" technique* was recognized but the equipment to implement it was not yet perfected. An experiment was therefore designed as best as possible. The capsule design permitted the "sterile" irradiation of a diffusion experiment comparable to a standard (out-of-pile) experiment; however, dissassembly of the capsule required exposure to air, which continued during the time allowed for the decay of radioactive impurities. The sleeve and the source used in the capsule were then characterized in standard sterile experiments. Experimental details, results of the capsule experiments, and interpretation of the results are presented below.

The basic method (which was described earlier in Refs. 4-3 and 4-4) uses highly sorptive, char-loaded graphite as the source and sink in measuring the transport of cesium across a barrier sleeve of the graphite to be studied. The capsule (in-pile) experiment was partially described in Ref. 4-6; an expanded description is presented below.

A standard diffusion assembly consisting of a source, sleeve and plugs, and sink and caps was placed in a tightly fitting spacer cylinder which in turn fitted into a crucible closed with screw caps at both ends. The crucible in turn fitted tightly into a niobium can fitted with a cover to which originally a thin niobium tube was attached.

*A "sterile" technique was developed for protecting the diffusion assembly from air or moisture during experiments after an initial bake-out (see Ref. 4-2).

In preparing for the capsule experiment, a reasonably well-characterized source/sleeve combination was chosen and subjected to a standard 2-hour permeation experiment in a quartz tube which contained also another sink and caps and the remaining capsule parts. It should be remembered that this was before introduction of the "sterile" technique so that the samples were prepared in air but degassed and annealed in 8% hydrogen in helium. The quartz tube was however opened within a glove-bag flushed several times with the 8% hydrogen in helium mixture. The sink was removed and replaced by the clean one which was placed in the spacer, crucible, and niobium can. At this point the tube of the niobium cover broke off (because of hydrogen embrittlement).

The can with the crucible was placed in a double plastic bag; the inner bag was sealed with adhesive tape adapted for remote opening; and the glove-bag was opened. A new niobium tube was welded to the lid. The can, with one plastic bag, was then placed in a welding jar. After purging and refilling with inert gas, the plastic bag was removed. The lid was placed in the can opening and welded on. The tube was then welded shut.

The can was then placed in the quartz tube under a stream of 8% H_2, the end of the niobium tube was snipped off, and the quartz tube was closed and evacuated promptly. The quartz tube was then purged twice with 8% H_2 at room temperature, purged at 500°C, promptly heated to 860°C, purged twice (which took about 6 minutes), and cooled in air until it reached room temperature. It was then opened again in a glove bag. The can was placed in an aluminum holder and the niobium tube was closed with a rubber stopper. The whole was enclosed in a plastic bag, removed from the glove bag, and placed in the welding jar. After repeated purging, the plastic bag and the rubber stopper were removed and the niobium tube was sealed off at the base. The sealed can was tested for vacuum tightness on a helium leak detector. Thus, the assembly can be assumed to have entered the irradiation test relatively free of impurities and with a negligible amount of cesium in the sink.

The diffusion assembly was exposed in capsule HB-2 to a design fluence of 4.6×10^{25} n/m^2 (E > 29 fJ)$_{HTGR}$ during 104 days of irradiation. The irradiation temperatures, calculated on the basis of design data and actual control rod positions, varied from 913 to 1123 K. The irradiation conditions were equivalent to 49.4 days at 1138 K (if the activation energy for the transport is taken as 140 kJ/mol (33 kcal/mol) on the basis of the data given in Ref. 4-3).

Remote dissasembly (in the hot cell) after irradiation was not simple and had to be done in air. In the process, one of the screw caps of the outer crucible was lost and some contamination may have been picked up. The graphite parts were removed from the hot cell, disassembled in air, placed in polyethylene vials, and counted. A number of impurities were found, increasing in concentration outwardly from the source, which made determination of the cesium imprecise. The parts were then kept in the vials for 4.5 months, during which time most of the impurities decayed sufficiently to permit proper estimation of the cesium content. It can be noted that the activity of the cesium increased considerably during irradiation as some of the Cs-133 carrier present became activated.

At this point the source was characterized by using it in a series of standard diffusion experiments with a previously characterized sleeve. The source was not baked out prior to the first experiment, the purpose of which was also to remove any oxidizing impurities. The "sterile" technique was used from this point on. The sleeve was in turn characterized by first subjecting it to two anneals with sinks, but without a source, to remove the surface-adsorbed cesium and then to two standard transport experiments using a previously characterized source. Again "sterile" handling was applied after the first anneal.

After extensive exposure to air, the source was paired with the sleeve used in the experiments of Table 4-3 of Ref. 4-2. That sleeve showed an average permeability of 2×10^{-12} m^2/s in the earlier experiments and took up 1.3% of the activity of the source. In the present experiment with the previously irradiated source it gave surprisingly similar results, taking up 1.3% of the source activity and showing a permeability of 2.1 x 10^{-8} m^2/s. Thus, in this experiment the source behaved as if it had not been irradiated.

The irradiated sleeve, after having been freed of surface-sorbed cesium from the high-activity source, was paired with the source from the experiment of Table 4-3 of Ref. 4-2 and showed a permeability of 5.6 x 10^{-12} m^2/s, which is reasonably close to that of 3.6 x 10^{-12} m^2/s showed prior to irradiation. Thus, again the sleeve seemed to behave as if it were quite unaffected by irradiation.

The results of the in-pile experiment are given in Table 4-1. After irradiation 94.2% of the cesium accounted for was in the source, 4.0% in the sleeve and plugs, 1.2% in the sink, 0.4% in the caps, and some 0.2% in the spacer and crucible. If the permeation coefficient of the sleeve is computed in the standard manner for the 49.4 day equivalent period on the basis of the sink content, the permeation coefficient is found to be 3.1 x 10^{-14} m^2/s. The original permeability of the sleeve on the basis of two non-sterile anneals of 6 and 16 hours duration is 3.6 x 10^{-12} m^2/s, i.e., about 100 times higher. If this difference were to be accounted for on the basis of a temperature error, the equivalent capsule temperature would have to be 590°C instead of 865°C, i.e., some 275°C lower, which seems highly unlikely.

One other observation shows that the transport during irradiation was not normal by out-of-pile standards. After irradiation the sleeve contained 3.85% of the source activity. Before irradiation the sleeve content was close to 0.7% of the source. Thus, although the sleeve accumulated 5.5 times more cesium during irradiation than expected, it allowed 100 times less to pass through it.

In out-of-pile experiments after a very short lag time, practically all the cesium leaving the source permeates through the sleeve and is found

TABLE 4-1
RESULTS OF CESIUM PERMEATION TESTS

Experiment	Source		Sleeve		Sink Activity (μCi)	Permeation Coefficient ($\times 10^{-12}$ m^2/s)	Comments
	Ident.	Activity (μCi)	Ident.	Activity (μCi)			
Preirradiation	A	74.5	C	0.788	(a)	3.6	Avg. of several experiments at 1138 K
In-pile (irradiation)	A	1330	C	51.2	16.4	0.031	Activity (μCi) on other components was 5.68 on plugs, 5.43 on cap, 0.76 on spacer, 5.86 on crucible, and 1.98 on crucible cap
Previous out-of-pile experiments	B	59.6	D	0.73	(a)	2.3	Avg. of earlier experiments at 1138 K using source B and sleeve D (Ref. 4-2)
Postirradiation[b]	A	1290	D	17.3	3.81		6 h at 1138K
	A	1250	D	18.3	5.28	2.1	6 h at 1138K
		None	C	(c)	6.01		5 h at 1138K
		None	C	41.2	0.860		6 h at 1138K
	B	61.0	C	41.8	0.636		6 h at 1138K
	B	60.1	C	41.4	0.679	5.6	6 h at 1138K

[a] Several different sinks were used.

[b] The gamma counting for the postirradiation tests was done on different equipment and corrected to be consistent with the preirradiation and capsule tests.

[c] Not measured after test.

in the sink. This was not the case in the capsule experiment. To appreciate the significance of this difference, a fictitious permeation coefficient can be computed on the assumption that the cesium which was held up by the sleeve can be included in the amount permeating. This gives a value some 3.5 times larger than actually found, but still 30 times smaller than expected from out-of-pile data.

Thus, the experiments show that after irradiation, both the source and the sleeve behaved quite normally. Yet during irradiation the sleeve absorbed most of the cesium, rather than letting it permeate through readily as happened under out-of-pile conditions. Also, during irradiation the source released very much less cesium than it would have out-of-pile.

To account for these somewhat paradoxical results, as well as for those previously obtained, the following model is proposed. Cesium is present in the graphite in two principal forms: (1) absorbed within the graphite crystallites where its motion is very slow and it has a high activation energy, and (2) adsorbed on the surface at sites of varying energy. Surface-adsorbed cesium can diffuse at a rate which depends on the energy with which it is adsorbed, jumping readily between low energy sites but lingering for a long time at the high energy sites. This surface adsorbed cesium can be removed rather readily (e.g., by exposure to a sink for 2 hours at 1140 K), whereas the absorbed cesium is practically unaffected by such a treatment.

There is competition for the high energy sites between cesium and oxidizing impurities, with the latter generally winning. Thus in the presence of such impurities, the surface transport (i.e., permeation) is much faster, and reproducible results are obtained only when such impurities are carefully controlled as in the "sterile" technique.

One of the effects of fast neutron irradiation is the formation of surface defects that provide high-energy adsorption sites which, in the absence of impurities, are very effective in immobilizing cesium. Exposure to air following capsule opening permits the access of impurities which displace the cesium and thus restore its original mobility. The implication is that the impurities either continue to occupy the most active sites or destroy them so that these are no longer available to the cesium even under "sterile" conditions. Thus it is possible for the components of the diffusion assembly to act essentially unchanged after irradiation and exposure to air, whereas under irradiation the transport of cesium is drastically reduced.

The model also accounts for the very fast permeation and "burst effects" found in the presence of oxidizing impurities and for the reproducibility obtained by controlling impurities by the "sterile" technique (see Ref. 4-2).

Permeation Experiments Using Char-Loaded Graphite. Char-loaded graphite of high sorptivity was used exclusively as source and sink material in a series of cesium permeation experiments. The experimental arrangement, described in Ref. 4-3, was the opposite of the usual one in that the sink was a small rod as normally used for the source and the source was a large hollow cylinder as normally used for the sink. Both were of char-loaded graphite. Between the sink and source there was a sleeve and plugs of char-loaded graphite whose permeability was being measured. This arrangement provided a large supply of cesium to compensate for the greater sorptivity and retentive power of the char-loaded sleeve as compared with a plain graphite sleeve. The whole assembly was enclosed in a niobium crucible having a slip-over cover with small clearances to permit degassing and yet reduce cesium loses. The "sterile" technique was used in handling the samples.

As reported earlier (Ref. 4-3), three consecutive anneals giving substantially constant permeation were obtained after 7 days of annealing at 1338 K. The experiments were, however, continued with the unexpected result that the permeation rate continued to increase, reaching an apparently steady rate twice as high between 18 and 24 days of annealing. This is shown in Fig. 4-1, where the originally reported steady state is shown

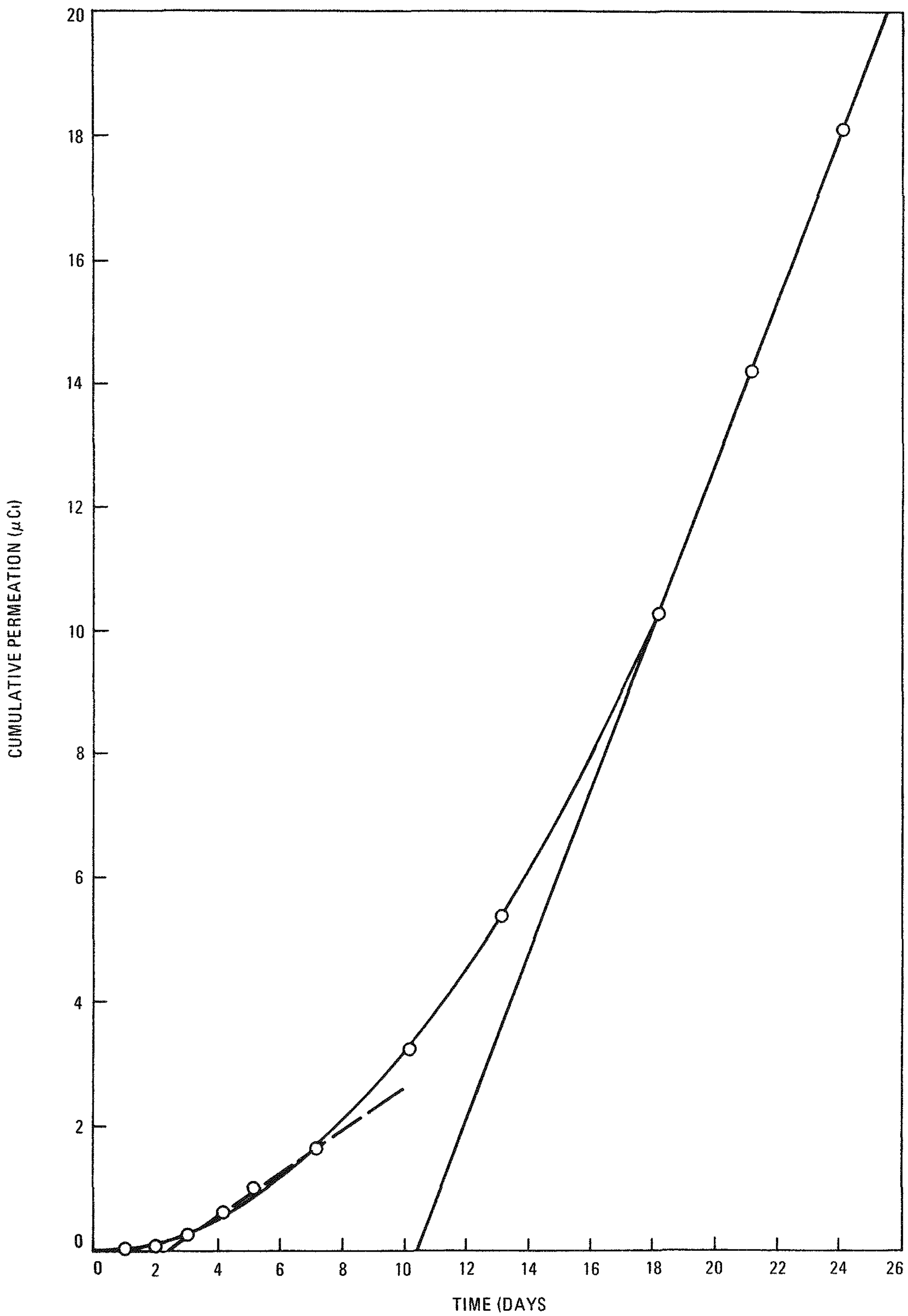

Fig. 1. Time dependence of cumulative permeation of cesium in char-loaded graphite

as a dotted line. It must be noted, however, that in these last experiments of 3 days duration, the small sinks were reaching 30% of the equilibrium value, and this must have slowed down the permeation. This also distorted the loading rate of the sleeve. As time did not permit conducting a series of shorter anneals to obtain more interpretable results, the only conclusion that can be drawn is that char-loaded graphite reaches steady state at a very slow rate but that its permeability finally becomes at least as high and probably appreciably higher than that of H-451 graphite.

TASK 200: FISSION PRODUCT TRANSPORT CODES

Subtask 220: Code Validation

Status Report on Fission Product Code Validation

The accuracy of predictions provided by the fission product transport codes RANDI, TRAFIC (FIPERQ), and PAD is being quantified via comparison of calculated and measured in-pile fission product behavior. This validation effort is being performed to ensure that GA fission product design codes meet appropriate federal regulations requiring verification of design methods. Acceptable agreements between measurements and predictions have been found for each validation test performed to date. The results for each code are summarized as follows:

1. RANDI (used to predict radionuclide inventories within the primary circuit): Although this code has yet to be submitted for verification, the basic transport assumptions relating to fission gas release are being checked using the SURVEY analysis of Fort St. Vrain rise to 18% power. A need in this work is to verify and quantify the gas phase diffusion effect (see Ref. 4-2, p. 4-19).

2. TRAFIC (FIPERQ) (used to predict fission metal release from fuel elements): Results from the GA-CEA SSL-1 loop test showed that

measured nominal cesium release was within 25% of that observed. The large uncertainty (40x) accompanying the predicted release resulted principally from uncertainties in the reference input data. It appears that release from particles was overpredicted and diffusion through fuel element graphite was underpredicted. (A topical report covering this work is in review.)

Preliminary cesium release comparisons for the GA-CEA CPL-2/1 test showed that release was overpredicted by a factor of three (see Ref. 4-6). This work is continuing.

3. PAD (used to predict condensable fission product plateout distribution in the primary circuit): Comparison of the fission product distribution measured during Peach Bottom primary circuit gamma scanning and the distribution calculated using the PAD code showed good agreement.

   PAD code calculations for the CPL-2/1 test provided acceptable fits of the observed plateout profiles in the heat exchanger (see Ref. 4-6). This work is on-going.

TASK 300: FISSION PRODUCT DATA ANALYSIS

Review of Release Rate Coefficient Data for Use in Core Heatup Analysis

Introduction and Summary

Release rate coefficient data are required to determine the release of radionuclides from the HTGR core during core heatup. The coefficients are used in the SORS code (Ref. 4-7). The reference release rate coefficient data (i.e., the data currently used in SORS calculations) are represented by the curves in Figs. 4-2 and 4-3. These figures were taken from Ref. 4-8.* The release rate coefficient data were derived from fractional

*Sets of the release rate coefficient curves are also given in Figs. 4-6 and 4-7 of Ref. 4-9, and it should be noted that curve 2 and the ordinate scale of Fig. 4-7 were incorrectly drawn.

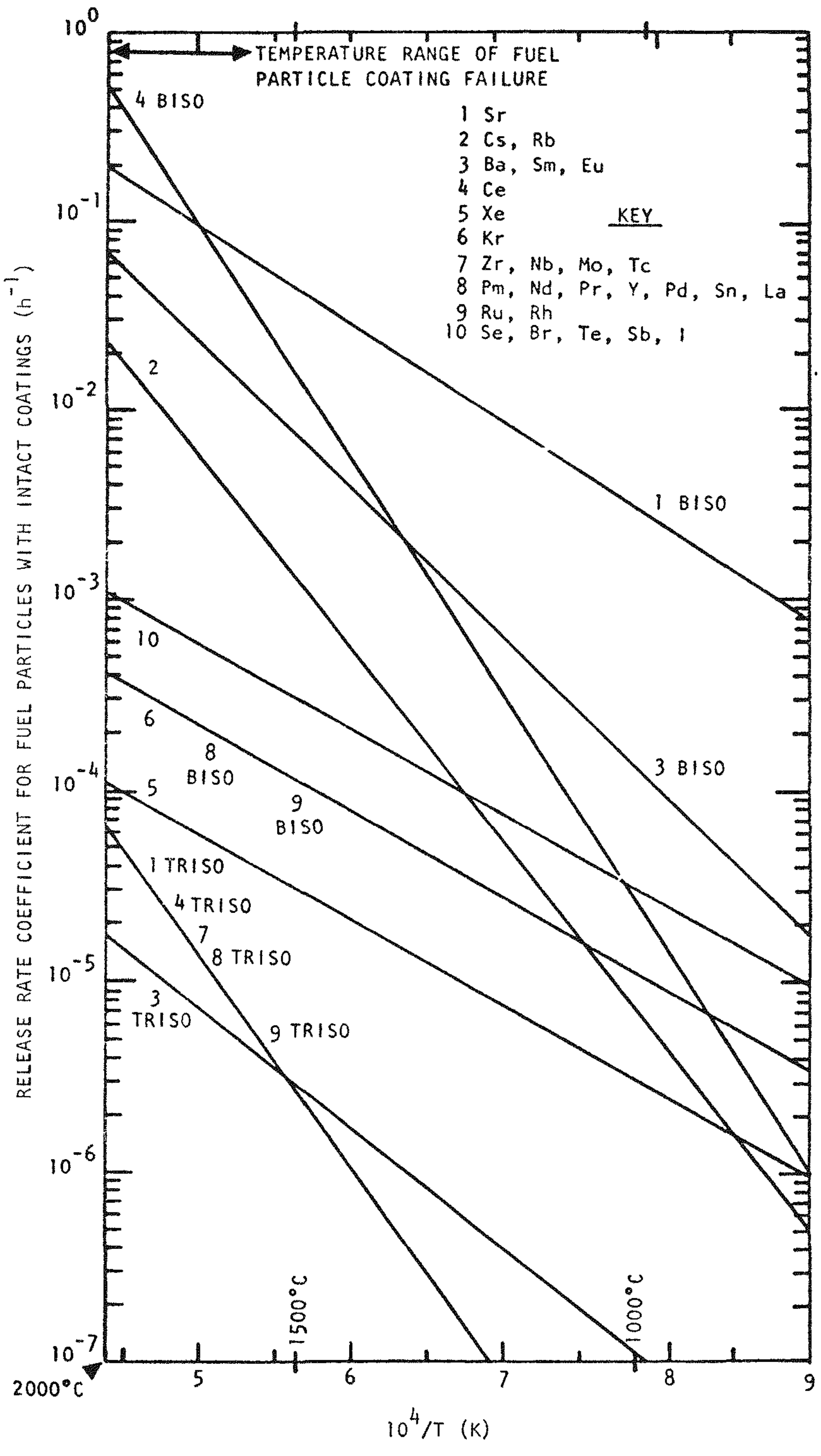

Fig. 4-2. Release rate coefficients for intact particles as a function of temperature

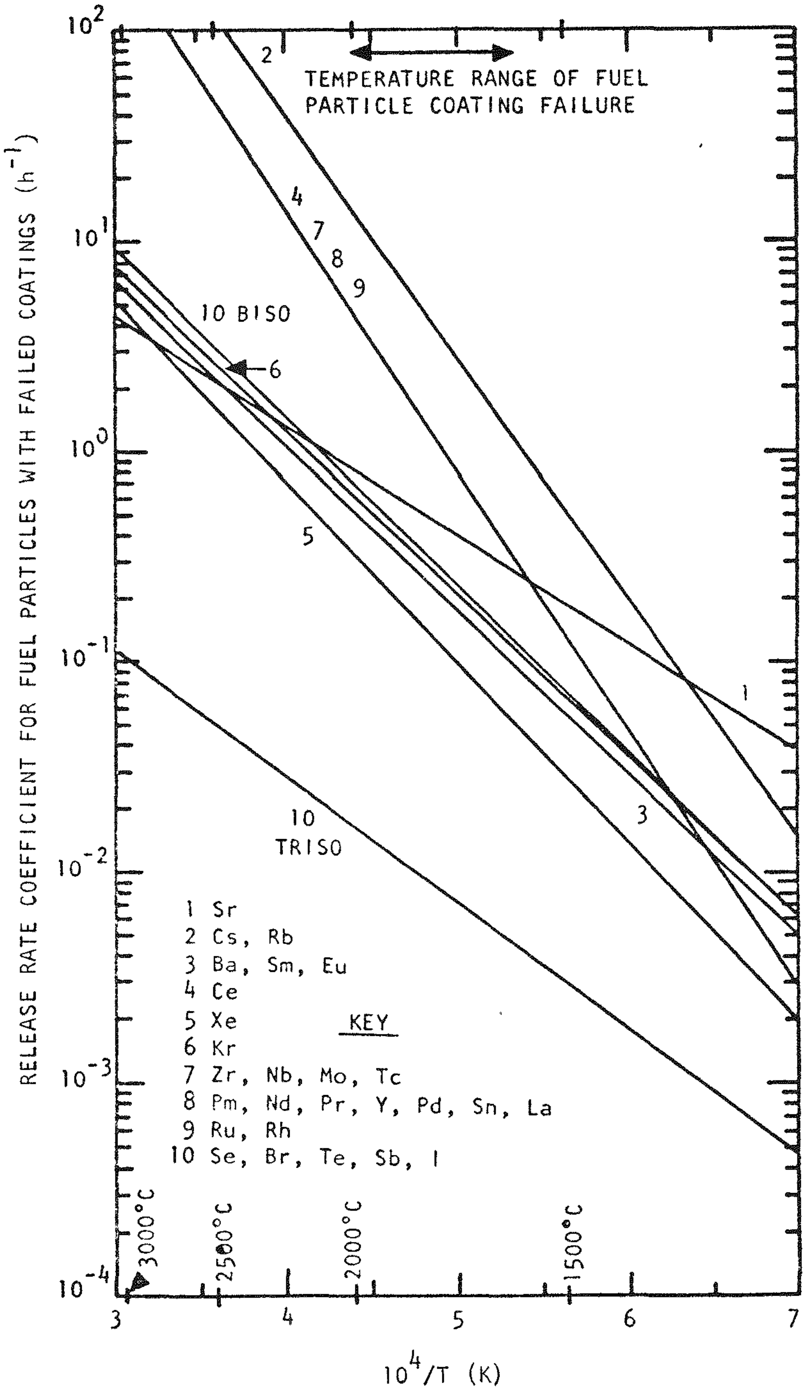

Fig. 4-3. Release rate coefficients for failed particles as a function of temperature

release rate data. References for the fractional release rate data used are given in Table 4-5 of Ref. 4-9. This table provides uncertainties for the release rate coefficient data in the form of standard deviation factors. Note that the curves designated 10 BISO and 10 TRISO in Fig. 4-3 are applied to reference particles with failed coatings (i.e., curve 10 BISO is applied to failed fertile particles with BISO coatings and ThO_2 kernels and curve 10 TRISO is applied to failed fissile particles with TRISO coatings and dense UC_2 kernels). The other curves of Fig. 4-3 are applied to both failed fertile and failed fissile particles.

The reference release rate coefficient curves of Figs. 4-2 and 4-3 and the standard deviation factors were derived from a review of fractional release data, including a statistical analysis of the data, conducted during the AIPA study (see Ref. 4-9, p. 4-21). This review has been extended and the following report is a documentation of the extended review.

At the end of this report, the presently recommended release rate coefficient data and standard deviation factors are summarized. There are no significant differences between the presently recommended release rate coefficient data and the data represented by the curves of Figs. 4-2 and 4-3. The presently recommended standard deviation factors for Xe and Kr release from failed particles are slightly larger than those in Ref. 4-9.

This report first discusses the treatment of fractional release data to obtain release rate coefficients and then presents the bases for the release rate coefficient curves for the following elements and particle configurations:

1. Iodine release from failed BISO particles with oxide kernels.
2. Iodine release from failed TRISO particles with dense UC_2 kernels.
3. Iodine release from intact particles.
4. Xenon release from failed particles.
5. Xenon release from intact particles.
6. Krypton release from failed particles.
7. Krypton release from intact particles.

8. Cesium release from intact BISO and failed particles.
9. Strontium release from intact BISO and failed particles.
10. Strontium release from intact TRISO particles.
11. Cerium release from intact BISO and failed particles.
12. Cerium release from intact TRISO particles.
13. Barium release from intact BISO and failed particles.
14. Barium release from intact TRISO particles.

For other elements, release rate coefficient curves were chosen on the basis of similarities in chemical or physical properties of these elements with the above listed elements.

Treatment of Fractional Release Data to Obtain Release Rate Coefficients

The release behavior of each nuclide from HTGR fuel under core heatup conditions is expressed by a release rate coefficient, R. The fractional release is calculated according to the equation:

$$F_{rel} = 1 - e^{-Rt} \quad , \tag{4-1}$$

where F_{rel} = fractional release, R = release rate coefficient, and t = time.

The release rate coefficient is a function of temperature, fuel type, fuel particle integrity, irradiation history, and nuclide.

Equation 4-1 generally fits the available experimental data only over a limited time interval. Thus to derive from the equation a value of R which yields a conservative estimate of the release function, F_{rel}, a small value of t should be chosen. In this review, the value 1 hour is chosen since this is the smallest measurement time for most of the data. This choice of time is still somewhat arbitrary since experimental data at times less than 1 hour are not available and no comparison of the fit of Eq. 4-1 to the experimental data can be made at shorter time intervals. The agreement of Eq. 4-1 with the experimental data appears to substantially improve as the temperature increases.

In computing uncertainties for the experimental data, a log normal distribution of errors is assumed.

Iodine Release From Failed BISO Particles with Oxide Kernels

The release rate coefficient curve representing iodine release from failed BISO particles (curve 10 BISO in Fig. 4-3) was generated using ORNL data for pyrolytic carbon coated UO_2 particles which were mechanically cracked to simulate failure and were in an unconstrained configuration during the measurements (Refs. 4-10, 4-11). These were the only available data for iodine release from failed particles with oxide kernels. It is reasoned that iodine release from UO_2 kernels is similar to that from ThO_2 kernels.

The fractional release data are given in Table 4-2. The data of Ref. 4-10 are given as mean and error bars (see Fig. 5.13 of Ref. 4-10). To better reflect in our calculations the spread of the data, we have listed in Table 4-2 the points representing the terminal points of the error bars. The average of each set of two points is identical to the average point given in Fig. 5.13 of Ref. 4-10.

Release rate coefficient data, calculated from the fractional release values using Eq. 4-1, are included in Table 4-2 and plotted in Fig. 4-4. A least-squares fit of the data yielded curve 2 in Fig. 4-4.

Curve 1 in Fig. 4-4 is an early least-squares fit of release rate coefficient values derived from the ORNL data. Curves 1 and 2 differ because of a difference in the way the data were treated. In the earlier least-squares treatment, five of the data points used were averages of other data and were inadvertently used. The difference in curves 1 and 2 is negligible in view of the other uncertainties.

Curve 3 in Fig. 4-4 is the 2-sigma lower limit relative to curve 1, the earlier least-squares fit of the release rate coefficient data. Curve 3 was adopted as the reference curve for failed BISO particles and is the same as curve 10 BISO in Fig. 4-3. In adopting curve 3, it was reasoned

TABLE 4-2

RELEASE RATE COEFFICIENTS (R) FOR IODINE RELEASE FROM FAILED BISO PARTICLES

Temp. (°C)	Percent Release[a]	R	Data Source
1100	3.2[b]	0.0325	Ref. 4-11, Table 5.4, p. 80; 1-hour anneal data
	0.8	0.0080	
	2.7	0.0274	
1200	1.6	0.0161	
	4.4	0.0450	
	2.9	0.0294	
1300	2.9	0.0294	
	5.4	0.0555	
1350	2.9	0.0294	
	7.7	0.080	
1400	12.8	0.137	
	13.9	0.150	
	8.7	0.091	
1500	33.3	0.405	
1000	0.63[c]	0.0032	Ref. 4-10, Fig. 5.13, p. 97; 2-hour anneal data
	1.15	0.0058	
1100	0.29	0.0015	
	3.1	0.0158	
1200	1.7	0.0086	
	4.5	0.0230	
1300	3.4	0.0173	
	10.3	0.0545	
1400	11.8	0.0630	
	18.9	0.1045	
1500	22.9	0.1300	
	53.5	0.383	

(a) Percent release values are for I-131 release from mechanically cracked pyrolytic carbon coated UO_2. The values resulted from anneal tests performed at ORNL (References given under Data Source).

(b) Five average values and one datum on a crushed particle were omitted from the Ref. 4-11 data.

(c) The two points at each temperature are from the error bar extremes in Fig. 5.13, p. 97 of Ref. 4-10. The average of these is the mean point for each temperature.

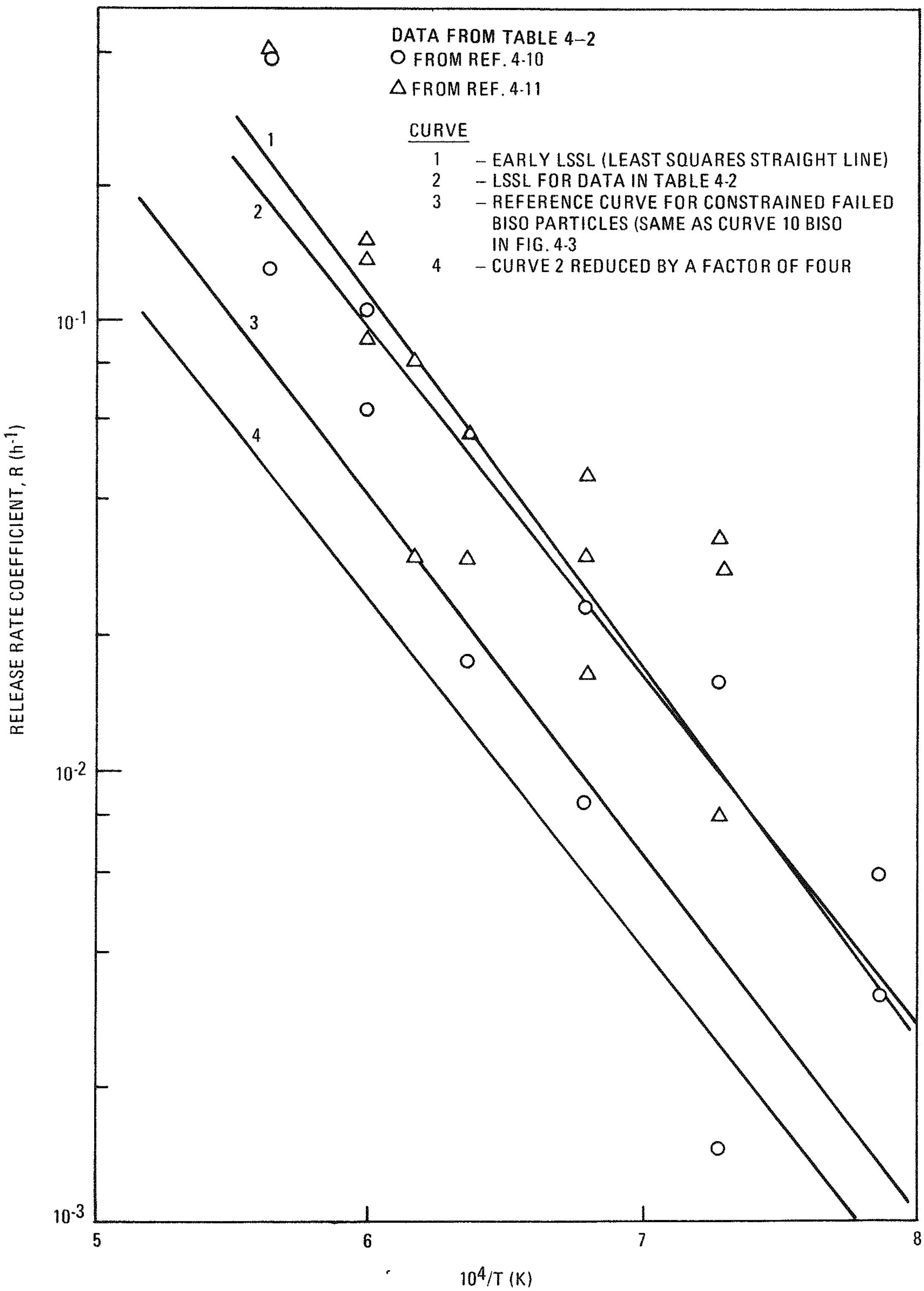

Fig. 4-4. Temperature dependence of release rate coefficients for iodine release from failed BISO particles (i.e., failed particles with oxide kernels)

that this curve represents release rate coefficient values for constrained failed particles as contrasted with unconstrained failed particles (see next two paragraphs) and that curve 1 represents the upper 2-sigma limit. This was an approximate means for accounting for lower release from constrained failed particles. It is recognized that this method of selecting the reference curve is questionable because it depends on the number and spread of the data points; however, as related below the curve is reasonable.

Burnette et al. (Ref. 4-12) found that fission gas release values for loose failed fuel particles are appreciably higher than values for failed particles in fuel rods. This led to the concept of the constrained failed particle, defined as a failed particle with a cracked coating in a fuel rod where the crack is constrained from opening by the matrix material and adjacent particles. The constrained particle appears to be representative of failed particles in fuel rods. (This needs to be verified for failed particles under high-temperature accident conditions.)

Curve 4 of Fig. 4-4, which is a factor of four lower than curve 2, is drawn on the basis of the following justification. Fission gas release (R/B) for Kr-85m at 1100°C has been measured (Ref. 4-12) to be a factor of about four smaller for constrained failed particles than for unconstrained failed particles. On the basis of this finding, one can lower the release rate coefficient for unconstrained failed particles by a factor of four. This is an approximation, of course, since it is not known if iodine isotopes behave as Kr-85m.

Curve 3 does not differ greatly from curve 4, and it is conservatively high relative to curve 4. This justifies the retention of curve 3 as the reference curve.

The fractional release data in Table 4-2 are for either 1 or 2 hours of annealing; ideally, one would like more annealing time to know more accurately the time dependence of the release. The application of Eq. 4-1 to the data adds uncertainty, as discussed above. There is the possibility that the fits according to Eq. 4-1 of the datum at 1 or 2 hours still result in an underestimation of the release at times less than 1 or 2 hours, but this error will become less important at higher temperatures (around 2200 K).

The temperature range of the ORNL annealing experiments was 1273 to 1773 K (1000° to 1500°C). It would be desirable to have data to at least 2200 K. Data are not required above 2200 K because the release rates would be very high and iodine retention times correspondingly low.

Burnups were 10% for Ref. 4-10 data and 11% for Ref. 4-11 data. These burnups are comparable to the maximum burnup for reference fertile particles (7.5% FIMA), but additional data for lower burnup values are needed. If more data were available at lower burnup, a reduction in R values might be obtained. The present burnup effect results in a conservative mean curve, other factors being neglected.

The somewhat arbitrary uncertainty limits placed on the reference curve (curve 3 of Fig. 4-4) are the 2-sigma upper bound represented by curve 1 and a lower bound which is symmetric to the upper bound.

Iodine Release From Failed TRISO Particles with UC_2 Kernels

Available fractional release data (taken from Ref. 4-10) for use in generating release coefficient values for iodine release from failed TRISO particles are given in Table 4-3. The data were measured in anneal tests on mechanically cracked pyrolytic carbon coated UC_2. These were the only available data for iodine release from failed particles with UC_2 kernels. It was reasonable to use these data, even though the particle coatings were not TRISO, because after failure the nature of the coatings becomes much less important in influencing release. The particles were irradiated to 15% burnup. The data in Table 4-3 are for 2-hour anneal tests.

Release rate coefficient values derived from the fractional release values using Eq. 4-1 are included in Table 4-3 and plotted in Fig. 4-5. A

TABLE 4-3
RELEASE RATE COEFFICIENTS (R) FOR IODINE RELEASE FROM FAILED TRISO PARTICLES[a]

Temp. (°C)	Percent Release	R
1000	0.04	0.0002
	0.2	0.001
	0.7	0.0035
	0.06	0.0003
	0.03	0.00015
1300	0.5	0.0025
	0.7	0.0035
	0.1	0.0005
	0.3	0.0015
1400	0.9	0.0045
	1.5	0.0076

[a]Percent release values taken from ORNL report (Ref. 4-10, Table 5.4, p. 96). Values are for I-131 release during 2-hour anneals. Particles used were mechanically cracked pyrolytic carbon coated UC_2.

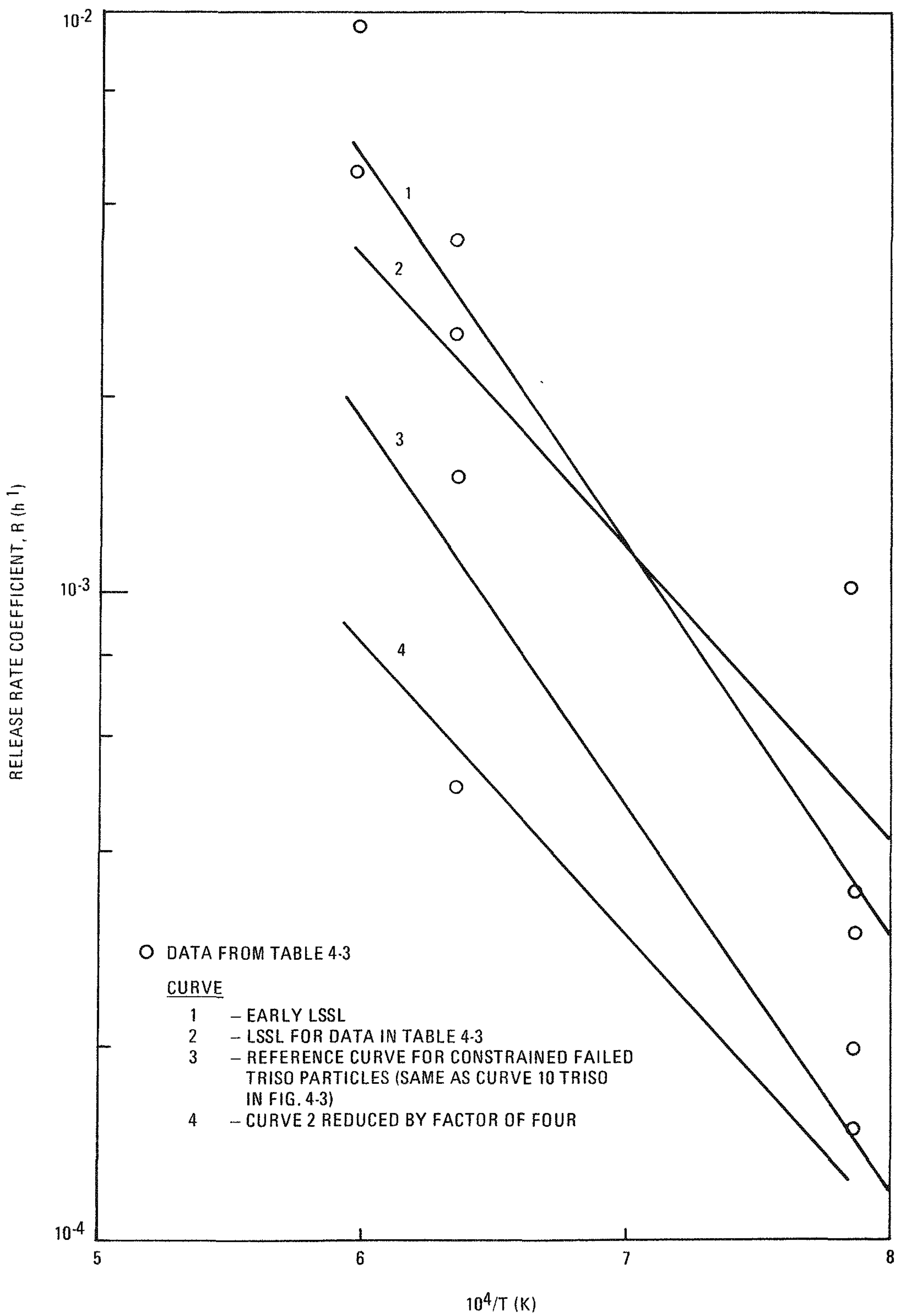

Fig. 4-5. Temperature dependence of release rate coefficients for iodine release from failed TRISO particles (i.e., failed particles with UC_2 kernels)

least-squares fit of the data, performed in the same manner as for the failed BISO particles, yielded curve 2 of Fig. 4-5.

Curve 1 in Fig. 4-5 is an early least-squares fit of the release rate coefficient data. Curve 1 differs from curve 2 because only averages of the release coefficient data at each temperature were used in obtaining the former. All data points were used in obtaining curve 2.

Curve 3 of Fig. 4-5 is the 2-sigma lower bound relative to curve 1. Curve 3 was adopted as the reference curve for failed TRISO particles and is the same as curve 10 TRISO in Fig. 4-3. In adopting curve 3, it was reasoned that this curve represents release rate coefficient values for constrained failed particles and that curve 1 represents the upper 2-sigma bound. This was an approximate means for accounting for lower release from constrained failed particles.

Curve 4 is a factor of four lower than curve 2. The justification for the factor of four is the above cited finding that Kr-85m release is a factor of four lower for constrained failed particles than for unconstrained failed particles.

Curve 3 does not differ greatly from curve 4; it is conservatively high relative to curve 4, and in view of the uncertainties involved, the difference between the two curves is probably not significant. This justifies the retention of curve 3 as the reference curve. (The procedure and reasoning which led to adopting curve 3 of Fig. 4-5 as the reference curve for failed TRISO particles is the same as that used in adopting curve 3 of Fig. 4-4 as the reference curve for failed BISO particles.)

The release rate coefficient curve for iodine release from failed TRISO particles is low relative to the failed BISO particle curve (compare curves 10 BISO and 10 TRISO in Fig. 4-3). The ORNL data clearly show that the release rate of iodine from carbide kernels is appreciably lower than that from oxide kernels. The appreciably lower release for failed particles with carbide kernels can readily be seen by examination of the release rate data given in Table 5.4 of Ref. 4-10. (This table compares iodine release from cracked coated UO_2 and UC_2 particles during post-irradiation anneals at 1000° to 1400°C. Percent releases of iodine are greater by a factor of 10 or more for the UO_2 kernels than for the UC_2 kernels.)

The temperature range of the anneal experiments which provided the release data in Table 4-3 was rather narrow (1000° to 1400°C) from the viewpoint of accident conditions. The activation energy for the release coefficient data is correspondingly uncertain.

The greatest uncertainty associated with the curves in Fig. 4-5 is probably the dependence of the release rate coefficient on burnup. The burnup of the particles from which the data of Table 4-3 were obtained was only 15%, whereas the range of burnup from zero to about 75% is of interest. Since there are no data on the dependence of iodine release on burnup, data on the release of noble gases were examined. From limited GA data, only a weak dependence of release of Kr-85m on burnup was found in the range between 25% and 54% FIMA for UC_2 particles (and also in the range between 0 and 30% FIMA for UO_2 particles). On the other hand, workers at CEA (Ref. 4-13) have found an order of magnitude increase in fission gas release in the range of burnup from 0 to about 6% FIMA for $(Th,U)O_2$ particles. The CEA experiments were performed on GA particles which were laser-drilled to simulate failure. The particles with about 6% FIMA had been irradiated in capsule test SSL-1 with a neutron flux of 7.4×10^{15} $n/m^2 \cdot s$. The applicability of the CEA data to the present situation is not established; however, allowing for the effect of burnup is prudent. Accordingly, allowance was made for the uncertainty in burnup dependence by extending the uncertainty limits relative to the reference curve (curve 3 of Fig. 4-5), and this is reflected in the standard deviation factor given in Table 4-5 of Ref. 4-9.

Iodine Release From Intact Particles

The data for iodine release from intact particles are shown in Table 4-4. In all cases, the particles are BISO coated with HTI coatings. Some of the particles were tested at rather long times after the initiation of the anneal, and using these data without a correction would result in underestimating the release rate coefficient. Therefore a correction to these data has been made as indicated in Fig. 4-6. The correction consists of extrapolating the fractional release data to 1 hour in an essentially conservative manner; i.e., the fractional release found by extrapolation to 1 hour is essentially the maximum such value that can be obtained by extrapolating the data. [For one datum of Table 2 of Ref. 4-15, only one measurement of fractional release has been obtained and this sample is therefore not used here (i.e., sample F-1409-17).]

The data of Table 4-4 are all for $(Th,U)C_2$ particles. However, if the coating contamination is the principal source of iodine for intact particles, the restriction to carbide particles should not be important. This is generally assumed to be the case (see Ref. 4-17).

The least-squares straight line for the data of Table 4-4 and the 95% confidence bounds, based on the standard deviation for a single estimated value of the dependent variable, are shown in Fig. 4-7. The least-squares straight line (LSSL) is the same as curve 10 in Fig. 4-2.

Xenon Release From Failed Particles

The xenon fractional release data and derived release rate coefficients are given in Table 4-5 for release from uncoated $(Th,U)C_2$ kernels. The data were obtained from measurements on kernels embedded in a graphite matrix. There are no data for failed constrained particles.

The data of Table 4-5 are plotted in Fig. 4-8. Curve 1 is the least-squares fit of the data, and one would expect this curve to be higher than a curve for failed constrained particles since retention of fission gases

TABLE 4-4
RELEASE RATE COEFFICIENTS (R) FOR IODINE RELEASE FROM INTACT PARTICLES[a]

Temp. (°C)	F_{rel}	Percent FIMA	Time (h)	R	Data Source
1600	$<1.4 \times 10^{-3}$	24.	2.5	$<5.6 \times 10^{-4}$	Ref. 4-14; pp. 136-138
1600	$<5.8 \times 10^{-4}$	24.	2.5	$<2.3 \times 10^{-4}$	
1100	$<3.2 \times 10^{-4}$	8.5	15.0[b]	$<3.4 \times 10^{-4}$	
1300	$<7.5 \times 10^{-4}$	8.5	14.9	$<7.5 \times 10^{-4}$	
1100	$<1.0 \times 10^{-4}$	∿0	15.0	$<1.0 \times 10^{-4}$	
1300	$<1.0 \times 10^{-4}$	∿0	15.0	$<1.0 \times 10^{-4}$	
1340	2.1×10^{-4}	24.	6.0	2.1×10^{-4}	
1700	3.0×10^{-3}	∿0	(c)	3.0×10^{-3}	Ref. 4-15; pp. 4-5
1700	3.3×10^{-4}	∿0	(c)	3.3×10^{-4}	
1700	1.2×10^{-4}	∿0	(c)	1.2×10^{-4}	
1000	6.0×10^{-6}	∿0	(c)	6.0×10^{-6}	Ref. 4-16; Table 6b, p. 34
1200	2.3×10^{-5}	∿0	(c)	2.3×10^{-6}	

[a] All particles are BISO type particles with HTI coatings.

[b] The listed times correspond to the one available datum; a conservative value of R was calculated by assuming t = 1 h.

[c] Data were extrapolated to 1 h as shown in Fig. 4-6.

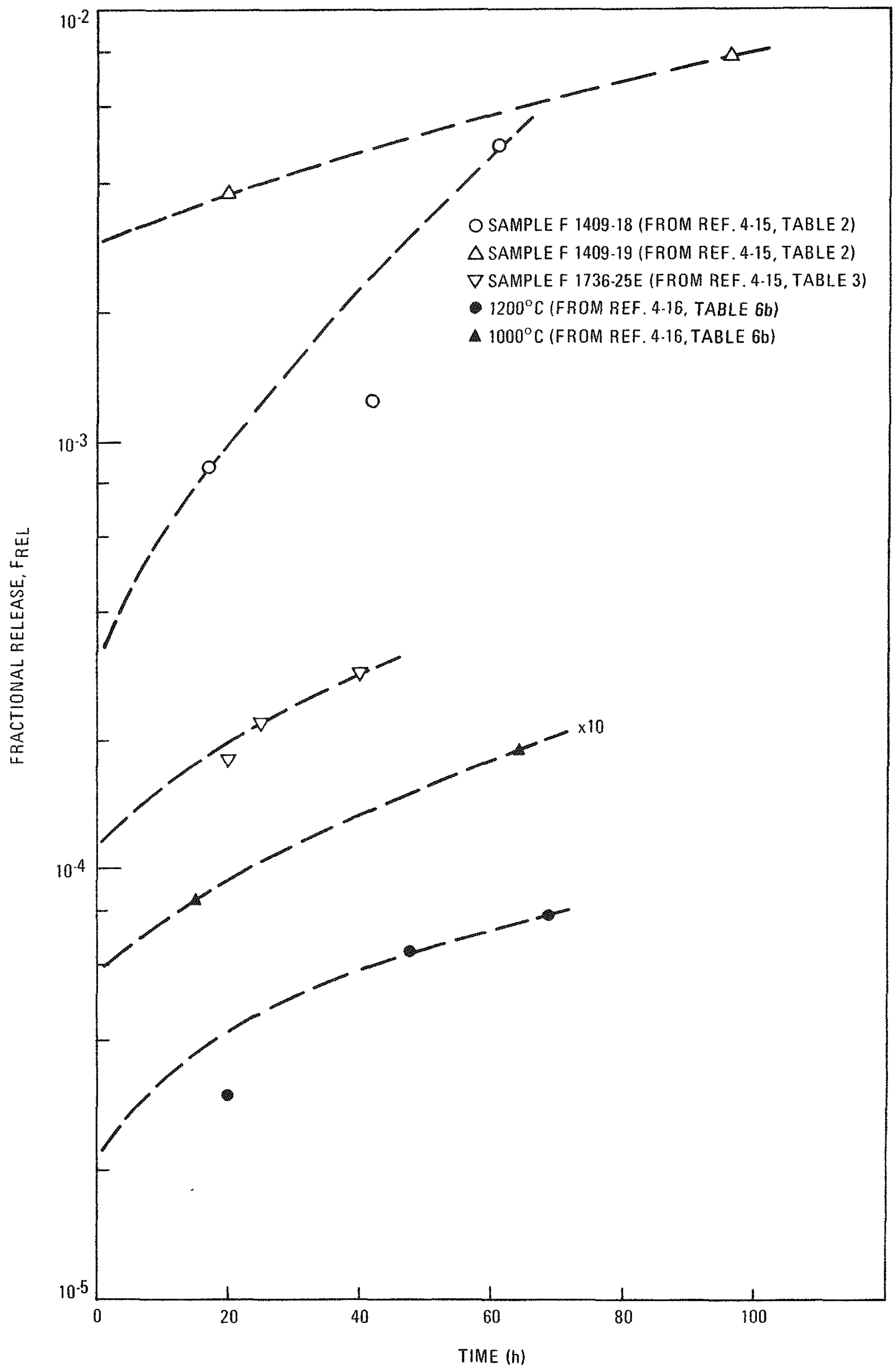

Fig. 4-6. Extrapolation of release data for iodine release from intact particles

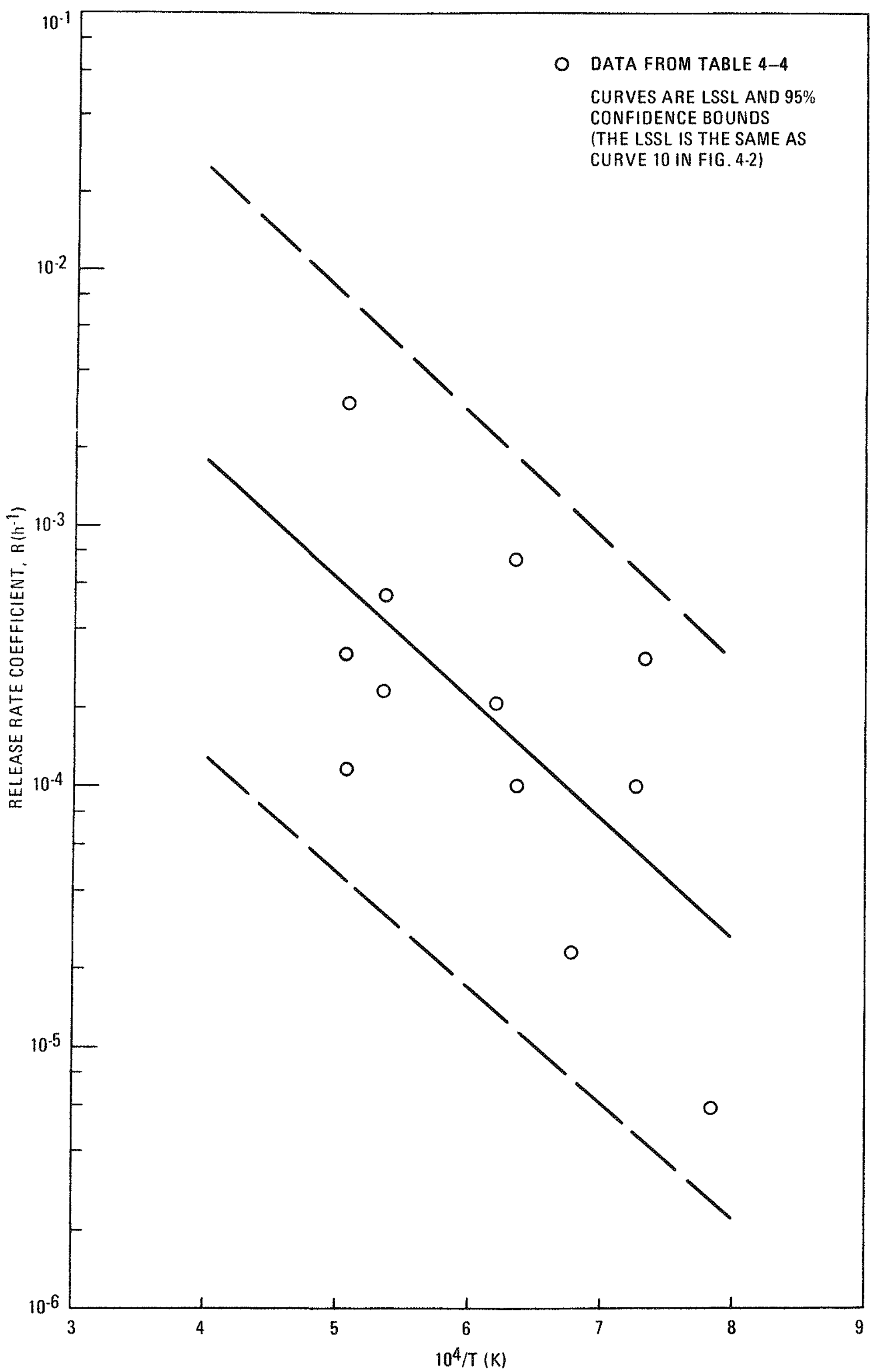

Fig. 4-7. Release rate coefficient - temperature curves for iodine release from intact particles

TABLE 4-5
RELEASE RATE COEFFICIENTS (R) FOR XENON RELEASE FROM "FAILED" (UNCOATED) PARTICLES OF $(Th,U)C_2$[a]

Temp. (°C)	F_{rel}	R	Data Source
2000	0.44	0.58	Ref. 4-16; Fig. 6, p. 14
2000	0.30	0.36	
1800	0.25	0.29	
1800	0.14	0.15	
1600	0.09	0.094	
1600	0.09	0.094	
1400	0.033	0.033	
1400	0.0095	0.0095	

[a] All data are for ∿0% FIMA; the data are from 1-h anneals.

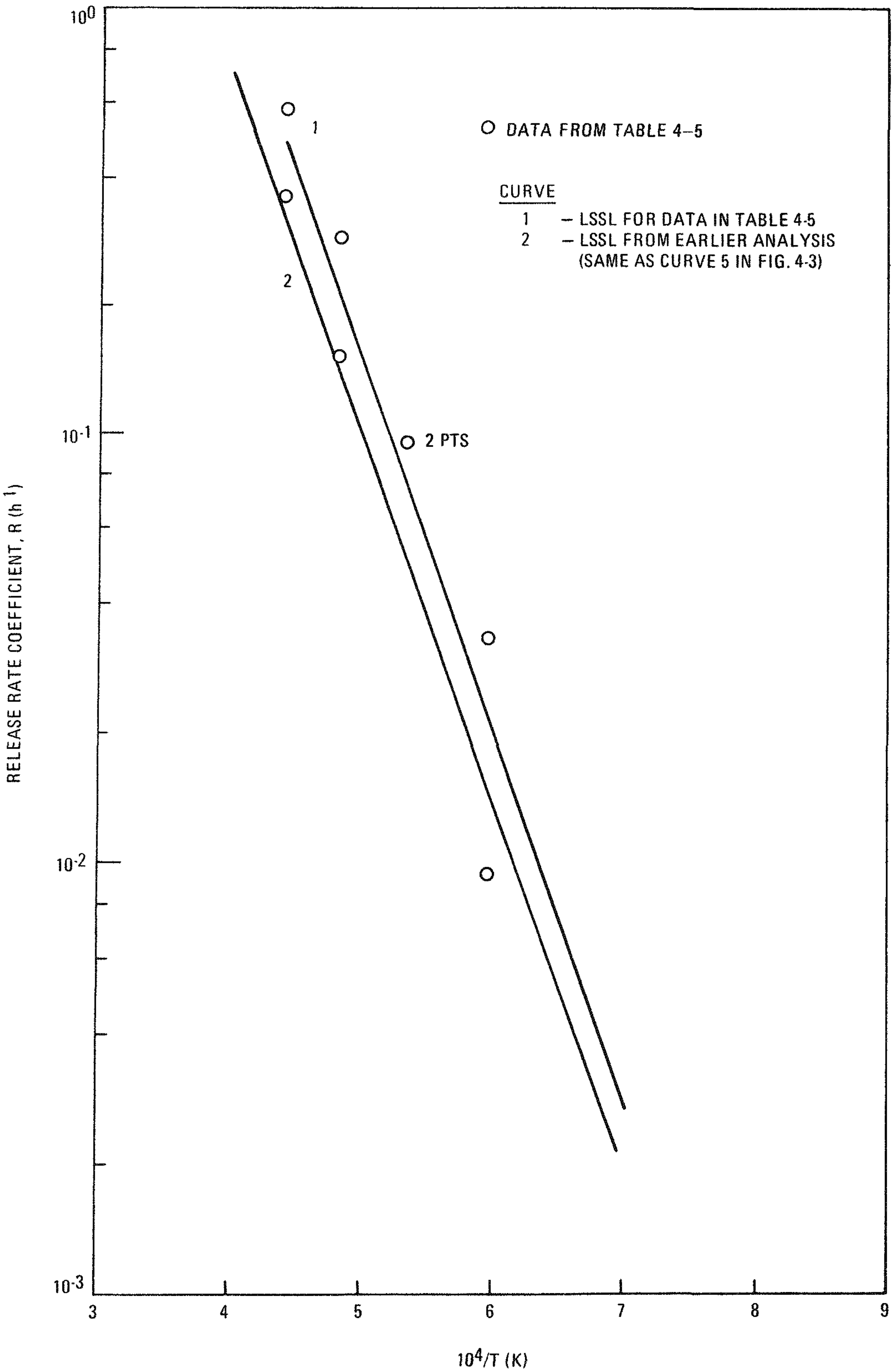

Fig. 4-8. Release rate coefficient - temperature curves for xenon release from "failed" particles

by the graphite matrix is less than by constrained coatings (Ref. 4-12). Therefore curve 1 should yield a conservatively high estimate of release. Curve 2, which is the same as curve 5 in Fig. 4-3, is an early least-squares fit of the release rate coefficient data, and this curve does not differ significantly from curve 1; therefore retention of curve 2 as the reference curve is justified.

The data of Table 4-5 are restricted to carbide kernels. There apparently are no data on the time dependence of xenon fractional release for oxide kernels. The only guide to estimating the relative fractional releases for oxide kernels compared to carbide kernels is the relation between these types of kernels as found for iodine in the previous section. For iodine the release rate coefficients for oxides are about a factor of twenty larger than those for carbides. [Compare the mean curves for constrained, failed particles of the present analysis in Figs. 4-4 and 4-5, for example, at $10^4/T$ (K) = 6.5.] Iodine is frequently assumed to behave like xenon and evidence for this exists (for example, see Table 4 of Ref. 4-16).

The xenon release rate coefficient curve for carbide kernels lies very close to the iodine curve for oxide kernels in failed constrained particles (compare curve 2 of Fig. 4-8 with curve 4 of Fig. 4-4). Thus, on the basis that the fractional release of xenon and iodine are the same, it is assumed that the xenon release rate coefficient curve for oxide kernels in constrained failed particles will be adequately represented by the present xenon release rate coefficient curve for carbide particles. Accordingly, curve 2 of Fig. 4-8 is taken to represent xenon release from both oxide and carbide kernels in constrained failed particles. Curve 2 should be especially conservatively high for carbide kernels considering the much lower iodine release rate observed for carbide kernels compared to oxide kernels.

For the data of Table 4-5, the burnup was very small. There are no data on the effect of burnup for xenon release from failed fuel particles. This effect is taken into account through the uncertainty assigned to curve 2 of Fig. 4-8. A moderately conservative estimate is made that the upper bound to curve 2 is a factor of 10 greater than the mean (LSSL) curve. This estimate accounts for the available data on burnup as presented previously in the case of iodine release from failed TRISO particles.

Xenon Release From Intact Particles

The data for xenon release at early times from intact BISO and TRISO coated particles are shown in Table 4-6. The values of F_{rel} in Table 4-6 are treated in an effectively conservative manner by assuming these values of F_{rel} correspond to measurements taken 1 hour after annealing began. The data from Refs. 4-16 and 4-19 have fractional releases 100 times smaller than the other data in Table 4-6. The reason for this discrepancy is unknown but on the basis of comparative studies (Ref. 4-18), the discrepancy possibly results from differences in the manufacturing processes for various lots of particles. Since data are not available for reference particles, a conservative position is taken, and the low-release data are excluded in computing the mean curve.

The data for R in Table 4-6 are plotted in Fig. 4-9. These release data are too limited to determine the temperature dependence of R. Instead, this dependence is fixed by taking the slope of the release rate coefficient - temperature curve to be the same as for iodine release from intact particles. The resulting mean curve, as shown in Fig. 4-9, was drawn so as to pass through the point $R = 2.2 \times 10^{-5}$ at $10^4/T$ (K) = 6.0, which is also a point on the least-squares straight line fit to the R data of Table 4-6. The bound curve of Fig. 4-9 is based on the same uncertainty as was assigned to the mean curve for iodine release from intact particles.

Krypton Release From Failed Particles

There are no available fractional release data which are suitable for calculating release rate coefficients for krypton release from failed particles. Steady-state release fraction (R/B) data are available (Ref. 4-16) for uncoated particles irradiated for 1 hour. These data are not directly applicable to core heatup accident analyses. However, these steady-state

TABLE 4-6

RELEASE RATE COEFFICIENTS (R) FOR XENON RELEASE FROM INTACT PARTICLES

Temp (°C)	F_{rel}	Percent FIMA	t (h)	Coating	R	Data Source
1600	$<6.2 \times 10^{-5}$	24.0	2.5	HTI	6.2×10^{-5}	Ref. 4-14;
1600	$<5.6 \times 10^{-5}$	24.0	2.5	HTI	5.6×10^{-5}	pp. 136-138,
1100	$<1.7 \times 10^{-5}$	8.5	15.0	HTI	1.7×10^{-5}	BISO particles
1300	$<4.4 \times 10^{-5}$	8.5	14.9	HTI	4.4×10^{-5}	
1400	1.1×10^{-5}	(a)	5	(a)	1.1×10^{-5}	Ref. 4-18;
1400	6.4×10^{-6}	(a)	5	(a)	6.4×10^{-6}	p. 140,
1400	7.4×10^{-6}	(a)	5	(a)	7.4×10^{-6}	TRISO particles
1400	1.3×10^{-5}	(a)	5	(a)	1.3×10^{-5}	
1400	5.2×10^{-5}	(a)	5	(a)	5.2×10^{-5}	
1400	2.4×10^{-5}	(a)	5	(a)	2.4×10^{-5}	
1700	$<1.7 \times 10^{-7}$ (b)	∿0	65	LTI		Ref. 4-16;
1400	$<2.7 \times 10^{-7}$	∿0	65	LTI		Table 6,
1200	$<2.2 \times 10^{-7}$	∿0	20	LTI		p. 34,
1000	$<1.8 \times 10^{-7}$	∿0	15	LTI		BISO particles
1400	3.2×10^{-7}	--	5	LTI		Ref. 4-19; Table V.11, p. 217, BISO particles

(a) Data not given in Ref. 4-18.

(b) Note that the very low release data are not used (see text).

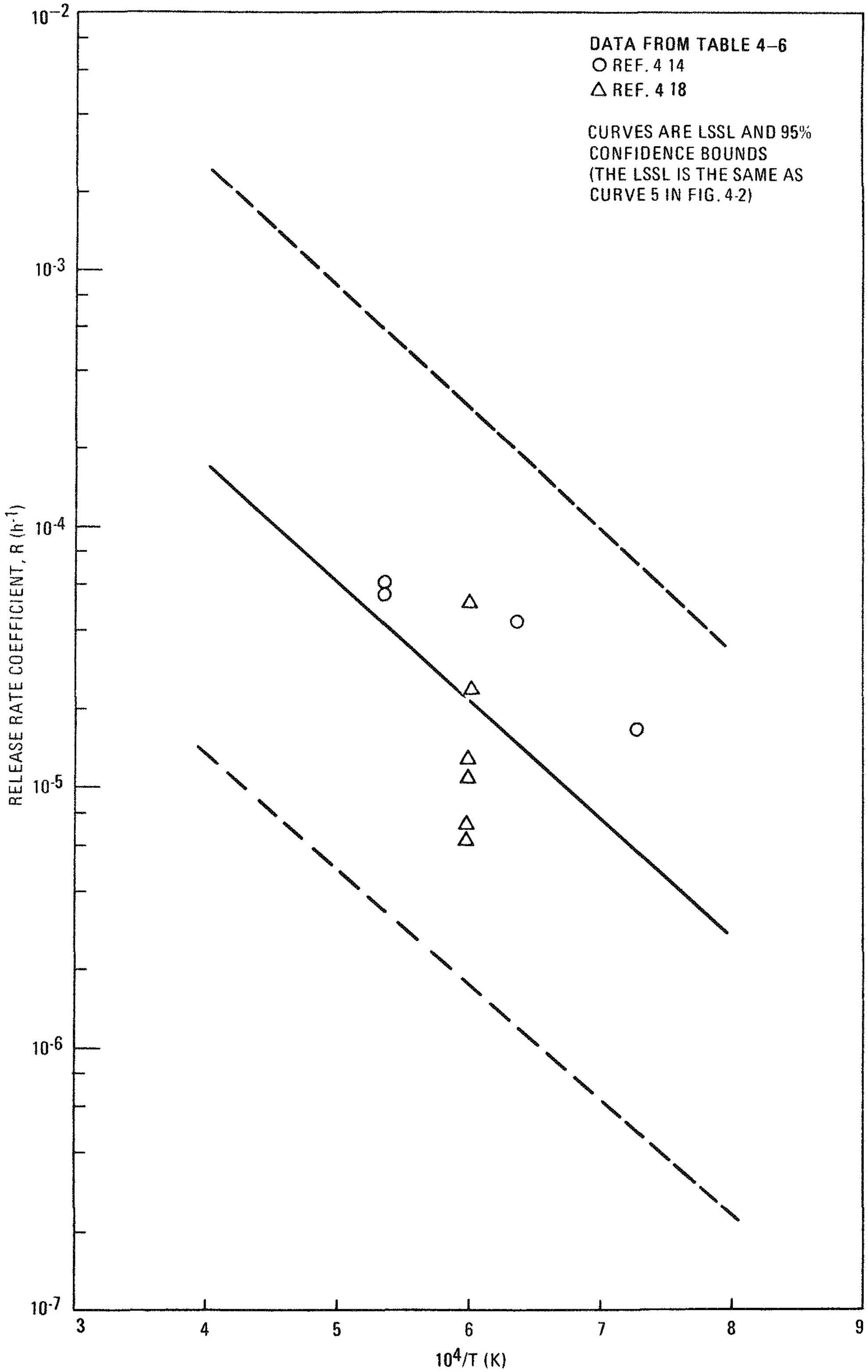

Fig. 4-9. Release rate coefficient - temperature curves for xenon release from intact particles

data were used in earlier estimates of the release rate coefficients and are the basis for the reference curve (curve 6 in Fig. 4-3).

A different approach, which is considered to be more reliable, is the following. The assumption is made that the ratio of the release rate coefficients for Kr to Xe is given by the ratio of the corresponding R/B values as measured in loops, reactors, etc. Ratios have been recently evaluated (Ref. 4-20). To estimate the release rate coefficient curve for krypton release from failed particles, the release rate coefficient curve for xenon release from failed particles, curve 2 of Fig. 4-8, was multiplied by appropriate values of the ratios. The resulting curve is shown in Fig. 4-10 as curve 1. To obtain this curve, points at 1100° and 1400°C on curve 2 of Fig. 4-8 were multiplied by the ratios 2.5 and 3.3, respectively.

This estimated mean curve is compared in Fig. 4-10 with the mean curve from the earlier analysis. The differences only exceed a factor of 3 above 2300°C; since extrapolation of any curve much beyond this temperature is not justified, the differences in the curves can be neglected. Therefore, the retention of curve 2 as the reference curve is justified.

The uncertainties of the krypton curve are unlikely to be smaller than those associated with the corresponding xenon curve and therefore a factor of ±10 in R values will give moderately conservative bounds.

<u>Krypton Release From Intact Particles</u>

The data on krypton release from intact particles are listed in Table 4-7 and shown in Fig. 4-11. The scatter in these data is large, but the data correspond roughly to those for xenon as presented in Table 4-6. To maintain consistency, the release rate coefficient curve for xenon release from intact particles is used but multiplied by the ratios given above to represent krypton release from intact particles. The resulting curve is shown in Fig. 4-11 as curve 1. This curve was obtained by multiplying points at 1100° and 1400°C on curve 1 of Fig. 4-9 by the ratios 2.5 and

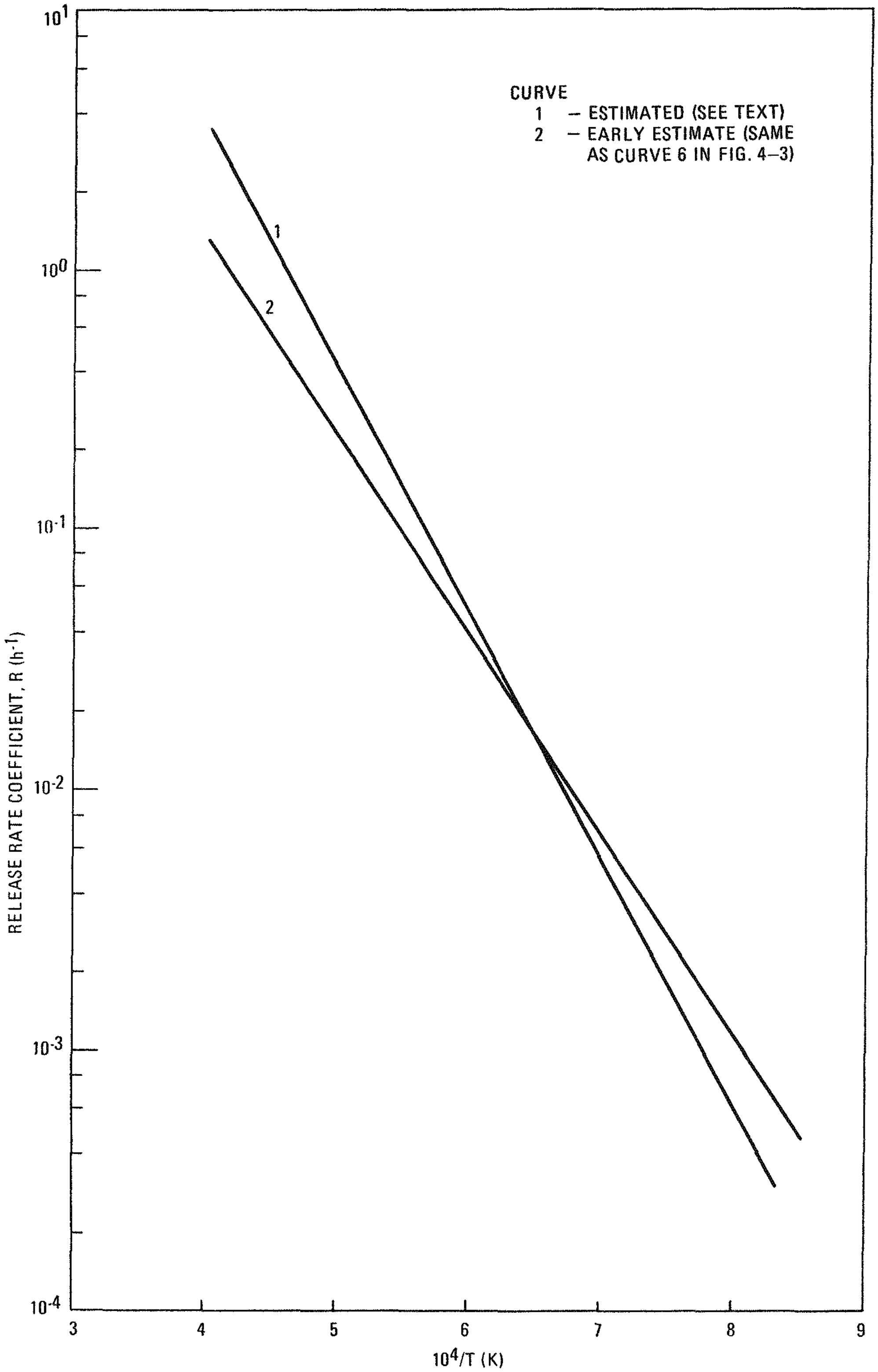

Fig. 4-10. Comparison of mean curves for krypton release from failed particles

TABLE 4-7
RELEASE RATE COEFFICIENTS (R) FOR KRYPTON
RELEASE FROM INTACT PARTICLES

Temp (°C)	F_{rel}	$R^{(a)}$	Data Source
1440	3.0×10^{-6}	$= F_{rel}$	Ref. 4-21
1600	6.0×10^{-6}		
1370	$<1 \times 10^{-6}$		
1700	1.0×10^{-6}		
1370	4.0×10^{-6}		
1660	$<1 \times 10^{-6}$		
1800	$<1 \times 10^{-6}$		
1370	$<1 \times 10^{-6}$		
1660	$<1 \times 10^{-6}$		
2000	4.5×10^{-5}		
1370	2.0×10^{-6}		
1370	4.2×10^{-4}		
1520	1.1×10^{-4}		
1370	9.0×10^{-6}		
1700	1.1×10^{-5}		
2000	1.6×10^{-5}		
1370	2.5×10^{-5}		
1700	1.8×10^{-5}		
2000	2.2×10^{-5}		

(a) $F_{rel} = 1 - e^{-Rt} \approx Rt \equiv R$, for t = 1 h.

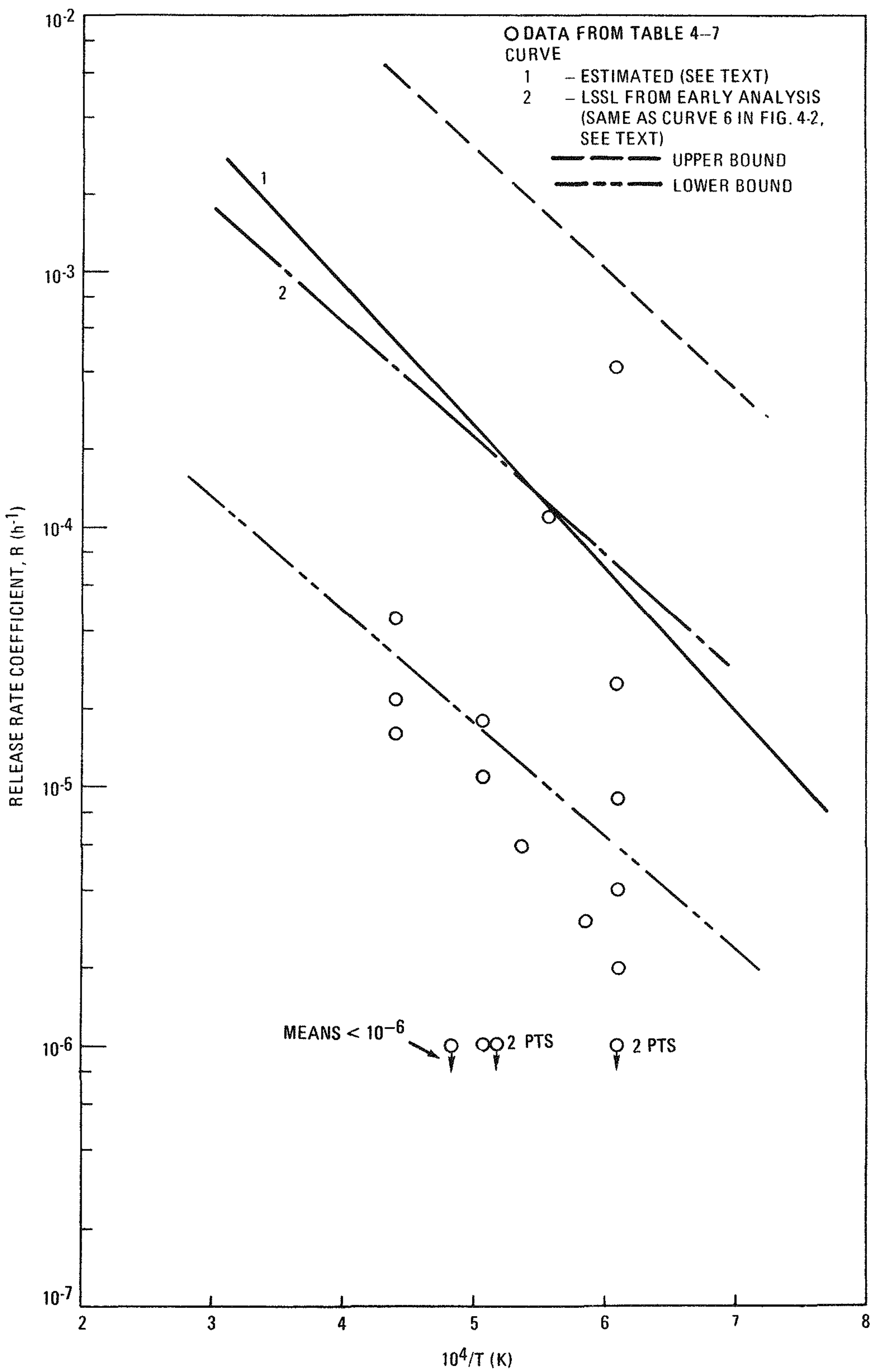

Fig. 4-11. Release rate coefficient - temperature curves for krypton release from intact particles

3.3, respectively. Curve 1 of Fig. 4-11 differs negligibly from curve 2 of an earlier analysis, justifying curve 2 as the reference curve. The assigned uncertainties shown in Fig. 4-11 are the same as used for xenon release from intact particles.

Cesium Release From Failed Particles

Recent experimental data (Ref. 4-22) for cesium release from failed particles are presented in Table 4-8. These data are plotted in Fig. 4-12. The least-squares straight line and 95% confidence bounds are also given in Fig. 4-12. The least-squares straight line is the reference curve (curve 2 in Fig. 4-3).

The data derived from the Peach Bottom element and from the FTE-2 laser-drilled particles are in agreement except for one datum at 1400°C. This agreement indicates that the coating type, HTI or LTI, is not important for release from failed particles, as expected.

For the particles with ThO_2 kernels, near peak burnup was achieved; for particles with carbide kernels, the burnup was small relative to peak burnup. Since no release rate data are available for carbide kernels at peak burnup, there is an unknown uncertainty in applying the mean curve of Fig. 4-12 to predict release of cesium from failed particles with carbide kernels. However, the release rate coefficients of Fig. 4-12 are quite high; for example, taking into account the upper confidence bound, all cesium would be released in 30 minutes at 1500°C. Thus, use of the mean curve and confidence limits of Fig. 4-12 for carbide particles should produce little error in times of the order of hours under accident conditions.

Cesium Release From Intact Particles

The data used for obtaining release rate coefficient curves for cesium release from intact particles are given in Table 4-9. The data from Ref. 4-23 are for BISO-type particles with essentially HTI coatings and FIMA of 8.5%. The data of Table 4-9 are plotted in Fig. 4-13 and the mean (LSSL)

TABLE 4-8
RELEASE RATE COEFFICIENTS (R) FOR CESIUM
RELEASE FROM FAILED PARTICLES[a]

Temp. (°C)	F_{rel}	Percent FIMA	Particles	R	Data Source
1000	9.0×10^{-4}	∿5	$(Th,U)C_2$ with HTI coating	9.0×10^{-4}	Peach Bottom element P13-05, 100% failed
1200	2.5×10^{-2}			2.5×10^{-2}	
1400	1.8×10^{-1}			2.0×10^{-1}	
1000	1.5×10^{-3}			1.5×10^{-3}	
1200	2.0×10^{-2}			2.0×10^{-2}	
1400	2.8×10^{-1}			3.3×10^{-1}	
1000	3.0×10^{-3}	∿7	ThO_2 BISO with LTI coating	3.0×10^{-3}	FTE-2; laser-drilled particles
1200	1.4×10^{-2}			1.4×10^{-2}	
1400	5.5×10^{-3}			5.5×10^{-3}	

[a] Data from Ref. 4-22. Anneal times are 1 h.

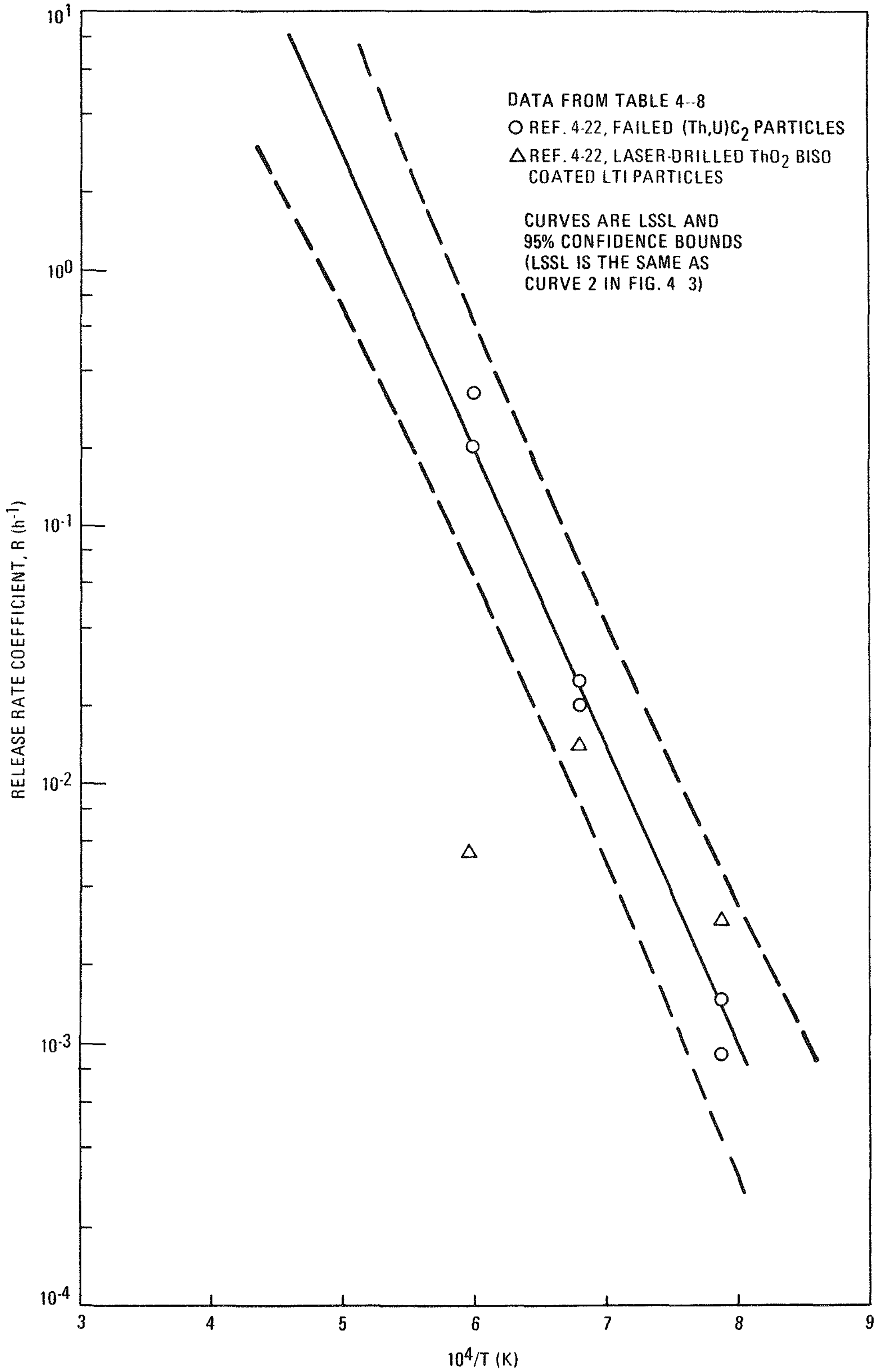

Fig. 4-12. Release rate coefficient - temperature curves for cesium release from failed particles

TABLE 4-9
RELEASE RATE COEFFICIENTS (R) FOR CESIUM
RELEASE FROM INTACT PARTICLES

Temp. (°C)	F_{rel}	Percent FIMA	R	Data Source
1370	3×10^{-4}	∼0	3×10^{-4}	Ref. 4-21;
1700	4×10^{-4}	∼0	4×10^{-4}	p. 104
2000	2×10^{-3}	∼0	2×10^{-3}	
1100	2.8×10^{-5}	8.5	2.8×10^{-5}	Ref. 4-23;
1250	5.5×10^{-5}	8.5	5.5×10^{-5}	pp. 104, 106
1500	1.2×10^{-4}	8.5	1.2×10^{-4}	
2000	$\sim 2 \times 10^{-2}$	8.5	$\sim 2 \times 10^{-2}$	
1100	2.2×10^{-5}	8.5	2.2×10^{-5}	
1250	4.9×10^{-5}	8.5	4.9×10^{-5}	
1500	1.2×10^{-4}	8.5	1.2×10^{-4}	
1750	2.3×10^{-4}	8.5	2.3×10^{-4}	

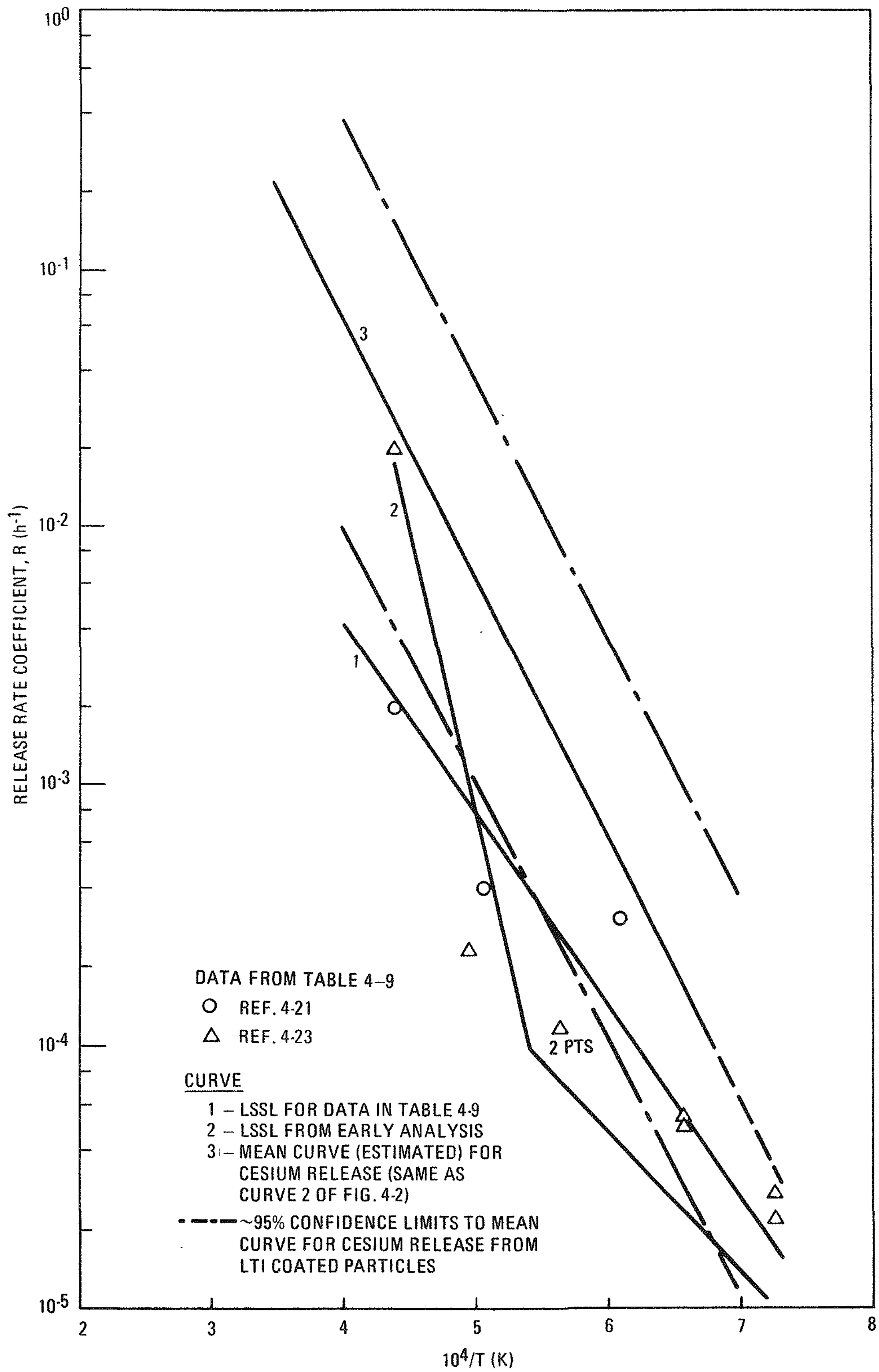

Fig. 4-13. Release rate coefficient – temperature curves for cesium release from intact particles

curve (curve 1) from the present analysis as well as curve 2 (a slightly revised version of the Ref. 4-7 mean curve) are drawn. The differences in the two mean curves are due primarily to the assumption in Ref. 4-23, and thus in Ref. 4-7, that the release rate coefficient curves (coefficients being evaluated at 20 hours) which exhibit two portions with different slopes reflect the operation of two different release mechanisms and not simply errors in the measurements. In the present analysis, this assumption has not been made on the basis that (1) the data are too few to draw such a strong conclusion, (2) other data (Ref. 4-24) for certain particles show no evidence for a changing slope of release rate coefficient curves, and (3) the evaluation of release rate coefficients at 20 hours is not satisfactory for accident analysis given that Eq. 4-1 has to be used. Consequently, the mean curve of the present analysis is an adequate representation of the data.

The data, as mentioned above, are primarily for HTI coatings, whereas LTI coatings are of primary interest in HTGRs. A clear demonstration has been given (Ref. 4-25) that the diffusion coefficient of cesium in LTI is significantly greater than the diffusion coefficient in HTI pyrocarbon. Therefore, a correction to the mean curve of the present analysis is in order. The correction is made as follows. The fractional release is proportional to the square root of the diffusion coefficient for small values of the products of reduced diffusion coefficient and time and decay frequency and time (Ref. 4-26). The approximation that this proportionality can be applied to correct the HTI coating data is used. Thus the mean curve of Fig. 4-13 is increased by factors derived from the square root of the ratio of diffusion coefficients for LTI to HTI pyrocarbon coatings as determined from Ref. 4-25. At $10^4/T$ (K) = 4.0, the factor is determined to be 14.6 and at $10^4/T$ (K) = 6.0, the factor is 4.1. The new mean curve for cesium release from LTI coated particles is shown by curve 3 of Fig. 4-13. Notice that in obtaining this new curve, the further assumption of a proportionality between fractional release and release rate coefficient has been made. This curve is the same as curve 2 in Fig. 4-2.

The uncertainty associated with the new mean curve will be the standard deviation of a single point based on the data of Table 4-9. The standard deviation of a single point rather than that of the mean is chosen to take into account differences in the materials to which the data may be applied from the materials on which the data were based. This consideration is in addition to the differences between HTI and LTI pyrocarbon which has been accounted for by the use of multiplying factors. The confidence bounds at the 95% limit are shown in Fig. 4-13.

Additional data at 4% FIMA (Ref. 4-24) are available but were overlooked in this review until completion of the analysis. Rather than revise the analysis, which could not be essentially altered thereby, the data will be briefly discussed. The data are given in the form of release rate coefficients which are calculated for initial release behavior; thus, qualitatively they are acceptable for the present review. At temperatures above 1400°C, these data are not significantly different from the data plotted in Fig. 4-13; for temperatures of 1400°C and smaller, the data lie below the data of Fig. 4-13. Thus the dependence of release rate coefficients on FIMA is apparently weak for intact particles as expected. On this basis, the effect of FIMA can be neglected and omission of the 4% FIMA data is not important.

Strontium Release From Intact BISO Particles

The data for strontium release at early times from BISO type particles are given in Table 4-10. All data are for intact particles except for the one case noted and only data at 1 hour after start of annealing are used except as noted.

All the particles considered in Table 4-10 had carbide kernels, whereas the reference BISO particles have ThO_2 kernels. However, this discrepancy is relatively unimportant because the release of strontium is controlled by diffusion through the pyrocarbon at temperatures above 1400°C. At lower temperatures, the release of strontium is controlled by

TABLE 4-10
RELEASE RATE COEFFICIENTS (R) FOR
STRONTIUM RELEASE

Temp. (°C)	F_{rel}	Percent FIMA	Kernel and Coating	R	Data Source
1300	7.4×10^{-4}	4.0	$(Th,U)C_2$	7.4×10^{-4}	Ref. 4-23;
1400	2.9×10^{-2}	4.0	HTI	2.9×10^{-2}	p. 112
1750	4.6×10^{-1}	4.0		6.2×10^{-1}	
1250	9.0×10^{-2}	7.5	UC_2[a]	9.4×10^{-2}	Ref. 4-27; p. 111
1100	4.0×10^{-3}	24.0	$(Th,U)C_2$	4.0×10^{-3}	Ref. 4-14;
1300	5.6×10^{-1}	24.0	HTI	8.2×10^{-1}	Table 3.19,
1100	2.6×10^{-3}	24.0		2.6×10^{-3}[b]	p. 137
1300	2.2×10^{-1}	24.0		2.5×10^{-1}[c]	
1400	3.5×10^{-3}[d]	0	Carbide LTI	3.5×10^{-3}	Ref. 4-19; Table V.11, p. 217
1100	2.0×10^{-3}	8.5	$(Th,U)C_2$	2.0×10^{-3}	Ref. 4-28;
1250	3.5×10^{-2}	8.5	HTI	3.6×10^{-2}	p. 105
1500	3.6×10^{-1}	8.5		4.5×10^{-1}	
2000	4.0×10^{-1}	8.5		5.1×10^{-1}	
1370	7.0×10^{-3}	∿0	$(Th,U)C_2$	7.0×10^{-3}	Ref. 4-21;
1700	1.1×10^{-1}	∿0	?	1.2×10^{-1}	p. 104
2000	3.8×10^{-1}	∿0		4.8×10^{-1}	

(a) All coatings were intact except for this case in which the coating was mechanically failed.

(b) 1.5 h point treated as a 1 h point.

(c) Based on extrapolated value to obtain F_{rel} at 1 h.

(d) Average of four lots.

kernel diffusion. The assumption of pyrocarbon control of release at temperatures below 1400°C will result in overpredicting the release but not by a significant amount since the contribution to total release below 1400°C is small as a result of the exponential dependence of release on temperature (considering the temperature ramp conditions of accidents). Therefore, it is assumed that the pyrocarbon controls the release of strontium at all temperatures of interest.

Unlike the case of cesium, as discussed earlier, the data for strontium migration through LTI and HTI pyrocarbon indicate there is little difference between the diffusion coefficients for strontium in LTI and HTI pyrocarbon (Refs. 4-25, 4-29). Most of the particles represented in Table 4-10 have HTI coatings but these were treated, along with the rest, as if they had LTI coatings.

The data of Table 4-10 are plotted in Fig. 4-14; examination of these data shows a dependence on FIMA with large release rate coefficients associated with large FIMA values. The FIMA values range from 0 to 24%. Such a correlation between the diffusion coefficient of cesium in pyrocarbon and FIMA has recently been noted (Ref. 4-30) and is apparently independent of kernel type. Further work is required to understand the correlation, although it appears not to extend much above 20% FIMA. In the present case, where FIMA values of less than 7.5% are of concern, this correlation is considered only in terms of the assigned uncertainties. The mean curve for the intact particle data plotted in Fig. 4-14 is shown as curve 1. Curve 2, which is derived from an earlier analysis and appears as curve 1 BISO in Fig. 4-2, is in error apparently due to a transcription error. However, it does not differ significantly from curve 1 within the uncertainty limits shown in Fig. 4-14. These limits are based on the standard deviation of a single estimated value of the dependent variable. Curve 1 is being used in current SORS calculations of strontium release from intact BISO coated particles.

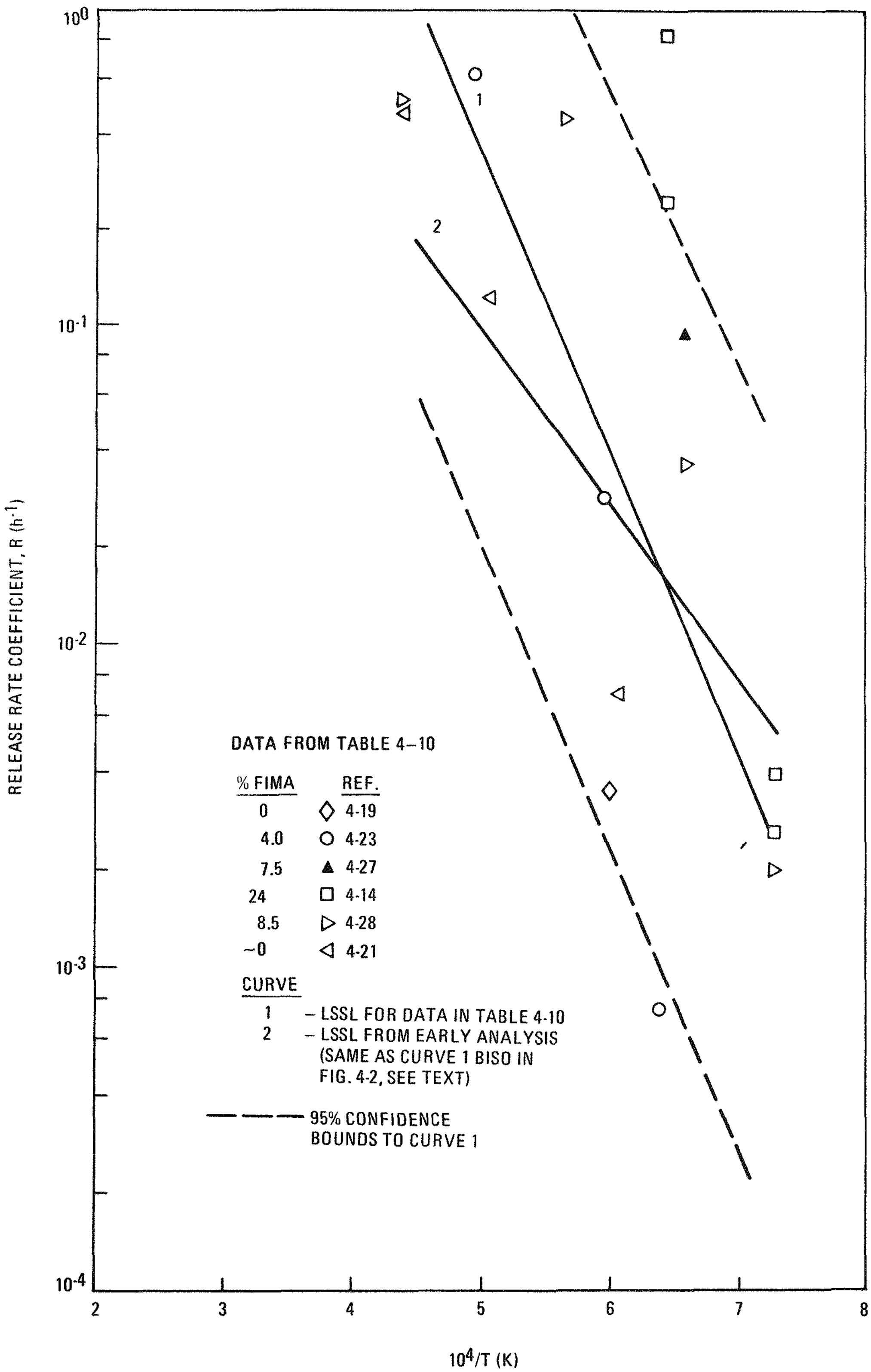

Fig. 4-14. Release rate coefficient - temperature curves for strontium release from BISO particles

Strontium Release From Failed Particles

For strontium release from failed particles, only one point is available from the existing data (Table 4-10). Therefore, the release rate coefficient curve for failed particles was established by multiplying curve 1 of Fig. 4-14 by the ratio of the failed particle datum to the datum of curve 1 at the same temperature. This ratio, from Fig. 4-14, is 8.2. The uncertainty is assumed to be the same as in the intact particle case.

The release rate coefficient curve of Fig. 4-3 for strontium release from failed particles (curve 1) differs from the recommended curve for the same reason as noted above in the case of strontium release from intact BISO particles. Again the difference is not significant but the recommended curve should be used.

Strontium Release From Intact TRISO Particles

The data for strontium release from intact TRISO particles are given in Table 4-11. Because of the high anneal temperatures involved, data are available on particles without some defect only at one temperature (1400°C) and it is necessary to consider defective particles to estimate the temperature dependence of the release rate coefficients. The particles listed in Table 4-11 are classified as defective if (1) the inner pyrocarbon coating is missing, (2) a high release of xenon was obtained, or (3) the coating contamination by uranium was large.

Classification of the data is given in the legend of Fig. 4-15 and a mean curve is drawn for classification sets 1, 4, and 5. Sets 3 and 6, with nonzero FIMA values, yield mean curves not significantly different from the curves for the corresponding zero FIMA data sets. Thus, no effect of FIMA on the release rate coefficient is shown by the data. The three mean curves have essentially the same slope. The mean curve for set 2, the particles without defects, is drawn parallel to the other mean curves and is passed through the mean value for data of this set at 1400°C. For this mean curve, the uncertainty is estimated to be a factor of about 50.

TABLE 4-11
RELEASE RATE COEFFICIENTS (R) FOR STRONTIUM
RELEASE FROM INTACT TRISO PARTICLES

Temp. (°C)	F_{rel}[a]	Percent FIMA	R	Defective	Symbol	Data Source
1400	3.7×10^{-5}	~ 0	3.7×10^{-5}		○	Ref. 4-31
1600	2.8×10^{-4}	~ 0	2.8×10^{-4}		○	
1800	7.7×10^{-4}	~ 0	7.7×10^{-4}		○	
1400	1.4×10^{-3}	~ 0	1.4×10^{-3}	x	●	Ref. 4-31
1600	3.5×10^{-3}	~ 0	3.5×10^{-3}	x	●	
1400	3.5×10^{-6}	~ 0	3.5×10^{-6}		●	Ref. 4-31
1600	1.0×10^{-3}	~ 0	1.0×10^{-3}	x	●	
1800	1.8×10^{-2}	~ 0	1.8×10^{-2}	x	●	
1400	2.2×10^{-4}	~ 0	2.2×10^{-4}	x	●	
1600	1.6×10^{-3}	~ 0	1.6×10^{-3}	x	●	
1800	1.1×10^{-2}	~ 0	1.1×10^{-2}	x	●	
1400	2.3×10^{-6}	~ 0	2.3×10^{-6}		○	Ref. 4-31
1600	4.5×10^{-5}	~ 0	4.5×10^{-5}		○	
1800	4.2×10^{-5}	~ 0	4.2×10^{-5}		○	
1400	3.5×10^{-5}	10.5	3.5×10^{-5}		◇	Ref. 4-31
1600	1.9×10^{-4}	10.5	1.9×10^{-4}		◇	
1800	3.8×10^{-4}	10.5	3.8×10^{-4}		◇	
1800	5.4×10^{-5}	13.2	5.4×10^{-5}		◇	
1600	2.8×10^{-3}	11.6	2.8×10^{-3}	x	◆	
1800	9.6×10^{-2}	11.6	1.0×10^{-1}	x	◆	
1800	4.4×10^{-2}	12.6	4.5×10^{-2}	x	◆	
1800	1.6×10^{-2}	13.2	1.6×10^{-2}	x	◆	
1400	1.1×10^{-7}	~ 0	1.1×10^{-7}		△	Ref. 4-19
1400	2.4×10^{-7}	~ 0	2.4×10^{-7}		△	
1400	1.9×10^{-5}	~ 0	1.9×10^{-5}	x	▲	
1400	1.3×10^{-5}	~ 0	1.3×10^{-5}	x	▲	
1400	1.9×10^{-6}	~ 0	1.9×10^{-6}		△	
1400	8.1×10^{-5}	~ 0	8.1×10^{-5}	x	▲	
1400	3.3×10^{-6}	~ 0	3.3×10^{-6}		△	
1400	4.8×10^{-7}	~ 0	4.8×10^{-7}		△	
1400	1.4×10^{-4}	~ 0	1.4×10^{-4}	x	▲	
1400	2.9×10^{-4}	~ 0	2.9×10^{-4}	x	▲	

[a] Fractional release values at 1 h.

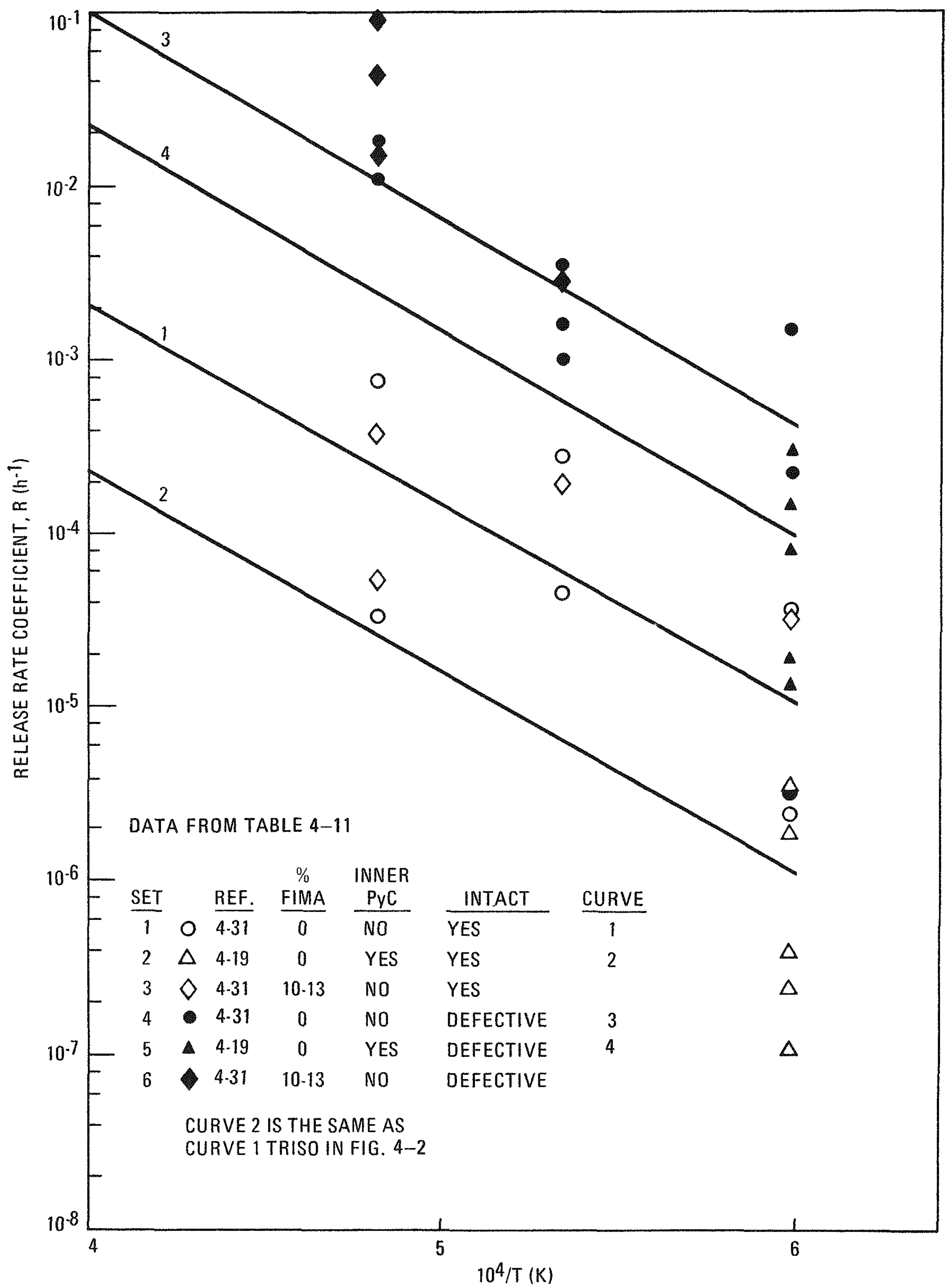

Fig. 4-15. Release rate coefficient - temperature curves for strontium release from intact TRISO particles

Cerium Release From Intact BISO and Failed Particles

The data for cerium release from intact BISO particles are given in Table 4-12 and shown in Fig. 4-16. These data represent only pyrocarbon coated $(Th,U)C_2$ kernels. Furthermore, for the particles represented by the GA data (Refs. 4-23 and 4-24), the coatings were HTI pyrocarbon.

There are fewer related experiments on which to base an approach to interpretation of these cerium data than for the cases of cesium or strontium, but the general procedure in the past has been to liken cerium to strontium in its behavior as a migrating fission product. With the assumption of similarity in transport for cerium and strontium, one expects little dependence on the pyrocarbon coatings represented by HTI or LTI. Thus, in Table 4-12 the data for particles with HTI coatings can be treated as representing data obtained on particles with LTI coatings. Furthermore, one expects a dependence of the release rate coefficient on FIMA, which is shown by the data of Fig. 4-16.

The choice of the mean curve is somewhat arbitrarily made by using the curve for the 8.5% FIMA case as shown in Fig. 4-16. The uncertainty associated with the mean curve is based on the standard deviation of a single estimated value of the dependent variable.

For failed particles, no data are available; in accordance with the assumption of the similarity of cerium and strontium, the same treatment and factor that were applied to strontium for failed particles are also applied to cerium.

Cerium Release From Intact TRISO Particles

As there are apparently no data for the case of cerium release from intact TRISO particles, the corresponding curve and uncertainties applicable to strontium release from intact TRISO particles can be used on the assumption of a similarity between cerium and strontium in regard to transport in particles.

TABLE 4-12
RELEASE RATE COEFFICIENTS (R) FOR CERIUM RELEASE
FROM INTACT BISO PARTICLES

Temp. (°C)	F_{rel}	Percent FIMA	R	Data Source
1370	4.0×10^{-4}	∿0	4.0×10^{-4}	Ref. 4-21; p. 104
1700	5.0×10^{-3}	∿0	5.0×10^{-3}	
2000	8.0×10^{-2}	∿0	8.3×10^{-2}	
1100	1.5×10^{-4}	8.5	1.5×10^{-4}	Ref. 23; pp. 105, 107
1250	5.1×10^{-3}	8.5	5.1×10^{-3}	
1500	2.4×10^{-2}	8.5	2.4×10^{-2}	
2000	4.7×10^{-1}	8.5	6.3×10^{-1}	
1100	8.0×10^{-5}	8.5	8.0×10^{-5}	
1250	1.2×10^{-3}	8.5	1.2×10^{-3}	
1500	2.2×10^{-3}	8.5	2.2×10^{-3}	
1750	1.8×10^{-1}	8.5	2.0×10^{-1}	
1300	(a)	4.0	1.3×10^{-5}	Ref. 4-24; P. 62
1400	(a)	4.0	1.6×10^{-4}	
1750	(a)	4.0	3.5×10^{-3}	
2000	(a)	4.0	1.0×10^{-1}	
1300	(a)	4.0	1.6×10^{-4}	
1750	(a)	4.0	8.5×10^{-3}	
2000	(a)	4.0	7.1×10^{-2}	

[a] R values are presented in Ref. 4-24.

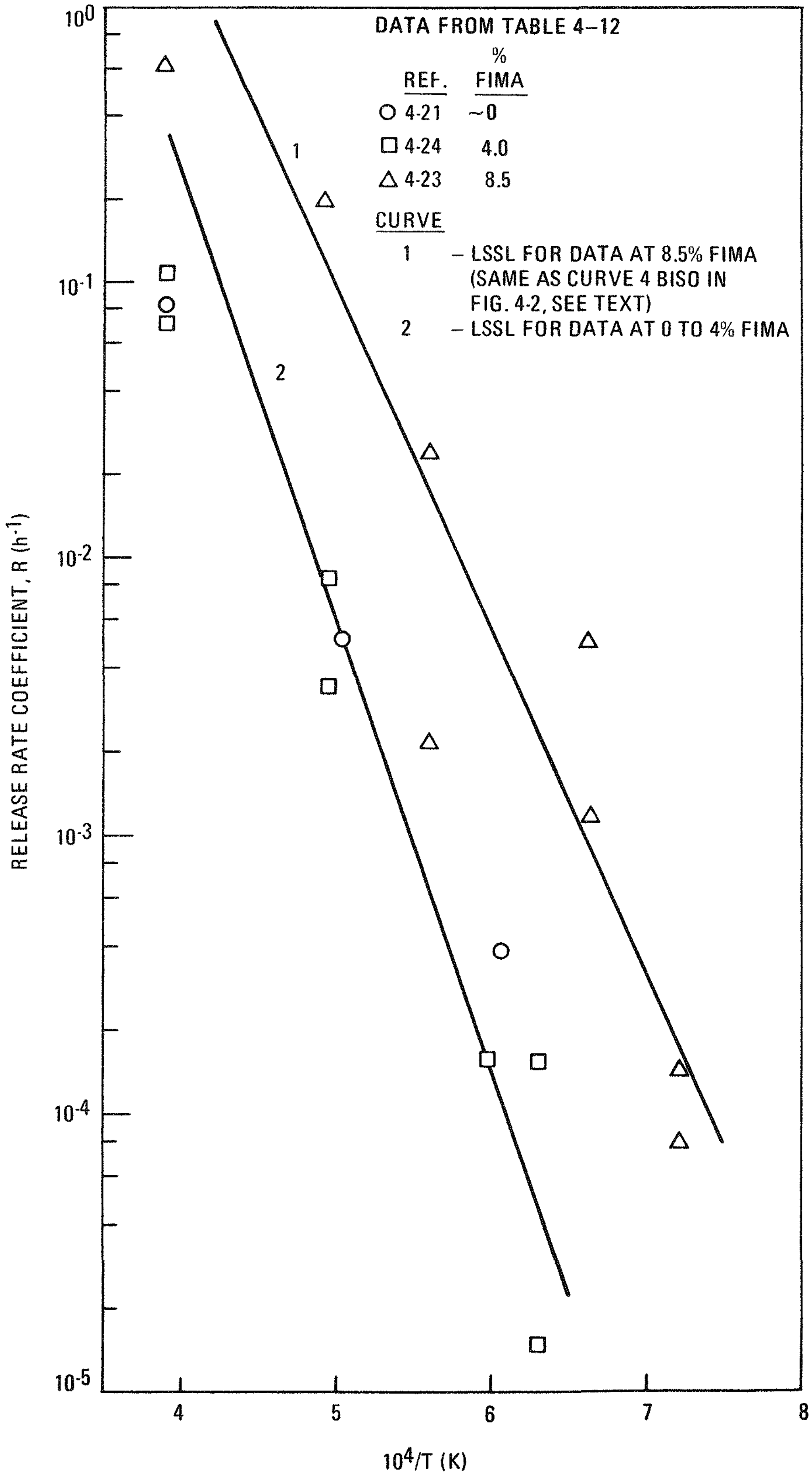

Fig. 4-16. Release rate coefficient – temperature curves for cerium release from intact BISO particles

Barium Release From Intact BISO and Failed Particles

The data on intact particles for barium are given in Table 4-13 and in Fig. 4-17; these data represent particles with carbide kernels and with both HTI and LTI coatings. These data indicate no significant difference between release rate coefficients for particles with LTI and HTI coatings, but clearly exhibit (excluding Ref. 4-21 data) a dependence of the release rate coefficient on FIMA. These statements provide the basis for considering a similarity between barium and strontium (or cerium). Thus, as in the case of strontium, all data are used to derive a mean curve for the release rate coefficients for barium. Note that three of the data points included in Table 4-13 were obtained by extrapolation of release-time data. The derived mean curve is shown in Fig. 4-17.

The uncertainty associated with the mean curve is taken to be the same as in the case of strontium; the 95% confidence bounds are shown in Fig. 4-17.

For failed particles, no data are available. Therefore, the same procedure as was used in the case of strontium was used for barium, i.e., an increase in all values from the mean curve for release rate coefficients for intact BISO particles by a factor of 8.2. The uncertainties are estimated to be a factor of about 50.

Barium Release From Intact TRISO Particles

The data for barium release from intact TRISO particles are similar to those for strontium and the treatment of the data for barium parallels that used in the case of strontium. The data are given in Table 4-14; some of the release fractions were obtained by extrapolation of release-time curves. The data are plotted in Fig. 4-18; the legend for Fig. 4-18 summarizes the group classification.

The best representation of barium release rate coefficients from intact TRISO particles is given by curve 2 of Fig. 4-18, which was derived

TABLE 4-13
RELEASE RATE COEFFICIENTS (R) FOR BARIUM RELEASE
FROM INTACT BISO PARTICLES

Temp. (°C)	F_{rel}[a]	Percent FIMA	Coating	R	Data Source
1300	(b)	4.0	HTI	1.2×10^{-4}	Ref. 4-24; p. 62
1400	(b)	4.0	HTI	3.5×10^{-3}	
1750	(b)	4.0	HTI	5.0×10^{-3}	
2000	(b)	4.0	HTI	1.4×10^{-1}	
1300	(b)	4.0	HTI	2.0×10^{-4}	
1750	(b)	4.0	HTI	1.4×10^{-2}	
2000	(b)	4.0	HTI	8.5×10^{-2}	
1100	$<2 \times 10^{-3}$	24.0	HTI	$<2 \times 10^{-3}$	Ref. 4-14; p. 137
1300	1.6×10^{-1}	24.0	HTI	1.7×10^{-1}	
1300	2.7×10^{-3}	8.5	HTI	2.7×10^{-3}	
1200	5.0×10^{-5}	∿0	LTI	5.0×10^{-5}	Ref. 4-16; p. 34
1000	1.0×10^{-3}	∿0	LTI	1.0×10^{-3}	
1370	4.0×10^{-3}	∿0	--	4.0×10^{-3}	Ref. 4-21; p. 104
1700	1.3×10^{-1}	∿0	LTI	1.4×10^{-1}	
2000	3.0×10^{-1}	∿0	LTI	3.6×10^{-1}	
1400	3.4×10^{-4}	∿0	LTI	3.4×10^{-4}	Ref. 4-19; p. 217

(a) Values for 1 h.

(b) R values are presented in Ref. 4-24.

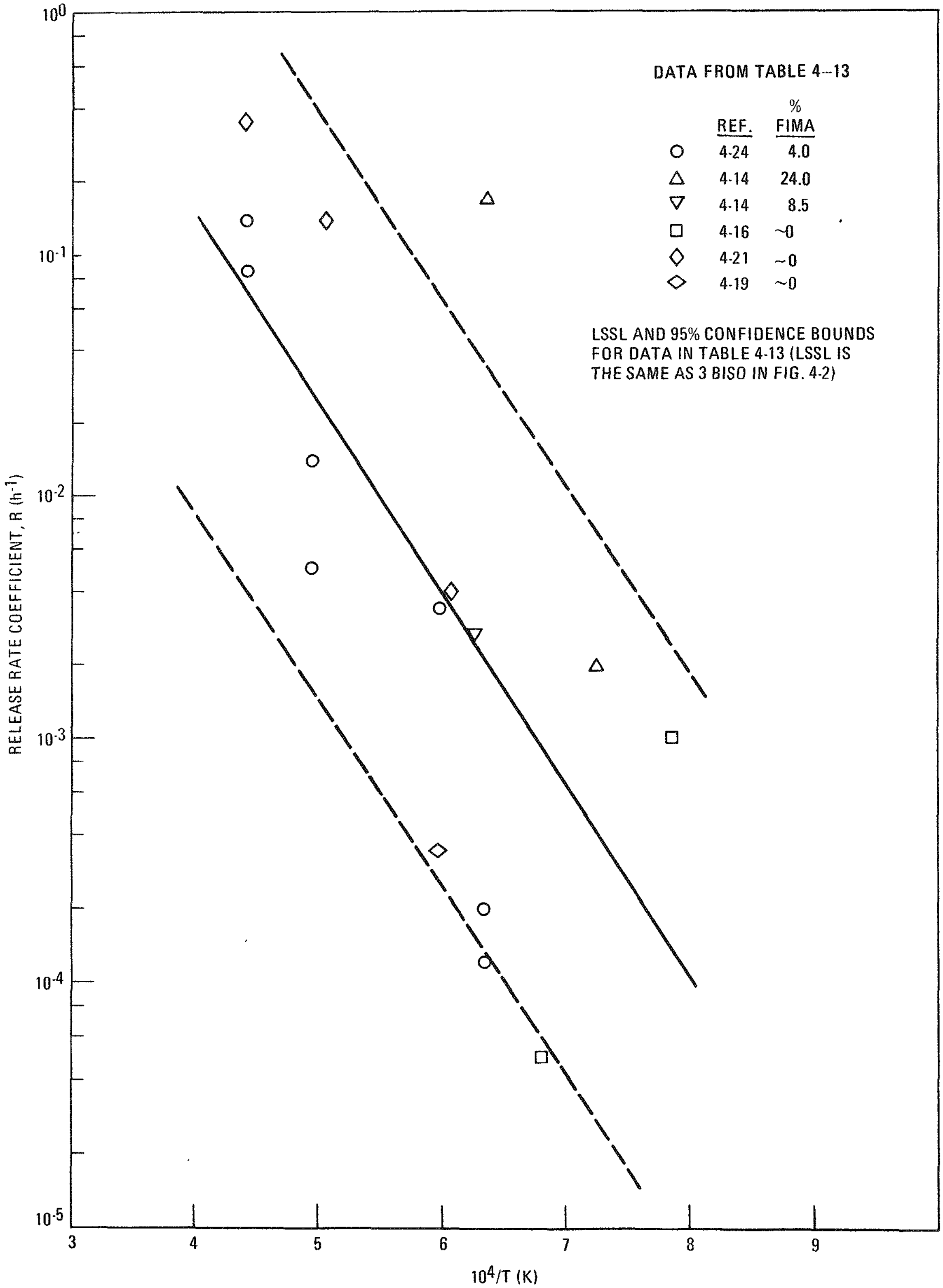

Fig. 4-17. Release rate coefficient - temperature curves for barium release from intact BISO particles

TABLE 4-14
RELEASE RATE COEFFICIENTS (R) FOR BARIUM RELEASE
FROM INTACT TRISO PARTICLES

Temp. (°C)	F_{rel} (a)	Percent FIMA	R	Defective	Symbol	Data Source
1400	4.9×10^{-5}	~ 0	4.9×10^{-5}		○	Ref. 4-31
1600	7.3×10^{-5}	~ 0	7.3×10^{-5}		○	
1800	1.6×10^{-4}	~ 0	1.6×10^{-4}		○	
1400	1.9×10^{-4}	~ 0	1.9×10^{-4}	x	●	
1600	4.1×10^{-3}	~ 0	4.1×10^{-3}	x	●	
1400	2.3×10^{-5}	~ 0	2.3×10^{-5}	x	●	
1600	2.0×10^{-4}	~ 0	2.0×10^{-4}	x	●	
1800	6.4×10^{-3}	~ 0	6.4×10^{-3}	x	●	
1400	2.4×10^{-5}	~ 0	2.4×10^{-5}	x	●	
1600	8.8×10^{-5}	~ 0	8.8×10^{-5}	x	●	
1800	2.9×10^{-3}	~ 0	2.9×10^{-3}	x	●	
1400	2.2×10^{-6}	~ 0	2.2×10^{-6}		○	
1600	5.9×10^{-6}	~ 0	5.9×10^{-6}		○	
1800	2.0×10^{-5}	~ 0	2.0×10^{-5}		○	
1400	1.2×10^{-4}	10.5	1.2×10^{-4}		◇	
1600	1.3×10^{-5}	10.5	1.3×10^{-5}		◇	
1800	4.2×10^{-5}	10.5	4.2×10^{-5}		◇	
1600	1.5×10^{-4}	13.2	1.5×10^{-4}		◇	
1800	1.3×10^{-4}	13.2	1.3×10^{-4}		◇	
1400	1.9×10^{-5}	11.6	1.9×10^{-5}	x	◆	
1600	8.5×10^{-4}	11.6	8.5×10^{-4}	x	◆	
1800	9.2×10^{-2}	11.5	9.7×10^{-2}	x	◆	
1800	3.4×10^{-2}	12.6	3.5×10^{-2}	x	◆	
1800	1.7×10^{-2}	13.2	1.7×10^{-2}	x	◆	
1400	2.9×10^{-7}	~ 0	2.9×10^{-7}	x	▲	Ref. 4-19
1400	9.9×10^{-7}	~ 0	9.9×10^{-7}		△	
1400	2.0×10^{-6}	~ 0	2.0×10^{-6}	x	▲	
1400	2.6×10^{-7}	~ 0	2.6×10^{-7}		△	
1400	1.8×10^{-4}	~ 0	1.8×10^{-4}	x	▲	

(a) Fractional release values at 1 h.

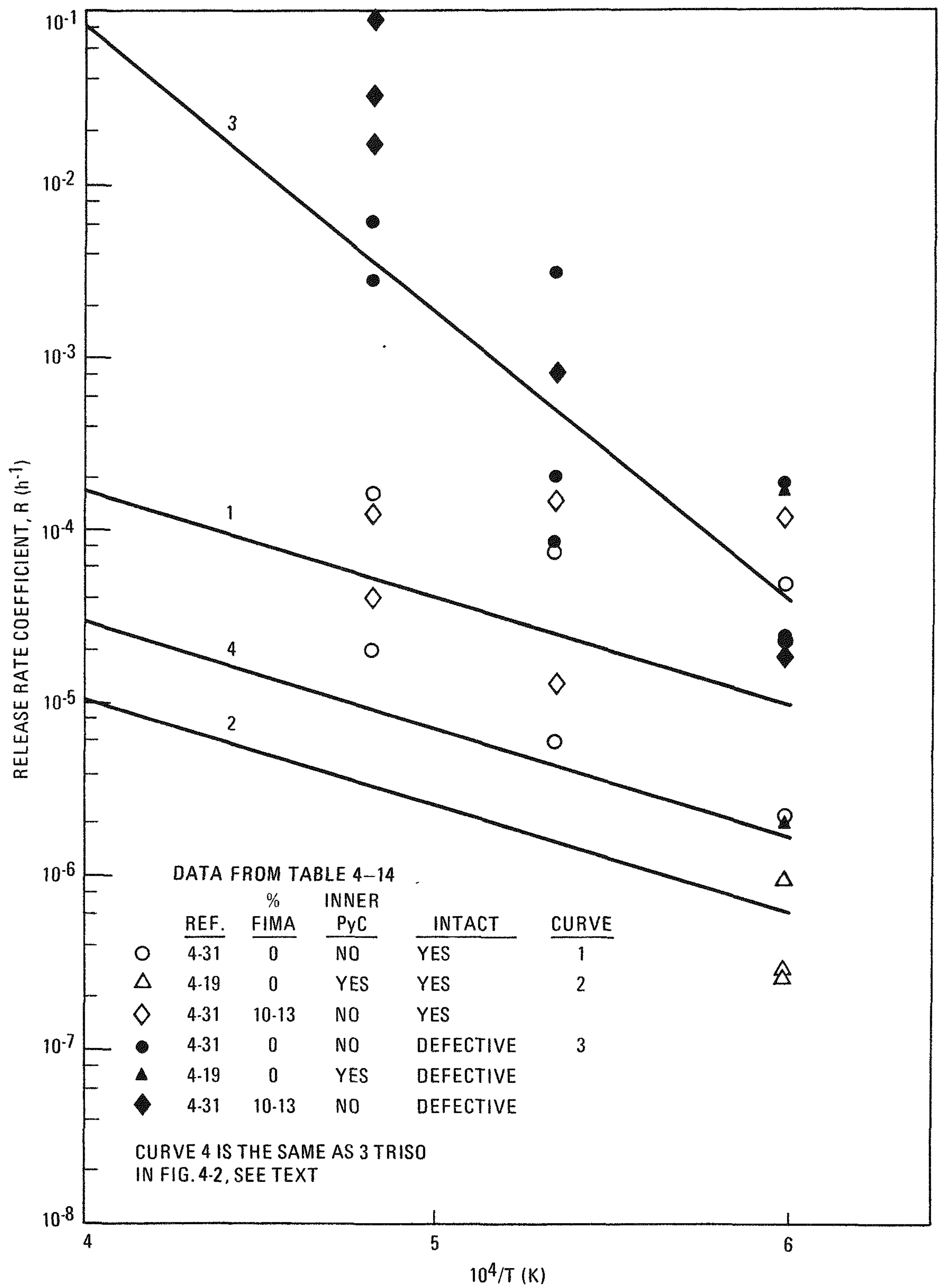

Fig. 4-18. Release rate coefficient – temperature curves for barium release from TRISO particles

as in the case of strontium. Curve 4, which is from an earlier analysis, is conservative with respect to curve 2 and, on this basis, is retained as the reference curve. The uncertainty estimate, as in the case of strontium, is given by a factor of about 50.

Release of Other Elements From Intact and Failed Particles

For elements other than those discussed above, there are no documented data. The release rate constants for Rb, Sm, Eu, Zr, Nb, Mo, Tc, Pm, Nd, Pr, Y, Pd, Sn, La, Ru, Rh, Se, Br, Te, and Sb are selected from the data presented here on the basis of the similarity of chemical or physical properties with the elements considered (see Figs. 4-2 and 4-3 and Ref. 4-7).

Summary of Release Rate Coefficient and Uncertainty Data

The release rate coefficients are calculated according to the equation

$$\log_{10} R = A - B\ [10^4/T\ (K)] \quad , \qquad (4\text{-}2)$$

where A and B are constants as given in Table 4-15. To calculate the associated uncertainties, standard deviation factors are employed. The standard deviation factor is defined by

$$S_F = e^S \quad , \qquad (4\text{-}3)$$

where S is the standard deviation in $\log_e R$ (the natural logarithm of R). The standard deviation factors are given in Table 4-16. To derive 95% confidence limits, the following equations are used:

Upper limit

$$R_u = R \cdot e^{1.645S} \qquad (4\text{-}4)$$

TABLE 4-15

PARAMETERS IN THE EQUATION FOR RELEASE RATE COEFFICIENTS AS A FUNCTION OF TEMPERATURE

$$\log_{10} R = A + B[10^4/T(K)]$$

Group[a]	Element(s)	Intact BISO		Intact TRISO		Failed BISO[b]		Failed TRISO[b]	
		A	B	A	B	A	B	A	B
1	Sr	1.55[c]	-0.521[c]	0.851	-1.134	2.23[d]	-0.521[d]	2.23[d]	-0.521[d]
2	Cs,Rb	2.81	-1.01	2.81	-1.01	6.19	-1.15	6.19	-1.15
3	Ba,Sm,Eu	2.28	-0.782	-2.03	-0.625	3.19	-0.782	3.19	-0.782
4	Ce	5.21	-1.242	0.851	-1.134	6.12	-1.242	6.12	-1.242
5	Xe	-1.95	-0.452	-1.95	-0.452	3.28	-0.856	3.28	-0.856
6	Kr	-1.951	-0.452	-1.951	-0.452	3.18	-0.768	3.18	-0.768
7	Zr,Nb,Mo,Tc	0.851	-1.134	0.851	-1.134	6.12	-1.242	6.12	-1.242
8	Pm,Nd,Pr,Y,Pd,Sn,La	-1.951	-0.452	0.851	-1.134	6.12	-1.242	6.12	-1.242
9	Ru,Rh	-1.951	-0.452	0.851	-1.134	6.12	-1.242	6.12	-1.242
10	Se,Br,Te,Sb,I	-0.951	-0.452	-0.951	-0.452	3.366	-0.796	0.8736	-0.599

(a) The group classification is that shown in Figs. 4-2 and 4-3.

(b) The factors for failed BISO and failed TRISO are applied to reference particles with failed coatings (i.e., failed fertile particles with BISO coatings and ThO_2 kernels and failed fissile particles with TRISO coatings and dense UC_2 kernels). Except for group 10, the parameters for each group are the same for failed BISO and failed TRISO.

(c) Current values are A = 4.23, B = -0.937.

(d) Current values are A = 5.14, B = -0.937.

TABLE 4-16

STANDARD DEVIATION FACTORS (S_F) FOR THE RELEASE RATE COEFFICIENTS

$S_F = e^S$; S = standard deviation in $\log_e R$[a]

Group[b]	Element(s)	S_F			
		Intact BISO	Intact TRISO	Failed BISO[c]	Failed TRISO[c]
1	Sr	5.4	10.0	5.4	5.4
2	Cs,Rb	3.0	3.0	2.0	2.0
3	Ba,Sm,Eu	5.4	10.0	10.0	10.0
4	Ce	10.0	10.0	10.0	10.0
5	Xe	4.7	4.7	4.1[d]	4.1[d]
6	Kr	4.7	4.7	4.1[d]	4.1[d]
7	Zr,Nb,Mo,Tc	10.0	10.0	10.0	10.0
8	Pm,Nd,Pr,Y,Pd,Sn,La	4.7	10.0	10.0	10.0
9	Ru,Rh	4.7	10.0	10.0	10.0
10	Se,Br,Te,Sb,I	4.7	4.7	1.7	2.7

[a] Note that logarithm to the base 10 is used in Table 4-15 but in this table logarithm to the base e is used.

[b] The group classification is that shown in Figs. 4-2 and 4-3.

[c] The factors for failed BISO and failed TRISO are applied to reference particles with failed coatings (i.e., failed fertile particles with BISO coatings and ThO_2 kernels and failed fissile particles with TRISO coatings and dense UC_2 kernels). Except for group 10, the factors for each group are the same for failed BISO and failed TRISO.

[d] The values are slightly larger than reported in Ref. 4-9.

Lower limit

$$R_1 = R \cdot e^{-1.645S} \quad . \qquad (4\text{-}5)$$

TASK 600: COOLANT IMPURITY/CORE MATERIAL INTERACTION

Subtask 610: Reaction of Coolant Impurities with Fuel Material

Work on this subtask during the past quarter included: (1) measurements of the expansive force due to hydrolyzing ThC_2 and (2) setup and checkout of equipment for measurements of the rate of hydrolysis of irradiated carbide fuel.

The former experiment utilizes equipment and procedures given in Ref. 4-4. In this test the internal pressure of hydrolyzing ThC_2 fuel samples contained by graphite crucibles is continuously measured using a load cell. Water concentrations of from 1000 to 30,000 ppmv in helium and temperatures of 200° to 700°C are utilized. The measured pressure can then be related to graphite stress and will be used to establish criteria for steam ingress and fuel element design.

The apparatus for monitoring the rate of hydrolysis of ThC_2 and UC_2 utilizes both thermogravimetry and gas analysis techniques. In this test the rate of uptake of moisture of a sample of carbide fuel is measured with a sensitive recording microbalance. Simultaneously, the rate of evolution of gaseous products, hydrogen, and/or hydrocarbons is continuously monitored with a gas chromatograph. Parameters of primary importance in this study are (1) degree of burnup in the sample of fuel materials, (2) moisture concentration, and (3) temperature. Thus far, experiments on unirradiated UC_2 have been performed and emphasis has been placed on measurements on small fuel samples consisting of a few fuel particles. This is of importance because only relatively small amounts of irradiated fuel can be handled in this apparatus due to the high radiation involved.

TASK 900: FORT ST. VRAIN CHEMISTRY SURVEILLANCE

Subtask 940: Fort St. Vrain Coolant Impurity Surveillance

Summary

During the recent steady operation of the Fort St. Vrain HTGR at 28% power, gaseous impurity concentrations have in general been below the technical specification limits for full-power operation. Using the GOP computer code, good correlations are found between calculated and measured concentrations indicating that radiolysis-induced chemical reactions contributed largely to the specific mixtures of impurities in the primary circuit.

Introduction

Primary coolant impurities were monitored during the recent 7-week-long steady operation of the reactor at 28% power (December 10, 1965 through January 30, 1977). During this period coolant impurities were observed to decrease to relatively low levels compared to those observed in the initial rise to 27% in July 1976. For example, the steady-state concentration of oxidizing impurities ($CO + CO_2 + H_2O$) was typically below 10 ppmv, which is the technical specification limit for full-power operation. The low impurity concentration was due to the excellent operation of the purification system and to diminished steady sources of impurities such as outgassing of primary circuit components. Transient impurity sources have occurred, however, which caused occasional spiking of certain impurity concentrations. These transient sources have been identified as (1) injection of emergency water to the circulator bearings via the accumulators, (2) pump-up of PCRV pressure from helium storage, and (3) changes in power or core temperature.

Computer analysis of the impurity data is being performed with the use of the GOP code by G. L. Tingey and W. C. Morgan of Battelle Pacific Northwest Laboratory. The GOP code is used to calculate steady-state impurity concentrations in the HTGR by considering core geometry, temperature, flow rate, pressure, and ten chemical reactions (four thermal and six radiolytic). The purpose of this effort is to determine to what degree chemical reactions control the impurity concentrations in the Fort St. Vrain HTGR. Details of the capability of the GOP code and the analysis of the initial rise to 27% power are given in the previous quarterly (Ref. 4-2). The present GOP analysis is much improved over that reported in Ref. 4-2 because of certain changes and corrections which have been made to the code. A discussion of the GOP analysis follows.

Results and Conclusions of GOP Analysis

During the current quarter, errors were found in the manner in which the GOP code computed some of the radiolytic reactions. These errors were corrected, and other relatively minor adjustments were made in the code.

In these studies, there are some parameters that must be inferred from the gas compositions because of the lack of input data. For example, there is no way of knowing the rate of steady inleakage of H_2O into the coolant gas. In these startup tests it is assumed that some portion, and perhaps most, of the impurity comes from outgassing of the reactor graphite and other components. Therefore, for these calculations the H_2O inleakage rate was set such that the total oxygen content ($H_2O + CO + 2CO_2$) equalled the measured value.

During the early tests conducted in July 1976, the hydrogen purification system was not operating effectively and even during the last test (28% power), there appears to be some source of hydrogen other than water vapor (total H_2 > total O). Therefore, in these calculations the hydrogen purification rate was adjusted such that at steady state the H_2 added to the coolant would equal the H_2 removed in the purifier:

Leak rate of H_2O = purification of all hydrogen species

$$= P.F.[H_2O] + 2P.F.[CH_4] + P.F._{(H_2)}[H_2] \qquad (4-6)$$

$$P.F._{(H_2)} = \frac{Lk\ H_2O - P.F.[H_2O] - 2P.F.[CH_4]}{[H_2]}$$

$P.F._{(H_2)}$ = computed purification factor of H_2

P.F. = purification factor of H_2O, CH_4 = $\frac{\text{purification flow}}{\text{coolant inventory}}$

Using the above assumptions and the input data for GOP given in the previous quarterly report (Ref. 4-2), the gas compositions for various power levels up to 28% power were calculated. The calculated compositions are compared with measured compositions in Table 4-17.

It is interesting to note that the predicted values are in reasonably good agreement with the measured compositions for all power levels. The main exception is the low calculated CO compositions. In the GOP model, the primary source of CO is the thermal reaction of H_2O with carbon. However, at the temperatures of these tests, the contribution from this reaction is significant only at the 28% power level, and even there yields only 18% of the measured value. In the absence of thermal reactions, CO is only formed by the radiolytically induced water gas shift reaction ($CO + H_2O \rightarrow CO_2 + H_2$) and the carbon dioxide - graphite reaction ($CO_2 + C \rightarrow 2CO$), and these are partially offset by the reverse shift reaction. To predict the high CO levels observed from these reactions, unreasonable G values for the radiolytic reactions would be required. The source of the CO composition is, therefore, uncertain at this point. Several sources appear possible: (1) CO is outgassing from the core slowly and continuously, (2) the thermal reaction is contributing more CO than expected, and (3) the radiolytic reaction of H_2O with C yields both CO and CO_2.

In actual fact, more than one of these possibilities may be involved. Carbon monoxide outgassing will undoubtedly make a contribution during the lower power experiments; however, it would not appear to be a feasible explanation during the 6-week operation at 28% power. At this power level,

TABLE 4-17
MEASURED AND CALCULATED GAS COMPOSITIONS DURING FORT ST. VRAIN STARTUP

	2% Power		7.5% Power		11.4% Power		19.5% Power		27% Power		28% Power	
	GOP	Measured	GOP	Measured	GOP	Measured	GOP	Measured	GOP	Measured	GOP	Measured
H_2O, ppm	32	30	53	50	36	34	98	100	77	80	4.4	2.7
CO, ppm	0.0002	0.2	0.008	1	0.01	1.5	0.1	2	0.3	3	0.2	1.7
CO_2, ppm	0.4	0.7	2.4	3	2.1	2.5	8.2	6	9.6	7	0.5	0.6
H_2, ppm	14	22	21	25	22	33	68	80	37	30	3.1	10.5
CH_4, ppm	0.1	0.3	0.5	1.2	1.0	2	5.1	3.5	2.9	3	0.3	0.5
Outlet temperature, °C	240	240	330	330	390	390	450	450	500	500	610	--
H_2O leak rate, lb/h	0.09	--	0.17	--	0.12	--	0.45	--	0.04	--	0.025	--
H_2/H_2O purification rate[a]	0.05	--	0.18	--	0.11	--	0.09	--	0.37	--	0.18	--

[a] Ratio of H_2 purification flow to main purification flow.

it appears that the contribution from the thermal reaction has been underestimated. One is tempted to conclude from the analogy with the thermal steam-graphite reaction that both CO and CO_2 would be formed in the radiolytic process. This conclusion, however is not verified by experiment (Ref. 4-32). A more conclusive answer to this problem will require data at higher power levels and temperatures.

REFERENCES

4-1. "HTGR Accident Initiation and Progression Analysis Status Report, Volume V, AIPA Fission Product Source Terms," ERDA Report GA-A13617, General Atomic Company, February 1976.

4-2. "HTGR Fuels and Core Development Program Quarterly Progress Report for the Period Ending November 30, 1976," ERDA Report GA-A14180, General Atomic Company, December 27, 1976.

4-3. "HTGR Fuels and Core Development Program Quarterly Progress Report for the Period Ending August 31, 1976," ERDA Report GA-A14046, General Atomic Company, September 24, 1976.

4-4. "HTGR Fuels and Core Development Program Quarterly Progress Report for the Period Ending May 31, 1975," ERDA Report GA-A13444, General Atomic Company, June 30, 1975.

4-5. "HTGR Fuels and Core Development Program Quarterly Progress Report for the Period Ending August 30, 1974," ERDA Report GA-A13126, General Atomic Company, September 30, 1974.

4-6. "HTGR Fuels and Core Development Program Quarterly Progress Report for the Period Ending May 31, 1976," ERDA Report GA-A13941, General Atomic Company, June 30, 1976.

4-7. Schwartz, M. H., D. B. Sedgley, and M. M. Mendonca, "SORS: Computer Programs for Analyzing Fission Product Release from HTGR Cores During Transient Temperature Excursions," General Atomic Report GA-A12462 (GA-LTR-10), April 15, 1974.

4-8. "GASSAR-6, General Atomic Standard Safety Analysis Report," Section 2A (NRC Docket STN 50-535), February 1975.

4-9. "HTGR Accident Initiation and Progression Analysis Status Report, Volume VI, Event Consequences and Uncertainties Demonstrating Safety R&D Importance of Fission Product Transport Mechanisms," ERDA Report GA-A13617, General Atomic Company, January 1976.

4-10. Baumann, C. D., et al., "Nuclear Safety Program Annual Progress Report for Period Ending December 31, 1969," ERDA Report ORNL-4511, Oak Ridge National Laboratory, March 1970, Section 5.3, "Fuel Integrity and Fission Product Release," pp. 93-100.

4-11. Morgan, M. T., R. L. Towns, and J. G. Morgan, "Gas-Cooled Reactor Program Semiannual Progress Report for Period Ending March 31, 1968," ERDA Report ORNL-4266, Oak Ridge National Laboratory, September 1968, Section 5, "Fission Product Release and Transport Studies; Fission Product Release from High-Burnup Coated Fuel Particles by Postirradiation Annealing," pp. 77-82.

4-12. Burnette, R. D., W. E. Bell, and N. L. Baldwin, "Fission Product Retention Characteristics of HTGR Fuel," in Proceedings of the International Conference on Nuclear Fuel Performance, British Nuclear Energy Society, London, October 15-19, 1973, paper No. 16, p. 16.1.

4-13. Commissariat a l'Energie Atomique (CEA), private communication.

4-14. "Public Service Company of Colorado 330-MW(e) High-Temperature Gas-Cooled Reactor Research and Development Program, Quarterly Progress Report for the Period Ending September 30, 1967," USAEC Report GA-8270, General Atomic, Division of General Dynamics, October 30, 1967, pp. 136-140.

4-15. Anderson, E. E., P. E. Gethard, and L. R. Zumwalt, "Recent Data Obtained on Fission Products Released from (Th,U)C_2-Particle - Graphite Fuels," General Atomic, Division of General Dynamics Report GA-3119, May 22, 1962.

4-16. Zumwalt, L. R., E. E. Anderson, and P. E. Gethard, "Fission-Product Retention Characteristics of Certain (Th,U)C_2-Graphite Fuels," General Atomic, Division of General Dynamics Report GA-4551, September 17, 1963.

4-17. Haire, M. J., and D. W. McEachern, "Gaseous Radioactivity Levels in the Primary Coolant of an HTGR," General Atomic Report GA-A12946 (GA-LTR-14), October 1, 1974.

4-18. "Public Service Company of Colorado 330-MW(e) High-Temperature Gas-Cooled Reactor Research and Development Program, Quarterly Progress Report for the Period Ending March 31, 1969," USAEC Report GA-9261, Gulf General Atomic, April 29, 1969, pp. 138-143.

4-19. "Public Service Company of Colorado 330-MW(e) High-Temperature Gas-Cooled Reactor Research and Development Program, Quarterly Progress Report for the Period Ending June 30, 1969," USAEC Report GA-9440, Gulf General Atomic, July 31, 1969, pp. 216-232.

4-20. Myers, B. F., et al., "The Behavior of Fission Product Gases in HTGR Fuel Materials," ERDA Report GA-A13723, General Atomic Company, to be published.

4-21. "Gas-Cooled Reactor Program Semiannual Progress Report for Period Ending March 31, 1965," USAEC Report ORNL-3807, Oak Ridge National Laboratory, June 1965, pp. 103-106.

4-22. Baldwin, N. L., General Atomic unpublished data.

4-23. "Public Service Company of Colorado 330-MW(e) High-Temperature Gas-Cooled Reactor Research and Development Program, Quarterly Progress Report for the Period Ending September 30, 1966," USAEC Report GA-7453, General Atomic, Division of General Dynamics, February 7, 1967, pp. 103-113.

4-24. "Public Service Company of Colorado 330-MW(e) High-Temperature Gas-Cooled Reactor Research and Development Program, Quarterly Progress Report for the Period Ending June 30, 1966," USAEC Report GA-7314, General Atomic, Division of General Dynamics, September 30, 1966, pp. 60-67.

4-25. Morgan, M. T., H. J. De Nordwall, and R. L. Towns, "Release of Fission Products from Pyrocarbon-Coated HTGR Fuel Particles During Post-Irradiation Anneals," USAEC Report ORNL-TM-4539, Oak Ridge National Laboratory, December 1974.

4-26. Beck, S. D., "The Diffusion of Radioactive Fission Products from Porous Fuel Elements," Batelle Memorial Institute Report BMI-1433, April 18, 1960.

4-27. Morgan, M. T., and R. L. Towns, "Gas-Cooled Reactor Program Semiannual Progress Report for Period Ending September 30, 1967," USAEC Report ORNL-4200, Oak Ridge National Laboratory, February 1968, Section 5, "Fission-Product Release and Transport Studies; Fission-Product Release from High-Burnup Coated Particles by Postirradiation Annealing," pp. 107-113.

4-28. "Public Service Company of Colorado 330-MW(e) High-Temperature Gas-Cooled Reactor Research and Development Program, Quarterly Progress Report for the Period Ending December 31, 1966," USAEC Report GA-7634, General Atomic, Division of General Dynamics, March 20, 1967, pp. 104-108.

4-29. Myers, B. F., and W. E. Bell, "Strontium Transport Data for HTGR Systems," ERDA Report GA-A13168 (GA-LTR-16), General Atomic Company, December 6, 1974.

4-30. Myers, B. F., and W. E. Bell, "Cesium Transport Data for HTGR Systems," ERDA Report GA-A13990, General Atomic Company, to be published.

4-31. Adams, C. C., et al., "Fission Product Release Measurements on TRISO Fuel Particles Irradiated in Capsule P-13F," USAEC Report GA-9383, Gulf General Atomic, October 22, 1969.

4-32. Woodley, R. E., "The Radiolytic Reaction of Graphite with Water Vapor," Battelle Pacific Northwest Laboratory Report BNWL-SA-1804, April 1968.

9. HTGR FUEL DEVELOPMENT AND ENGINEERING
189a NO. 00551

TASK 100: FUEL PRODUCT SPECIFICATION

The ThO_2 BISO portion of the draft Fuel Product Specification support document was reviewed at ORNL and at GA and work continues on the remainder of the document.

TASK 200: ACCELERATED IRRADIATION TESTING

Subtask 210: Fresh Fuel Qualification

Summary

The postirradiation examination (PIE) of capsule P13T was continued during the reporting period. The following items have been completed:

1. The irradiation-induced dimensional fuel rod changes have been determined and compared with predicted values. The results indicated that the irradiation-induced strain in P13T fuel rods is anisotropic and that the observed dimensional changes are less than predicted.

2. A significant portion of the metallographic evaluation of P13T fuel rods has been completed. The high porosity in the OPyC coating is suspected of enhancing matrix/OPyC interactions, which led to high OPyC failure in UC_2 TRISO fissile particles in the 1300°C cell. These results coupled with those of P13R and P13S capsules indicates that an OPyC surface porosity on the order of 32 μℓ/g PyC or less will be needed to minimize OPyC-matrix interactions.

3. With OPyC failure as high as as 70%, only 3% of the SiC coating failed at a fluence of 3.5×10^{25} n/m^2. In the BISO ThO_2 and TRISO WAR particle batches where the degree of OPyC coating failure was much lower (<2.6%), failure of the total particle coating was always less than 1% up to maximum exposure conditions [8×10^{25} n/m^2 (E > 29 fJ)$_{HTGR}$ and 1300°C].

4. The P13T dosimetry analysis was completed and indicates that the fast and thermal fluences were approximately 11% less than the capsule design values, resulting in a maximum fast neutron exposure of 8×10^{25} n/m^2 (E > 29 fJ).

5. The dimensional changes of the H-451 and TS-1240 graphite crucibles agree well with predicted changes based on graphite irradiation capsule results.

6. The postirradiation fission gas release measurements were completed on all removed P13T fuel rods. The results are in fair agreement with the previous measurements on P13T fuel bodies prior to removal of fuel rods.

7. The push-out shear stress from P13T cure-in-place (CIP) fuel rods was determined. The results indicate a higher push-out force is required for H-451 than for TS-1240.

The postirradiation examinations of HT-31 and HT-33 were completed. The results were as follows:

1. No pressure vessel failure was observed in the TRISO ThO_2 particles irradiated at 1200°C, but high failure was observed in the 1500°C sample. An analysis is under way to determine the cause of the high failure in the 1500°C sample. The entry of moisture into the capsules is suspected as a possible cause.

2. A range of failure rates was observed in the BISO ThO_2 particles at both 1200° and 1500°C. The outer coating anisotropy (BAF_o) appears to have a strong effect. At a BAF_o greater than 1.05, the samples exhibited high failure at both 1200° and 1500°C.

Capsule P13T

Introduction. Capsule P13T is the ninth in a GA series of LHTGR fuel irradiation tests conducted under the HTGR Fuels and Core Development Program. P13T is a large-diameter capsule containing two cells. Cell 1 is a qualification test of reference fresh fuel [TRISO UC_2 (VSM) and BISO ThO_2 particles] irradiated at 1300°C. Cell 2 is an evaluation test of reference fresh fuel and recycle fissile fuel [TRISO UC_xO_y (WAR) particles] irradiated at 1100°C. The capsule was inserted in the ORR reactor in May 1975. The capsule was discharged from the core on July 6, 1976 after being irradiated to a peak fast fluence of 8×10^{25} n/m^2 (E > 29 fJ)$_{HTGR}$. A detailed description of the capsule is given in Ref. 9-1.

The postirradiation examination of P13T was started on September 10, 1976. Approximately 90% of the hot cell work on P13T has now been completed. Work is continuing on the analysis of the broad range of data generated by this PIE. Some of these results are presented in the discussions which follow.

Irradiation-Induced Dimensional Changes in P13T Fuel Rods. The mean irradiation-induced diametral, axial, and volumetric changes are plotted in Figs. 9-1 through 9-3. The range for the predicted dimensional and volumetric changes is also shown on these plots.

Dimensional changes were predicted using the SHRINK computer code. The model assumes that the particles in the fuel rod are in point-to-point contact (close-packed array) and the fuel rod dimensional change is isotropic. It is also assumed that the percent volume change of a fuel rod during irradiation is equal to the percent volume change of the constituent

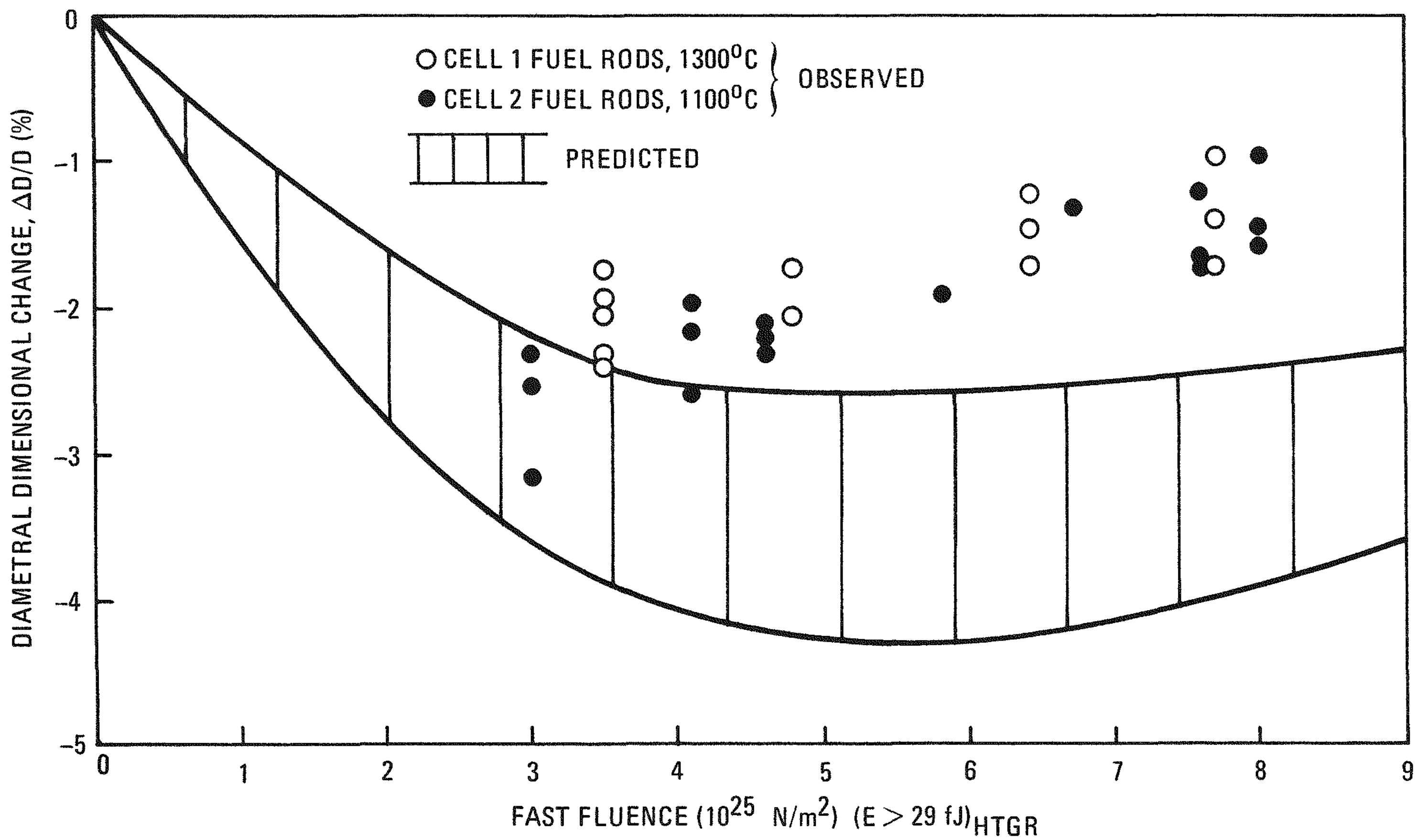

Fig. 9-1. Diametral dimensional change in P13T fuel rods versus fast fluence

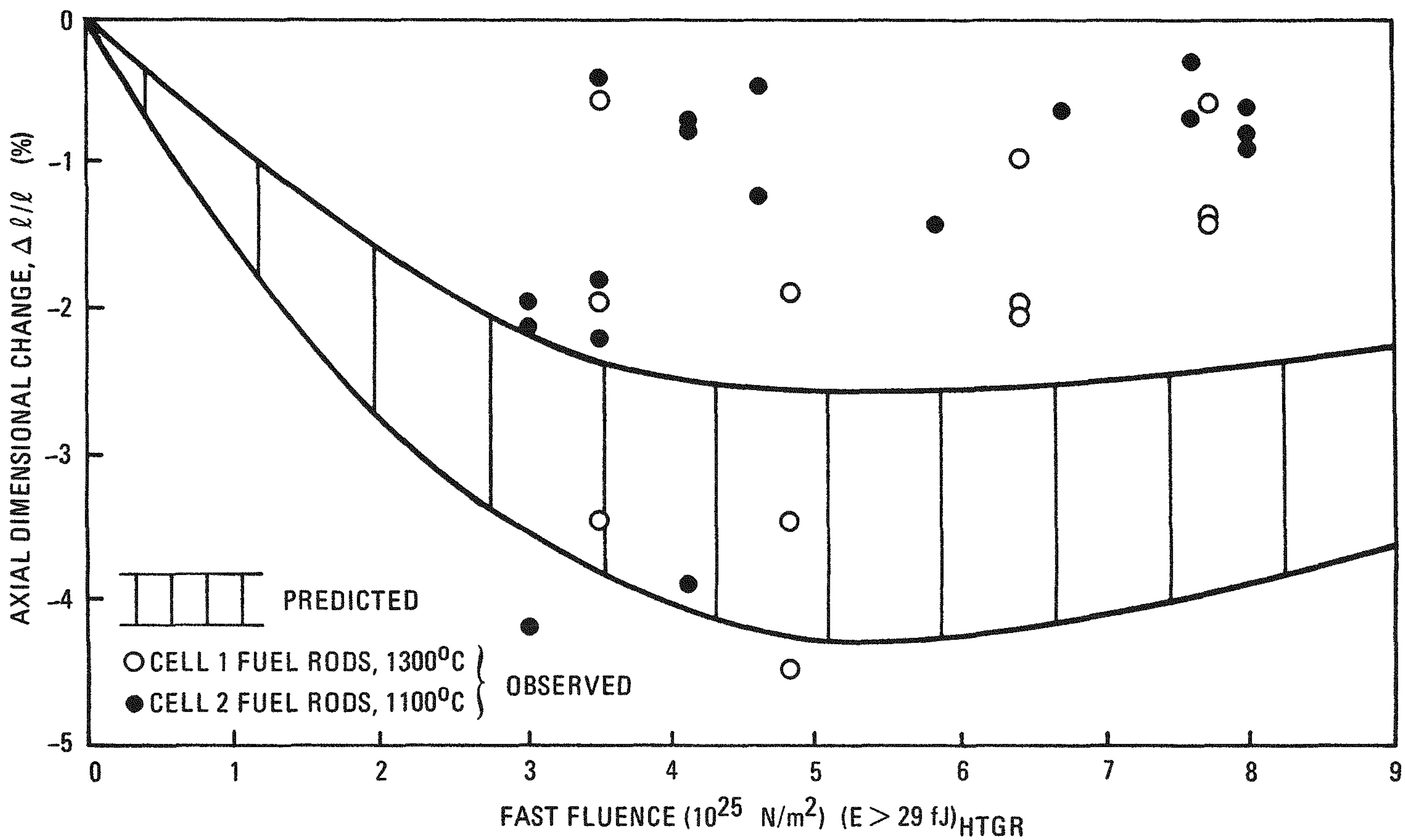

Fig. 9-2. Axial dimensional change in P13T fuel rods versus fast fluence

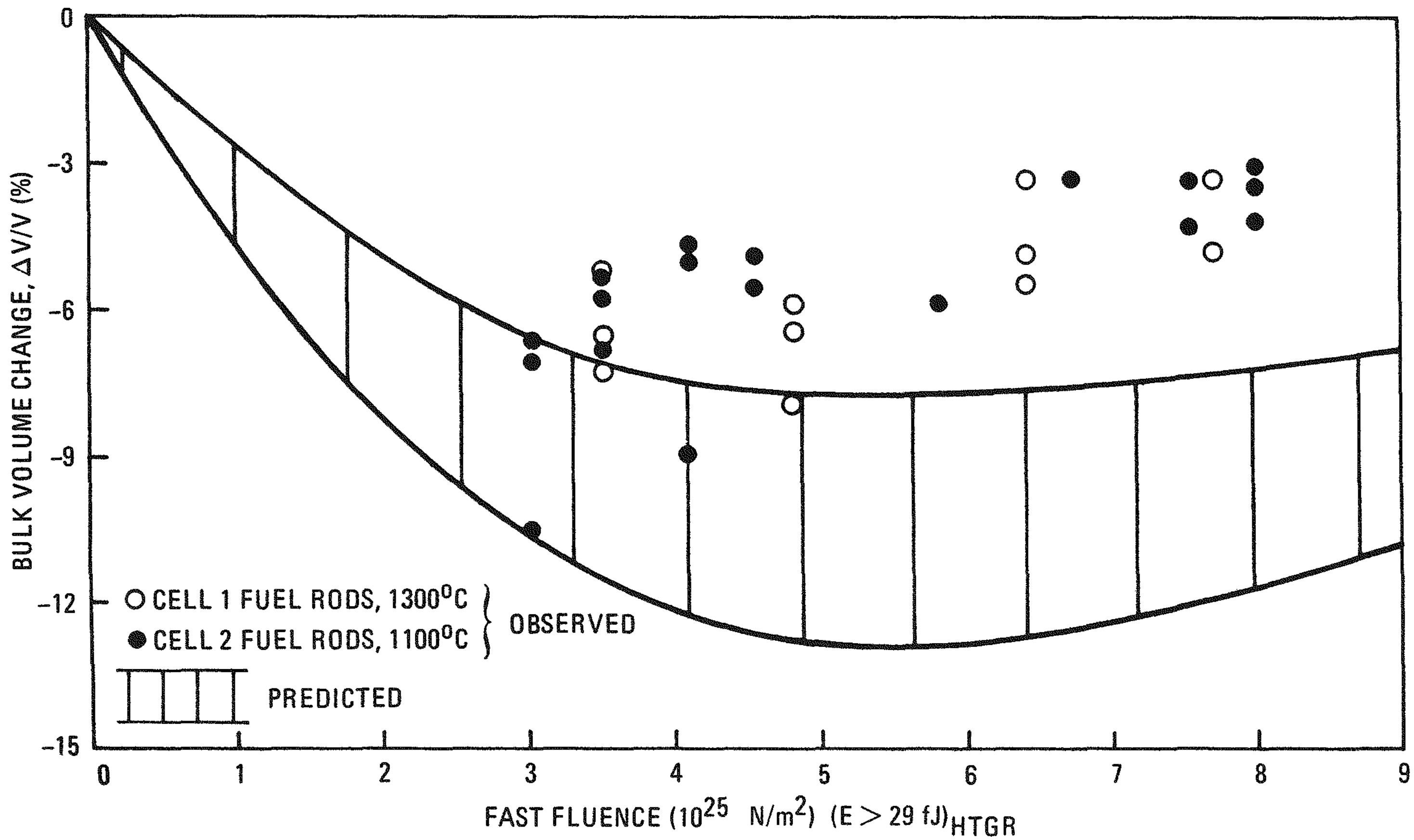

Fig. 9-3. Bulk volume change in P13T fuel rods versus fast fluence

particle types weighted by their respective volume fractions. The percent linear dimensional change of the rod is equal to one-third the percent volume change and is calculated using the following equation:

$$\% \Delta D/D_o = 1/3 \sum_i X_i (\% \Delta V/V_o)i \quad , \qquad (9\text{-}1)$$

where $\% \Delta D/D_o$ = percent diameter change of the fuel rod,

$\% \Delta V/V_o$ = percent volume change of the i^{th} particle type,

X_i = particle volume fraction of the i^{th} particle type.

Two general trends are evident from Figs. 9-1 through 9-3:

1. Irradiation-induced strain in fuel rods is anisotropic (axial and diametral strains are unequal).

2. Observed bulk volume changes are less than predicted using the SHRINK computer code.

In general, fuel rod anisotropy in P13T is such that axial strain undergoes less contraction than radial strain for 1100°C exposure. This trend is consistent with the observations in capsules HT-24 and HT-25 (Ref. 9-2) and capsule P13Q (Ref. 9-3). Strain anisotropy for P13T fuel rods is arbitrarily defined as:

$$\Delta t = t_A - t_D \quad , \qquad (9\text{-}2)$$

where Δt = % strain anisotropy,

t_A = % axial strain ($100 \times \Delta\ell/\ell$),

t_D = % diametral strain ($100 \times \Delta D/D$).

Figure 9-4 is a linear regression plot of Δt versus fast fluence for rods tested in capsule P13T. The wide scatter in the data in Fig. 9-4 is attributed to the large uncertainty in preirradiation measurements; viz, the 95% confidence bounds on the mean diametral and axial strains are

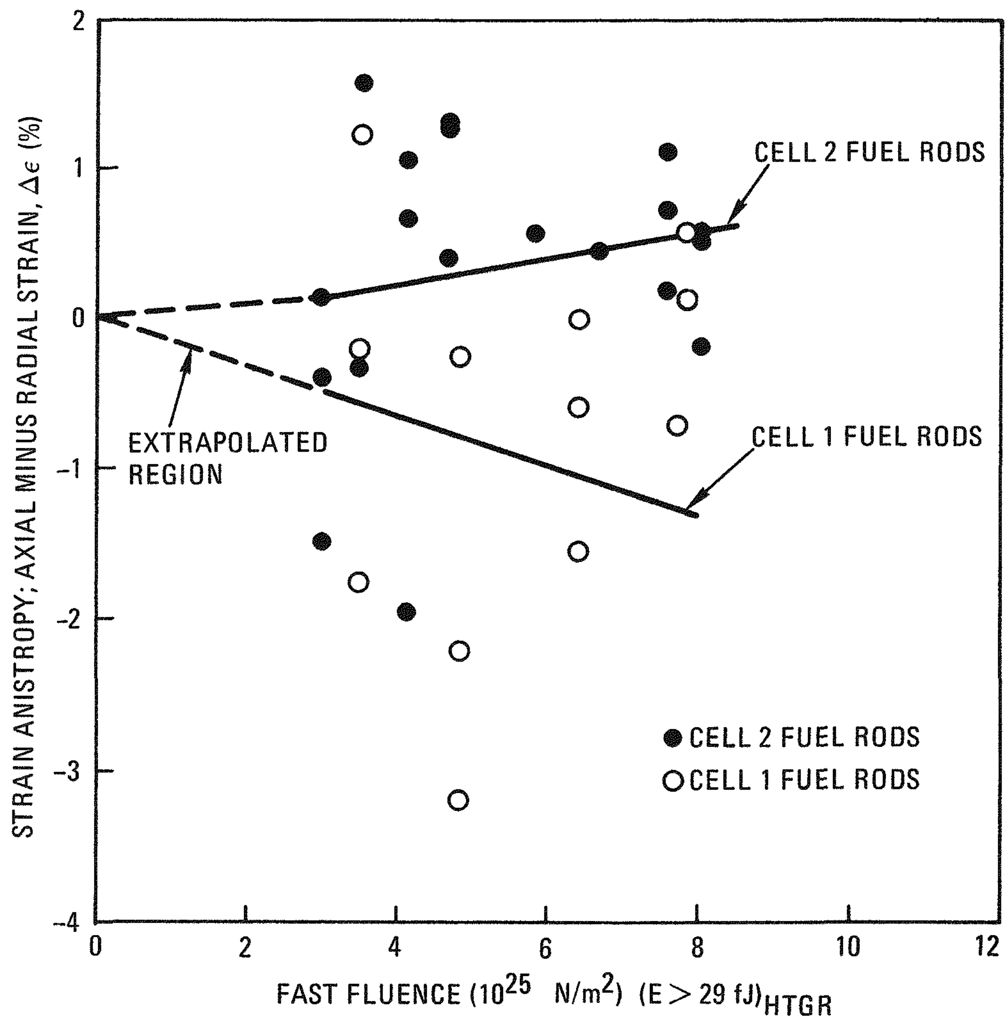

Fig. 9-4. Strain anisotropy versus fast fluence in P13T fuel rods

typically ±0.4% (absolute) and ±2.5% absolute, respectively. The trend in anisotropy in Fig. 9-4 is reversed for fuel rods tested in cell 1 at a nominal peak design temperature of 1300°C. The bias in these rods indicates that the axial strain underwent contraction relative to the radial strain.

Metallographic Evaluation of P13T Fuel Rods. Nine fuel rods irradiated in graphite bodies 1, 2, and 4 have been sectioned longitudinally and polished to the midplane. Table 9-1 summarizes the results of the TRISO coated fissile and inert particle evaluation. Table 9-2 summarizes the results of the BISO coated fertile particle evaluation. The most significant P13T PIE results which impact on particle design considerations are summarized as follows:

Fissile Particles

1. High OPyC failure (3.9% to 70.4%) occurred on TRISO coated fissile particles tested at a nominal peak design temperature of 1300°C. This failure correlates strongly with evidence of matrix/OPyC interactions, e.g., OPyC tearing.

2. The maximum fission product attack observed in SiC layers in TRISO coated VSM UC_2 particles tested at a peak fuel rod design temperature of 1300°C was 4 to 5 μm. This observation is consistent with the kinetics of fission product attack developed from out-of-pile tests. Figures 9-5 and 9-6 are representative metallographic cross sections of VSM UC_2 fissile particles tested at a nominal peak fuel rod design temperature of 1300°C.

3. WAR particles ($U \cdot C_{2.92} \cdot O_{0.64}$) tested at a peak fuel rod design temperature of 1100°C did not show an optically active IPyC layer under polarized light. This is taken as evidence that the concentration of fission products beyond the kernel phase is markedly reduced when compared to VSM UC_2 particles tested under comparable conditions. However, a fine dispersoid (∿2 to 3 μm in

TABLE 9-1
SUMMARY OF P13T METALLOGRAPHIC RESULTS ON TRISO COATED FISSILE AND INERT PARTICLES

Particle Batch Data Retrieval Number	Capsule Position	Irradiation Conditions: Nominal Peak Fuel Rod Design Temp. (°C)	Irradiation Conditions: Fast Fluence (10^{25} n/m^2) $(E > 29 fJ)_{HTGR}$	Results of Metallographic Examination: No. of Particles Examined	Cracked Or Consumed Buffer[a] (%)	IPyC Debonded From SiC (%)	IPyC Failed (%)	IPyC Coating Reaction[b] (%)	SiC Coating Reaction[c] (%)	Sic Failure (%)	SiC+ OPyC Failure (%)	OPyC Tear[d] (%)	OPyC Failure (%)	OPyC Tear And Failure (%)	Severely Faceted Particle[e] (%)
Triso Coated VSM UC_2 Particles															
6151-12-015	1B4	1300	7.7	102	1.0	14.7	1.0	100	46.1	0	0	0	3.9	0	0
6151-12-015	4A1	1100	4.6	96	1.0	2.0	0	86.5	0	0	0	0	2.1	0	ND[f]
6151-17-025	1C1	1300	3.5	98	0	38.8	1.0	100	23.5	3.1	3.1	3.1	70.4	3.1	1.0
6151-17-025	1C4	1300	7.7	91	0	14.3	1.1	97.8	40.7	1.1	1.1	19.8	54.9	18.7	4.4
6151-17-025	2A1	1100	8.0	170	6.5	21.2	0	48.8	0	0	0	0	0	0	ND
Triso Coated War $U{\cdot}C_{2.92}{\cdot}O_{0.64}$ Particles															
6157-02-015	2C1	1100	8.0	106	60.4	0	0	0	0	0	0	0.9	0	0	ND
↓	2C2	1100	7.6	150	56.7	0	0	0	0	0	0	0	0	0	ND
↓	4C1	1100	4.6	77	29.9	0	0	0	0	0	0	0	0	0	0
↓	4C4	1100	3.0	116	53.4	1.7	0	0	0	2.6	0	2.6	2.6	0.9	6.9
Triso Coated Inert Particles															
6351-01-020	1B4	1300	7.7	69	ND	ND	ND	ND	ND	ND	ND	0	30.4	0	ND
↓	1C1	1300	3.5	63	↓	↓	↓	↓	↓	↓	↓	0	58.7	0	ND
↓	1C4	1300	7.7	132	↓	↓	↓	↓	↓	↓	↓	3.0	47.0	0.8	ND
↓	2A1	1100	8.0	157	↓	↓	↓	↓	↓	↓	↓	ND	0.6	ND	ND
↓	2C1	1100	8.0	143	↓	↓	↓	↓	↓	↓	↓	ND	0	ND	ND
↓	2C2	1100	7.6	128	↓	↓	↓	↓	↓	↓	↓	ND	0	ND	ND
↓	4A1	1100	4.6	58	↓	↓	↓	↓	↓	↓	↓	ND	0	ND	ND
↓	4C1	1100	4.6	56	↓	↓	↓	↓	↓	↓	↓	ND	0	ND	ND

(a) Buffer layers in VSM UC_2 particles are characterized as either cracked or not; however, buffer layers in WAR $U{\cdot}C_{2.9}{\cdot}O_{0.6}$ particles are characterized as consumed when >50% of the buffer layer reacts with the kernel.

(b) Particles which exhibited large concentrations of metallic fission products in the IPyC layer.

(c) Particles which exhibited metallic fission product attack of the SiC layer up to 5 μm penetration; attack of ≤1 μm was not observable.

(d) Classed as any degradation of OPyC layer other than failure.

(e) Generally defined as particles with an aspect ratio ≥2:1.

(f) ND = not determined.

TABLE 9-2
SUMMARY OF P13T METALLOGRAPHIC RESULTS ON BISO COATED FERTILE PARTICLES

Particle Batch Data Retrieval Number	Capsule Position	Irradiation Conditions		Results of Metallographic Examination							
		Nominal Peak Full Rod Design Temp. (°C)	Fast Fluence (10^{25} n/m^2) (E > 29 fJ)$_{HTGR}$	No. of Particles Examined	Cracked Kernel (%)	Cracked Buffer (%)	Buffer Debonded From OPyC (%)	OPyC Tear[(a)] (%)	OPyC Failure (%)	OPyC Tear and Failure (%)	Severely Faceted Particle[(b)] (%)
6542-27-015	1C1	1300	3.5	156	1.3	0	5.8	0	0	0	1.9
6542-27-015	1C4	1300	7.7	156	0.6	0	2.6	0.6	0	0	0.6
6542-27-015	2A1	1100	8.0	268	8.5	0.7	27.6	0	0	0	ND[(c)]
6542-27-015	2C1	1100	8.0	116	6.0	0.9	15.5	0.9	0	0	ND
6542-29-015	4C4	1100	3.0	144	0	1.4	22.2	0	0	0	ND
6542-31-015	4C1	1100	4.6	266	0.8	0	26.7	0	0	0	ND
6542-32-015	1B4	1300	7.7	167	0	0	0	0.6	0.6	0.6	0
6542-33-025	2C2	1100	7.6	371	3.2	1.1	22.6	0	0.8	0	0.3
6542-35-015	4A1	1100	4.6	265	1.5	0.4	16.2	0	0	0	1.9

(a) Classed as any degradation of OPyC layer other than complete failure.

(b) Generally defined as particles with an aspect ratio $\geq$2:1.

(c) ND = not determined.

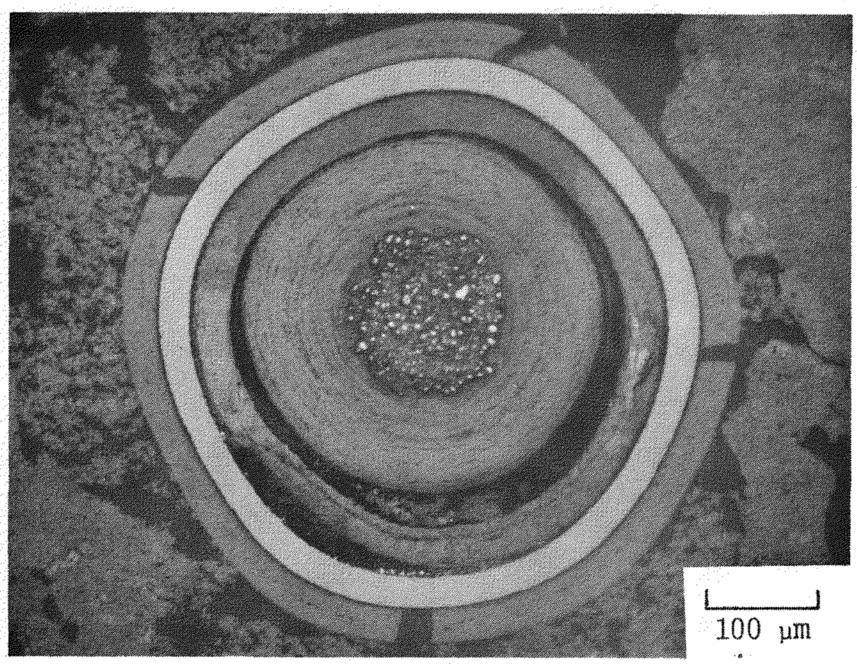

L7630-228

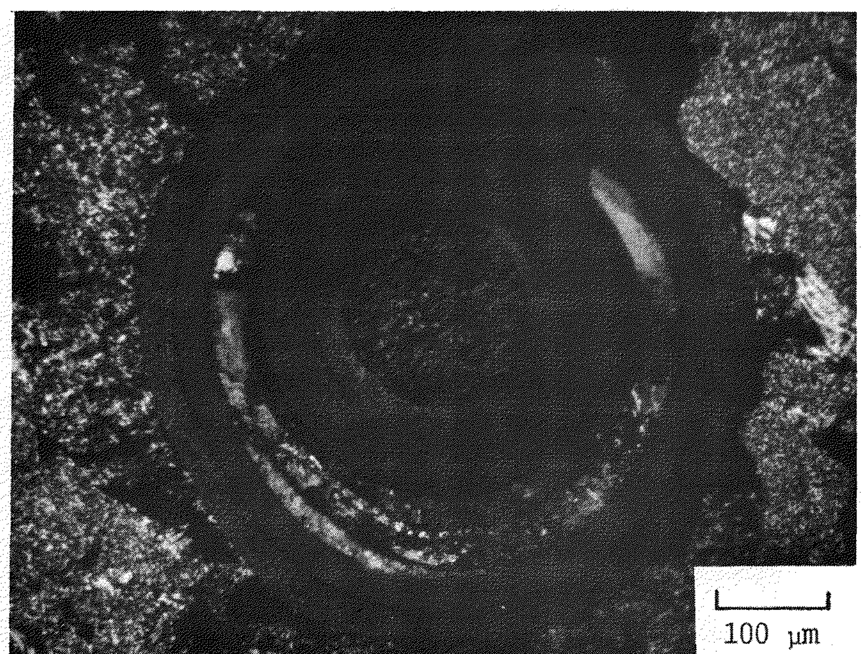

L7630-229

Fig. 9-5. Metallographic cross section of VSM fissile particle (batch 6151-17-025) in fuel rod 1C1. Depicts OPyC failure and fission product concentration for an exposure of 1300°C and 3.5×10^{25} n/m^2 (E > 29 fJ)$_{HTGR}$.

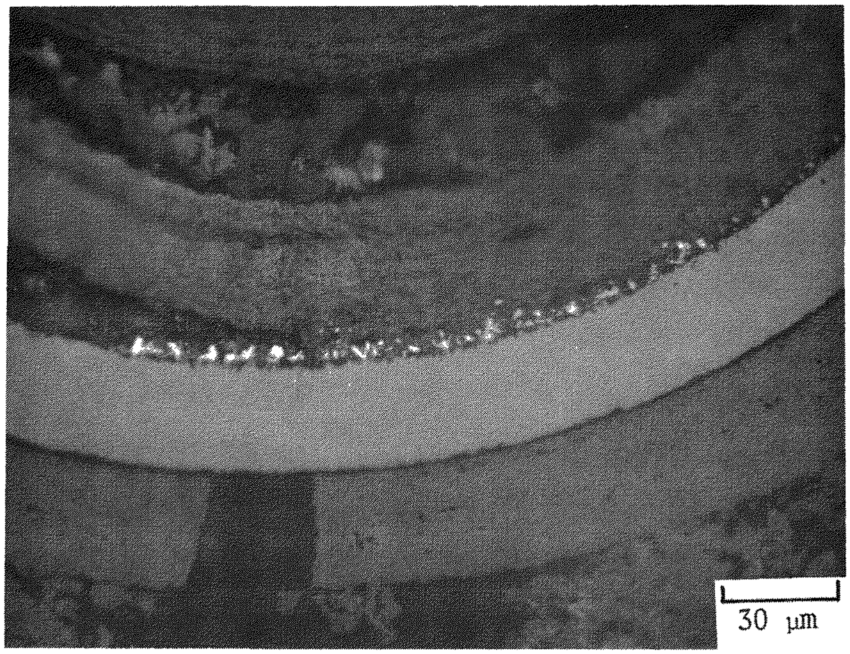

L7630-230

Fig. 9-6. Metallographic cross section depicting fission product attack in a fissile particle (batch 6151-17-025) in fuel rod 1C1; 1300°C and 3.5×10^{25} n/m^2 $(E > 29\ fJ)_{HTGR}$

extent near the SiC interface) was present in some WAR particles. When observed, the position of this phase bore no consistent relation to the thermal gradient and is apparently randomly distributed about the inner SiC interface. Figures 9-7 and 9-8 are representative metallographic cross sections of WAR $U \cdot C_{2.92} \cdot O_{0.64}$ fissile particles tested at a nominal temperature of 1100°C and to a fluence of 7.6 x 10^{25} n/m^2 (E > 29 fJ)$_{HTGR}$.

Fertile Particles

1. No OPyC failure was observed in the "near reference" BISO coated particle design (batch 6542-27-015) exposed to a nominal peak fuel rod temperature of 1300°C and a fluence of 7.7 x 10^{25} n/m^2 (E > 29 fJ)$_{HTGR}$ (see Fig. 9-9).

2. OPyC failure in batch 6542-33-025 was 0.8%. This batch had a mean OPyC thickness of 66 μm with a standard deviation of 7 μm. If it is assumed that all failure occurred in the thin coating portion of the thickness distribution, the failure implies a critical limit of 49 μm. These data provide support for a critical limit in fuel product specifications of OPyC thickness. As a point of comparison, the mean reference BISO coated OPyC thickness currently specified is 80 μm and the critical limit is 46 μm.

OPyC Failure on TRISO Coated Fissile Particles. Previous evidence based on the HRB-4, -5, and -6 PIEs (Ref. 9-4) indicates that in some instances premature OPyC failure can result from excessive matrix/coating interactions. An increase in particle-matrix bond strength is equivalent to potentially subjecting the OPyC layer to a greater tensile component. The tensile component exerted on the OPyC layer is a result of the differential volume contraction between the TRISO coated particle and the surrounding matrix phase. In previous work, failure of particles in fuel rods was correlated with irradiation conditions (temperature and fluence), as well as structural properties of the matrix (ratio of binder coke weight to

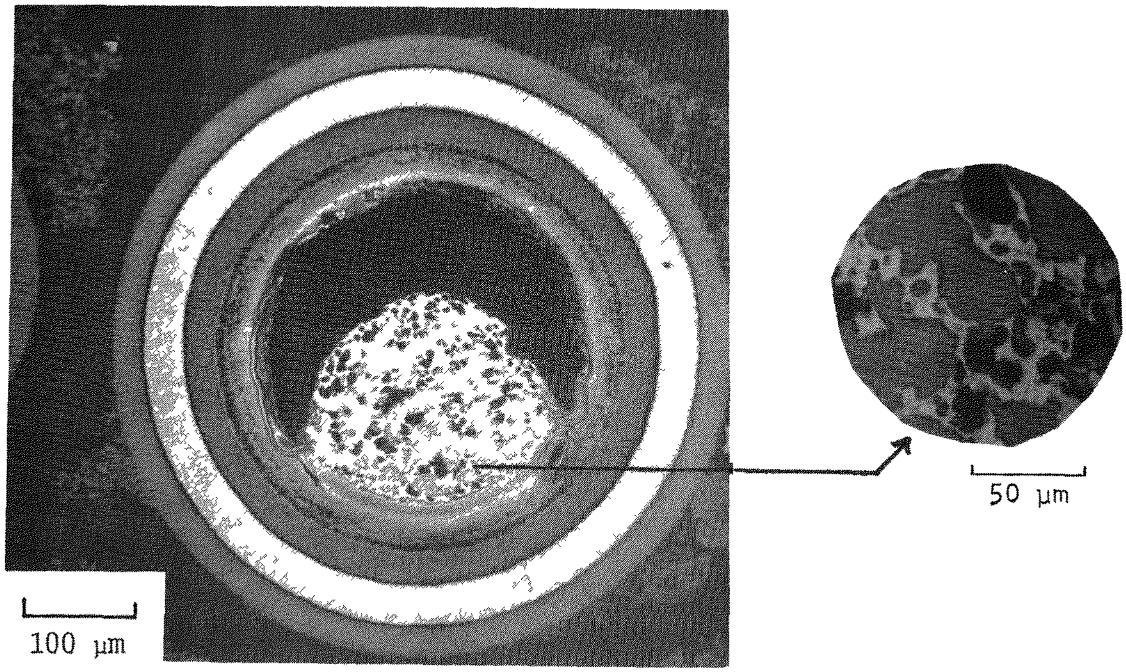

L7630-73

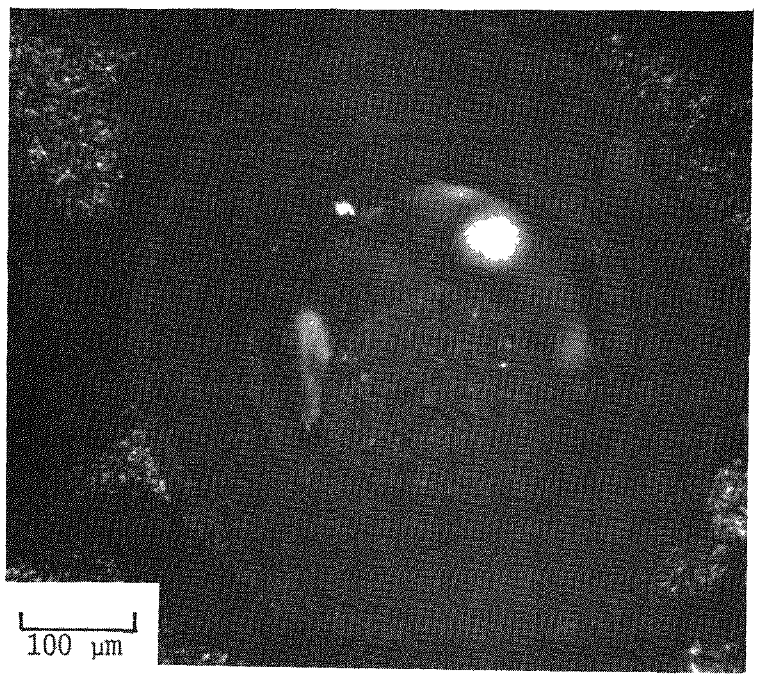

L7630-74

Fig. 9-7. Metallographic cross section depicting morphology of WAR kernels ($U \cdot C_{2.9} \cdot O_{0.6}$) in fuel rod 2C2 (batch 6157-02-015); nominally 1100°C and 7.6×10^{25} n/m^2 (E > 29 fJ)$_{HTGR}$

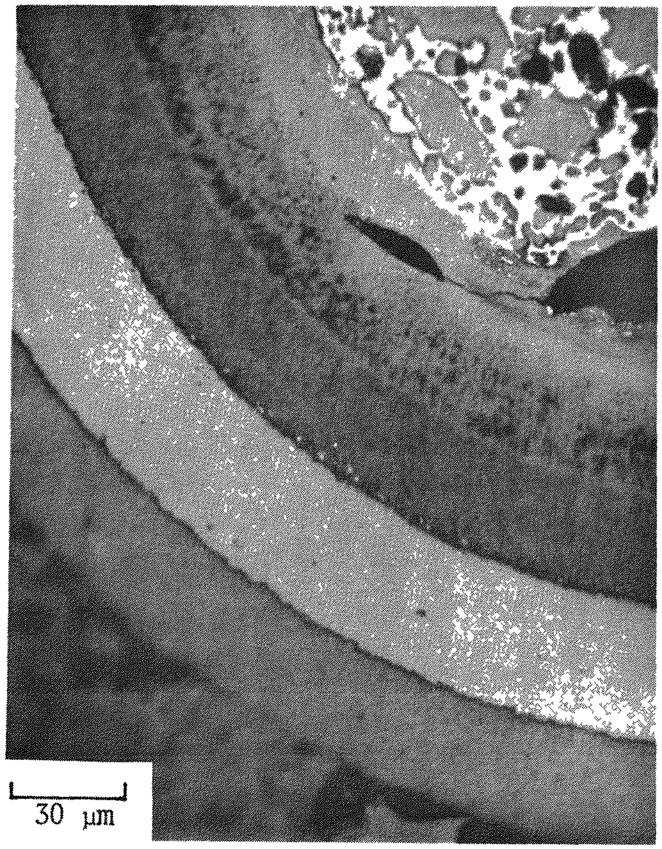

L7630-109

Fig. 9-8. Metallographic cross section depicting fission product distribution in WAR fissile particle ($U \cdot C_{2.9} \cdot O_{0.6}$) located in fuel rod 2C2 (batch 6157-02-015); nominally 1100°C and 7.6×10^{25} n/m^2 $(E > 29\ fJ)_{HTGR}$

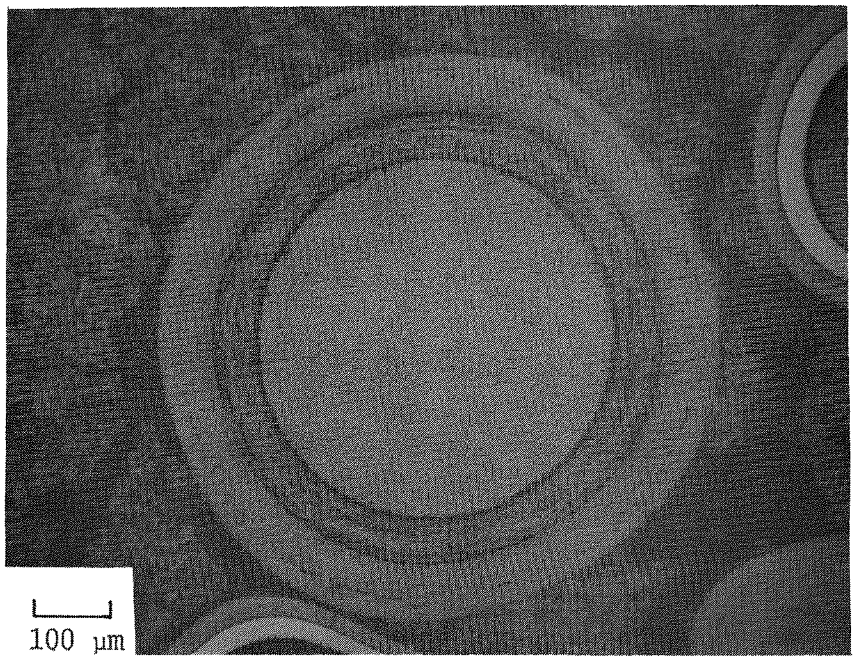

L7630-216

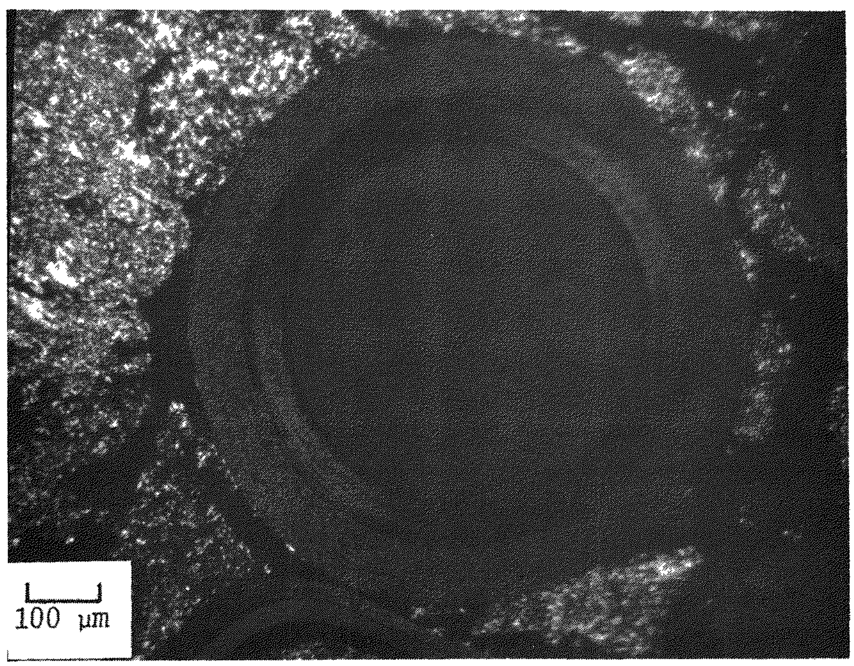

L7630-217

Fig. 9-9. Metallographic cross section of BISO coated fertile particle in fuel rod 1C4 (batch 6542-27-015); 1300°C and 7.7×10^{25} n/m^2 $(E > 29\ fJ)_{HTGR}$

matrix surface area) (Ref. 9-4). However, the most significant property variation capable of explaining differences in OPyC failure between P13T and other capsule tests was microporosity in the OPyC layer. TRISO coated fissile particles tested in capsules P13R and P13S had OPyC microporosity* values of <32 μℓ/g OPyC and there was no evidence of matrix/OPyC interactions in these batches. However, four of the fuel rods examined in the P13T PIE showed evidence of matrix/OPyC coating interactions.

Figures 9-10 through 9-12 are metallographic cross sections of typical interactions observed. Tearing in Figs. 9-10 and 9-11 is described in terms of the OPyC fracture morphology; i.e., the crack opens at the OPyC surface and propagates inward. Figure 9-12 is a more descriptive photomicrograph which depicts a BISO particle (partially torn) with a TRISO coated OPyC fragment adhered. The presence of an interface phase is taken as evidence that the matrix partially impregnated the OPyC layers of both particle types.

Figure 9-13 is a series of metallographic cross sections depicting the microporosity present in preirradiated OPyC layers of TRISO coated fissile particles tested in capsule P13T. It should be noted that two batches had a preirradiated microporosity of 58 μℓ/g OPyC and one batch had a microporosity of 43 μℓ/g OPyC. The outer OPyC region (∿5 to 10 μm) in all fissile particle batches was characterized as being substantially porous. The increase in porosity in the OPyC layer has two deleterious effects:

1. Allows for a more tenacious bond to form between the OPyC and matrix.

2. Degrades the fracture strength of the OPyC layer.

Results from the P13R and P13S experiment indicate that a microporosity equivalent to <32 μℓ/g OPyC will provide satisfactory performance.

*Measured by Hg intrusion at ∿0.069 MPa (10 psi).

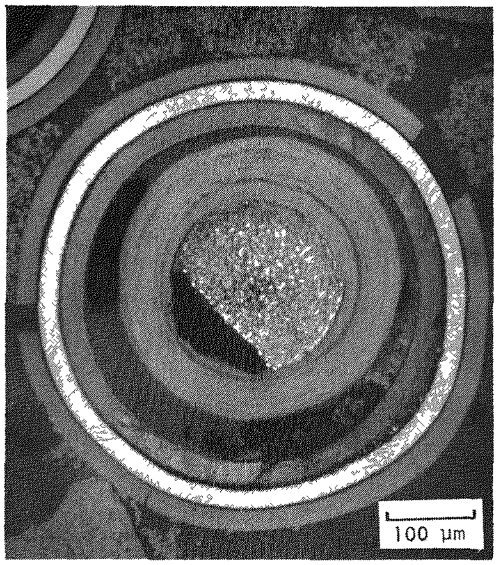

L7630-423

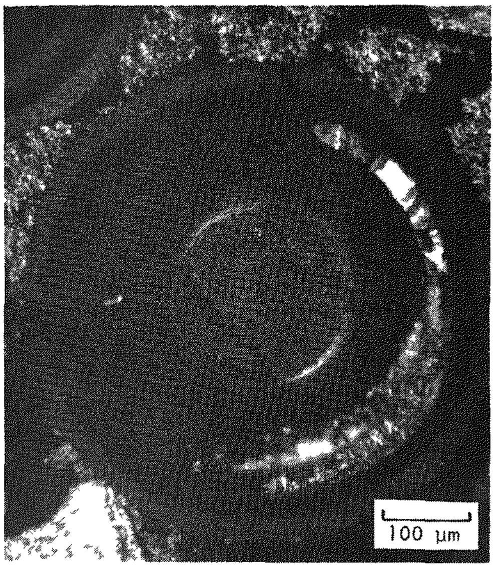

L7630-424

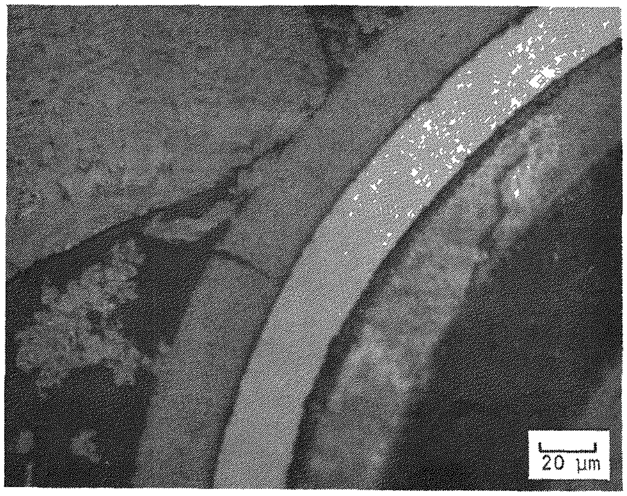

L7630-425

Fig. 9-10. Metallographic cross section of fuel rod 1C4 (batch 6151-17-025); 1300°C and 7.7×10^{25} n/m^2 $(E > 29\ fJ)_{HTGR}$. Depicts localized tearing and OPyC failure in TRISO fissile particle.

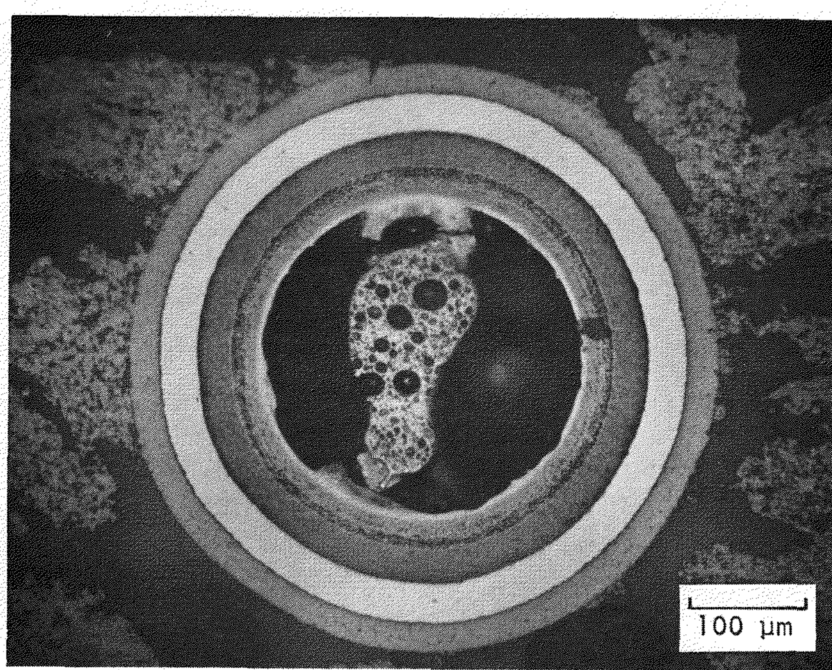

L7630-311

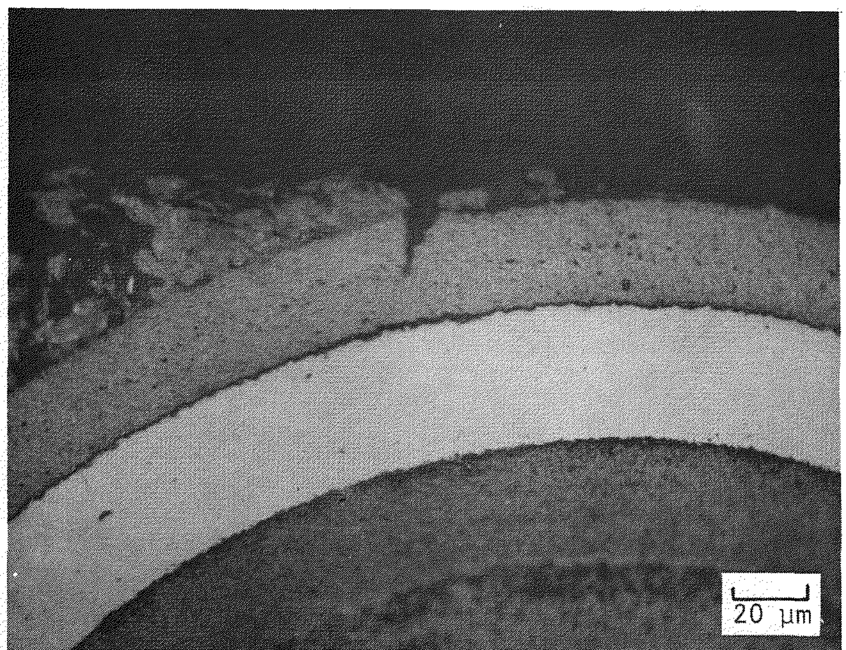

L7630-313

Fig. 9-11. Metallographic cross section of fuel rod 4C4 (batch 6157-02-015); 1100°C and 3.0×10^{25} n/m^2 (E > 29 fJ)$_{HTGR}$. Depicts torn OPyC layer on TRISO coated $U{\cdot}C_{2.92}{\cdot}O_{0.64}$ kernel.

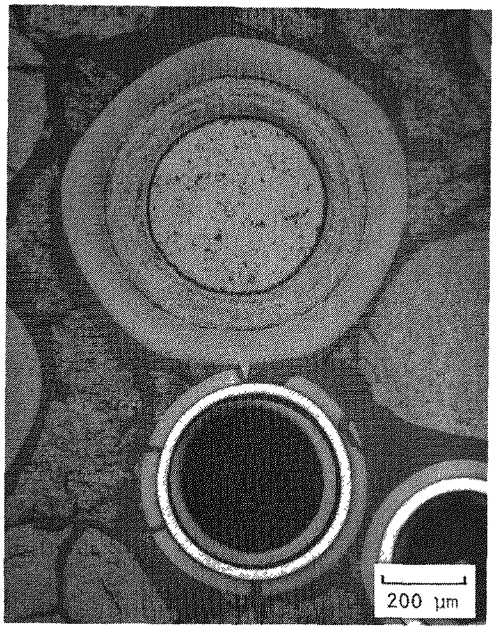

L7630-420

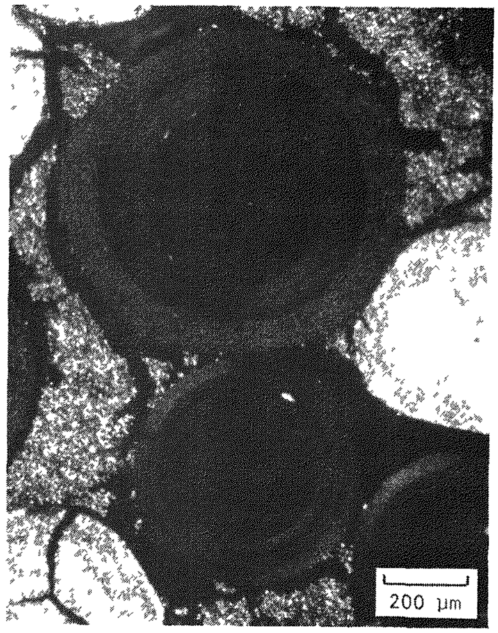

L7630-421

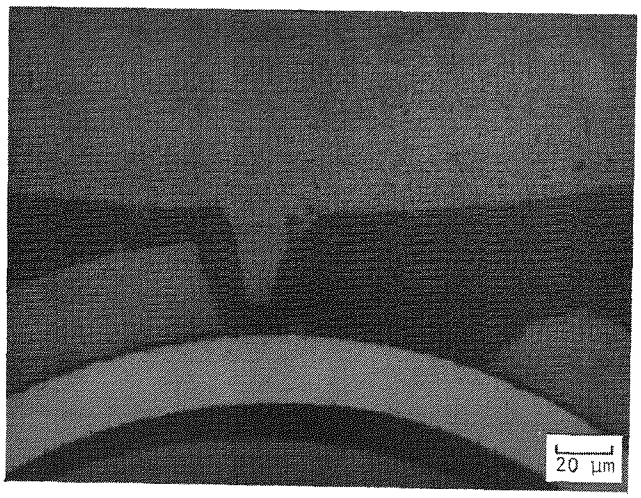

L7630-422

Fig. 9-12. Metallographic cross section of fuel rod 1C4 (batch 6351-01-020); 1300°C and 7.7 x 10^{25} n/m^2 (E > 29 fJ)$_{HTGR}$. Depicts localized interaction between BISO particle (batch 6542-27-015) and TRISO inert particle.

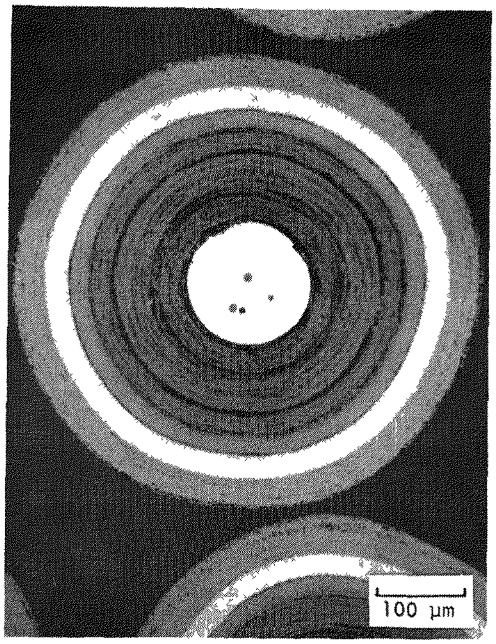

MP74024-6 (Not currently determined)

(a)

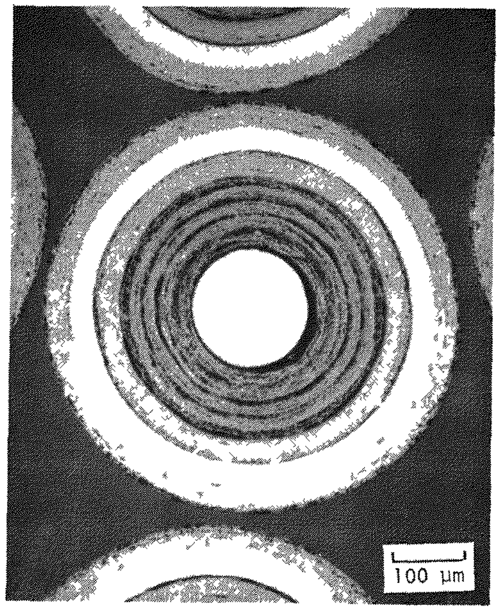

MP7406 (58 μℓ/g OPyC)

(b)

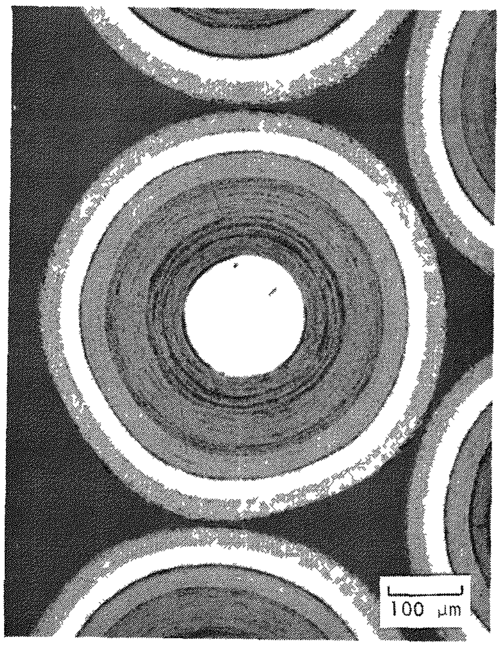

MP74073-10 (58 μℓ/g OPyC)

(c)

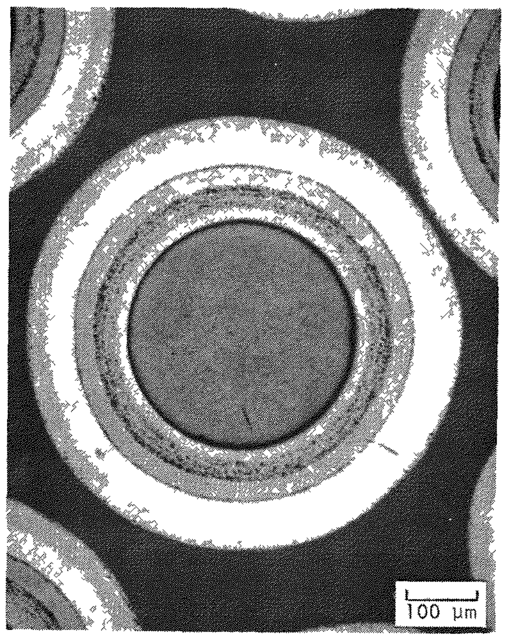

MP74068-10 (43 μℓ/g OPyC)

(d)

Fig. 9-13. Metallographic cross sections depicting porosity in pre-irradiated OPyC layers on TRISO coated fissile particles: (a) batch 6151-12-015, (b) batch 6151-17-015, (c) batch 6151-17-025, and (d) batch 6157-02-010. OPyC porosity referenced in parentheses.

P13T Dosimetry Results. The analysis of the thermal (Va-Co) and fast fluence (Va-Fe) dosimeters has been completed. Results indicate that the fast and thermal fluences experienced by P13T were approximately 11% less than the design values. A third-order least-squares fit was performed on these data to establish equations for fast and thermal fluences and fast and thermal fluxes. The flux and fluence values were fit in an equation of the form:

$$f(x) = a + bx + cx^2 + dx^3 \quad , \qquad (9\text{-}3)$$

where x is the distance from the bottom of the core. The values for the coefficients are presented in Table 9-3. The calculated P13T fuel rod fast and thermal flux and fluence values are shown in Table 9-4.

A comparative plot of the actual and design P13T fast and thermal fluence data is shown in Fig. 9-14. This figure indicates that the shape of the design axial fast flux curve for the Oak Ridge Reactor (ORR) is well known, but that the design axial thermal flux curve is apparently somewhat uncertain, especially at the top and bottom of the ORR core.

P13T Graphite Dimensional Changes. The measured graphite dimensional changes for P13T fuel crucibles have been previously reported (Ref. 9-5). A comparative analysis has been performed on these data to determine if the P13T observed graphite dimensional changes were of the same order as had been previously determined (Refs. 9-6 and 9-7) for these graphites. The results are shown in Figs. 9-15 through 9-17 for the H-451 and TS-1240 graphites used in P13T. The curves shown in these figures indicate the established values based on graphite irradiation capsule results. The data points shown are from P13T crucibles. (The fluence values have been corrected to account for the final P13T dosimetry results discussed in the previous section. The temperatures shown are subject to correction when the final P13T thermal analysis is completed.)

TABLE 9-3

P13T DOSIMETRY COEFFICIENTS FOR EQ. 9-3 COEFFICIENTS

	a	b	c	d
Thermal flux	0.60	0.26	-0.018	2.70×10^{-4}
Thermal fluence	1.88	0.81	-0.056	8.48×10^{-4}
Fast flux $(E > 29\ fJ)_{HTGR}$	0.75	0.46	-0.034	6.34×10^{-4}
Fast fluence $(E > 29\ fJ)_{HTGR}$	2.36	1.45	-0.108	1.99×10^{-3}

TABLE 9-4
P13T FUEL ROD FAST AND THERMAL FLUXES AND FLUENCES

Rod No.	Distance from Bottom of Core (cm)	Thermal		Fast $(E > 29\ fJ)_{HTGR}$	
		Flux (x 10^{19} n/m^2-s)	Fluence (x 10^{25} n/m^2)	Flux (x 10^{19} n/m2-s)	Fluence (x 10^{25} n/m^2)
1-1	2.03	0.8	2.49	1.10	3.45
1-2	5.08	1.05	3.28	1.54	4.84
1-3	9.65	1.34	4.19	2.04	6.42
1-4	15.75	1.58	4.95	2.44	7.67
2-1	25.37	1.66	5.22	2.57	8.04
2-2	30.38	1.59	4.99	2.44	7.64
3-1	37.06	1.39	4.39	2.14	6.69
3-2	42.06	1.19	3.76	1.85	5.77
4-1	47.75	0.92	2.91	1.50	4.64
4-2	50.80	0.76	2.42	1.32	4.05
4-3	53.85	0.60	1.92	1.14	3.49
4-4	56.90	0.43	1.41	0.99	2.98

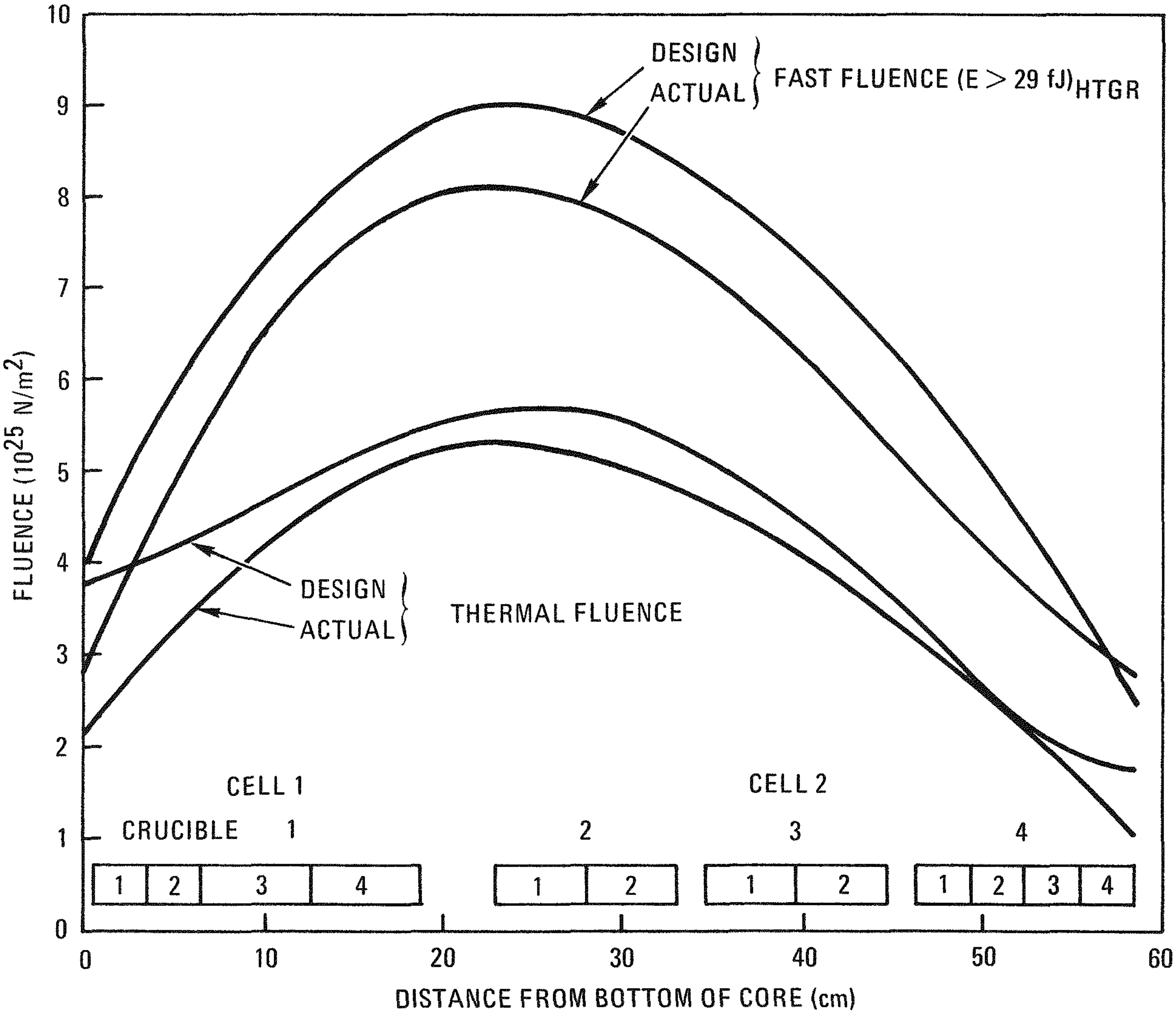

Fig. 9-14. EOL fast and thermal fluences for capsule P13T

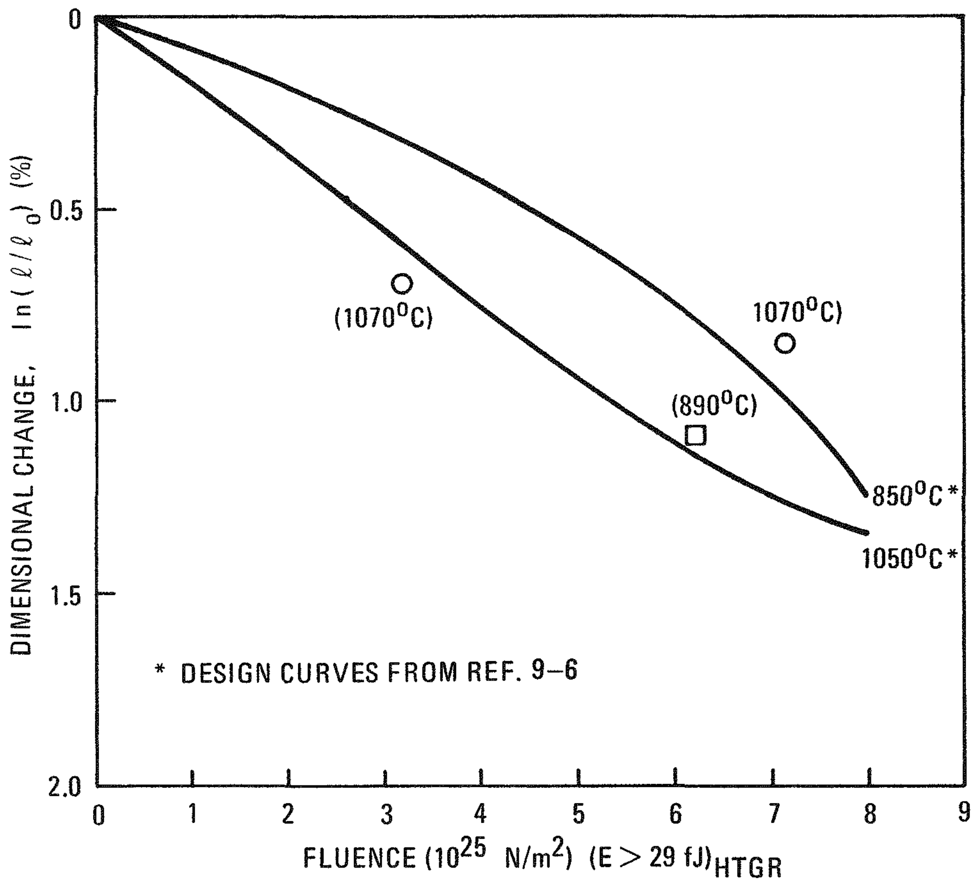

Fig. 9-15. Dimensional change of H-451 graphite in the radial directional as a function of fast fluence - capsule P13T

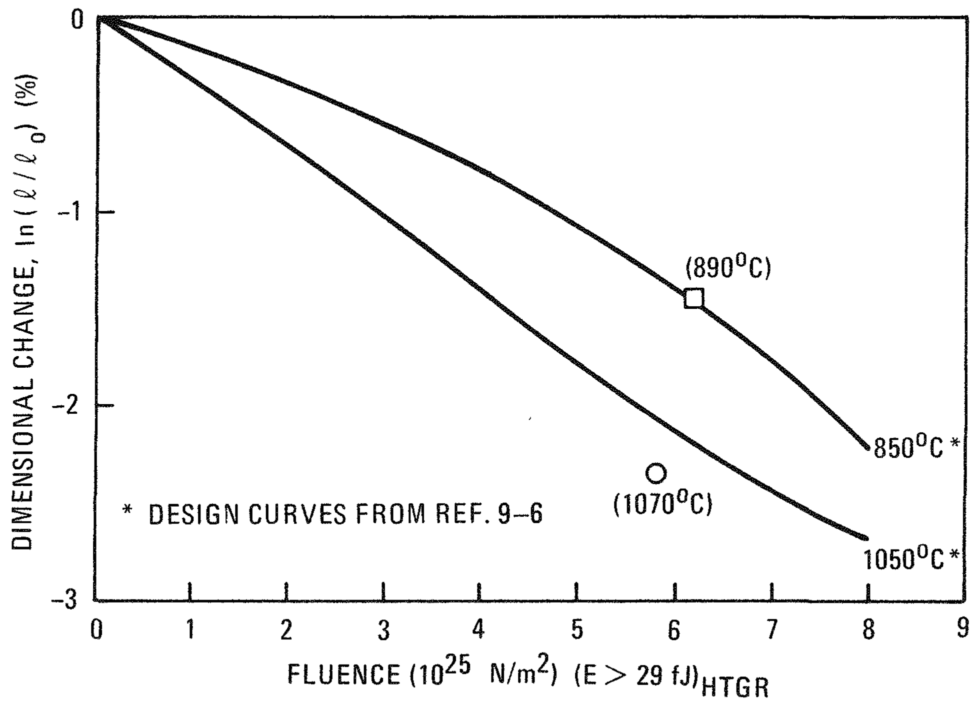

Fig. 9-16. Dimensional change of H-451 graphite in the axial direction as a function of fast fluence - capsule P13T

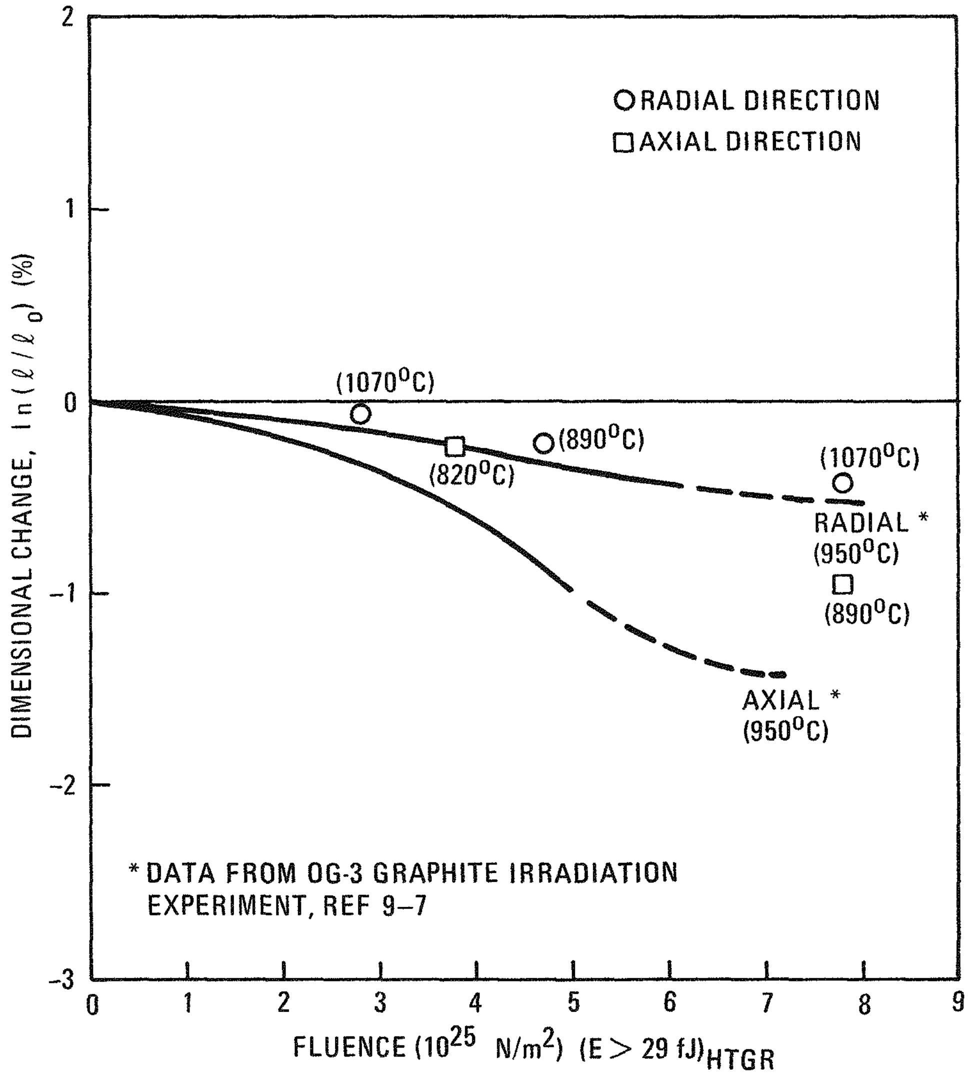

Fig. 9-17. Dimensional change of TS-1240 graphite as a function of fast neutron fluence - P13T capsule

It is not expected that these data are sufficiently accurate to add to the H-451 and TS-1240 data base, but it is interesting to note that reasonable agreement exists between the P13T data and the already established data for graphites H-451 and TS-1240.

P13T Fission Gas Release Data. As part of the PIE of capsule P13T, fission gas release measurements were made on the fuel bodies and individual fuel rods contained in the capsule. The Kr-85m R/B values obtained for all four fuel bodies were reported earlier (Ref. 9-5). After disassembly of the fuel bodies, the fuel rods were submitted for individual R/B measurements.

Table 9-5 lists the fuel rods tested and the resulting Kr-85m R/B at 1100°C. Only two of six rods from body 3 were submitted for fission gas release measurements. The equivalent U-235 loading given in Table 9-5 takes into account the contribution from U-233 plus U-235 remaining in the fuel rods at end-of-life.

As discussed in Ref. 9-5, the R/B measurement on fuel body 1 was made at room temperature due to failure of the heating element in the TRIGA King furnace. Therefore, a temperature dependence study was performed on fuel rods from body 1 to obtain a correction factor to be applied to the room-temperature data. Table 9-6 shows the results of the temperature dependence study on all 1B rods in body 1. Fission gas release was measured from all four rods at room temperature and 1100°C on the same day. A repeat of the 1100°C measurement was made 24 hours later to determine the effect of consecutive TRIGA irradiations on the apparent steady-state birth rate. As can be seen in Table 9-6, this effect was small and therefore the 1100°C R/B values were averaged. Rod 1B1 was an exception in that the repeat 1100°C measurement was a factor of 20 lower, possibly indicating a problem in collection of the released fission gases.

Rod 1B4 was the only rod showing significant release at room temperature. The R/B was found to increase by a factor of 11 between the room temperature and 1100°C measurements. This correction factor, while lower

TABLE 9-5
R/B VALUES FOR INDIVIDUAL FUEL RODS IRRADIATED IN CAPSULE P13T

Fuel Rod No.	Fuels Chemistry Branch Identification No.	Equivalent U-235 Loading (mg)	Kr-85m R/B at 1100°C
1A1	7298-138	123.1	2.44×10^{-5}
1B1	7299-12	121.9	6.25×10^{-6}
1C1	7299-37	123.1	1.01×10^{-5}
1A2	7298-139	94.5	5.70×10^{-5}
1B2	7299-13	95.2	6.29×10^{-6}
1C2	7299-38	95.2	5.24×10^{-5}
1A3	7298-140	159.0	1.46×10^{-5}
1B3	7299-10	159.7	1.90×10^{-5}
1C3	7299-16	158.9	5.79×10^{-6}
1A4	7298-141	146.1	3.99×10^{-5}
1B4	7299-11	146.5	1.05×10^{-4}
1C4	7299-17	146.6	5.21×10^{-5}
2A1	7298-143	87.1	9.68×10^{-5}
2B1	7299-35	85.7	5.08×10^{-5}
2C1	7298-149	86.9	2.22×10^{-5}
2A2	7298-144	97.2	1.58×10^{-5}
2B2	7299-36	95.5	2.33×10^{-5}
2C2	7298-150	93.1	3.66×10^{-6}
3B1	7299-39	106.9	7.11×10^{-5}
3B2	7299-40	133.5	4.02×10^{-5}
4A1	7298-145	112.6	6.03×10^{-6}
4B1	7299-31	112.1	4.99×10^{-6}
4C1	7298-151	112.7	8.42×10^{-6}
4A2	7298-146	113.6	3.55×10^{-6}

TABLE 9-5 (Continued)

Fuel Rod No.	Fuels Chemistry Branch Identification No.	Equivalent U-235 Loading (mg)	Kr-85m R/B at 1100°C
4B2	7299-32	112.4	3.65×10^{-8}
4C2	7298-152	114.5	8.91×10^{-7}
4A3	7299-23	147.2	5.57×10^{-5}
4B3	7299-25	145.8	1.44×10^{-6}
4C3	7299-33	145.9	1.85×10^{-6}
4A4	7299-24	196.9	6.37×10^{-8}
4B4	7299-26	196.8	4.08×10^{-7}
4C4	7299-34	192.7	5.15×10^{-7}

TABLE 9-6
R/B TEMPERATURE DEPENDENCE FOR P13T CELL 1 FUEL RODS

Number	Fuel Chem. Branch Ident. Number	Date	Time	Temp. (°C)	Equiv. U-235 Loading (mg)	Kr-85m R/B
1B1	7299-2	10/28/76	0918	RT	121.9	$<10^{-7}$
	7299-4	10/28/76	1109	1100		6.25×10^{-6}
	7299-12	10/29/76	1101	1100		3.33×10^{-7}
1B2	7299-3	10/28/76	0918	RT	95.2	$<10^{-7}$
	7299-5	10/28/76	1109	1100		6.99×10^{-6}
	7299-13	10/29/76	1101	1100		5.58×10^{-6}
				1100 avg.		6.29×10^{-6}
1B3	7299-6	10/28/76	1317	1100	159.7	2.32×10^{-5}
	7299-8	10/28/76	1507	RT		$<10^{-7}$
	7299-10	10/29/76	0923	1100		1.47×10^{-5}
				1100 avg.		1.90×10^{-5}
1B4	7299-7	10/28/76	1317	1100	146.5	1.19×10^{-4}
	7299-9	10/28/76	1507	RT		9.18×10^{-6}
	7299-11	10/29/76	0923	1100		9.05×10^{-5}
				1100 avg.		1.05×10^{-4}

than would be calculated based on past experience, was used to correct the room temperature R/B value obtained from body 1.

Table 9-7 shows a comparison of the in-pile R/B and postirradiation TRIGA R/B values obtained for each cell. The average R/B values found for individual rod measurements for each fuel body are included. The postirradiation TRIGA values for the fuel body and the individual rod averages show reasonably good agreement with the exception of body 3. However, only two of the six rods in body 3 were tested individually. For the other three bodies, the fuel body and average rod values were within a factor of two for the TRIGA tests.

A comparison of the in-pile end-of-life R/B and postirradiation TRIGA R/B on the fuel bodies indicates a higher release for the TRIGA tests. As shown in Table 9-8, the end-of-life TRIGA R/B for cell 1 when corrected for estimated volume-average temperature was found to be a factor of 7 higher than the in-pile release value. The in-pile release measurement for cell 2 was a composite of fuel bodies 2, 3, and 4. Applying corrections for estimated volume-average temperature and fissions per crucible results in an R/B for Kr-85m for cell 2 of 9.7×10^{-6}. This is a factor of approximately 3 higher than the in-pile release. Corrections for final dosimetry need to be made to the in-pile release values, and the TRIGA crucible Kr-85m R/B measurements need to be corrected for the actual in-pile volume-average temperatures before a final comparison of the in-pile and TRIGA data can be made.

<u>P13T Fuel Rod/Fuel Hole Gaps and Shear Stress</u>. A comparison has been made between the preirradiation and postirradiation shear stress as a function of graphite type, fuel rod/fuel hole gap, and matrix type. The results are shown in Table 9-9. Analysis of these data indicates a stronger bond exists between the fuel rods and the surrounding H-451 graphite (Great Lakes Carbon Corporation) than between the fuel rods and the TS-1240 graphite (Union Carbide Corporation). This effect holds true for both the preirradiation and postirradiation data, as shown in Table 9-9. Since the bond results from the cure-in-place (CIP) processing, different

TABLE 9-7
COMPARISON OF IN-PILE AND TRIGA R/B MEASUREMENTS

Cell Number	Body Number	Kr-85m R/B In-Pile at Cell Temp.	Kr-85m R/B TRIGA at 1100°C [a]	Kr-85m R/B Individual Rod Average at 1100°C
1	1	1.6×10^{-5}	7.1×10^{-5} [b]	3.3×10^{-5}
2	2	2.8×10^{-6} [c]	2.2×10^{-5}	3.5×10^{-5}
	3	--	1.3×10^{-5}	5.6×10^{-5} [d]
	4	--	4.4×10^{-6}	7.0×10^{-6}

[a] The R/B values shown for bodies 2, 3, and 4 are slightly higher than those given in Ref. 9-5 due to a correction for collection efficiency.

[b] R/B temperature corrected to 1100°C.

[c] The release from cell 2 was a composite of bodies 2, 3, and 4.

[d] Average of two rods out of a total of six rods in the body.

TABLE 9-8

COMPARISON BETWEEN FINAL IN-PILE AND CRUCIBLE TRIGA R/B MEASUREMENTS

Cell Number	Final In-Pile Kr-85m R/B	Estimated Final In-Pile Volume-Average Cell Temp. (°C)	Crucible Kr-85m R/B at Same Temp.
1	1.6×10^{-5}	1230[a]	11.6×10^{-5}
2	2.8×10^{-6}[b]	1080[a]	9.7×10^{-6}[c]

[a] Subject to correction when the P13T thermal analysis has been completed.

[b] The release from cell 2 was a composite of crucibles 2, 3, and 4.

[c] Average for crucibles 2, 3, and 4 corrected for temperature and fissions per crucible.

TABLE 9-9
COMPARISON OF P13T PREIRRADIATION AND POSTIRRADIATION FUEL ROD SHEAR STRESS AS A FUNCTION OF GRAPHITE TYPE, FUEL ROD/FUEL HOLE GAP, AND MATRIX TYPE

Fuel Rod Column No.	Graphite Type	Matrix Type[(a)]	Pre-Irrad. Fired Radial Gap (mm)	Pre-Irrad. Shear Stress (kPa)	Post-Irrad. Radial Gap (mm)	Post-Irrad. Shear Stress (kPa)
1A	H-451	1	0.043	122.7	0.099	76.5
1B	↓	2	0.039	108.2	0.104	60.7
1C	↓	3	0.036	34.5	0.102	55.2
2A	TS-1240	1	0.042	90.1	0.137	9.0
2B	↓	1	0.046	45.5	0.097	4.8
2C	↓	1	0.051	81.4	0.137	4.8
3B	H-451	2	0.042	90.3	0.097	73.8
4A	TS-1240	3	0.045	29.6	0.218	2.8
4B	↓	3	0.061	29.6	0.241	9.0
4C	↓	3	0.043	29.6	0.211	4.2

(a) Matrix 1 is 30 wt % Asbury 6353 natural-flake graphite flour, 65 wt % A-240 pitch, and 5 wt % octadecanol. Matrix 2 is 38 wt % Lonza KS-15 graphite flour, 47 wt % A-240 pitch, 5 wt % polystyrene, and 10 wt % octadecanol. Matrix 3 is 38 wt % Lonza KS-15 graphite flour, 57 wt % A-240 pitch, and 5 wt % octadecanol.

matrix types might be expected to affect the bond. However, examination of the data for the three matrix types used in P13T does not generally support this theory. Currently, data from other capsule irradiation experiments are being examined to determine if a stronger bond exists for CIP fuel rods processed in H-451 graphite as opposed to TS-1240 graphite.

Capsules HT-31 and HT-33

Capsules HT-31 and HT-33 are part of the continuing HT-capsule series, which is a cooperative effort between GA and ORNL. The uninstrumented capsules were the first to test TRISO and BISO coated ThO_2 particles fabricated in the pilot plant 240-mm-diameter coater. The OPyC coating properties of these particles were varied. The samples were irradiated at design temperatures of 1200° and 1500°C to fluences and burnups beyond peak LHTGR conditions. A detailed description of the capsules is given in Ref. 9-8.

Capsules HT-31 and HT-33 were discharged from the HFIR reactor on June 16, 1971 and October 21, 1971, respectively. The capsules were disassembled and the fuel samples were examined at the hot cells at ORNL. Each sample was examined under a stereomicroscope.

The TRISO ThO_2 particle samples were irradiated in both capsules. The irradiation conditions and the results of the visual examination are presented in Table 9-10. The 1200°C samples irradiated in HT-31 and HT-33 to a fluence of 4.1 to 8.3 x 10^{25} n/m^2 (E > 29fJ)$_{HTGR}$ and a burnup of 4.9 to 9.1% FIMA exhibited zero pressure vessel failure (both the OPyC and SiC coating failed) and low OPyC coating failure (≤3.8%). High pressure vessel failure was observed in the 1500°C samples irradiated to a fluence of 7.4 to 10.4 x 10^{25} n/m^2 (E > 29 fJ)$_{HTGR}$ and a burnup of 8.2 to 12.8% FIMA. Lower failure was usually detected in samples located at the ends of the 1500°C magazines in HT-31 and HT-33, indicating the temperatures may have been lower. It should be noted that only the nominal particles from each parent batch were tested, which means that low pressure vessel failure in a capsule sample would not necessarily imply low failure in the parent batch.

TABLE 9-10

PARTICLE DESCRIPTION AND COMPARISON OF RESULTS OF TRISO ThO_2 SAMPLES[a] OF CAPSULES HT-31 AND HT-33

Parent Batch Number	Particle Properties							Variables[c]			HT-31 Samples				HT-33 Samples			
	Nominal Kernel Diameter (μm)	Coater Size (mm)	Charge Size for OPyC Coating (kg of Heavy Metal)	OPyC Coating: Density (Mg/m^3) Liquid Gradient	OPyC Coating: Density (Mg/m^3) Bulk	OPyC Coating: Coating Rate (μm/min)	OPyC Coating: BAF_o[b]	Coating Rate	Bulk Density	OPyC Charge Size	Fast Fluence (10^{25} n/m^2) $(E > 29 fJ)_{HTGR}$	Burnup (% FIMA)	OPyC Coating Failure (%)	Pressure Vessel Failure[d] (%)	Fast Fluence (10^{25} n/m^2) $(E > 29 fJ)_{HTGR}$	Burnup (% FIMA)	OPyC Coating Failure (%)	Pressure Vessel Failure[d] (%)
1200^oC Magazine (Design)																		
6252-05-015[e]	500	127	1.8	1.85	1.66	4.5	1.026	Low	Medium	Small	5.9	6.7	0	0	7.1	7.5	0	0
6252-06-015	450	240	11.0	1.74	1.59	5.0	1.033	Low	Low	Large	4.6	5 4	0	0	6.2	6.5	0	0
6252-06-025	450	240	6.6	1.70	1.57	5.6	1.038	Low	Low	Small	4.8	5.6	0	0	6.8	7.1	3.8	0
6252-07-015	450	240	13.2	1.81	1.59	5.9	1.042	Low	Low	Large	5.3	6.1	3.7	0	7.6	8.1	0	0
6252-07-025	450	240	6.6	1.80	1.65	5.3	1.041	Low	Medium	Small	5.5	6.3	1.9	0	7.9	8.5	0	0
6252-08-015	450	240	6.6	1.89	1.73	5.9	1.045	Low	High	Small	4.1	4.9	0	0	5.9	6.2	0	0
6252-09-015	450	240	5.5	1.78	1.59	7.5	1.036	High	Low	Small	6.1	6.9	1.9	0	8.3	9.1	0	0
6252-10-015	450	240	5.5	1.98	1.75	8.4	1.052	High	High	Small	6.5	7.2	1.9	0	5.3	5.6	0	0
1500^oC Magazine (Design)																		
6252-05-015[e]	500	127	1.8	1.85	1.66	4.5	1.026	Low	Medium	Small	8.1	8.9	(f)	94.1	10.4	12.5	(f)	100
6252-06-015	450	240	11.0	1.74	1.59	5.0	1.033	Low	Low	Large	7.4	8.2	0	0	10.1	12.1	(f)	100
6252-06-025	450	240	6.6	1.70	1.57	5.6	1.038	Low	Low	Small	7.6	8.4	(f)	11.7	10.2	12.2	(f)	100
6252-07-015	450	240	13.2	1.81	1.59	5.9	1.042	Low	Low	Large	7.7	8.5	(f)	52.5	9.8	11.5	(f)	98.7
6252-07-025	450	240	6.6	1.80	1.65	5.3	1.041	Low	Medium	Small	7.9	8.6	(f)	38.5	9.9	11.7	(f)	100
6252-08-015	450	240	6.6	1.89	1.73	5.9	1.045	Low	High	Small	8.1	8.8	(f)	80.0	10.4	12.8	(f)	27.5
6252-09-015	450	240	5.5	1.78	1.59	7.5	1.036	High	Low	Small	7.9	8.7	(f)	94.9	9.4	11.0	(f)	51.3
6252-10-015	450	240	5.5	1.98	1.75	8.4	1.052	High	High	Small	8.0	8.8	(f)	53.2	10.4	12.6	(f)	98.7

[a] All samples were screened, density separated to parent batch average and heat treated at 1800^oC for 30 minutes in Ar.

[b] Measured with Seibersdorf optical anisotropy unit using 24 μm circle.

[c] Word descriptions are relative to these particle batches only.

[d] Based on visual examination.

[e] This sample was previously tested in capsules HT-28 and HT-29.

[f] OPyC failure with pressure vessel failure was not observed.

Also, the sample sizes are small and, therefore, the uncertainty in the failure fractions is relatively high.

The results of the TRISO ThO_2 samples are discussed below. The irradiation performance of particles fabricated in a prototype 127-mm-diameter coater and the pilot plant 240-mm-diameter coater was similar. The OPyC coatings having a range of properties performed acceptably at 1200°C. Although high pressure vessel failure occurred in the high-temperature magazines of capsules HT-31 and HT-33, the irradiation conditions were severe and the cause of the failure cannot be determined until further analysis is performed. The failure fractions will be correlated with particle performance model prediction to compare the performance to that of previously irradiated particles. The 1500°C results may be clouded by the fact that ORNL detected corrosion of exposed SiC coatings of the driver fuel in capsules HT-31 and HT-33 (Ref. 9-9). It is possible that the OPyC coating failed initially in the TRISO particles and then the SiC coating was degraded by corrosion, causing increased SiC coating failure.

The BISO ThO_2 particle samples were irradiated in capsule HT-33. The irradiation conditions and the results of the visual examination are given in Table 9-11. The OPyC coating failure (same as pressure vessel failure for BISO particle) ranged from 0 to 59% for the 1200°C samples irradiated to a fluence of 5.3 to 8.3 x 10^{25} n/m^2 $(E > 29\ fJ)_{HTGR}$ and a burnup of 5.6 to 9.1% FIMA. The 1500°C samples exhibited 0 to 95% failure after irradiation to fluences of 9.4 to 10.4 x 10^{25} n/m^2 $(E > 29\ fJ)_{HTGR}$ and burnups of 11.0 to 12.8% FIMA.

The results of BISO coated ThO_2 particles are described below. The irradiation performance of particles fabricated in the small- and large-diameter coaters was similar, as it was for the TRISO particles. Two types of diluent gases were used for the deposition of the OPyC coating. Inert diluent gases (N_2, Ar, and He) have been used primarily at GA in the small-diameter coaters. H_2 dilution appeared to produce a more uniform OPyC coating for the large coater batches. Capsule HT-33 was the first experiment to test OPyC coatings deposited using H_2 diluent gas. The initial

TABLE 9-11

DESCRIPTION AND RESULTS OF VISUAL EXAMINATION OF BISO ThO_2 SAMPLES[(a)] IN CAPSULE HT-33

Sample Number	Variables									Irradiation Conditions			Results of Visual Exam	
	Process			OPyC Coating				Capsule Sample Heat-Treatment Condition						
	Coater Size (mm)	Initial Load Size (kg)	OPyC Coating Diluent Gas	Density (Mg/m^3) Liquid Gradient	Density (Mg/m^3) Bulk	Coating Rate (μm/min)	BAF_o[(b)]	As-Coated	1650°C[(c)]	Capsule Position[(d)]	Fast Fluence[(e)] ($\times 10^{25}$ n/m^2) ($E > 29$ fJ)$_{HTGR}$	Burnup[(d)] (% FIMA)	Number of Particles	OPyC Coating Failure (%)
1200°C Magazine (Design)														
6542-39-0161-001	240	20	N_2	1.98	1.92	3.9	1.079		X	2	5.3	5.6	38	7.9
6542-40-0161-001	240	13	H_2	1.74	1.67	5.8	1.043		X	4	5.9	6.2	41	0
6542-40-0261-001	240	13	H_2	1.77	1.70	5.8	1.038		X	5	6.2	6.5	41	0
6542-40-0260-001	240	13	H_2	1.77	1.69	5.6	1.038	X		7	6.8	7.1	41	0
6542-27-0161-001[(f)]	127	2	Ar	1.86	1.78	4.2	1.041		X	8	7.1	7.5	40	0
6542-29-0261-001	240	20	N_2	1.96	1.89	4.4	1.081		X	10	7.6	8.1	39	59.0
6542-41-0161-001	240	13	N_2	2.02	1.93	5.5	1.081		X	11	7.9	8.5	40	35.0
6542-41-0160-001	240	13	N_2	2.00	1.93	5.6	1.060	X		13	8.3	9.1	40	30.0
1500°C Magazine (Design)														
6542-29-0261-002	240	20	N_2	1.96	1.89	4.2	1.081		X	15	9.4	11.0	55	89.1
6542-27-0161-002[(f)]	127	2	Ar	1.86	1.78	4.2	1.041		X	17	9.8	11.5	57	0
6542-41-0161-002	240	13	N_2	2.02	1.93	5.5	1.081		X	18	9.9	11.7	56	94.6
6542-41-0160-002	240	13	N_2	2.00	1.93	5.4	1.060	X		20	10.1	12.1	56	Lost
6542-39-0161-002	240	20	N_2	1.98	1.92	4.1	1.079		X	21	10.2	12.2	54	92.6
6542-40-0161-002	240	13	H_2	1.74	1.67	5.7	1.043		X	23	10.4	12.5	58	91.4
6542-40-0261-002	240	13	H_2	1.77	1.70	5.6	1.038		X	24	10.4	12.6	56	0
6542-40-0260-002	240	13	H_2	1.77	1.69	5.7	1.038	X		26	10.4	12.8	58	17.2

(a) All samples were screened and density separated to the batch average density.

(b) Measured with Seibersdorf optical anisotropy unit using 24 μm circle.

(c) Heat treated at 1650°C for 90 minutes in Ar.

(d) The number designates the axial position in capsule; the numbers increase consecutively toward the bottom of capsule (relative to the reactor core).

(e) Design values.

(f) Batch previously tested in capsules HT-28 and HT-29.

results indicate the irradiation performance of OPyC coatings made with H_2 and inert gas diluents was comparable. The OPyC coating failure is plotted as a function of fast fluence in Fig. 9-18. This figure indicates a fluence dependence although there is a great deal of scatter in the data points.

The most influential effect on the coating failure appears to be anisotropy. Figure 9-19 is a plot of coating failure as a function of anisotropy. This figure shows that all samples which had a OPyC coating optical anisotropy (BAF_o) of greater than or equal to 1.06 exhibited high failure at both 1200° and 1900°C. All these samples had a high OPyC density. The failure is attributed to the irradiation-induced dimensional change of the OPyC coating due to the high anisotropy rather than the high density (Ref. 9-10). All samples which had an OPyC $BAF_o \leq 1.04$ exhibited zero failure at 1200°C and a range of failure at 1500°C. These samples included the particles with the OPyC coating deposited using H_2 dilution. Some failure would be expected in the high-temperature samples since the particles were irradiated to burnups which were 30% to 45% higher than the peak LHTGR burnup, and higher temperatures produce higher OPyC coating failure (Ref. 9-11). The reason for the large differences in failure in the 1500°C BISO samples with $BAF_o \leq 1.04$ is not known; this difference will be evaluated during further analysis.

TASK 300: INTEGRAL FUEL SYSTEM TESTING

Subtask 310: Peach Bottom Fuel Test Elements

Differential Thermal Expansivity Measurements for H-327 Graphite Strips From Peach Bottom Fuel Test Elements

Summary. Five thin strips from Peach Bottom fuel elements FTE-5 and FTE-6 were submitted for a heatup experiment in order to establish the sensitivity of irradiation-induced thermal expansivity changes and to find a possible explanation for the fact that four of these five strips experienced residual bow in a direction contrary to prediction.

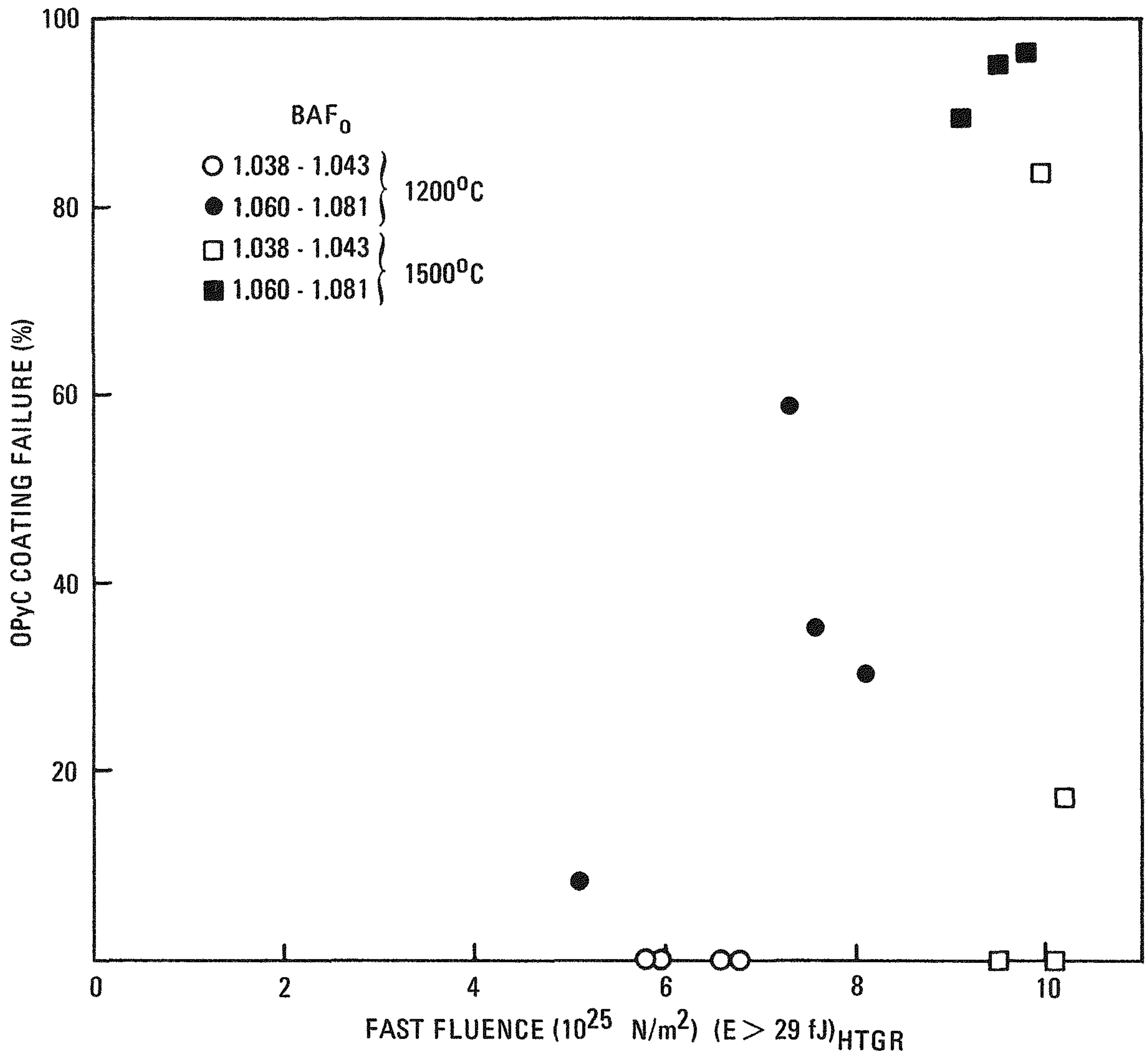

Fig. 9-18. Total coating failure of BISO ThO_2 samples irradiated in capsule HT-33 as a function of fluence

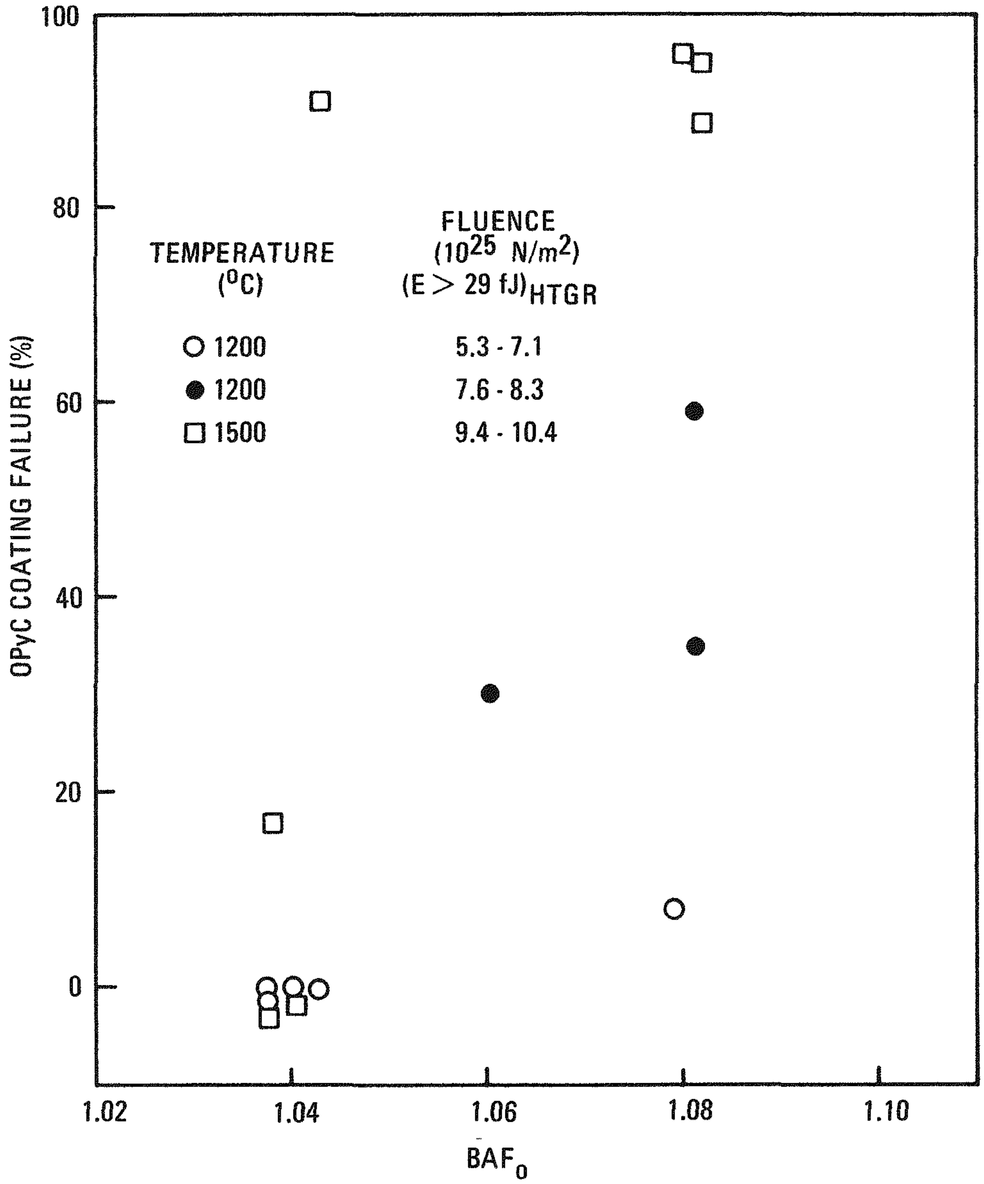

Fig. 9-19. Total coating failure of BISO ThO_2 samples irradiated in capsule HT-33 as a function of anisotropy

For all five cases, the presence of a larger coefficient of thermal expansion (CTE) at the location of the hotter fiber of the strip during irradiation was unambiguously established. All five strips showed abnormalities in thermal strain starting at furnace temperatures above 600° to 800°C, which are possibly annealing effects when reaching irradiation damage temperatures. This can be explained either by a sudden recovery of larger irradiation-induced shrinkages at the hotter fiber or a partial recovery of larger irradiation-induced reduction of thermal expansivity at the cooler fiber.

The established amount of differential CTE was found to be larger than present predictions and in some cases in the opposite direction. This is not unexpected, considering the second-order nature of a differential effect and the high sensitivity to irradiation temperatures. The magnitude of the shutdown stress component due to measured differential CTE was found to be equal to, or larger than, the amount due to temperature gradients along the cross section of the tested strip. Mean CTE measurements on samples taken from the same strip and differential expansivity measurements on the complete strip by the described method are a good means for establishing shutdown stresses independently of other methods.

Residual stresses* should be derived from residual bow measurements. By this means operational stresses prior to shutdown could be established. Because of the inverse direction of the bow, compressive operational stresses were deduced at the hottest fiber of the strip, where tensile stresses are predicted based on the well established dimensional changes of the material. Any contribution from the thermal expansivity toward this abnormality was ruled out by the described sensitivity experiment. The cutting mode of the saw is suspected as a possible cause. The cutting characteristics of the saw will be examined using irradiated graphite as the inversion in bow was found to increase with irradiation exposure.

---

*Only differential stresses between the inner hotter and cooler outer fiber are discussed.

Experiment Description. An experiment was conducted on five thin strips obtained from the destructive stress examination of Peach Bottom fuel test elements. One end of the strips was cantilevered inside a horizontal furnace, which had glass windows at the front and rear. The deflection of the free end of the strip was photographically recorded during heatup to 1000°C and subsequent cooldown.

Figures 9-20a and 9-20b show one of the strips at furnace temperatures of 84° and 1000°C, respectively. From the auxiliary grid in the photographs, a lateral movement of the free end in the direction of the original bow of the strip can clearly be identified. The plane of the bow was approximately horizontal in order to eliminate gravitational effects. A slight inclination in the longitudinal direction was required for better visibility. An additional but smaller movement of the strip in an upward direction can be seen from a comparison of Figs. 9-20a and 9-20b. This movement is apparently due to a slight asymmetry in the cross section of the strip. Only the lateral movement of the strips was analysed.

The deflection of the five strips versus furnace temperature is given in Figs. 9-21 and 9-22. The measurements have been corrected for parallax and scale. The nominal graduation of the photographed scale is 1 mm, the actual scale was calibrated as 0.9878 mm, and the parallax factor was 0.8636, which resulted in a conversion factor of 0.8531 from the photographed to the actual scale at the plane of the free end of the strip.

The precision of the photographic measurements was assessed as (Ref. 9-12)

$$p = \pm \frac{e}{\sqrt{12n}} \qquad (1\sigma) \quad , \qquad (9\text{-}4)$$

where e is the smallest graduation of the scale and n is the number of measurements taken. This resulted in

$$p = \pm 0.246 \text{ mm}$$

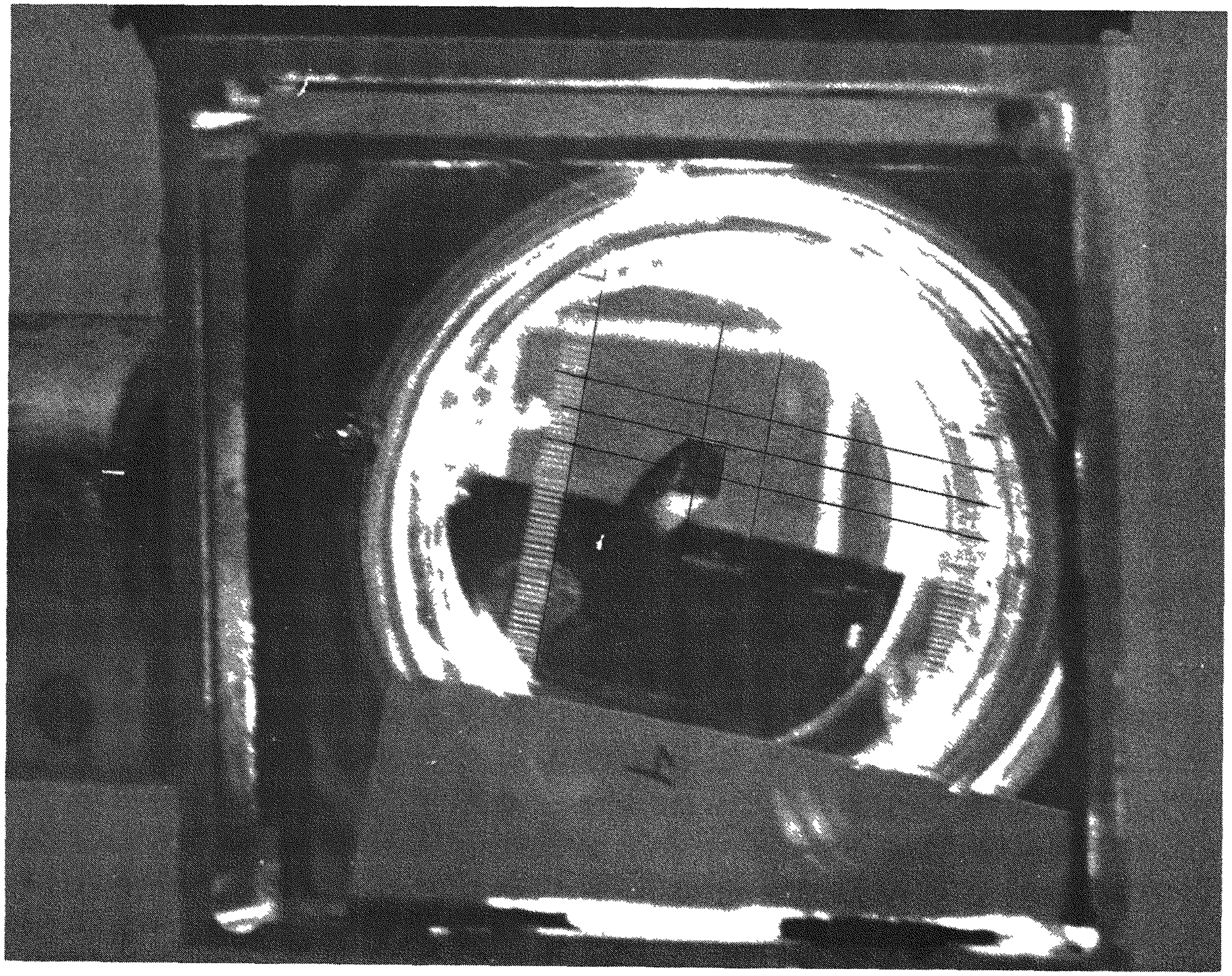

Fig. 9-20. FTE-5 strip 5-2-1-1 heatup experiment: (a) furnace temperature 84°C

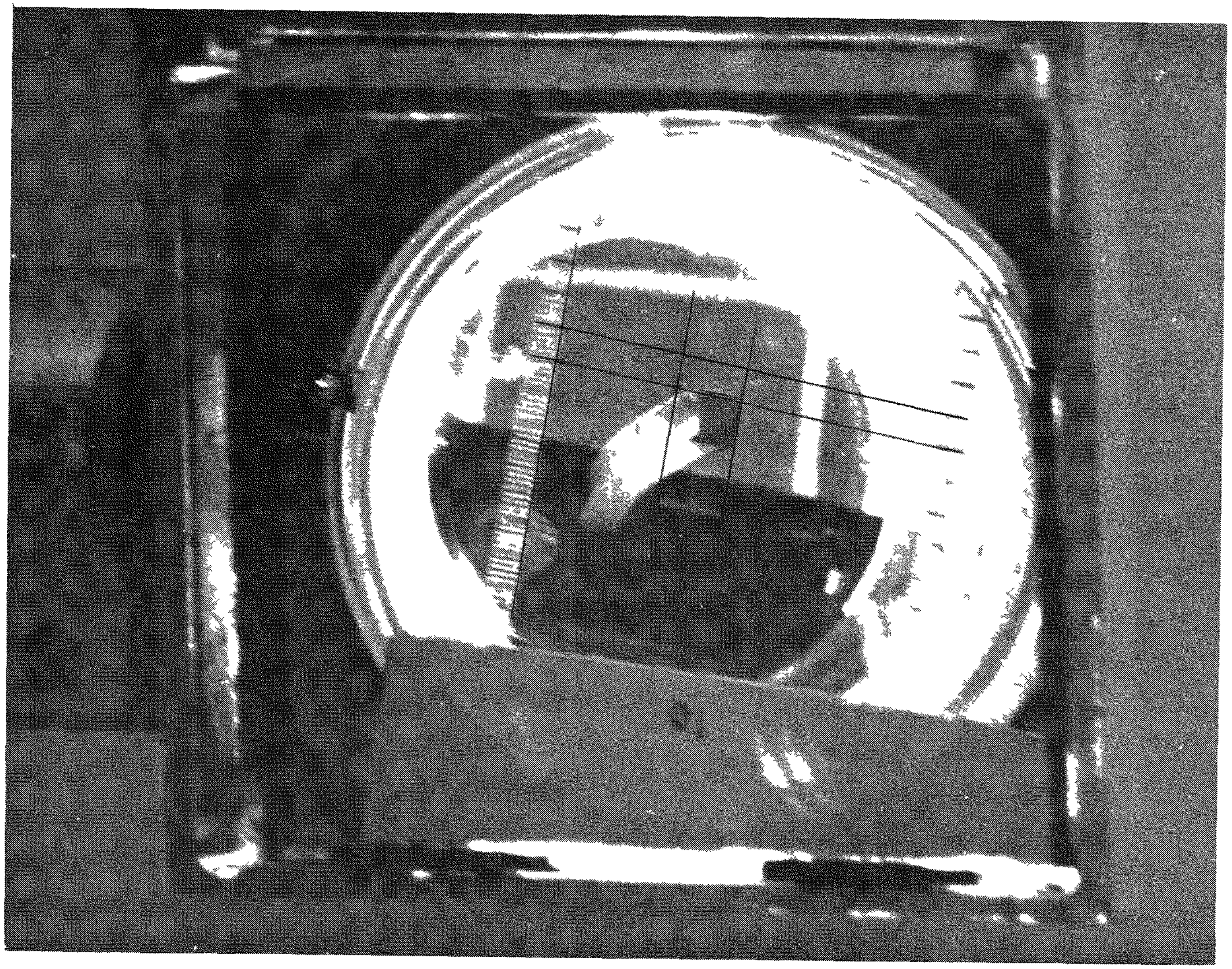

Fig. 9-20. FTE-5 strip 5-2-1-1 heatup experiment: (b) furnace temperature 1003°C

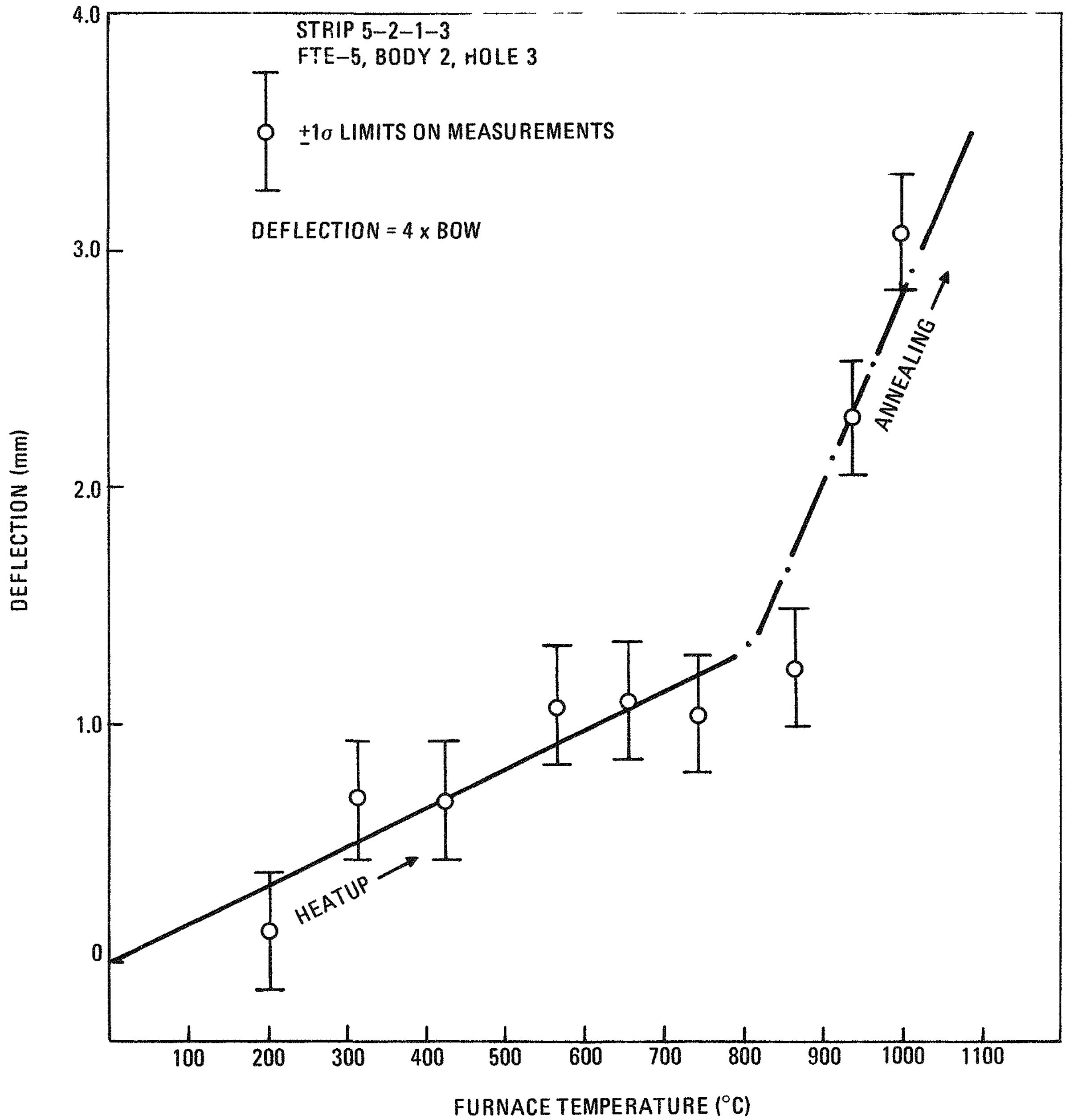

Fig. 9-21. FTE-5 thin strip heatup experiment, differential deflection versus furnace temperature: (a) body 2, hole 3

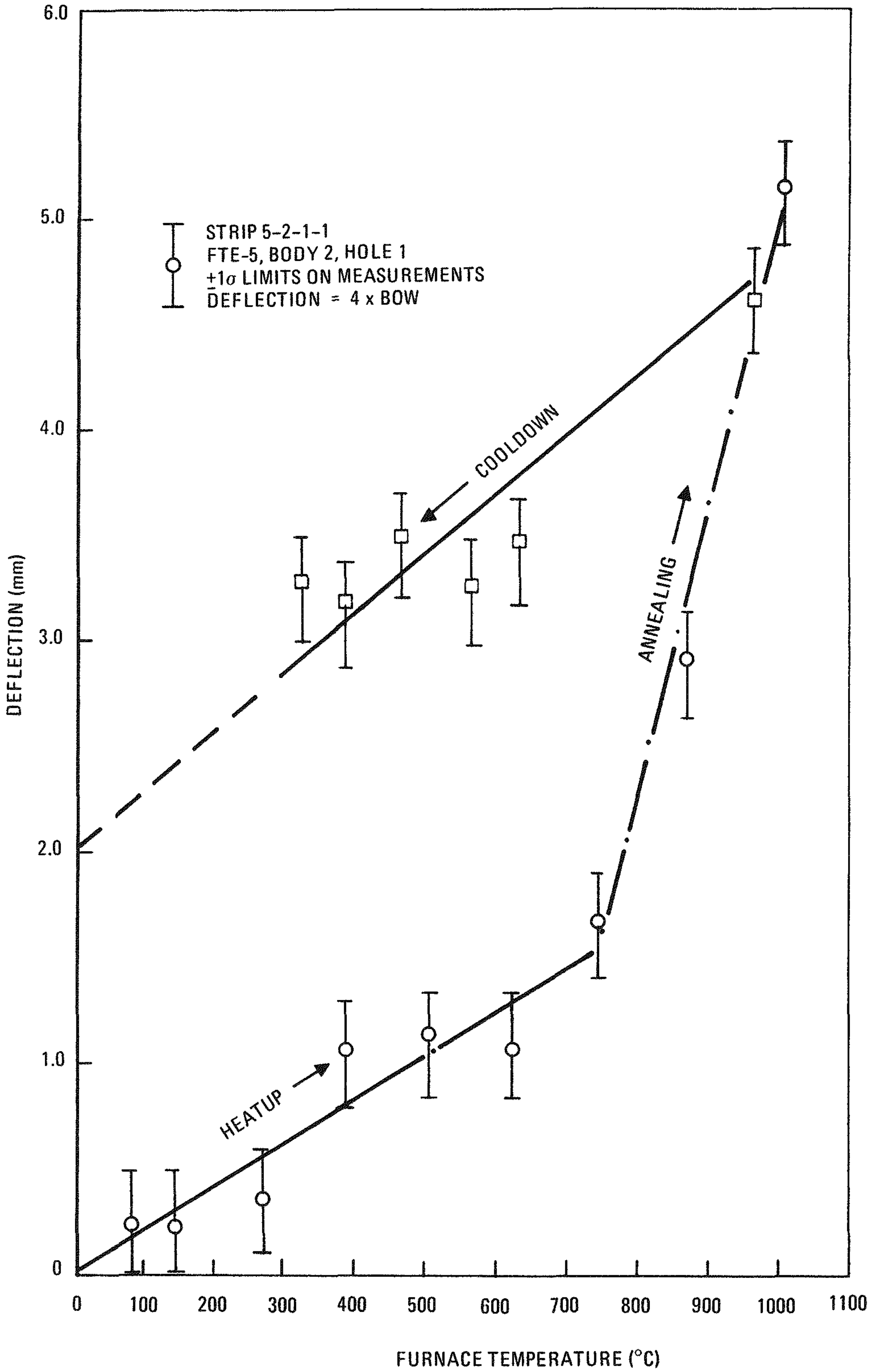

Fig. 9-21. FTE-5 thin strip heatup experiment, differential deflection versus furnace temperature: (b) body 2, hole 1

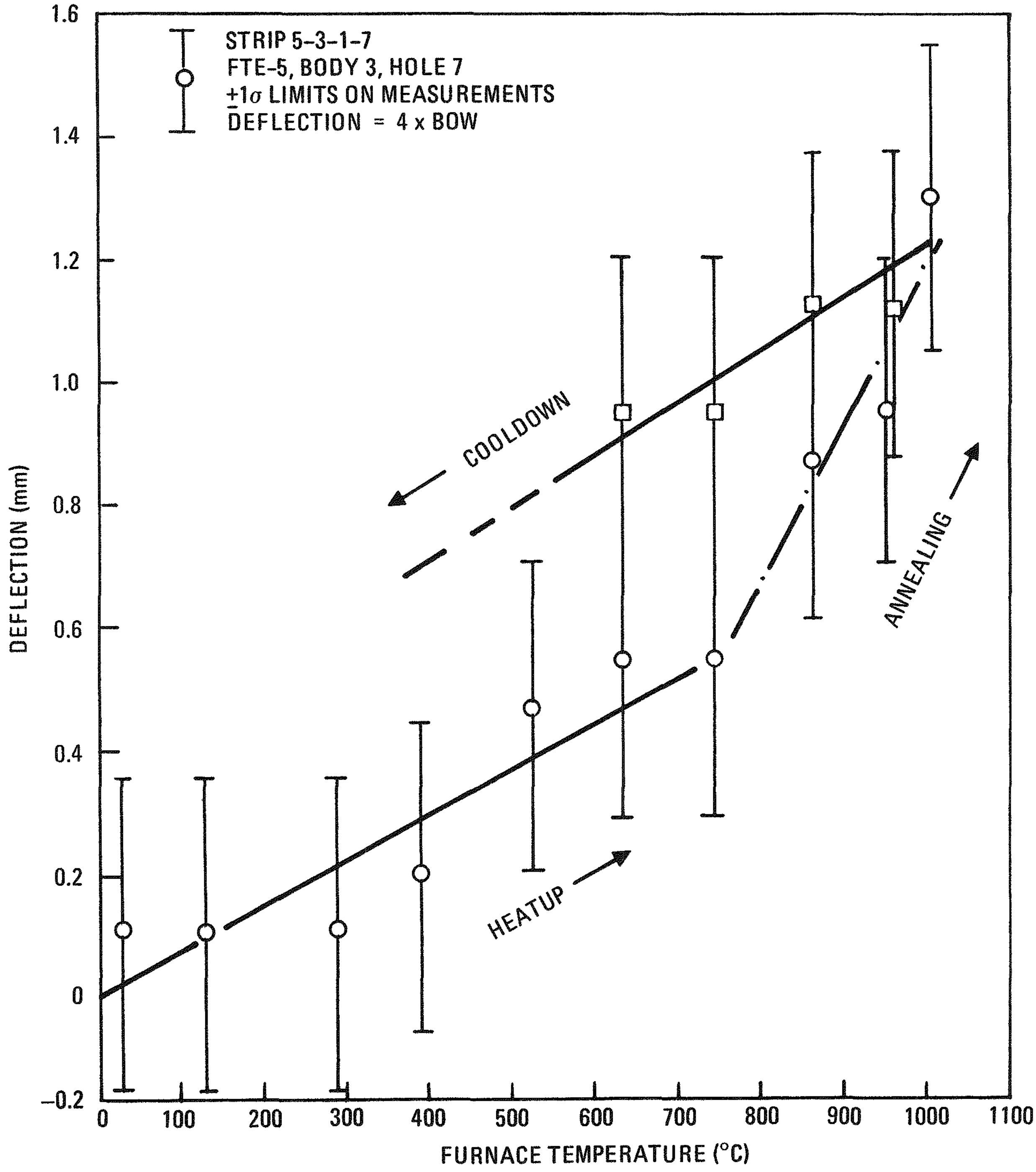

Fig. 9-21. FTE-5 thin strip heatup experiment, differential deflection versus furnace temperature: (c) body 3, hole 7

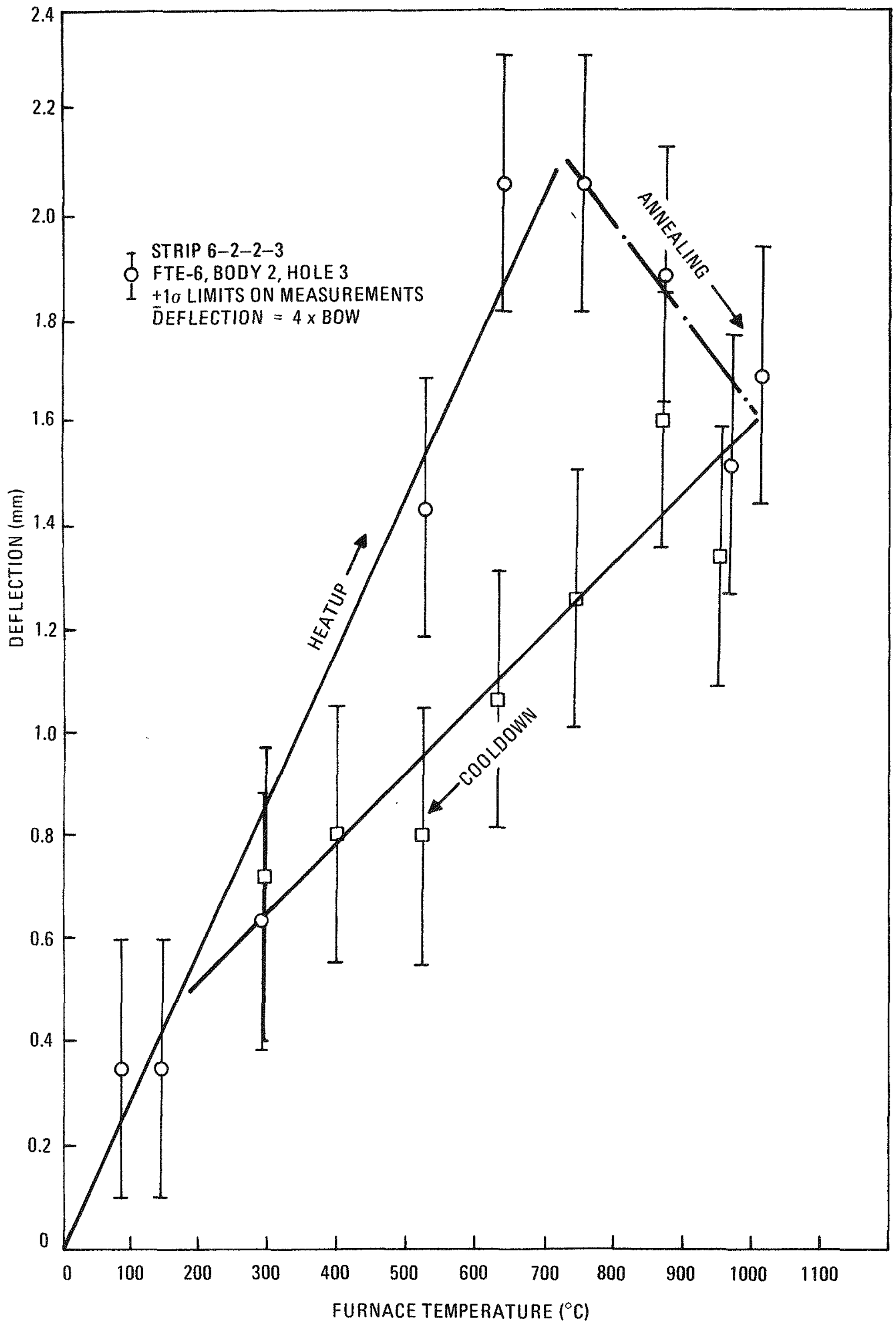

Fig. 9-22. FTE-6 thin strip heatup experiment, differential deflection versus furnace temperature: (a) body 2, hole 3

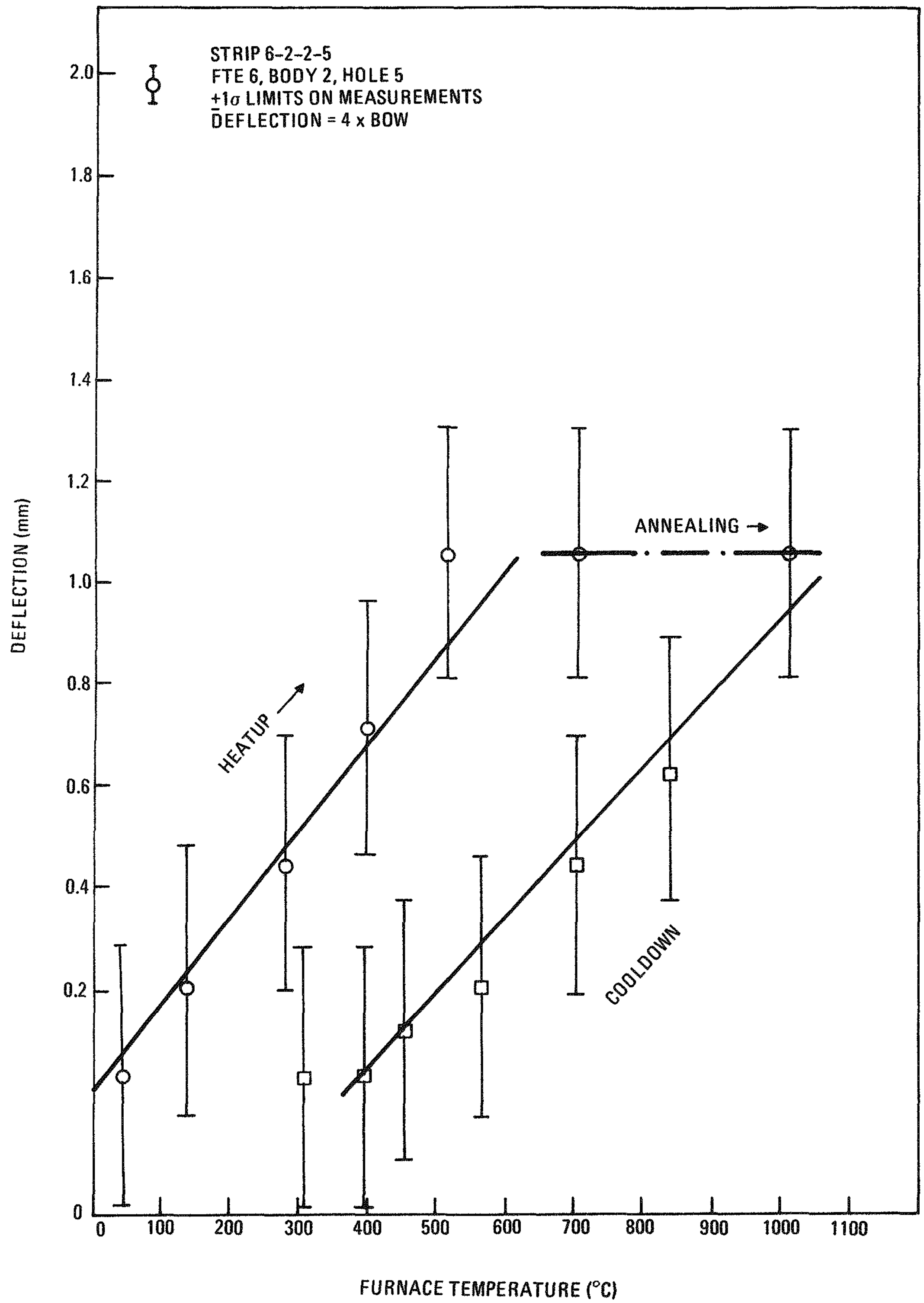

Fig. 9-22. FTE-6 thin strip heatup experiment, differential deflection versus furnace temperature: (b) body 2, hole 5

for a single measurement, as shown in Figs. 9-21 and 9-22.

A preliminary calibration of the furnace was done with an unirradiated strip which did not show lateral movement. The calibration will be repeated in conjunction with a temperature field determination. The present analysis is based on a nominal furnace temperature, i.e., isothermal conditions are assumed. In the likely event of axial temperature buckling, the presently deduced sensitivity of the thermal expansivity between the inner and outer fibers of the strip with regard to the center of the teledial graphite fuel bodies, from where the strips were cut, will increase. The inner fiber is the concave side of the strip cross section, as shown in Fig. 9-20b. This side was part of the fuel hole surface and was therefore the hotter fiber during irradiation. The nominal strip dimensions of the thin strips were:

Length, ℓ_o	457.2 mm (18.0 in.)
Width, w	8.99 mm (0.35 in.)
Min. thickness, t_{min}	5.59 mm (0.22 in.)
Mean thickness, t	5.84 mm (0.23 in.)
Max. thickness, t_{max}	7.11 mm (0.28 in.)

The analysis was based on an idealized strip with a rectangular cross section (width t x thickness w). Circular bending was assumed, which gives a deflection at the free end four times larger than the maximum bow (arc-to-chord displacement):

$$f = 4h \quad ,$$

where f is the deflection and h is the bow. The experimental arrangement took advantage of this magnifying effect.

Data Evaluation. The experiment was designed to identify the direction and approximate magnitude of a differential CTE along the cross section of an irradiated strip. A difference in CTE between the inner and outer fibers will result in a differential strain during isothermal heatup of the strip:

$$\delta\varepsilon = \frac{2t\delta f}{\ell_o^2} \quad . \tag{9-6}$$

The differential deflection δf is the observed change in deflection during heatup. The sign convention is based on a larger CTE at the inner hotter fiber, which results in a positive differential strain during isothermal heatup for the inner fiber and consequently in a bow direction away from the center of the fuel. All five measured strips unambiguously support this assumption of a larger CTE at the inner fiber. This demonstrates a lower reduction of the beginning-of-life CTE at a higher irradiation temperature for the temperature range experienced by the five strips.

The differential strain can be divided by the differential temperature, which results in a differential CTE:

$$\delta CTE = \frac{\delta\varepsilon}{\delta T} = \frac{2t}{\ell_o^2} \cdot \frac{\delta f}{\delta T} = \frac{2t}{\ell_o^2} \cdot a_1 \quad . \tag{9-7}$$

The term $\delta f/\delta T$ is the first derivative of the deflection versus temperature plot. Under a linearity assumption, this would be the slope a_1 of a linear regression of the measurements presented in Figs. 9-21 and 9-22.

Three distinctive ranges can be recognized: (1) heatup, (2) annealing, and (3) cooldown. The second range is distinguished from the first by an abrupt change in slope, which is positive for all three strips from FTE-5. This may be explained by annealing of irradiation-induced dimensional changes, especially at the hotter inner fiber (rather than a differential CTE), which would begin when the end-of-life (EOL) irradiation temperature is exceeded. During cooldown, the measured differential strain is approximately the same as that during the heatup phase. Strips 5-2-1-1 and 5-3-1-7 (Figs. 9-21b and 9-21c) show a slightly steeper slope during cooldown than during heatup, which supports a more isothermal temperature field and hence a more pronounced differential strain than during heatup. (Strip 5-2-1-3 was not measured during cooldown; strips 5-2-1-1 and strip 5-2-1-3 were sister strips taken from the same graphite body.) Table 9-12 includes the EOL irradiation conditions as determined through an irradiation simulation of the experiment with HTGR design codes. The predicted EOL temperatures (volume averages) are close to the so-called annealing temperatures, determined as the intersection between the linear regression analysis.

The two sister strips 6-2-2-3 and 6-2-2-5 taken from the center body of FTE-6 again show an annealing range; however, no further increase in strain is observed, but rather a leveling off (Fig. 9-22a) or even a decrease (Fig. 9-22b). In neither case was the predicted EOL temperature reached when the change was observed. In both cases the slope during cooldown is lightly flatter than during heatup; this is contrary to a more pronounced differential strain in a more isothermal temperature field, as postulated earlier and experienced for FTE-5. A partial reduction in differential expansivity especially at the cooler outer fiber (rather than, or in excess of, recovery from irradiation-induced changes) during the annealing phase would be a possible explanation, which could also explain a lower differential CTE during cooldown. The lack of agreement between the predicted EOL irradiation temperature and the observed "annealing" temperature could have originated with the different temperature history of FTE-6 as compared with FTE-5. Also, the Peach Bottom Reactor was run on a downward transient during the last weeks of operation, which made predictions of EOL temperatures difficult. The "memory" of graphite with regard to a representative irradiation damage temperature is also not fully established. Strip 6-2-2-3 (Fig. 9-22a) shows recovery toward the original deflection. The hysteresis of the strips can be established through remeasurement of the deflection after cooldown.

Table 9-12 presents a summary of the differential CTE values deduced for the different ranges observed for the five strips. The 1σ uncertainty statements were derived from the standard error determined for the slope of the linear regression. The correlation coefficient was greater than 0.8

TABLE 9-12

COMPARISON OF PREDICTED AND MEASURED DIFFERENTIAL CTE[(a)] ACROSS STRIP IN FTE-5 AND FTE-6 HEATUP EXPERIMENT

Strip ($\bar{t}$ = 0.23 in.)			Measured EOL Differential Thermal Expansivity				δCTE	CTE($\bar{T}_{irr.}$) Ref. Value[(b)] (10^{-8} deg^{-1})		δCTE/CTE	δCTE/CTE	Irradiation Parameters				
													Irrad. Temp.		EOL Temp.	
Identi-fication	Length, ℓ_o (in.)	Symbols	Heatup A (10^{-8} deg^{-1})	"Annealing" B (10^{-8} deg^{-1})	Cooldown C (10^{-8} deg^{-1})	All Data D (10^{-8} deg^{-1})	Mean Meas. (A+C)/2 (10^{-8} deg^{-1})	BOL	EOL	Measured Rel. Diff. CTE (%)	Predicted Rel. Diff. CTE (%)	Fast Fluence (10^{25}n/m^2) (E > 29 fJ)	Mean (°C)	δT (°C)	Pred. (°C)	"Anneal." (°C)
5-2-1-3	18.0321	x,$\bar{x}$	8.92	44.6	ND[(c)]	15.4	8.92	178 4	170.3	5.24	-1.03	3.67	905	35	685	∿810
		S_x,$S_{\bar{x}}$	2.08	12.9		3.3	2.08			1.22					δT=25	
5-2-1-1	18.0390	x,$\bar{x}$	11.49	77.5	15.77	22.6	13.63	178.4	170.3	8.00	-1.03	3.67	905	35	685	∿750
		S_x,$S_{\bar{x}}$	1.42	6.9	3.60	10.8	2.46			1.44					δT=25	
Mean		$\bar{x}$	10.20		15.77		12.06	178.4	170 3	7.08	-1.03	3.67	905	35		∿780
		$S_{\bar{x}}$	1.55		3.60		2.19			1.29						
6-2-2-5	18.0978	x,$\bar{x}$	9.38	0	8.04	5.3	8.71	184.2	177.3	4.91	-1.69	2 83	950	39	930	∿710
		S_x,$S_{\bar{x}}$	1 19		0.81	1.8	0.86			0.49					δT=38	
6-2-2-3	17.9155	x,$\bar{x}$	16.51	-10.2	7.68	8.4	12.10	184.2	177.3	6.82	-1.69	2.83	950	39	930	∿630
		S_x,$S_{\bar{x}}$	1.71	3.6	1.09	1.4	4.64			1.85					δT=38	
Mean		$\bar{x}$	12.95		7.86		10.40	184.2	177.3	5.87	-1.69	2.83	950	39		∿670
		$S_{\bar{x}}$	2.73		0.98		1.90			1.07						
5-3-1-7	17.9158	x,$\bar{x}$	4.19	14.6	4.90	7.0	4.54	177.2	176.5	2.57	+0.06	2.38	896	22	735	∿750
		S_x,$S_{\bar{x}}$	0.76	3.4	1.25	5.2	0.77			0.44					δT=20	

(a) Differential CTF is the difference between the EOL CTEs at the hotter inner fiber and the cooler outer fiber of the strip. A negative δCTE means that the irradiation-induced changes resulted at a lower EOL CTE for the inner fiber. All experimental data indicate a positive δCTE as predicted for irradiation temperatures <900°C.

(b) From Ref. 9-6.

(c) ND = not determined.

for the three distinct ranges. The so-called annealing range is clearly distinguished from the heatup and cooldown ranges and has been excluded from further analysis. For comparison only, all measurements have been combined to one estimate of the differential CTE, which resulted in relatively low correlation coefficients. For further evaluation purposes, the heatup and cooldown δCTE data have been pooled as the best estimate and compared with predictions. Predictions are based on present design data (Ref. 9-6) and temperature history simulations (Ref. 9-13). The following data are taken from Table 9-12:

Fuel Element	Fast Fluence (10^{25} n/m^2) (E > 29 fJ)	Mean Irradiation Temperature (°C)	Measured δCTE/CTE (% ± 1σ%)	Predicted δCTE/CTE (%)
FTE-5, body 2	3.7	905	+7.1 ± 1.3	-1.0
FTE-5, body 3	2.4	896	+2.6 ± 0.4	+0.1
FTE-6, body 2	2.8	950	+5.9 ± 1.1	-1.7

The absolute mean CTE was taken from Ref. 9-13 and was corrected for irradiation temperature and fluence. The temperature and fluence dependences are presently being updated through additional measurements on control and irradiation samples, which should change the predicted differential CTE to a larger extent than the predicted mean CTE. The present data basis identifies a minimum for the differential CTE at 900°C irradiation temperature, which happens to coincide with the time-weighted temperature ranges established for the FTE-5 and FTE-6 strips. The observed disagreement in sign and magnitude is therefore not surprising.

Stress Assessment. The absolute operational stresses for the strip prior to cutting are predicted to be compressive with a stress gradient toward the cooler outer fiber. Thermal shutdown stresses are superimposed. The cutting operation releases the compressive axial stresses for the neutral fiber and the differential stresses between inner and outer fibers result in residual bow of the strip. The amount of axial stresses relieved can be determined from the length change of the neutral fiber. These measurements have not been completed for the presented five strips. Measurements from other strips confirm an extension of the neutral fiber, i.e., release of compressive stresses. Only the differential stresses in the axial direction along the cross section of the strip are discussed below.

Being a second-order effect, the impact of the measured differential CTE on shutdown stresses has to be established. The same sign convention as established earlier for strains is used: positive stresses at the inner fiber are tensile, and negative stresses are compressive.

The strain at the inner fiber due to thermal stresses is determined by two terms, one resulting from the temperature difference, δT, between the hot and cool fiber and a mean CTE, and the other from the differential CTE and the temperature difference, ΔT, between the mean EOL operational temperature and the shutdown temperature:

$$\varepsilon_{th} = \underbrace{\overline{CTE} \cdot \delta T}_{\text{First order term}} + \underbrace{\delta CTE \cdot \Delta T}_{\text{Second order term}} \quad (9\text{-}8)$$

The proportion between both terms has been established in Table 9-13 for all five strips and found to be about equal or slightly larger for the second-order term. According to the present design data base, the differential CTE becomes negative for irradiation temperatures above 900°C, which results in a reduction of shutdown stresses. The sensitivity of the thermal expansivity has therefore a significant impact on shutdown stresses. Measurement of absolute and differential CTE is a good means of establishing shutdown stresses independent of predictions.

In the unrelieved state (prior to cutting), the thermal strain results in tensile stresses which are maximum at the hottest fiber:

$$\sigma_{th} = \varepsilon_{th} \cdot E \quad . \quad (9\text{-}9)$$

TABLE 9-13

FTE-5 AND FTE-6 STRESS ASSESSMENT FOR INVERSELY BOWED STRIPS AT HOTTEST FIBER[a]

Strip		Material Properties			Maximum Shutdown Strain				Maximum Fiber Stresses, EOL			Material Strength, EOL	
Identification	Residual Deflection, f[b] (in.)	Elastic Mod., E_{EOL}[c] (10^6 psi)	Ref. $\overline{CTE}$[c] (10^{-8} deg^{-1})	Measured δCTE (10^{-8} deg^{-1})	$\varepsilon(\overline{CTE})$ (10^{-5})	$\varepsilon(\delta CTE)$ (10^{-5})	ε (10^{-5})	$\varepsilon(\delta CTE)/\varepsilon$ (%)	Thermal σ_{th} (psi)	Residual[d] σ_{resid} (psi)	Operational[d] σ_{oper} (psi)	Tensile σ_{UTS} (psi)	Bending[e] σ_{UBS} (psi)
5-2-1-1	-0.5156	3.23	170.3	8.92	4.26	5.93	10.19	58	329	-1176	-1505	5111	6797
5-2-1-3	-0.4523	3.23	170.3	13.63	4.26	9.06	13.32	68	430	-1031	-1461	5111	6797
6-2-2-5	+0.0276	3.17	177.3	8.71	6.74	7.93	14.66	54	464	+61	-403	4990	6636
6-2-2-3	-0.0786	3.17	177.3	12.10	6.74	11.01	17.74	62	562	-178	-740	4990	6636
5-3-1-7	-0.2132	3.22	176.5	4.54	3.53	3.25	6.78	48	218	-492	-710	5106	6792

[a]Only differential stresses between inner and outer fiber of thin strip are considered; release of axial stresses through extension of neutral fiber takes place in addition.

[b]Difference in maximum deflection before and after cutting (f = 4 x bow). Positive direction toward fuel coincides with tensile stresses in the unreleased state.

[c]From Ref. 9-6. Mean values for edge location within graphite log, axial direction.

[d]*It is hypothesized that these compressive stresses are erroneous as a result of artificial deformation of the strips during cutting. The irradiation-induced* dimensional changes are higher for higher irradiation temperatures, which should lead to restraint shrinkage and consequently tensile rather than compressive stresses at the hottest fiber.

[e]A ratio of 1.33 between ultimate bending and ultimate tensile stresses was taken from Ref. 9-14.

The differential deflection f between the fuel body and the strip can be converted to residual axial tensile stresses, which are the sum of operational and shutdown stresses. (The positive direction of bow or deflection is defined as the direction toward the fuel.)

$$\sigma_{resid} = \frac{t \cdot f \cdot E}{\ell_o^2} \tag{9-10}$$

$$\sigma_{oper} = \sigma_{resid} - \sigma_{th} \tag{9-11}$$

In four of the five cases, the observed residual bow of the strip was in the direction away from the fuel, i.e., negative. The corresponding residual stresses were therefore compressive. The resulting operational stresses at EOL were compressive at the hottest fiber for all five evaluated cases. The results are given in Table 9-13.

Dimensional changes in the axial direction are increasingly negative with increasing irradiation temperatures. This results in significant tensile stress at the hottest fiber. The stated amount of bow, its direction, and the resulting compressive stresses lack a possible explanation from a material property basis. Thermal expansivity has to be ruled out because of the evidence presented.

Distortion of the strip during the cutting process still remains a possible explanation, which has to be evaluated. Inversion of the direction of bow has been found to increase with irradiation exposure. A parameter study on the cutting characteristics of the saw using irradiated material is required.

Subtask 320: FSV Fuel Test Elements

The manufacture of FTE-7 and FTE-8 was completed in December 1976. These elements were made from H-451 graphite machined by CEA Marcoule in France. The fuel loaded in these elements was standard FSV segment 7 reload fuel.

During the loading of these blocks, a considerable amount of surveillance was accomplished. Approximately 2000 graphite measurements were made and over 2500 fuel rods were measured. For each rod, two sets of three diameter measurements and two length measurements were taken. This amounts to over 20,000 data points taken on these two elements.

Similar programs are planned for FTE-1 through FTE-6. These elements will be cured-in-place.

TASK 400: OUT-OF-PILE PARTICLE TESTING AND EVALUATION

No conclusions to report.

REFERENCES

9-1. Young, C. A., and D. P. Harmon, "Preirradiation Report of Fuel Materials for P13T Capsule Irradiation," ERDA Report GA-A13343, General Atomic Company, April 1976.

9-2. Johnson, W. R., et al., "Postirradiation Examination of Capsules HT-24 and -25," ERDA Report GA-A13486, General Atomic Company, September 15, 1975, pp. 44-48.

9-3. Young, C., and C. B. Scott, "Postirradiation Examination of Capsule P13Q," ERDA Report GA-A14174, General Atomic Company, to be issued.

9-4. Scott, C. B., and D. P. Harmon, "Postirradiation Examination of Capsules HRB-4, HRB-5, and HRB-6," ERDA Report GA-A13267, General Atomic Company, November 28, 1975, pp. 113-118.

9-5. "HTGR Fuels and Core Development Program Quarterly Progress Report for the Period Ending November 31, 1976," ERDA Report GA-A14180, General Atomic Company, December 1976.

9-6. "Fuel Design Data Manual, Issue B," General Atomic unpublished data.

9-7. Price, R. J., and L. A. Beavan, "Final Report on Graphite Irradiation Test OG-3," ERDA Report GA-A14211, General Atomic Company, January 1977.

9-8. Kovacs, W. J., C. A. Young, and D. P. Harmon, "Preirradiation Report of TRISO and BISO Coated ThO_2 Particles for Irradiation in Capsules HT-31 and HT-33," ERDA Report GA-A13923, General Atomic Company, November 1976.

9-9. Tiegs, T. N., Oak Ridge National Laboratory, private communication, January 19, 1977.

9-10. Harmon, D. P., and C. B. Scott, "Development and Irradiation Performance of LHTGR Fuel," ERDA Report GA-A13173, General Atomic Company, October 31, 1975.

9-11. Scott, C. B., D. P. Harmon, and J. F. Holzgraf, "Postirradiation Examination of Capsules P13R and P13S," ERDA Report GA-A13827, General Atomic Company, October 8, 1976.

9-12. Wallroth, C. F., et al., "Postirradiation Examination and Evaluation of Peach Bottom Fuel Test Element FTE-4," ERDA Report GA-A13452, General Atomic Company, to be published.

9-13. Wallroth, C. F., J. F. Holzgraf, and D. D. Jensen, "Postirradiation Examination and Evaluation of Peach Bottom Fuel Test Element FTE-6," ERDA Report GA-A13943, General Atomic Company, to be published.

9-14. Price, R. J., "Strength of Graphite Webs in Fort St. Vrain Fuel Elements," General Atomic Report GA-A14201, November 1976.

11. GRAPHITE DEVELOPMENT
189a NO. 00552

Graphites that will satisfy the requirements for LHTGR components are being developed and evaluated. Characterization and irradiation studies to establish reference and backup grades for fuel elements, core support components, and side reflectors are in progress. Support technology is being developed to provide data for design and safety analyses. The support technology studies include the mechanics of graphite strength, fatigue behavior, structural integrity, analysis for impurity content, and oxidation effects. Development of control materials is included in the long-range program but no work is funded during FY-77.

Work has been completed on preproduction lots of graphite H-451, which is the fuel element reference material, and current work is concentrated on the first available production logs. Work has been suspended temporarily on backup grades S0818 and TS-1240. Initial characterization work on graphite grades for core support structures and side reflectors is in the preliminary stage. This work is aimed at completing a preliminary characterization data set, which should permit the selection of reference grades for these components.

The irradiation work has been suspended during FY-77 due to the temporary closing of the ORR and will resume in FY-78.

Progress in support technology has been made in areas of determining fatigue behavior, verification of stress calculation methods, and oxidation effects.

TASK 100: FABRICATION AND OPERATION OF IRRADIATION CAPSULES

Capsule OG-5

Work on capsule OG-5 remains suspended during the FY-77 shutdown of the Oak Ridge Reactor. Assembly of the capsule will be resumed during the final quarter of FY-77 in preparation for insertion in the Oak Ridge Reactor early in FY-78.

TASK 200: GRAPHITE SPECIMEN PREPARATION AND PROPERTY MEASUREMENTS FOR CAPSULE IRRADIATION

Capsule OG-3

The final topical report on the OG-3 capsule (Ref. 11-1) was completed and issued. An abstract of the report follows:

"This report documents the results of dimensional, thermal expansivity, thermal conductivity, Young's modulus, and tensile strength measurements on graphite specimens irradiated in capsule OG-3. The graphite grades investigated included near-isotropic H-451 (three different preproduction lots), TS-1240, and S0818; needle coke H-327; and European coal tar pitch coke grades P_3JHA_2N, P_3JHAN, and ASI2-500. Data were obtained in the temperature range 823 K to 1673 K. The peak fast neutron fluence in the experiment was 3×10^{25} n/m^2 (E > 29 fJ)$_{HTGR}$; the total accumulated fluence exceeded 9×10^{25} n/m^2 on some H-451 specimens and 6×10^{25} n/m^2 on some TS-1240 specimens.

Irradiation-induced dimensional changes on H-451 graphite differed slightly from earlier predictions. For an irradiation temperature of about 1225 K, axial shrinkage rates at high fluences were somewhat higher than predicted, and the fluence at which radial expansion started (about 9×10^{25} n/m^2 at 1275 K) was lower. TS-1240 graphite underwent smaller dimensional changes than H-451 graphite, while limited data on S0818 and ASI2-500 graphites showed similar behavior to H-451. P_3JHAN and P_3JHA_2N graphites displayed anisotropic behavior with rapid axial shrinkage. Comparison of dimensional changes between specimens from three logs of H-451 and of TS-1240 graphites showed no significant log-to-log variations for H-451, and small but significant log-to-log variations for TS-1240.

The thermal expansivity of the near-isotropic graphites irradiated at 865 K to 1045 K first increased by 5% to 10% and then decreased. At higher irradiation temperatures the thermal expansivity decreased by up to 50%. Changes in thermal conductivity were consistent with previously established curves. Specimens which were successively irradiated at two different temperatures took on the saturation conductivity for the new temperature.

The fractional increase in Young's modulus as a function of irradiation conditions was similar for all near-isotropic graphite specimens, regardless of orientation or location in the parent log. The tensile strength increased in a manner similar to Young's modulus, but the exact relationship between strength and modulus was different for different materials. The coefficient of variation of the strength determinations was not significantly changed by irradiation."

TASK 300: CHARACTERIZATION OF CANDIDATE GRAPHITES FOR PROPERTIES AND PURITY

Replaceable Fuel and Reflector Elements

H-451 Production Logs

Current work is concentrated on production logs of H-451 manufactured for Fort St. Vrain (FSV) fuel element reloads. Approximately 350 logs were processed through the bake state during FY-76 by GLCC and 98 of these logs were further processed through graphitization and purification. The disposition of the 98 logs was discussed in the previous quarterly report (Ref. 11-2). Tensile testing has been completed on eight axial specimens taken at the approximate midlength center (MLC) of each log and on four radial specimens taken from the end center (EC). The data have been analyzed and a topical report (Ref. 11-3) was written to cover the work. A summary of this report follows:

"Ninety-eight production logs of H-451 graphite, from three separate extrusion lots, were sampled for tensile testing. Eight replicate axial specimens from the midlength center and four replicate radial specimens from the end center of each log were tested. The following observations were made:

1. The axial strengths (average value 12.7 MPa) showed wide lot-to-lot and log-to-log variations, while the radial strengths (average value 15.8 MPa) were more uniform.

2. There was no statistically significant correlation between axial strength and radial strength in the same log, or between strength and the position of the log in the graphitizing furnace.

3. Acceptance criteria for assigning logs to a minimum strength category should be based on axial tensile tests, and each log should be sampled. A statistical model incorporating a separate lot-to-lot variance, log-to-log variance, and within-log variance was adopted for this purpose.

4. Acceptance criteria for assigning a log to strength category A [minimum strength 10.3 MPa (1500 psi)], B [minimum strength 8.3 MPa (1200 psi)], or C [minimum strength 5.5 MPa (800 psi)] were derived. Calculations were made for either four or eight replicate specimens per log and for two alternative definitions of "minimum strength." The first definition would require 90% of the material at the midlength center of the log to exceed the specified minimum strength, with 90% confidence (90/90); the second, more stringent,

definition would require 99% of the material to exceed the specified minimum, with 95% confidence (99/95).

5. The criteria were applied to the axial test data from the 98 logs. Using the 90/90 definition of minimum strength and testing eight specimens per log, two logs would fail to qualify for category C while almost half of the logs would qualify for category A.

6. Adoption of the more stringent 99/95 definition of minimum strength would increase the number of logs rejected to 18; the yield of logs accepted in each strength category would fall slightly short of the requirements of a typical core segment.

7. Decreasing the number of tests per log from eight to four causes a small reduction in the yields.

8. The differences in quality between the three extrusion lots represented in the 98-log order have a clear effect on the yields of logs in each strength category. Using the 99/95 definition of minimum strength, only two of the 56 logs in the best lot (478) would be rejected and about 25% would qualify for category A. This compares with a rejection rate of about 40% for logs from the other two lots."

In conjunction with testing the strength of the 98 production logs, a round-robin test program was carried out with GLCC to assure that tensile and flexural test procedures at the two laboratories give equivalent results. A log of H-451 was sampled and the specimens divided randomly; one portion was tested by GLCC and a second portion by GA.

Summaries of the flexural and tensile data are given in Tables 11-1 and 11-2,* respectively. Comparisons and conclusions are given in Table 11-3. Full data sets are given in Tables 11-4 through 11-10. No significant differences were found when GLCC and GA tensile tests were made with cylindrical specimens; however, GLCC's tensile data averaged about 8% lower when square dogbone specimens were used. Cylindrical flexural specimens were about 13% stronger than square cross-section specimens. This experiment assures that future tensile strength data, whether measured at GA or GLCC, will be equivalent.

Side Reflector Graphite

Great Lake Carbon Corporation's grade HLM, an extruded graphite 1.14 m in diameter by 1.83 m long, is under investigation as a candidate graphite for side reflector blocks. One-half of a HLM log has been characterized and the results reported in Ref. 11-2. This log was a standard GLCC commercial production log. A second "special production" log was purchased from GLCC for delivery in March 1977. The special log was manufactured under more controlled conditions than the regular commercial grade. The special HLM log will be characterized in the same manner as the first log.

Core Support Floor Graphites

Union Carbide's grade PGX is under investigation as a candidate graphite for core support floor blocks. Grade PGX is a molded graphite 1.14 m in diameter by 1.83 m long. A full log (No. 6484-112, lot 805-3) was purchased for characterization. A summary of the mean values of tensile and compressive strengths of PGX was reported in Ref. 11-2. Flexural strength data are summarized in Table 11-11. The complete data set is given in Table 11-12. The uniformity of the PGX with respect to flexural strength is excellent.

Core Support Post and Seat Graphites

Stackpole Carbon's (SC) grade 2020 and GLCC's grade H-440N are candidate materials for core support post and seat components. Grades 2020 and

*Tables appear at the end of Section 11.

H-440N are fine-grained isostatically molded graphites. Grade 2020 is manufactured as logs 254 mm in diameter by 1.83 m long, and grade H-440N is manufactured as a preproduction log with a cross section of 330 mm by 330 mm and a length of 1.83 m. Production logs of H-440N will be 254 mm in diameter by 2.1 m long.

Grade 2020 was characterized first. The tensile, flexural, and compressive strengths of 2020 were reported in Ref. 11-2.

Strength data for preproduction grade (log 6484-81) H-440N are summarized in Table 11-13. Complete data sets are given in Tables 11-14 through 11-16.

This H-440N log was weaker at the middle than at the top. The tensile strength of radial specimens ranged from 10.4 MPa at the middle of the log to 13.1 MPa at the top, and axial specimens ranged from 10.9 MPa at the middle to 11.2 MPa at the top. Flexural and compressive strengths showed the same gradient. This log, which was one of the first preproduction logs in the development of grade H-440N, has a lower strength than grade 2020.

TASK 400: FRACTURE MECHANICS (FORMERLY STATISTICAL STRENGTH STUDIES)

No work funded under this subtask in FY-77.

TASK 500: FATIGUE BEHAVIOR OF GRAPHITE

A series of ambient temperature uniaxial fatigue tests on PGX graphite has been completed. Test procedures were the same as those reported earlier for H-451 graphite (Ref. 11-3).

The previous two quarterly reports (Refs. 11-2 and 11-4) described tests on radial specimens of PGX graphite tested with a zero-tension loading cycle (R = 0) and with a tension-compression loading cycle (R = -1) and tests on axial specimens with R = 0. During the current reporting period, the tests were completed with a set of 50 fatigue tests on axial specimens with R = -1. The data are tabulated in Table 11-17.

Figure 11-1 shows the data plotted as the logarithm of the peak tensile stress versus the logarithm of the number of cycles to failure. The lower population tolerance limits calculated by statistical analysis are included in the figures. The analysis included the single-cycle tensile data but excluded the specimens which ran out beyond 10^5 cycles.

A summary of the endurance limits, normalized by dividing by the average tensile strength, is given in Table 11-18. For a given number of cycles, the endurance limits are lower for the tests with R = -1 than with R = 0, as found earlier with H-451 graphite (Ref. 11-3). The normalized endurance limits are somewhat lower for axial specimens than for radial specimens. The normalized endurance limits for PGX graphite are higher than H-451 graphite tested under similar conditions (Ref. 11-3), indicating better fatigue resistance for grade PGX.

TASK 600: RDT AND ASTM GRAPHITE STANDARDS

This section concerns the writing of RDT graphite standards for HTGR graphite component materials. ASTM standard work on nuclear graphite will be monitored and progress will be reported. The ASTM work is by industry concensus and as such is not a part of the Task 11 scope.

RDT Standards

Fuel Element and Replaceable Reflector Graphites

The final draft (No. 5) of E6-1 is under review by ERDA. Resolution of remaining controversial issues is in progress.

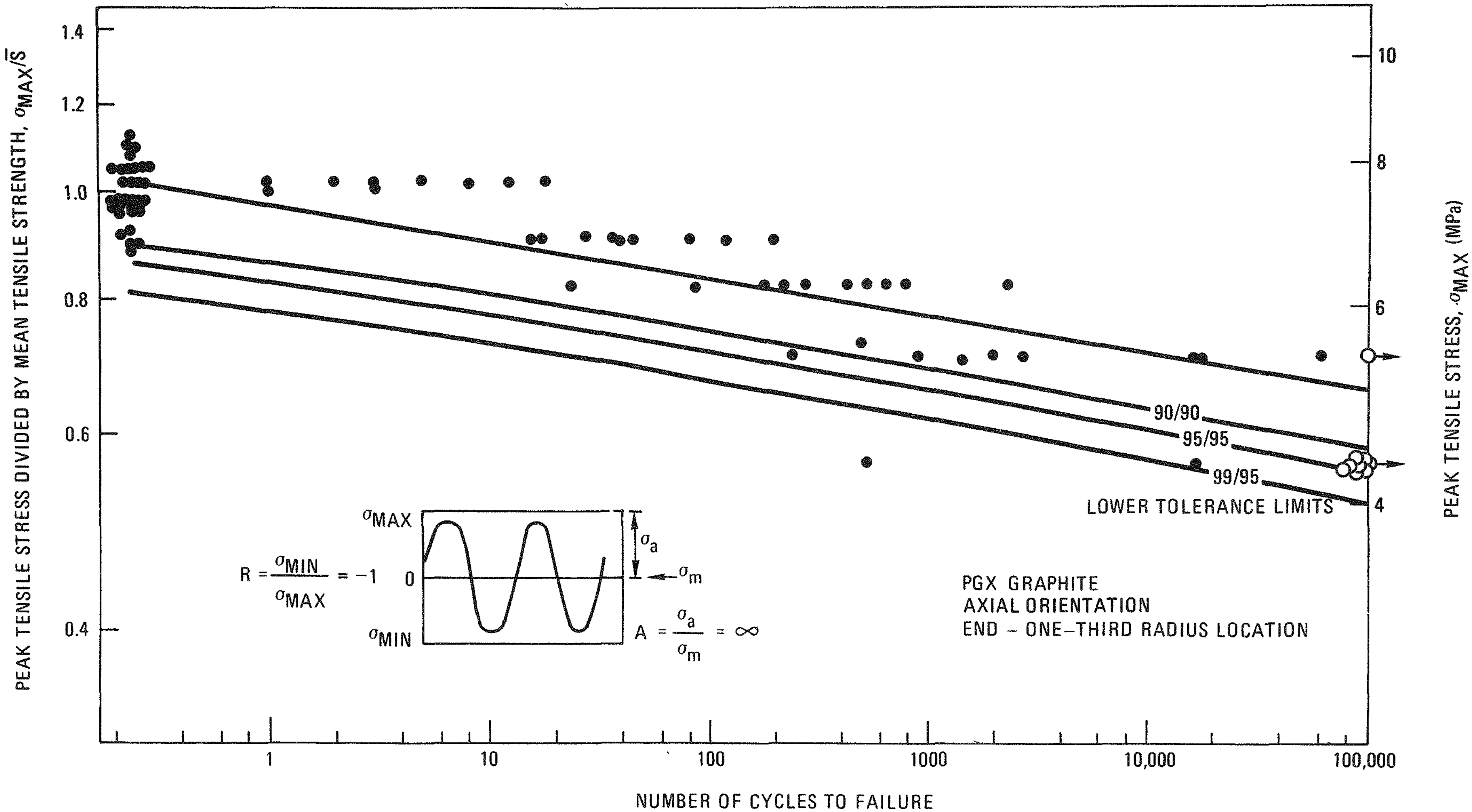

Fig. 11-1. Fatigue test data for PGX graphite, axial orientation, end - one-third radius location, in air at ambient temperature. Log-log plot of normalized maximum stress versus number of cycles to failure with stress ratio R = -1. Lower x/y tolerance limits represent the limits above which at least x% of the points fall, with y% confidence. Open circles represent runouts.

Core Support and Side Reflectors

Work has been suspended on standards for core support posts, core support blocks, and side reflector graphites until E6-1 is resolved. Drafts will not be submitted for review at this time.

TASK 700: IRRADIATION-INDUCED CREEP IN GRAPHITE

This work is funded at ORNL.

TASK 800: STRUCTURAL INTEGRITY OF GRAPHITE BLOCKS

Summary

In the previous quarterly report (Ref. 11-2), large differences were reported between analytical and experimental strip cutting results. Experiments in which strips were heated indicated that the temperature dependence of the irradiated thermal expansivity of H-327 graphite needs better definition. However, lack of precise thermal expansivity data could not account for the discrepancies in the strip cutting results. The possibility of the strip cutting technique inducing strain in the graphite strips is currently under investigation.

Diametral compression tests were conducted on unirradiated test elements. Maximum loads at failure and the load-deflection relations of six-hole and eight-hole teledial elements were determined. Analytical calculations were obtained through the finite element idealization of a linear elastic model. The results were used to estimate the maximum stresses at failure and will also be used to interpret data from tests of geometrically identical specimens of irradiated graphite.

Evaluation of Primary Loading Tests

Diametral compression tests to failure were performed on 61 six-hole and 43 eight-hole unirradiated H-327 teledial disks. Finite element models of a one-quarter sector of each type of specimen are shown in Figs. 11-2 and 11-3. Twelve of the 43 eight-hole teledial disks were tested after pressure burst tests had been performed on holes 2, 4, 6, and 8, which led to failure of the webs as shown in section 2 in Fig. 11-3. The disks that had been altered by previous pressure burst tests are represented approximately by the mesh in Fig. 11-4. The section which fails first during loading is shown as section 1 in Figs. 11-2 through 11-4.

Load-Deflection Relation

Typical results of load-deflection curves selected from all 20-mm-thick specimens are given in Figs. 11-5 and 11-6. Nonlinearity is apparently not pronounced before the failure load is reached. The average initial slopes of the load-deflection curves were measured to be 0.46 mm/kN for six-hole teledial disks (Fig. 11-2), 0.72 mm/kN for eight-hole teledial disks (Fig. 11-3), and 2.76 mm/kN for eight-hole teledial disks without center portions (Fig. 11-4).

Linear elastic stress calculations were performed for the three types of disks with the GTEPC program (Ref. 11-5). Young's modulus and Poisson's ratio were assumed to be 4.4 GPa and 0.117, respectively. The ratios of deflection to load were calculated to be 0.24 mm/kN for the six-hole teledial disks, 0.50 mm/kN for the eight-hole disks, and 1.79 mm/kN for the eight-hole disks without the center portions. The measured displacement is 40% to 92% higher than the calculated values. The Instron machine used for the tests will be recalibrated to show if this can account for the discrepancy.

Failure Stresses

The average failure loads obtained from the load-deflection curves of the 20-mm-thick specimens were 1.023 kN for six-hole teledial disks, 0.485 kN for eight-hole teledial disks, and 0.182 kN for eight-hole teledial disks without the center portions. The peak stresses obtained by finite

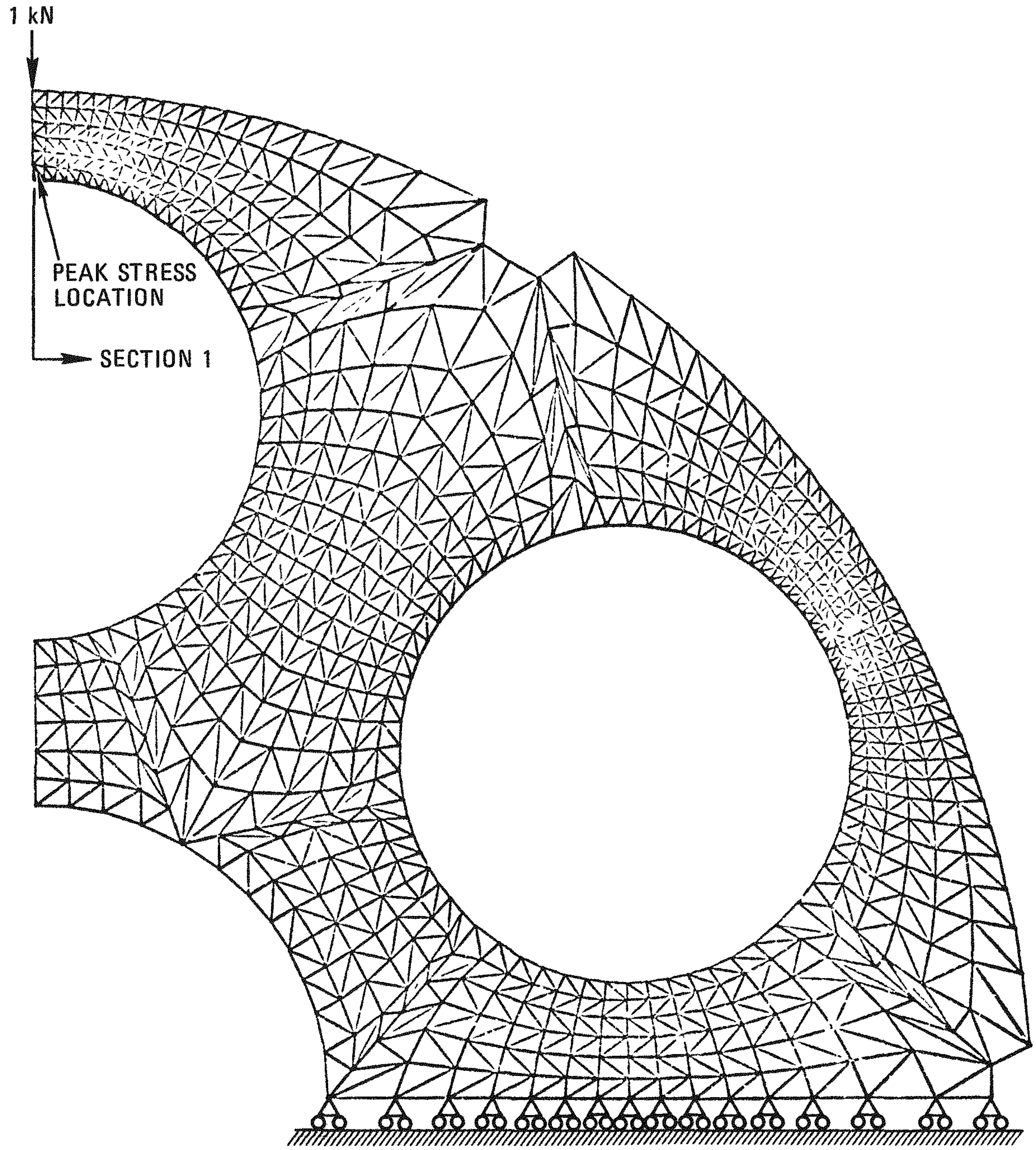

Fig. 11-2. Finite element model of six-hole teledial fuel body under diametral compression loading

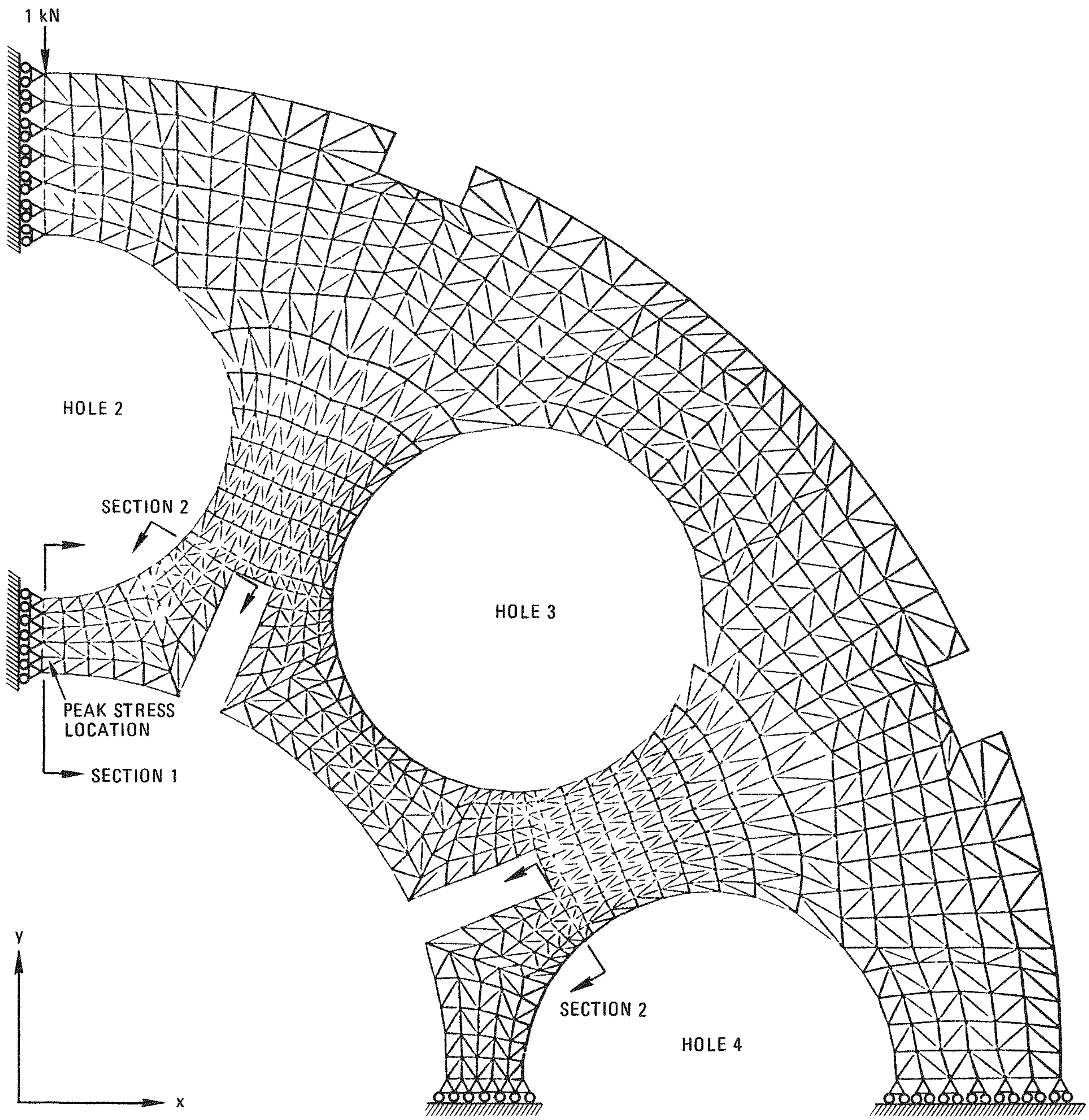

Fig. 11-3. Finite element model of eight-hole teledial fuel body under diametral compression loading

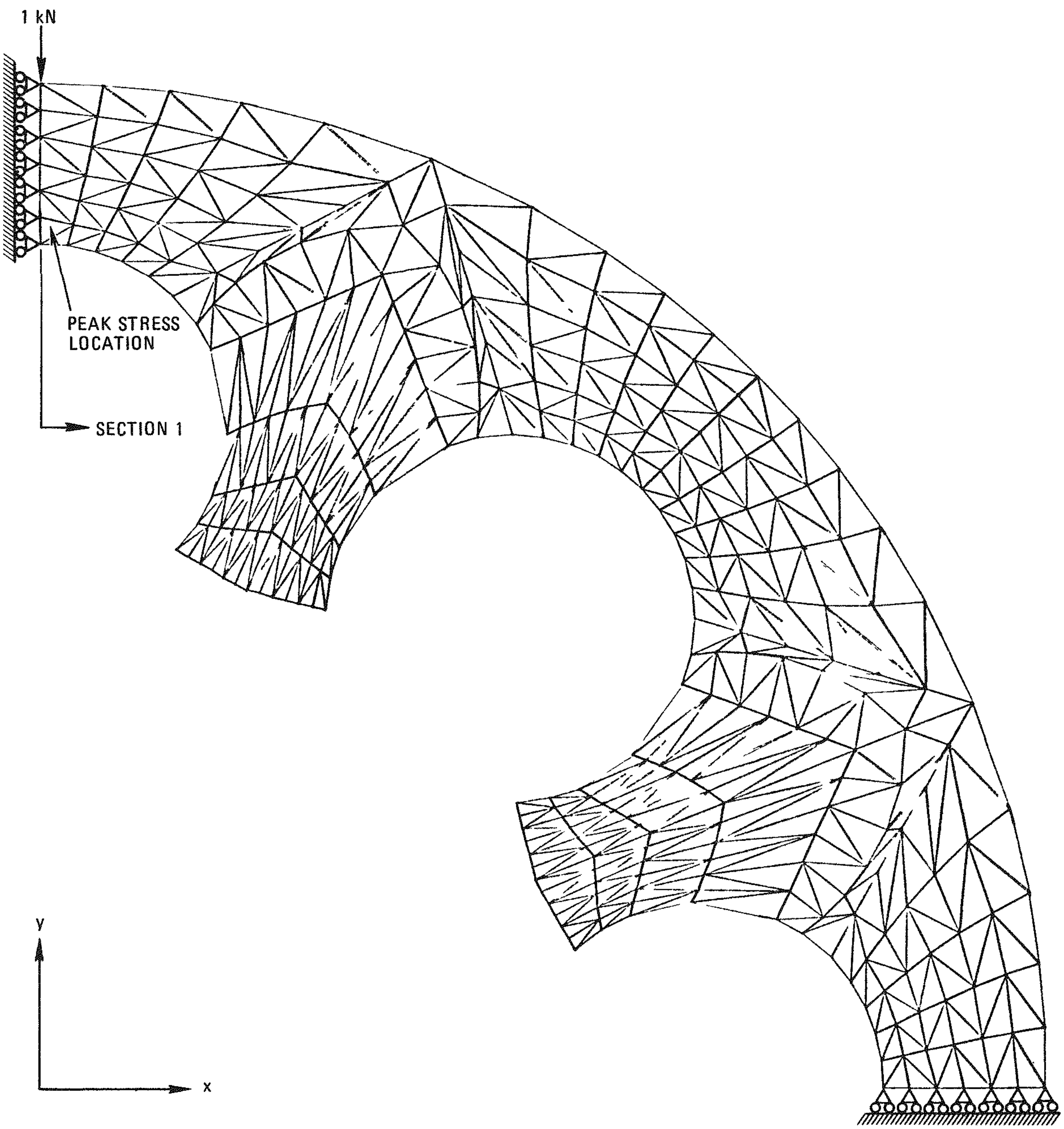

Fig. 11-4. Finite element model of eight-hole teledial fuel body under diametral compression after pressure burst tests

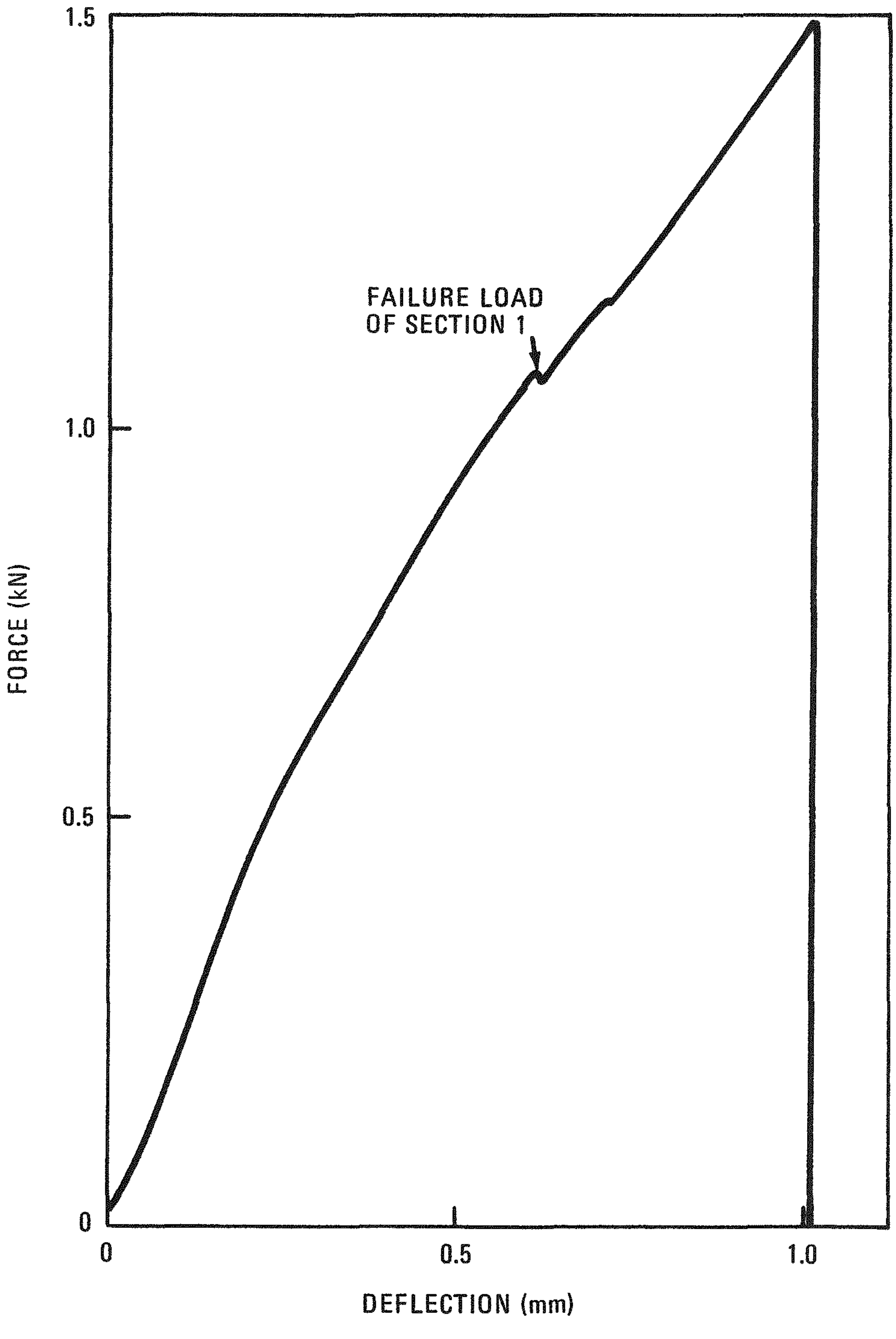

Fig. 11-5. Load-deflection curve for six-hole teledial disk under diametral compression

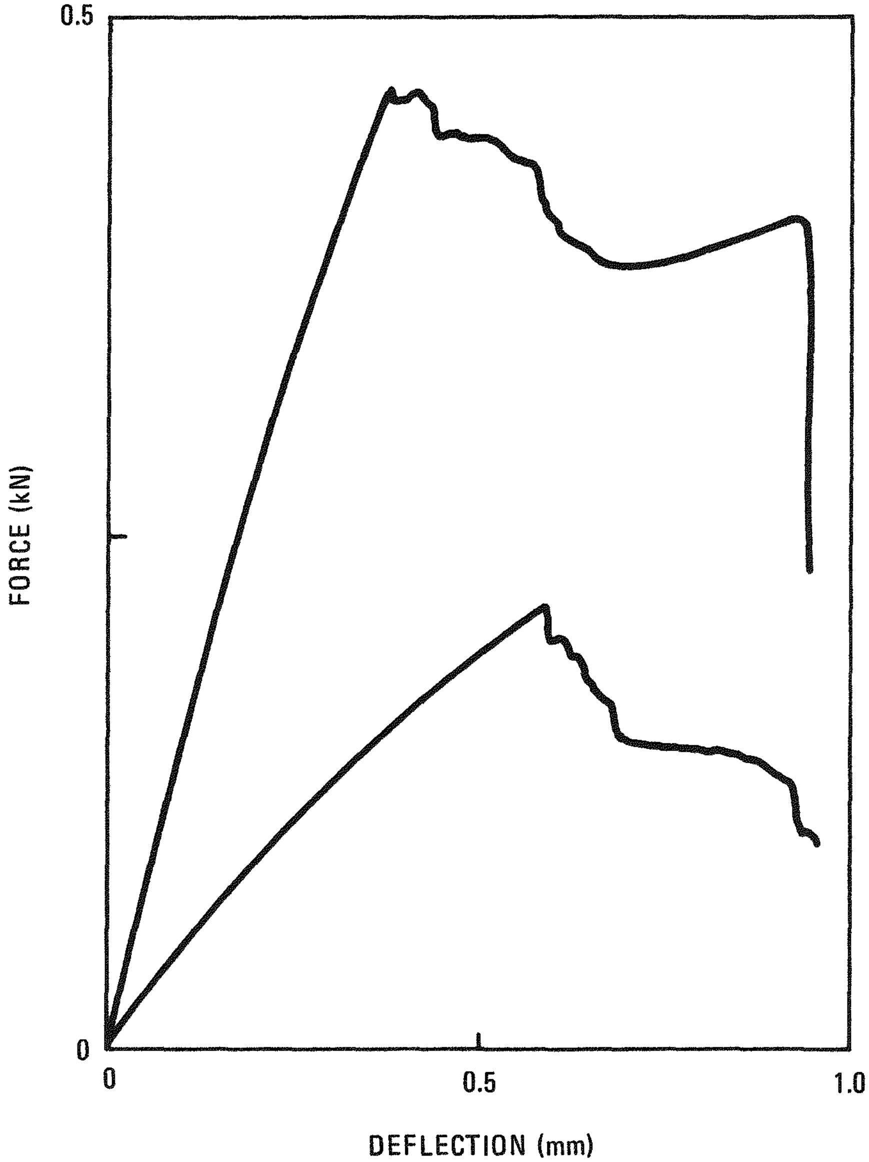

Fig. 11-6. Load-deflection curves for eight-hole teledial disks under diametral compression

element computation were 36.13, 18.57, and 16.66 MPa, respectively. Locations at which the peak stress occurred are indicated in Figs. 11-2 through 11-4. The mean ultimate tensile strength of H-327 graphite at the log location from which the specimen is taken is 8.5 MPa. The calculated peak stress is 2 to 4.2 times higher than the mean tensile strength. These results indicate that there is a large degree of conservatism in a failure criterion equating the maximum calculated elastic stress to the tensile strength.

The eight-hole teledial disk without center portions (Fig. 11-4), which had an inner- to outer-radius ratio of 0.84, failed at a peak stress of 16.6 MPa. This result appears to be in reasonable agreement with the maximum tensile stress at failure in diametrally loaded rings (Ref. 11-6). The calculated stresses along the fracture surface are plotted in Fig. 11-7. The six-hole disk reached the maximum stress of 36 MPa with the highest stress gradient.

TASK 900: CONTROL MATERIALS DEVELOPMENT

No work funded under this subtask in FY-77.

TASK 1000: GRAPHITE OXIDATION STUDIES

The HTGR Fuels and Core Development Program work on graphite oxidation, previously reported under Task 4, 189a No. SU001, is being reported under this task of 189a No. 00552 in FY-77. Experimental work is in progress to determine oxidation rates and the effect of oxidation on the mechanical properties of fuel element and core support graphites.

Fuel Element Graphites

A series of oxidation rate experiments on preproduction H-451 graphite has been completed. The reaction rate constants were determined for use in the Langmuir-Hinshelwood equation at low water vapor concentrations, 10 to

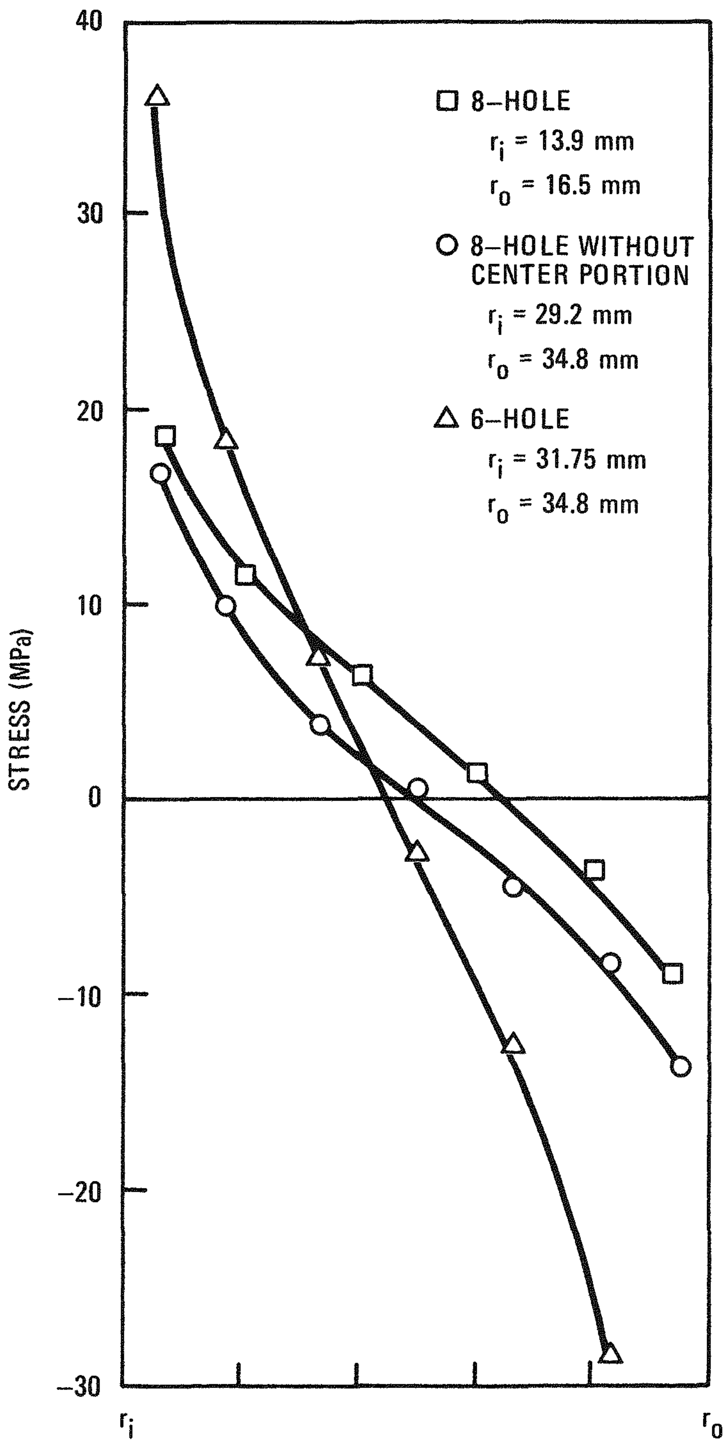

Fig. 11-7. Stresses along the fracture surface of teledial disks under diametral compression

200 Pa (100 to 2000 μatm H_2O), and at H_2 concentrations varying from 100 to 2000 Pa (1,000 to 20,000 μatm H_2); analysis of the test data is in progress.

A series of experiments to determine the effect of oxidation burnup on the mechanical properties of preproduction H-451 graphite has begun.

Core Support Graphites

Summary

A series of experiments to determine the effect of oxidation burnoff on the mechanical properties of Stackpole grade 2020 graphite is under way. The oxidation portion of the experiments is complete and is reported herein. Mechanical testing of all oxidized samples is proceeding and will be reported later. The oxidation rates of the samples were variable and were found to correlate with position in the log, with high rates observed in top-edge samples. Also, the rates appeared to correlate with iron impurity content, but not with density.

Procedure

Oxidation of 236 cylindrical samples of Stackpole 2020 graphite (12.8-mm diameter) for mechanical property testing has been completed. Of the total number of samples, 126 were for compression testing (length = 25.4 mm) and 110 were for tensile testing (length = 76.2 mm). All samples were obtained from the parent log of Stackpole 2020 (No. 6799) according to the sampling plans given in Figs. 11-8 through 11-14. The tensile samples which were obtained radially from the 152-mm-diameter log were equal in length to the log radius. These samples were designated "whole radius." Axial tensile samples obtained within two sample widths of the edge were designated "edge" and those from the remaining center of the log were designated "center." The radial compression samples were obtained by cutting the whole radius cores in half, yielding edge radial and center

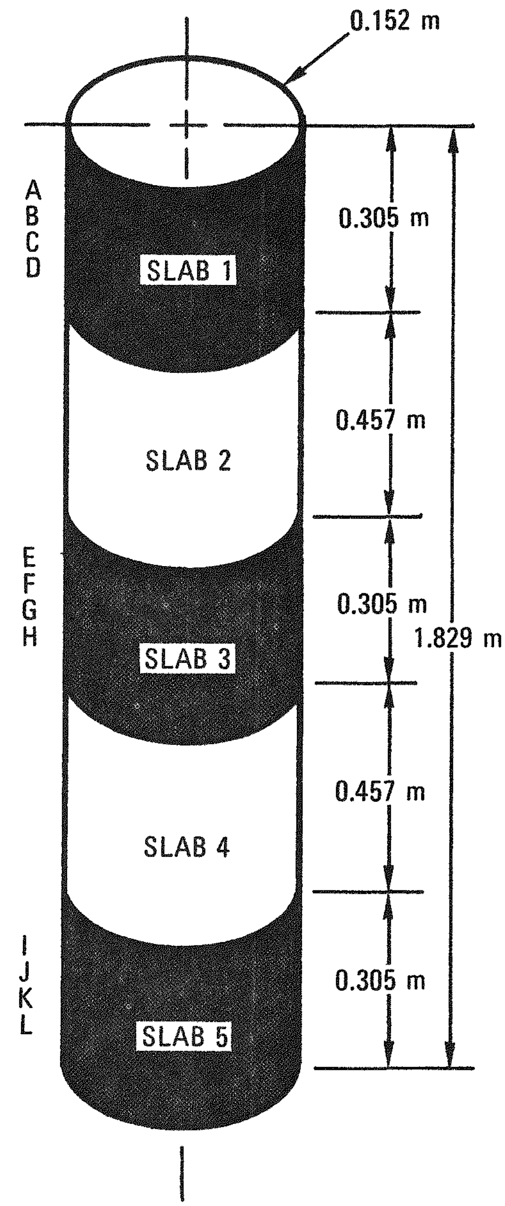

Fig. 11-8. Stackpole 2020 graphite

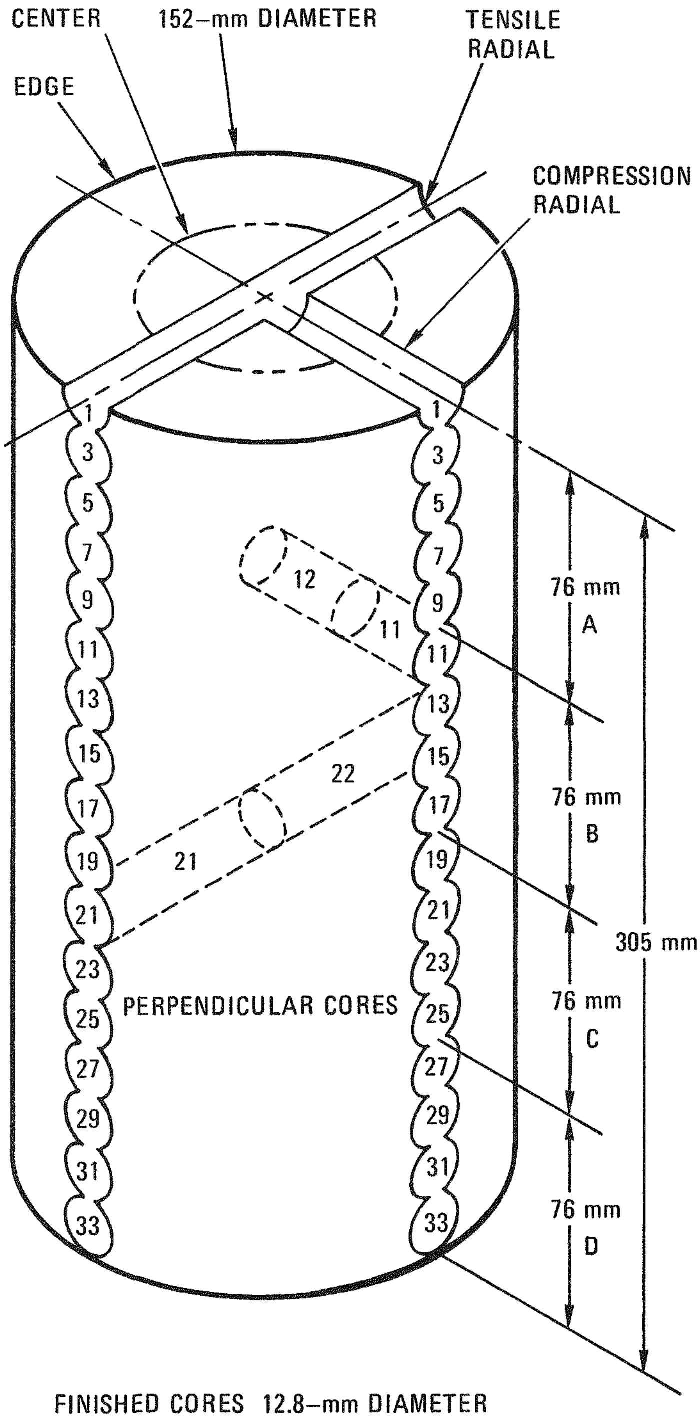

NO. 11–6799

S = SPECTROGRAPHIC ANALYSIS

C = CONTROL

SECTION	CORE	SAMPLES EDGE	SAMPLES CENTER
	25.4 mm	COMPRESSION	
A	1	1	2C
	3	3C	4
	5	5	6C
	7	7	8
	9	9	10C
B	11	11S	12
	13	13	14C
	15	15C	16
	17	17	18C
C	19	19C	20
	21	21	22C
	23	23C	24
	25	25	26C
D	27	27C	28
	29	29	30
	31	31C	32
	33	33	34S
	76.2 mm	TENSILE	
A	1	1	2C
	3	3C	4
	5	5	6C
	7	7C	8
	9	9	10C
B	11	11C	12
	13	13	14C
	15	15C	16
	17	17	18C
C	19	19C	20
	21	21	22C
	23	23C	24
	25	25	26C
D	27	27C	28
	29	29	30C
	31	31C	32
	33	33	34C

Fig. 11-9. Coring diagram, Stackpole 2020, slab 1, tensile and compression radial samples

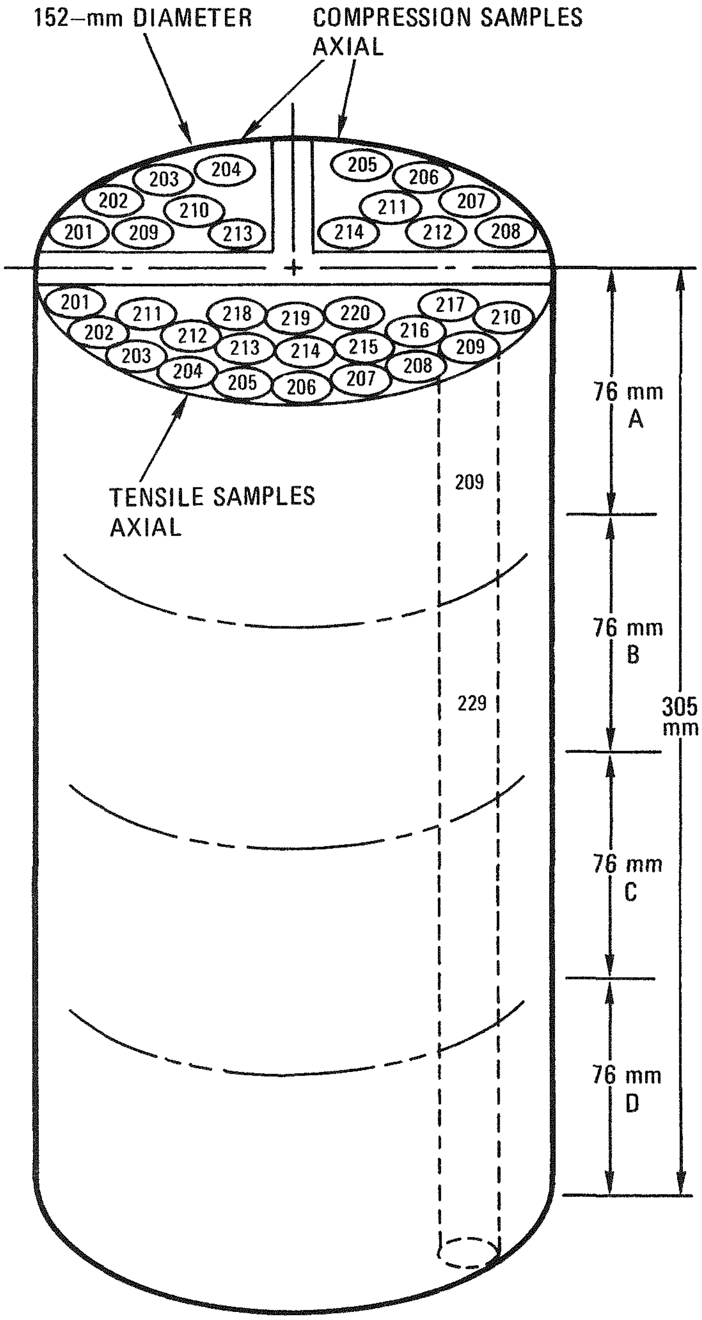

FINISHED CORES 12.8–mm DIAMETER

NO. 12–6799

C = CONTROL

	CORE	SECTION A	SECTION B	SECTION C
	CORE	SAMPLES		
	COMPRESSION SAMPLES			
EDGE	201	201	215	229
	202	202C	216C	230
	203	203	217	231
	204	204	218C	232C
	205	205	219	233
	206	206C	220C	234C
	207	207	221	235
	208	208C	222C	236C
	209	209	223	237
	210	210C	224C	238C
	211	211	225	239
	212	212C	226C	240C
CENTER	213	213	227	241
	214	214C	228C	242C
	TENSILE SAMPLES			
EDGE	201	201	221	
	202	202C	222C	
	203	203	223	
	204	204C	224C	
	205	205	225	
	206	206C	226C	
	207	207	227	
	208	208C	228C	
	209	209	229	
	210	210C	230C	
	211	211	231	
	212	212C	232C	
	213	213	233	
	214	214C	234C	
	215	215	235	
	216	216C	236C	
	217	217	237	
CENTER	218	218C	238C	
	219	219	239	
	220	220C	240C	

Fig. 11-10. Coring diagram, Stackpole 2020, slab 1, tensile and compression axial samples

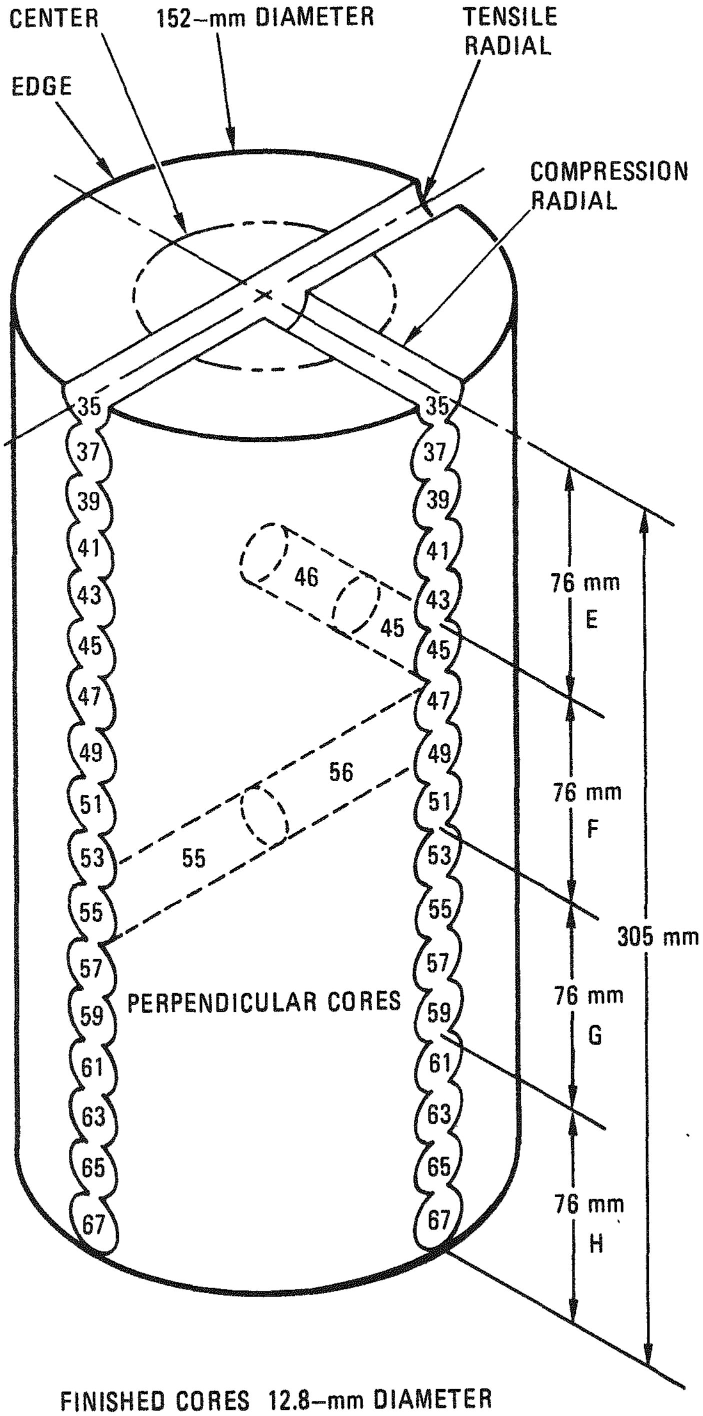

NO. 11-6799

S = SPECTROGRAPHIC ANALYSIS

C = CONTROL

SECTION	CORE	SAMPLES EDGE	SAMPLES CENTER
	25.4 mm COMPRESSION		
E	35	35C	36
	37	37	38C
	39	39C	40
	41	41	42C
	43	43S	44
F	45	45	46C
	47	47	48
	49	49	50C
	51	51C	52
G	53	53	54C
	55	55C	56
	57	57	58S
	59	59C	60
H	61	61	62
	63	63C	64
	65	65	66C
	67	67C	68
	76.2 mm TENSILE		
E	35	35C	36
	37	37	38C
	39	39C	40
	41	41	42C
	43	43C	44
F	45	45	46C
	47	47C	48
	49	49	50C
	51	51C	52
G	53	53	54C
	55	55C	56
	57	57	58C
	59	59C	60
H	61	61	62C
	63	63C	64
	65	65	66C
	67	67C	68

Fig. 11-11. Coring diagram, Stackpole 2020, slab 3, tensile and compression radial samples

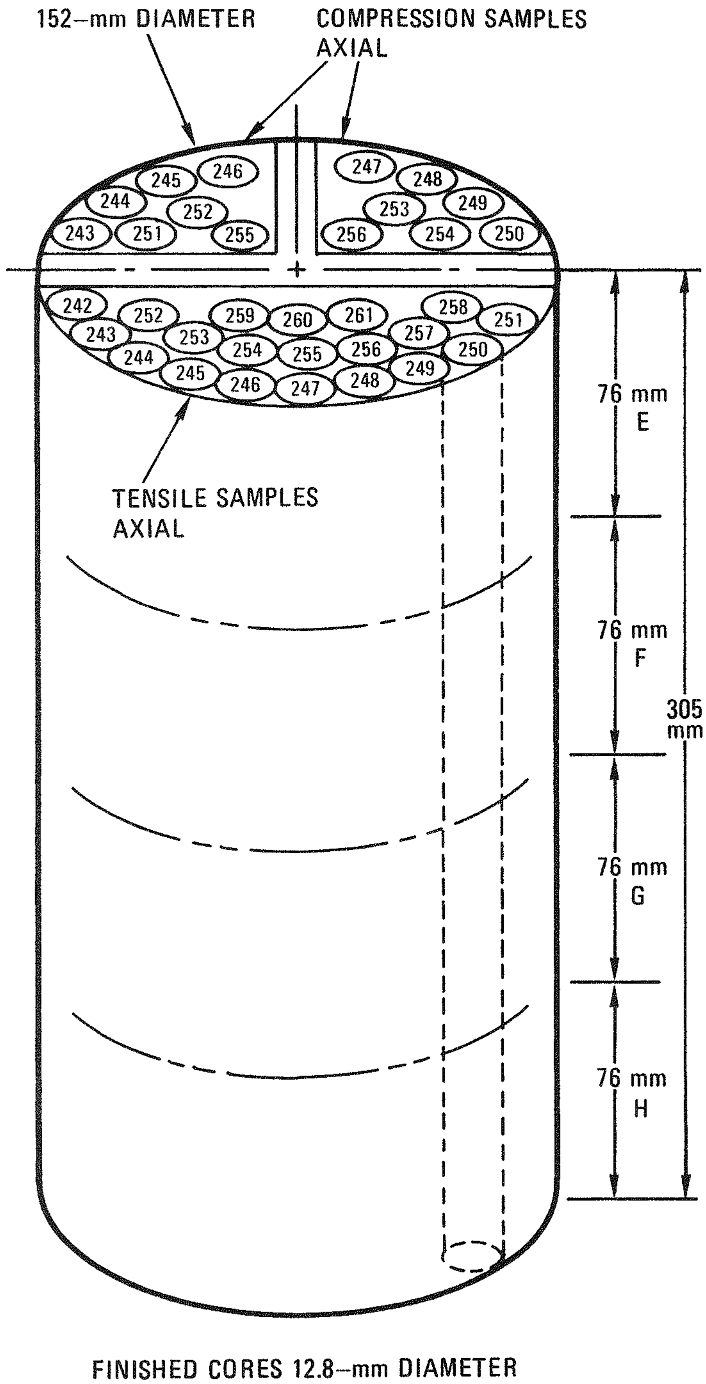

NO. 12-6799
C = CONTROL

	CORE	SAMPLES (SECTION E)	SAMPLES (SECTION F)	SAMPLES (SECTION G)
COMPRESSION SAMPLES				
EDGE	243	243	257	271
	244	244C	258C	272C
	245	245	259	273
	246	246C	260C	274C
	247	247	261	275
	248	248C	262C	276
	249	249	263	277
	250	250	264C	278C
	251	251	265	279
	252	252C	266C	280C
	253	253	267	281
	254	254C	268C	282C
CENTER	255	255	269	283
	256	256C	270C	284C
TENSILE SAMPLES				
EDGE	242	242C	262C	
	243	243	263	
	244	244C	264C	
	245	245	265	
	246	246C	266C	
	247	247	267	
	248	248C	268C	
	249	249	269	
	250	250C	270C	
	251	251	271	
	252	252C	272C	
	253	253	273	
	254	254C	274C	
	255	255	275	
	256	256C	276C	
	257	257	277	
	258	258C	278C	
CENTER	259	259	279	
	260	260C	280C	
	261	261	281	

Fig. 11-12. Coring diagram, Stackpole 2020, slab 3, tensile and compression axial samples

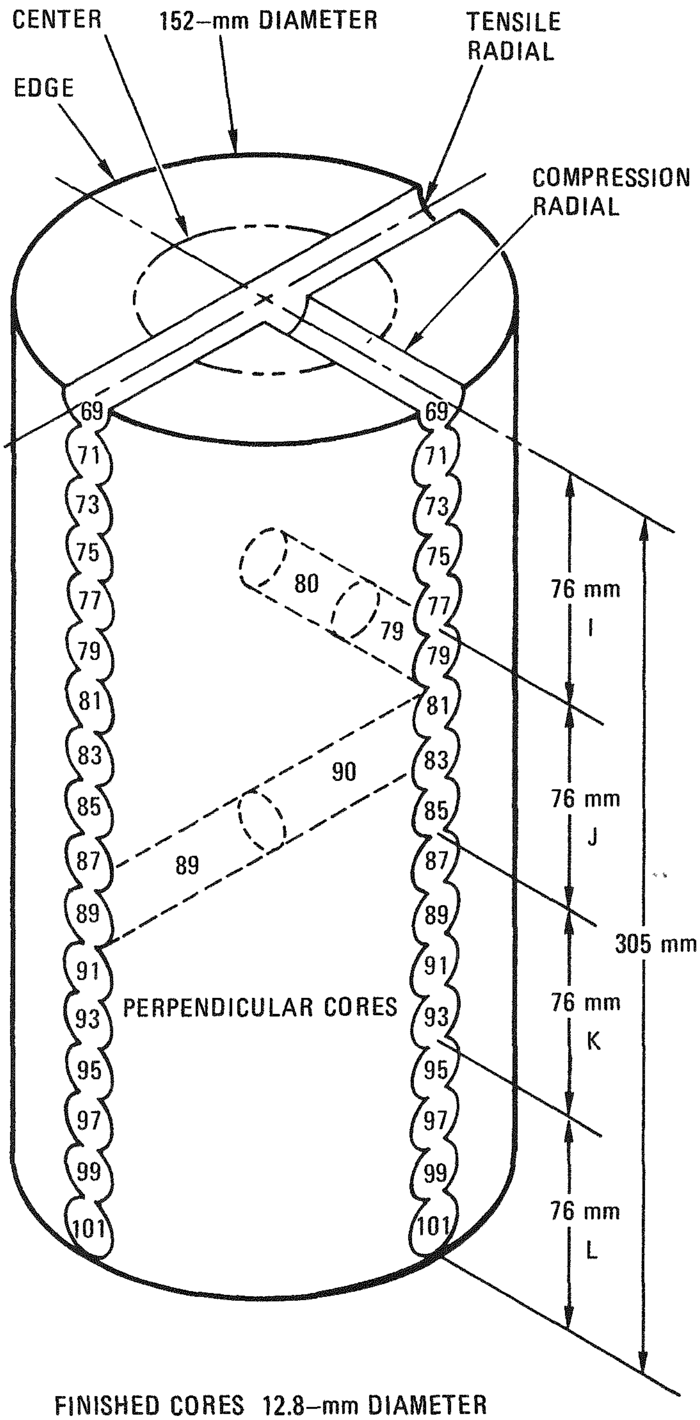

NO. 11–6799
S = SPECTROGRAPHIC ANALYSIS
C = CONTROL

SECTION	CORE	SAMPLES EDGE	SAMPLES CENTER
	25.4 mm COMPRESSION		
I	69	69	70C
	71	71S	72
	73	73	74C
	75	75C	76
	77	77	78
J	79	79C	80
	81	81	82C
	83	83C	84
	85	85	86C
K	87	87C	88
	89	89	90C
	91	91C	92
	93	93	94C
L	95	95C	96
	97	97	98S
	99	99C	100
	101	101	102
	76.2 mm TENSILE		
I	69	69	70C
	71	71C	72
	73	73	74C
	75	75C	76
	77	77	78C
J	79	79C	80
	81	81	82C
	83	83C	84
	85	85	86C
K	87	87C	88
	89	89	90C
	91	91C	92
	93	93	94C
L	95	95C	96
	97	97	98C
	99	99C	100
	101	101	102C

Fig. 11-13. Coring diagram, Stackpole 2020, slab 5, tensile and compression radial samples

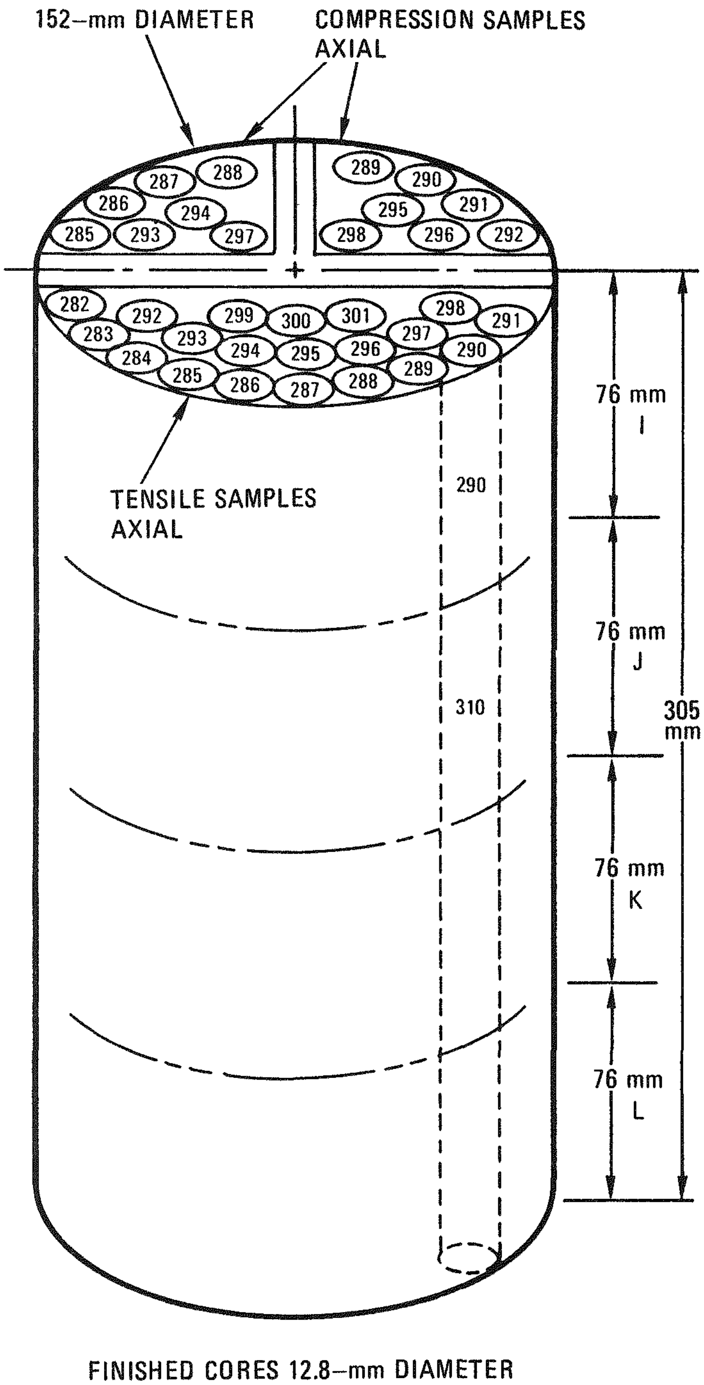

NO. 12–6799
C = CONTROL

	CORE	SAMPLES SECTION I	SAMPLES SECTION J	SAMPLES SECTION K
COMPRESSION SAMPLES				
EDGE	285	285	299	313
	286	286	300C	314C
	287	287	301	315
	288	288C	302C	316C
	289	289	303	317
	290	290C	304C	318C
	291	291	305	319
	292	292C	306C	320C
	293	293	307	321
	294	294C	308	322C
	295	295	309	323
	296	296C	310C	324C
CENTER	297	297	311	325
	298	298C	312C	326
TENSILE SAMPLES				
EDGE	282	282C	302C	
	283	283	303	
	284	284C	304C	
	285	285	305	
	286	286C	306C	
	287	287	307	
	288	288C	308C	
	289	289	309	
	290	290C	310C	
	291	291	311	
	292	292C	312C	
	293	293	313	
	294	294C	314C	
	295	295	315	
	296	296C	316C	
	297	297	317	
	298	298C	318C	
CENTER	299	299	319	
	300	300C	320C	
	301	301	321	

Fig. 11-14. Coring diagram, Stackpole 2020, slab 5, tensile and compression axial samples

radial specimens. Axial compression samples were designated "edge" and "center" in the same manner as the axial tensile samples.

All samples were oxidized at 1148 K (875°C) in an atmosphere of 5% H_2 and 3% H_2O in helium. The samples were placed on graphite racks which were positioned inside quartz tube furnaces. Each furnace load contained 14 samples. The process gas entered the furnace through a 6-mm-diameter quartz tube, which extended the length of the furnace below the sample racks. Several outlet holes in the gas inlet tube were spaced at frequent intervals along the tube length so that the graphite specimens were exposed to the process gas uniformly.

Results and Discussion

A summary of the rate data is given in Table 11-19 and total burnoffs (% $\Delta W/W$) and the average reaction rates (%/h) for all samples are given in Table 11-20. The total oxidation burnoffs ranged up to 25%. Average reaction rates were observed to vary by as much as a factor of 60 within a given furnace load. No correlation with sample position in the furnace was noted. In some cases adjacent samples exhibited vastly different oxidation rates.

Using the detailed coring diagrams, it was possible to determine the exact location of each sample in the original log (Figs. 11-8 through 11-14). Table 11-19 summarizes the reaction rates as a function of location in the log. For each section, the average and the range of the reaction rates and densities were computed. These results are shown in Figs. 11-15 and 11-16. For slab 1, the slab which showed the greatest variation in rate, rate versus location was plotted for each sample (Fig. 11-17).

Table 11-21 gives the results of the emission spectrographic analysis of samples taken from several positions in the log. Figure 11-18 is a plot of iron impurity versus position. The highest iron impurity concentrations were found in the top part of the log, particularly close to the edge.

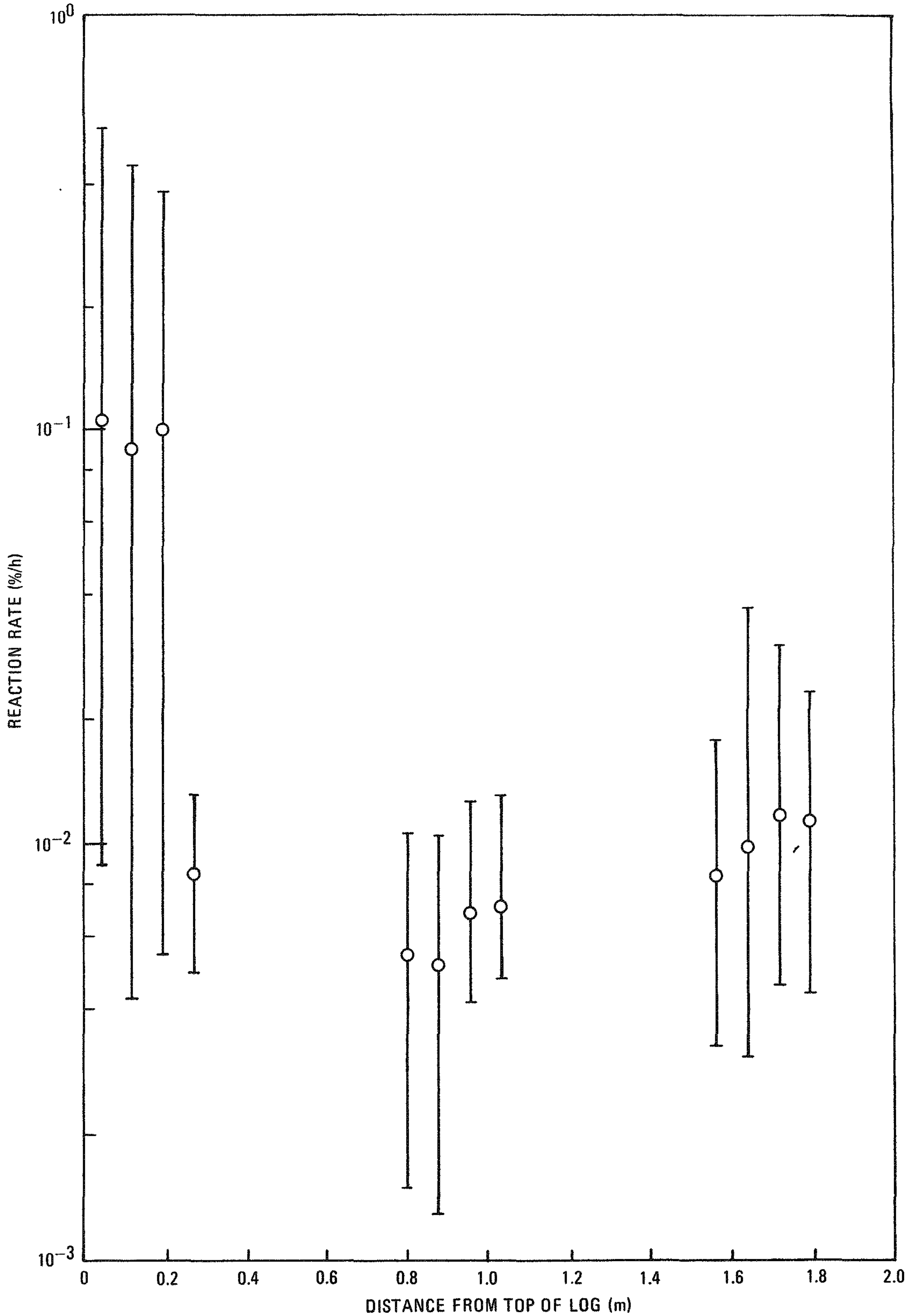

Fig. 11-15. Average and range of reaction rates of each section versus distance from top of log

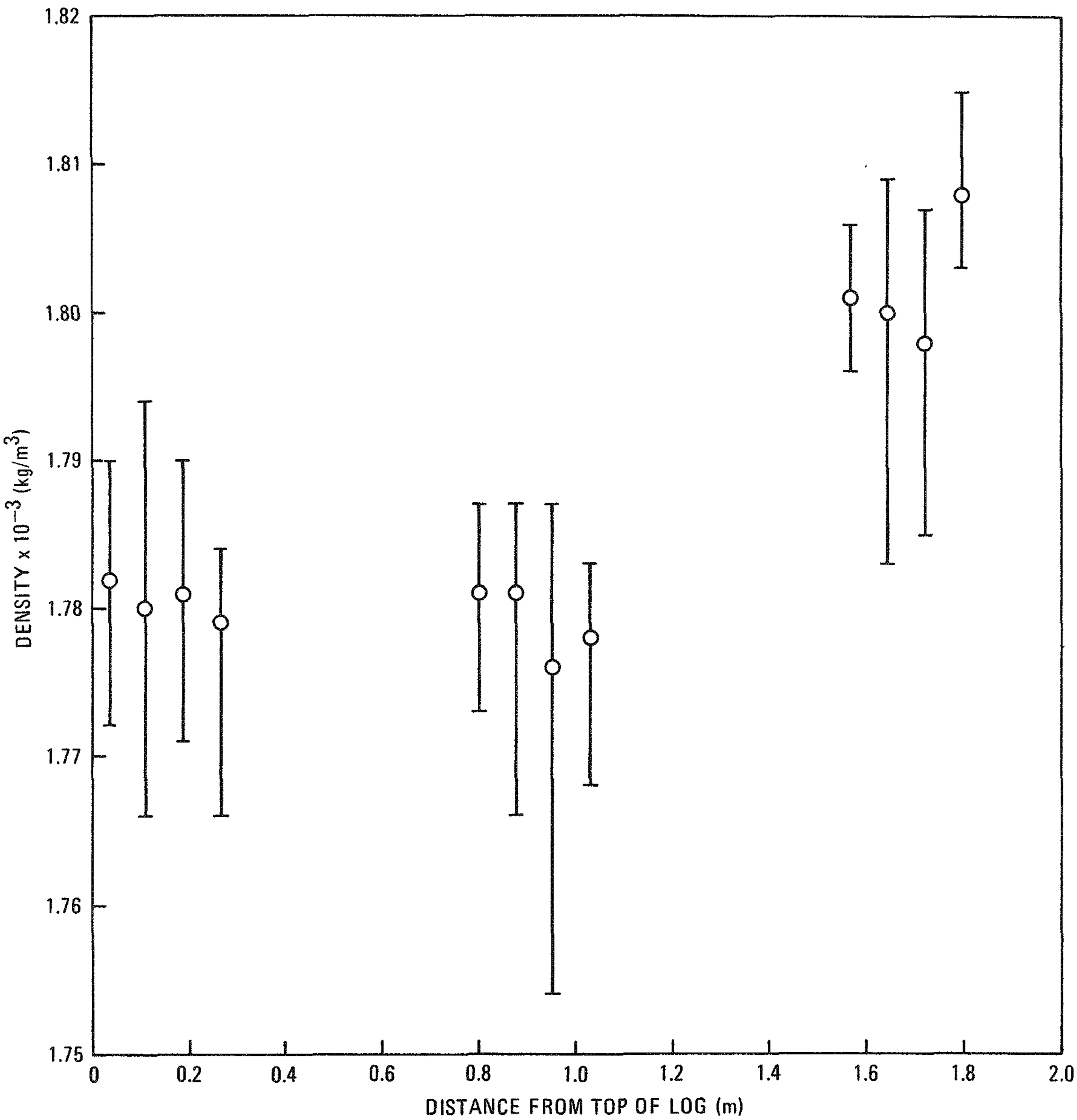

Fig. 11-16. Average and range of densities of each section versus distance from top of log

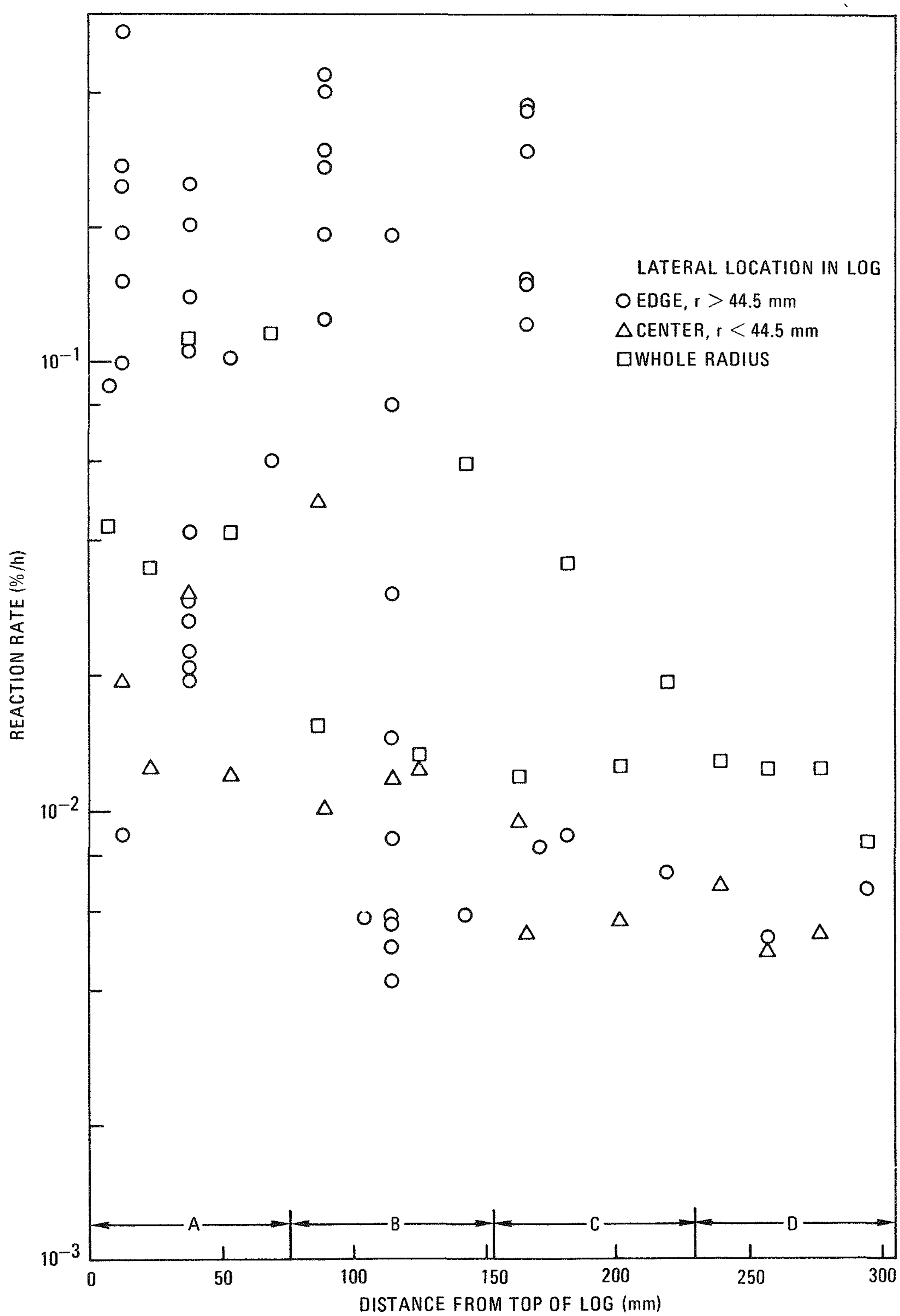

Fig. 11-17. Reaction rate versus position in log for slab 1

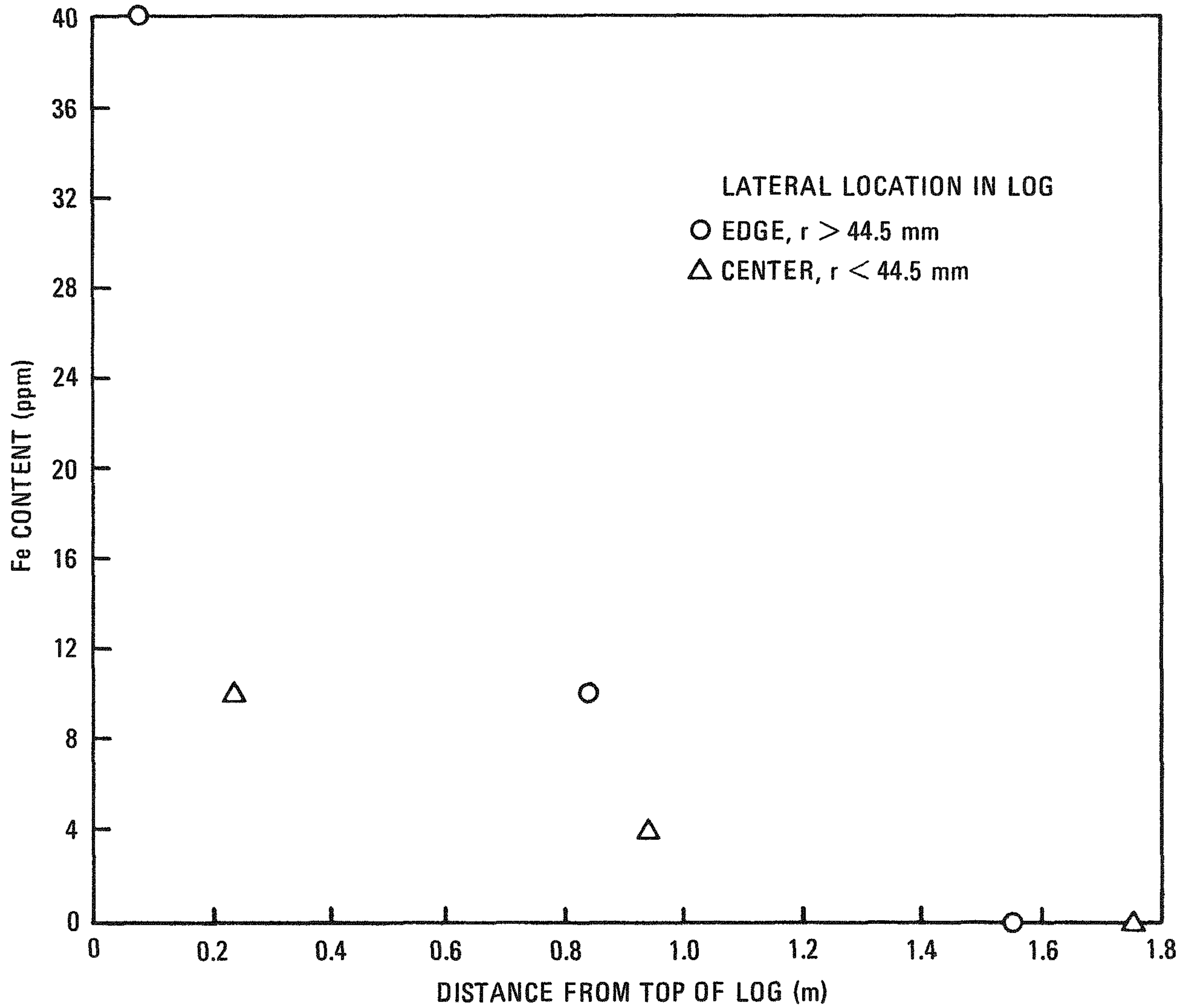

Fig. 11-18. Fe contamination versus position in log

Conclusions

Figure 11-15 shows that the highest rates occur at the top of the log. A sharp decrease in rate appears between sections C and D. Referring to Fig. 11-17, this is seen to occur at about 180 mm from the top of the log. With regard to lateral position, samples with the highest rates (0.12%/h) were all taken from the edge of the log. Samples from the center of the log all had rates less than 0.05%/h. Note that tensile radial samples extend across the whole radius of the log; therefore, their reaction rates and densities should show an approximate average between the extremes of the edge and center samples. This was indeed the case for the top slab where wide variations in rate were observed, as shown in Table 11-19 and Fig. 11-18.

Figure 11-16 is a plot of density versus position. No correlation of reaction rate with density is apparent.

Referring to Fig. 11-18, it is seen that the highest iron concentration was observed in samples taken from the top edge of the log, which correlates well with the observed reaction rates. Since iron is known to be a potent catalyst in the steam-graphite reaction, it is concluded that the variations in oxidation rate were due to variations in iron content.

Validation Tests

Writing of a test plan, mentioned previously in Ref. 11-2, to determine the effect of a nonuniform radial oxidation burnoff profile on the mechanical properties of a core support post graphite has been delayed and will be reported in the next quarterly report.

REFERENCES

11-1. Price, R. J., and L. A. Beavan, "Final Report on Graphite Irradiation Capsule OG-3," ERDA Report GA-A14211, General Atomic Company, January 1977.

11-2. "HTGR Fuels and Core Development Program Quarterly Progress Report for the Period Ending November 30, 1976," ERDA Report GA-A14180, General Atomic Company, December 27, 1976.

11-3. "HTGR Fuels and Core Development Program Quarterly Progress Report for the Period Ending May 31, 1976," ERDA Report GA-A13941, General Atomic Company, June 30, 1976.

11-4. "HTGR Fuels and Core Development Program Quarterly Progress Report for the Period Ending August 31, 1976, ERDA Report GA-A14046, General Atomic Company, September 30, 1976.

11-5. Tzung, F. K., "GTEPC-2D, a Computer Program for Two-Dimensional Graphite Thermal-Elastic-Plastic-Creep Analysis, User's Manual," General Atomic Report GA-A13532, January 31, 1976.

11-6. Brocklehurst, J. E., and M. I. Darby, "Concerning the Fracture of Graphite Under Different Test Conditions," Mater. Sci. Eng. 16, 99 (1974).

TABLE 11-1
GA-GLCC ROUND-ROBIN FLEXURAL TESTS: DATA SUMMARY (CORRECTED FOR NONLINEARITY)

Specification Size	Orientation	Location	GA Results			GLCC Results			Strength Difference, GA - GLCC (MPa)
			No. of Specimens	Mean Strength (MPa)	Standard Deviation (MPa)	No. of Specimens	Mean Strength (MPa)	Standard Deviation (MPa)	
6.4-mm-diameter cylinder	Axial	Midlength edge	35	26.2	1.3	35	26.6	1.3	-0.4
	Axial	End center	35	21.3	1.8	35	21.1	2.3	0.2
	Radial	End edge	36	22.7	1.2	36	22.0	2.5	0.7
	Radial	Midlength center	35	18.6	2.5	36	18.4	2.1	0.2
8.9-mm square cross-section beam	Axial	Midlength edge	23	23.9	1.5	24	23.8	1.3	0.1
	Axial	End center	25	19.7	1.7	25	18.2	1.4	1.5
	Radial	End edge	26	18.8	2.8	26	19.4	2.4	-0.6
	Radial	Midlength center	36	16.7	1.9	36	16.6	1.8	0.1

TABLE 11-2
GA-GLCC ROUND-ROBIN TENSILE TESTS: DATA SUMMARY

Specification Size	Orientation	Location	GA Results			GLCC Results			Strength Difference, GA - GLCC (MPa)
			No. of Specimens	Mean Strength (MPa)	Standard Deviation (MPa)	No. of Specimens	Mean Strength (MPa)	Standard Deviation (MPa)	
12.8-mm-diameter cylinder	Axial	Midlength edge	52	19.9	1.4	52	19.3	1.5	0.6
	Axial	End center	50	13.0	1.6	50	12.8	1.0	0.2
	Radial	End edge	30	13.6	3.5	36	13.6	3.5	0.0
	Radial	Midlength center	30	10.4	2.1	36	10.7	1.9	-0.3
7.6-mm square cross-section dogbone	Axial	Midlength edge	No GA tests			47	18.8	1.4	-
	Axial	End center				48	11.8	1.5	-
	Radial	End edge				26	11.8	3.0	-
	Radial	Midlength center				36	9.8	2.4	-

TABLE 11-3
GA-GLCC ROUND-ROBIN STRENGTH TESTS: CONCLUSIONS

Type of Test	Comparison	Average Difference (%)	Number of Cases Where Difference was Significant (at 95% Confidence Level)	Conclusion
Tensile (cylinder)	GA vs GLCC	+1	1 out of 4	No real difference between test laboratories
Flexural	GA vs GLCC	+1	1 out of 8	No real difference between test laboratories
Tensile	Cylinder vs dogbone (GLCC only)	+8	2 out of 4	Real effect; probably caused by sharp edges, radiused shoulders, or worse alignment of dogbone
Flexural	Cylinder vs rectangular beam	+13	8 out of 8	Real effect; rectangular beam stresses more material to peak stress and has larger thickness-to-span ratio

TABLE 11-4

ROUND-ROBIN TENSILE DATA: CYLINDRICAL SPECIMENS (GA DATA)

LOT NO. RR — SPEC. DIA. 12.8 MM
LOG NO. 6484-82 — SPEC. LENGTH 76. MM
LOG DENSITY -- MG/M**3

SPECIMEN NUMBER	ORIENT-ATION	LOCA-TION	DENSITY (MG/M**3)	YOUNGS MODULUS (GPA)	PERM-ANENT SET (PCT)	FRAC-TURE STRAIN (PCT)	TENSILE STRENGTH (MPA)
3A-M-002A	AX	MLE					19.9
M-002B	AX	MLE					19.6
M-032A	AX	MLE					18.6
M-032B	AX	MLE					20.7
M-058A	AX	MLE					18.0
M-058B	AX	MLE					20.4
M-088A	AX	MLE					20.6
M-088B	AX	MLE					19.6
M-004A	AX	MLE					21.2
M-004B	AX	MLE					17.5
M-034A	AX	MLE					19.2
M-034B	AX	MLE					17.2
M-066A	AX	MLE					19.7
M-066B	AX	MLE					19.1
M-006A	AX	MLE					19.8
M-006B	AX	MLE					20.4
M-036A	AX	MLE					18.1
M-036B	AX	MLE					17.2
M-068A	AX	MLE					19.6
M-068B	AX	MLE					18.2
M-098A	AX	MLE					21.3
M-098B	AX	MLE					21.6
M-106A	AX	MLE					21.7
M-106B	AX	MLE					22.0
M-102A	AX	MLE					21.4
M-102B	AX	MLE					20.9
3B-M-218A	AX	MLE					21.3
M-218B	AX	MLE					20.3
M-188A	AX	MLE					18.6
M-188B	AX	MLE					16.7
M-158A	AX	MLE					18.4
M-158B	AX	MLE					19.5
M-128A	AX	MLE					19.5
M-128B	AX	MLE					21.9
M-196A	AX	MLE					20.3
M-196B	AX	MLE					20.5
M-166A	AX	MLE					21.3
M-166B	AX	MLE					21.6
M-136A	AX	MLE					20.8
M-136B	AX	MLE					20.2
M-198A	AX	MLE					19.5
M-198B	AX	MLE					19.8
M-168A	AX	MLE					18.9
M-168B	AX	MLE					17.7
M-138A	AX	MLE					22.7
M-138B	AX	MLE					21.3
M-220A	AX	MLE					21.3
M-220B	AX	MLE					20.6
M-224A	AX	MLE					18.8
M-224B	AX	MLE					20.7
M-226A	AX	MLE					20.7
M-226B	AX	MLE					20.5
	MEAN						19.9 (2889.PSI)
	STD. DEV.						1.4 (201.PSI)

TABLE 11-4 (Continued)

LOT NO. RR
LOG NO. 6484-82
LOG DENSITY -- MG/M**3

SPEC. DIA. 12.8 MM
SPEC. LENGTH 76. MM

SPECIMEN NUMBER	ORIENT- ATION	LOCA- TION	DENSITY (MG/M**3)	YOUNGS MODULUS (GPA)	PERM- ANENT SET (PCT)	FRAC- TURE STRAIN (PCT)	TENSILE STRENGTH (MPA)
1A-E-002A	AX	EC					13.3
E-002B	AX	EC					15.7
E-012A	AX	EC					14.4
E-012B	AX	EC					13.7
E-022A	AX	EC					12.4
E-022B	AX	EC					12.1
E-032A	AX	EC					11.0
E-032B	AX	EC					13.4
E-042A	AX	EC					13.6
E-042B	AX	EC					12.7
E-052A	AX	EC					12.2
E-052B	AX	EC					10.6
E-062A	AX	EC					13.8
E-062B	AX	EC					14.4
E-072A	AX	EC					12.2
E-072B	AX	EC					11.1
E-082A	AX	EC					10.3
E-082B	AX	EC					11.2
E-092A	AX	EC					13.8
E-092B	AX	EC					13.8
E-102A	AX	EC					11.6
E-102B	AX	EC					12.0
E-112A	AX	EC					12.4
E-112B	AX	EC					12.8
E-122A	AX	EC					7.6
E-122B	AX	EC					11.7
1B-E-132A	AX	EC					15.8
E-132B	AX	EC					14.2
E-142A	AX	EC					15.2
E-142B	AX	EC					14.2
E-152A	AX	EC					15.8
E-152B	AX	EC					14.1
E-162A	AX	EC					15.1
E-162B	AX	EC					13.7
E-172A	AX	EC					14.7
E-172B	AX	EC					14.4
E-182A	AX	EC					12.3
E-182B	AX	EC					13.4
E-192A	AX	EC					12.0
E-192B	AX	EC					14.1
E-202A	AX	EC					13.9
E-202B	AX	EC					14.0
E-212A	AX	EC					12.1
E-212B	AX	EC					13.7
E-222A	AX	EC					13.2
E-222B	AX	EC					13.8
E-232A	AX	EC					13.6
E-232B	AX	EC					10.7
E-242A	AX	EC					12.2
E-242B	AX	EC					12.0
	MEAN						13.0 (1891.PSI)
	STD. DEV.						1.6 (231.PSI)

TABLE 11-4 (Continued)

LOT NO. RR — SPEC. DIA. 12.8 MM
LOG NO. 6484-92 — SPEC. LENGTH 76. MM
LOG DENSITY -- MG/M**3

SPECIMEN NUMBER	ORIENT-ATION	LOCA-TION	DENSITY (MG/M**3)	YOUNGS MODULUS (GPA)	PERM-ANENT SET (PCT)	FRAC-TURE STRAIN (PCT)	TENSILE STRENGTH (MPA)
1B-E--001	RAD	EE					10.9
E--011	RAD	EE					8.5
E--021	RAD	EE					9.1
E--031	RAD	EE					8.2
E--041	RAD	EE					10.6
E--051	RAD	EE					9.4
E--061	RAD	EE					12.4
E--091	RAD	EE					10.8
E--101	RAD	EE					12.9
E--111	RAD	EE					12.8
E--121	RAD	EE					16.5
E--131	RAD	EE					15.6
E--141	RAD	EE					16.3
E--151	RAD	EE					15.8
E--161	RAD	EE					15.7
E--171	RAD	EE					15.8
1A-E--181	RAD	EE					12.7
E--191	RAD	EE					13.4
E--201	RAD	EE					11.8
E--211	RAD	EE					12.5
E--221	RAD	EE					7.9
E--231	RAD	EE					12.4
E--241	RAD	EE					18.3
E--251	RAD	EE					18.5
E--261	RAD	EE					18.5
E--271	RAD	EE					18.4
E--281	RAD	EE					18.9
E--291	RAD	EE					18.9
1B-E-0071	RAD	EE					11.0
E--081	RAD	EE					12.0
	MEAN						13.6 (1965.PSI)
	STD. DEV.						3.5 (505.PSI)

TABLE 11-4 (Continued)

LOT NO. RR SPEC. DIA. 12.8 MM
LOG NO. 6484-82 SPEC. LENGTH 76. MM
LOG DENSITY -- MG/M**3

SPECIMEN NUMBER	ORIENT-ATION	LOCA-TION	DENSITY (MG/M**3)	YOUNGS MODULUS (GPA)	PERM-ANENT SET (PCT)	FRAC-TURE STRAIN (PCT)	TENSILE STRENGTH (MPA)
3A-M--001	RAD	MLC					12.0
M--011	RAD	MLC					10.7
M--021	RAD	MLC					12.2
M--031	RAD	MLC					11.4
M--041	RAD	MLC					8.4
M--051	RAD	MLC					9.6
M--061	RAD	MLC					11.9
M--071	RAD	MLC					8.6
M--081	RAD	MLC					11.2
M--091	RAD	MLC					9.7
M--101	RAD	MLC					9.0
M--111	RAD	MLC					11.3
M--121	RAD	MLC					5.9
M--131	RAD	MLC					8.9
M--141	RAD	MLC					8.3
M--151	RAD	MLC					8.6
M--161	RAD	MLC					10.4
M--171	RAD	MLC					11.5
3A-M--181	RAD	MLC					7.8
M--191	RAD	MLC					9.6
M--201	RAD	MLC					8.4
M--211	RAD	MLC					7.9
M--221	RAD	MLC					8.9
M--231	RAD	MLC					10.3
M--241	RAD	MLC					13.3
M--251	RAD	MLC					11.9
M--261	RAD	MLC					14.4
M--271	RAD	MLC					13.8
M--281	RAD	MLC					11.8
M--291	RAD	MLC					14.4
	MEAN						10.4 (1509.PSI)
	STD. DEV.						2.1 (304.PSI)

TABLE 11-5
ROUND-ROBIN TENSILE DATA: CYLINDRICAL SPECIMENS (GLCC DATA)

LOT NO. RR(GL) SPEC. DIA. 12.8 MM
LOG NO. 6484-82 SPEC. LENGTH 76. MM
LOG DENSITY -- MG/M**3

SPECIMEN NUMBER	ORIENT-ATION	LOCA-TION	DENSITY (MG/M**3)	YOUNGS MODULUS (GPA)	PERM-ANENT SET (PCT)	FRAC-TURE STRAIN (PCT)	TENSILE STRENGTH (MPA)
3A- M8A	AX	MLE					19.3
M10A	AX	MLE					19.7
M12A	AX	MLE					18.9
M38A	AX	MLE					20.0
M42A	AX	MLE					16.2
M44A	AX	MLE					18.0
M64A	AX	MLE					19.3
M72A	AX	MLE					19.8
M74A	AX	MLE					18.9
M94A	AX	MLE					19.3
M104A	AX	MLE					19.0
M108A	AX	MLE					19.6
M112A	AX	MLE					21.0
3B-M126A	AX	MLE					21.8
M130A	AX	MLE					20.0
M132A	AX	MLE					21.6
M152A	AX	MLE					17.0
M160A	AX	MLE					21.8
M162A	AX	MLE					19.3
M182A	AX	MLE					18.1
M190A	AX	MLE					20.3
M192A	AX	MLE					18.4
M212A	AX	MLE					17.6
M232A	AX	MLE					20.2
M244A	AX	MLE					19.0
M248A	AX	MLE					20.3
3A-M8B	AX	MLE					18.5
M38B	AX	MLE					18.9
M64B	AX	MLE					18.3
M94B	AX	MLE					21.1
M10B	AX	MLE					18.7
M42B	AX	MLE					15.3
M12B	AX	MLE					18.9
M72B	AX	MLE					19.7
M44B	AX	MLE					17.9
M74B	AX	MLE					16.3
M104B	AX	MLE					21.5
M112B	AX	MLE					21.0
M108B	AX	MLE					22.3
3B-M212B	AX	MLE					20.6
M182B	AX	MLE					18.0
M152B	AX	MLE					19.3
M126B	AX	MLE					21.0
M190B	AX	MLE					19.8
M160B	AX	MLE					19.5
M130B	AX	MLE					18.9
M192B	AX	MLE					17.2
M162B	AX	MLE					19.3
M132B	AX	MLE					20.1
M244B	AX	MLE					17.6
M248B	AX	MLE					20.4
M232B	AX	MLE					20.5
	MEAN						19.3 (2803.PSI)
	STD. DEV.						1.5 (216.PSI)

TABLE 11-5 (Continued)

LOT NO. RR(GL) SPEC. DIA. 12.8 MM
LOG NO. 6484-82 SPEC. LENGTH 76. MM
LOG DENSITY -- MG/M**3

SPECIMEN NUMBER	ORIENT-ATION	LOCA-TION	DENSITY (MG/M**3)	YOUNGS MODULUS (GPA)	PERM-ANENT SET (PCT)	FRAC-TURE STRAIN (PCT)	TENSILE STRENGTH (MPA)
1A-E4A	AX	EC					14.8
E14A	AX	EC					11.8
E24A	AX	EC					13.2
E34A	AX	EC					12.6
E44A	AX	EC					11.8
E54A	AX	EC					10.8
E64A	AX	EC					11.7
E74A	AX	EC					12.7
E84A	AX	EC					12.0
E94A	AX	EC					12.4
E104A	AX	EC					13.2
E114A	AX	EC					11.9
E124A	AX	EC					12.3
1B-E134A	AX	EC					14.2
E144A	AX	EC					15.1
E154A	AX	EC					14.4
E164A	AX	EC					14.1
E174A	AX	EC					11.9
E184A	AX	EC					13.6
E194A	AX	EC					12.7
1B-E204A	AX	EC					12.3
E214A	AX	EC					13.6
E224A	AX	EC					11.9
E234A	AX	EC					12.5
E244A	AX	EC					12.5
1A-E4B	AX	EC					12.6
E14B	AX	EC					12.7
E24B	AX	EC					12.6
E34B	AX	EC					12.8
E44B	AX	EC					12.6
E54B	AX	EC					13.1
E64B	AX	EC					12.8
E74B	AX	EC					13.1
E84B	AX	EC					10.8
E94B	AX	EC					12.8
E104B	AX	EC					13.1
E114B	AX	EC					13.4
E124B	AX	EC					13.4
1B-E134B	AX	EC					15.4
E144B	AX	EC					13.8
E154B	AX	EC					13.8
E164B	AX	EC					12.7
E174B	AX	EC					12.4
E184B	AX	EC					13.1
E194B	AX	EC					12.0
E204B	AX	EC					12.0
E214B	AX	EC					12.9
E224B	AX	EC					11.3
E234B	AX	EC					12.9
E244B	AX	EC					12.4
	MEAN						12.8 (1858.PSI)
	STD. DEV.						1.0 (140.PSI)

TABLE 11-5 (Continued)

LOT NO. RR(GL) SPEC. DIA. 12.8 MM
LOG NO. 6484-82 SPEC. LENGTH 76. MM
LOG DENSITY -- MG/M**3

SPECIMEN NUMBER	ORIENT-ATION	LOCA-TION	DENSITY (MG/M**3)	YOUNGS MODULUS (GPA)	PERM-ANENT SET (PCT)	FRAC-TURE STRAIN (PCT)	TENSILE STRENGTH (MPA)
1B-E3A	RAD	EE					10.7
E13A	RAD	EE					7.8
E23A	RAD	EE					8.7
E33A	RAD	EE					9.1
E43A	RAD	EE					8.4
E53A	RAD	EE					6.9
E63A	RAD	EE					13.6
E73A	RAD	EE					12.2
E83A	RAD	EE					12.5
E93A	RAD	EE					10.5
E103A	RAD	EE					11.9
E113A	RAD	EE					11.1
E123A	RAD	EE					14.2
E133A	RAD	EE					16.8
E143A	RAD	EE					15.5
E153A	RAD	EE					15.1
E163A	RAD	EE					15.5
E173A	RAD	EE					15.7
1A-E183A	RAD	EE					12.8
E193A	RAD	EE					12.1
E203A	RAD	EE					10.6
E213A	RAD	EE					13.3
E223A	RAD	EE					9.0
E233A	RAD	EE					10.3
E243A	RAD	EE					17.1
E253A	RAD	EE					15.5
E263A	RAD	EE					18.8
E273A	RAD	EE					18.9
E283A	RAD	EE					17.5
E293A	RAD	EE					19.1
E303A	RAD	EE					17.6
E313A	RAD	EE					16.0
E323A	RAD	EE					15.8
E333A	RAD	EE					15.8
E343A	RAD	EE					16.7
E353A	RAD	EE					18.0
	MEAN						13.6 (1978.PSI)
	STD. DEV.						3.5 (505.PSI)

TABLE 11-5 (Continued)

LOT NO. RR(GL) SPEC. DIA. 12.8 MM
LOG NO. 6484-82 SPEC. LENGTH 76. MM
LOG DENSITY -- MG/M**3

SPECIMEN NUMBER	ORIENT-ATION	LOCA-TION	DENSITY (MG/M**3)	YOUNGS MODULUS (GPA)	PERM-ANENT SET (PCT)	FRAC-TURE STRAIN (PCT)	TENSILE STRENGTH (MPA)
3B- M3	RAD	MLC					9.6
M13	RAD	MLC					12.4
M23	RAD	MLC					11.4
M33	RAD	MLC					9.4
M43	RAD	MLC					12.7
M53	RAD	MLC					11.4
M63	RAD	MLC					10.6
M73	RAD	MLC					11.7
M83	RAD	MLC					11.5
M93	RAD	MLC					11.0
M103	RAD	MLC					9.7
M113	RAD	MLC					11.4
M123	RAD	MLC					5.0
M133	RAD	MLC					9.7
M143	RAD	MLC					10.4
M153	RAD	MLC					9.3
M163	RAD	MLC					9.0
M173	RAD	MLC					7.4
3A-M183	RAD	MLC					8.3
M193	RAD	MLC					7.9
M203	RAD	MLC					10.2
M213	RAD	MLC					9.7
M223	RAD	MLC					8.9
M233	RAD	MLC					10.0
M243	RAD	MLC					12.5
M253	RAD	MLC					13.0
M263	RAD	MLC					12.4
M273	RAD	MLC					12.5
M283	RAD	MLC					14.1
M293	RAD	MLC					14.3
M303	RAD	MLC					11.4
M313	RAD	MLC					10.2
M323	RAD	MLC					10.9
M333	RAD	MLC					13.4
M343	RAD	MLC					11.1
M353	RAD	MLC					11.1
	MEAN						10.7 (1554.PSI)
	STD. DEV.						1.9 (279.PSI)

TABLE 11-5 (Continued)

LOT NO. RR(GL) SPEC. DIA. 6.4 MM
LOG NO. 6484-82 SPEC. LENGTH 51. MM
LOG DENSITY -- MG/M**3

SPECIMEN NUMBER	ORIENT-ATION	LOCA-TION	DENSITY (MG/M**3)	MODULUS OF RUPTURE (MPA) (UNCORRECTED)	FLEXURAL STRENGTH (MPA) (CORRECTED)
3A- 6	AX	MLE		39.5	29.4
10	AX	MLE		37.3	28.5
12	AX	MLE		36.1	28.0
16	AX	MLE		33.6	26.8
22	AX	MLE		34.5	27.3
26	AX	MLE		37.9	28.8
28	AX	MLE		33.6	26.8
32	AX	MLE		36.1	28.0
38	AX	MLE		34.1	27.0
44	AX	MLE		33.2	26.6
46	AX	MLE		38.0	28.8
50	AX	MLE		36.4	28.1
52	AX	MLE		36.6	28.2
58	AX	MLE		33.4	26.7
64	AX	MLE		34.8	27.4
66	AX	MLE		36.8	28.3
68	AX	MLE		35.7	27.8
3B- 78	AX	MLE		32.3	26.1
80	AX	MLE		32.0	26.0
82	AX	MLE		33.0	26.5
84	AX	MLE		35.9	27.9
94	AX	MLE		36.6	28.2
96	AX	MLE		35.9	27.9
98	AX	MLE		32.3	26.1
100	AX	MLE		38.9	29.2
110	AX	MLE		35.7	27.8
112	AX	MLE		28.2	23.6
114	AX	MLE		33.0	26.5
116	AX	MLE		36.4	28.1
118	AX	MLE		36.6	28.2
130	AX	MLE		37.5	28.6
132	AX	MLE		36.4	28.1
136	AX	MLE		37.7	28.7
138	AX	MLE		40.2	29.6
140	AX	MLE		32.3	26.1
	MEAN			35.4 MPA (5131. PSI)	27.6 MPA (4003. PSI)
	STD. DEV.			2.5 MPA (362. PSI)	1.2 MPA (177. PSI)

TABLE 11-5 (Continued)

LOT NO. RR(GL)   SPEC. DIA.   6.4 MM
LOG NO. 6484-82   SPEC. LENGTH   51. MM
LOG DENSITY --   MG/M**3

SPECIMEN NUMBER	ORIENT- ATION	LOCA- TION	DENSITY (MG/M**3)	MODULUS OF RUPTURE (MPA) (UNCORRECTED)	FLEXURAL STRENGTH (MPA) (CORRECTED)
1A-144	AX	EC		18.6	16.8
148	AX	EC		25.5	21.9
152	AX	EC		30.3	24.9
156	AX	EC		27.4	23.1
160	AX	EC		26.0	22.2
164	AX	EC		24.9	21.5
168	AX	EC		18.0	16.2
172	AX	EC		27.4	23.1
176	AX	EC		20.6	18.3
180	AX	EC		22.8	20.0
184	AX	EC		24.6	21.3
188	AX	EC		23.6	20.5
192	AX	EC		21.6	19.1
196	AX	EC		22.8	19.9
200	AX	EC		26.7	22.7
204	AX	EC		24.0	20.8
208	AX	EC		25.6	21.9
1B-212	AX	EC		25.1	21.6
216	AX	EC		27.4	23.1
220	AX	EC		28.9	24.1
1B-224	AX	EC		29.3	24.3
228	AX	EC		23.9	20.7
232	AX	EC		24.8	21.4
236	AX	EC		26.6	22.6
240	AX	EC		27.6	23.2
244	AX	EC		22.3	19.6
248	AX	EC		28.7	24.0
252	AX	EC		28.7	24.0
256	AX	EC		32.7	26.3
260	AX	EC		28.3	23.7
264	AX	EC		29.5	24.4
268	AX	EC		31.9	25.9
272	AX	EC		27.2	23.0
276	AX	EC		29.4	24.4
280	AX	EC		29.5	24.5
	MEAN			26.1 MPA (3781. PSI)	22.1 MPA (3211. PSI)
	STD. DEV.			3.5 MPA (501. PSI)	2.4 MPA (344. PSI)

TABLE 11-5 (Continued)

LOT NO. RR(GL)　　SPEC. DIA.　6.4 MM
LOG NO. 6484-62　　SPEC. LENGTH　51. MM
LOG DENSITY --　　MG/M**3

SPECIMEN NUMBER	ORIENT-ATION	LOCA-TION	DENSITY (MG/M**3)	MODULUS OF RUPTURE (MPA) (UNCORRECTED)	FLEXURAL STRENGTH (MPA) (CORRECTED)
1B-147	RAD	EE		19.1	16.7
151	RAD	EE		24.5	20.4
155	RAD	EE		28.0	22.3
159	RAD	EE		17.3	15.3
163	RAD	EE		23.9	19.9
167	RAD	EE		25.2	20.8
171	RAD	EE		25.7	21.0
175	RAD	EE		25.5	20.9
179	RAD	EE		25.0	20.6
183	RAD	EE		29.5	23.1
187	RAD	EE		24.1	20.1
191	RAD	EE		26.1	21.3
195	RAD	EE		33.0	24.5
199	RAD	EE		28.6	22.6
203	RAD	EE		30.5	23.5
207	RAD	EE		28.6	22.6
211	RAD	EE		29.8	23.2
215	RAD	EE		35.5	25.2
1A-219	RAD	EE		30.7	23.6
223	RAD	EE		33.4	24.6
227	RAD	EE		34.5	25.0
231	RAD	EE		29.1	22.9
235	RAD	EE		26.6	21.6
239	RAD	EE		28.2	22.4
243	RAD	EE		36.4	25.4
247	RAD	EE		31.4	23.9
251	RAD	EE		28.2	22.4
255	RAD	EE		32.0	24.2
259	RAD	EE		35.2	25.2
263	RAD	FE		35.5	25.2
267	RAD	EE		32.0	24.2
271	RAD	EE		35.0	25.1
275	RAD	EE		31.6	24.0
279	RAD	EE		34.8	25.0
283	RAD	EE		34.5	25.0
287	RAD	EE		37.3	25.6
	MEAN			29.6 MPA (4295. PSI)	22.8 MPA (3301. PSI)
	STD. DEV.			4.8 MPA (698. PSI)	2.4 MPA (347. PSI)

TABLE 11-5 (Continued)

LOT NO. RR(GL) SPEC. DIA. 6.4 MM
LOG NO. 6484-82 SPEC. LENGTH 51. MM
LOG DENSITY -- MG/M**3

SPECIMEN NUMBER	ORIENT-ATION	LOCA-TION	DENSITY (MG/M**3)	MODULUS OF RUPTURE (MPA) (UNCORRECTED)	FLEXURAL STRENGTH (MPA) (CORRECTED)
3B- 3	RAD	MLC		24.5	20.3
7	RAD	MLC		15.0	13.6
11	RAD	MLC		25.0	20.6
15	RAD	MLC		20.0	17.3
19	RAD	MLC		18.6	16.3
23	RAD	MLC		27.3	21.9
27	RAD	MLC		20.7	17.8
31	RAD	MLC		17.7	15.7
35	RAD	MLC		25.5	20.9
39	RAD	MLC		20.0	17.3
43	RAD	MLC		25.5	20.9
47	RAD	MLC		22.3	18.9
51	RAD	MLC		19.8	17.2
55	RAD	MLC		20.2	17.5
59	RAD	MLC		21.1	18.1
63	RAD	MLC		22.0	18.7
67	RAD	MLC		23.0	19.3
71	RAD	MLC		24.3	20.2
3A- 75	RAD	MLC		21.6	18.4
79	RAD	MLC		17.5	15.5
83	RAD	MLC		19.5	17.0
87	RAD	MLC		22.0	18.7
91	RAD	MLC		22.5	19.0
95	RAD	MLC		24.8	20.5
99	RAD	MLC		29.3	23.0
103	RAD	MLC		19.9	17.3
107	RAD	MLC		26.4	21.4
111	RAD	MLC		28.6	22.6
115	RAD	MLC		24.3	20.2
119	RAD	MLC		24.5	20.4
123	RAD	MLC		26.6	21.6
127	RAD	MLC		24.8	20.5
131	RAD	MLC		27.3	21.9
135	RAD	MLC		25.2	20.8
139	RAD	MLC		22.7	19.2
143	RAD	MLC		25.7	21.0
	MEAN			22.9 MPA (3327. PSI)	19.2 MPA (2788. PSI)
	STD. DEV.			3.3 MPA (482. PSI)	2.2 MPA (316. PSI)

TABLE 11-6
ROUND-ROBIN TENSILE DATA: SQUARE DOGBONE SPECIMENS (GLCC DATA)

LOT NO. RR   SPEC. DIA.   6.4 MM
LOG NO. 6484-82   SPEC. LENGTH   51. MM
LOG DENSITY --   MG/M**3

SPECIMEN NUMBER		ORIENT-ATION	LOCA-TION	DENSITY (MG/M**3)	MODULUS OF RUPTURE (MPA) (UNCORRECTED)	FLEXURAL STRENGTH (MPA) (CORRECTED)
SLAB 3-A	42	AX	MLE		35.2	27.6
	62	AX	MLE		34.6	27.3
	2	AX	MLE		32.9	26.4
	18	AX	MLE		29.5	24.5
	34	AX	MLE		32.9	26.4
	54	AX	MLE		34.5	27.3
	4	AX	MLE		32.8	26.4
	20	AX	MLE		32.4	26.1
	36	AX	MLE		32.1	26.0
	56	AX	MLE		35.3	27.6
	70	AX	MLE		35.8	27.9
	14	AX	MLE		35.4	27.7
	30	AX	MLE		34.4	27.2
	48	AX	MLE		33.9	26.9
	8	AX	MLE		31.4	25.6
	24	AX	MLE		31.8	25.8
	40	AX	MLE		35.5	27.7
	60	AX	MLE		37.1	28.5
SLAB 3-B	122	AX	MLE		32.0	25.9
SLAB 3-B	134	AX	MLE		33.1	26.6
	72	AX	MLE		31.1	25.4
	88	AX	MLE		32.0	25.9
	104	AX	MLE		30.6	25.1
	124	AX	MLE		31.2	25.5
	74	AX	MLE		29.2	24.3
	90	AX	MLE		34.6	27.3
	106	AX	MLE		30.2	24.9
	126	AX	MLE		30.3	24.9
	76	AX	MLE		31.3	25.5
	92	AX	MLE		36.3	28.1
	108	AX	MLE		30.9	25.3
	128	AX	MLE		25.6	22.0
	86	AX	MLE		31.0	25.4
	102	AX	MLE		30.5	25.1
	120	AX	MLE		32.8	26.4
		MEAN			32.6 MPA (4726. PSI)	26.2 MPA (3798. PSI)
		STD. DEV.			2.4 MPA (348. PSI)	1.3 MPA (193. PSI)

TABLE 11-6 (Continued)

LOT NO. RR — SPEC. DIA. 6.4 MM
LOG NO. 6484-82 — SPEC. LENGTH 51. MM
LOG DENSITY -- MG/M**3

SPECIMEN NUMBER		ORIENT-ATION	LOCA-TION	DENSITY (MG/M**3)	MODULUS OF RUPTURE (MPA) (UNCORRECTED)	FLEXURAL STRENGTH (MPA) (CORRECTED)
SLAB 1-A	142	AX	EC		23.1	20.2
	146	AX	EC		21.8	19.2
	150	AX	EC		24.5	21.2
	154	AX	EC		26.1	22.3
	158	AX	EC		24.9	21.5
	162	AX	EC		21.6	19.1
	166	AX	EC		26.7	22.7
	170	AX	EC		24.9	21.5
	174	AX	EC		24.1	20.9
	178	AX	EC		23.3	20.3
	182	AX	EC		26.4	22.5
	186	AX	EC		23.3	20.3
	190	AX	EC		23.6	20.5
	194	AX	EC		17.9	16.2
	198	AX	EC		21.7	19.1
	202	AX	EC		22.0	19.4
	206	AX	EC		23.7	20.6
	210	AX	EC		23.7	20.6
SLAB 1-B	214	AX	EC		29.0	24.2
SLAB 1-B	218	AX	EC		23.4	20.4
	222	AX	EC		23.7	20.6
	226	AX	EC		25.9	22.1
	230	AX	EC		28.7	24.0
	234	AX	EC		27.9	23.5
	238	AX	EC		29.1	24.2
	242	AX	EC		26.7	22.6
	246	AX	EC		21.2	18.8
	250	AX	EC		24.3	21.0
	254	AX	EC		27.7	23.3
	258	AX	EC		22.8	19.9
	262	AX	EC		29.3	24.3
	266	AX	EC		25.1	21.6
	270	AX	EC		22.9	20.0
	274	AX	EC		27.0	22.9
	278	AX	EC		27.4	23.1
		MEAN			24.7 MPA (3587. PSI)	21.3 MPA (3084. PSI)
		STD. DEV.			2.6 MPA (380. PSI)	1.8 MPA (266. PSI)

TABLE 11-6 (Continued)

LOT NO. RR — SPEC. DIA. 6.4 MM
LOG NO. 6484-82 — SPEC. LENGTH 51. MM
LOG DENSITY -- MG/M**3

SPECIMEN NUMBER	ORIENT-ATION	LOCA-TION	DENSITY (MG/M**3)	MODULUS OF RUPTURE (MPA) (UNCORRECTED)	FLEXURAL STRENGTH (MPA) (CORRECTED)
SLAB 1-B 145	RAD	EE		26.7	21.6
149	RAD	EE		29.9	23.3
153	RAD	EE		29.0	22.8
157	RAD	EE		26.8	21.7
161	RAD	EE		29.9	23.3
165	RAD	EE		24.1	20.1
169	RAD	EE		26.2	21.3
173	RAD	EE		25.0	20.7
177	RAD	EE		28.2	22.4
181	RAD	EE		29.5	23.1
185	RAD	EE		27.2	21.9
189	RAD	EE		28.2	22.4
193	RAD	EE		25.1	20.7
197	RAD	EE		30.9	23.7
201	RAD	EE		30.3	23.4
205	RAD	EE		29.9	23.3
209	RAD	EE		25.5	20.9
213	RAD	EE		27.8	22.2
SLAB 1-A 217	RAD	EE		29.9	23.3
SLAB 1-A 221	RAD	EE		30.7	23.6
225	RAD	EE		27.3	22.0
229	RAD	EE		30.2	23.4
233	RAD	EE		28.0	22.3
237	RAD	EE		25.0	20.6
241	RAD	EE		31.4	23.9
245	RAD	EE		30.4	23.5
249	RAD	EE		28.6	22.6
253	RAD	EE		29.3	23.0
257	RAD	EE		29.5	23.1
261	RAD	EE		32.8	24.5
265	RAD	EE		26.8	21.7
269	RAD	EE		30.0	23.3
273	RAD	EE		29.4	23.0
277	RAD	EE		31.4	23.9
281	RAD	EE		33.1	24.5
285	RAD	EE		33.2	24.6
	MEAN			28.8 MPA (4180. PSI)	22.7 MPA (3286. PSI)
	STD. DEV.			2.3 MPA (339. PSI)	1.2 MPA (169. PSI)

TABLE 11-6 (Continued)

LOT NO. RR   SPEC. DIA. 6.4 MM
LOG NO. 6484-82   SPEC. LENGTH 51. MM
LOG DENSITY -- MG/M**3

SPECIMEN NUMBER		ORIENT-ATION	LOCA-TION	DENSITY (MG/M**3)	MODULUS OF RUPTURE (MPA) (UNCORRECTED)	FLEXURAL STRENGTH (MPA) (CORRECTED)
SLAB 3-B	1	RAD	MLC		26.6	21.6
	5	RAD	MLC		25.0	20.6
	9	RAD	MLC		26.0	21.2
	13	RAD	MLC		26.9	21.8
	17	RAD	MLC		25.9	21.1
	21	RAD	MLC		25.2	20.8
	25	RAD	MLC		19.3	16.8
	29	RAD	MLC		21.8	18.6
	33	RAD	MLC		22.8	19.3
	37	RAD	MLC		18.8	16.5
	41	RAD	MLC		25.1	20.7
	45	RAD	MLC		19.4	16.9
	49	RAD	MLC		18.8	16.5
	53	RAD	MLC		21.5	18.4
	57	RAD	MLC		10.1	9.5
	61	RAD	MLC		18.0	15.9
	65	RAD	MLC		21.8	18.6
	69	RAD	MLC		21.8	18.6
SLAB 3-A	73	RAD	MLC		19.1	16.7
SLAB 3-A	77	RAD	MLC		20.8	17.9
	81	RAD	MLC		25.6	21.0
	85	RAD	MLC		22.7	19.2
	89	RAD	MLC		24.3	20.2
	93	RAD	MLC		25.0	20.6
	97	RAD	MLC		22.3	18.9
	101	RAD	MLC		24.1	20.1
	105	RAD	MLC		18.9	16.6
	109	RAD	MLC		24.8	20.5
	113	RAD	MLC		22.7	19.2
	117	RAD	MLC		24.0	20.0
	121	RAD	MLC		22.8	19.3
	129	RAD	MLC		22.1	18.8
	133	RAD	MLC		22.1	18.8
	137	RAD	MLC		20.2	17.5
	141	RAD	MLC		14.0	12.7
		MEAN			22.0 MPA (3192. PSI)	18.6 MPA (2698. PSI)
		STD. DEV.			3.5 MPA (514. PSI)	2.5 MPA (365. PSI)

TABLE 11-7

ROUND-ROBIN FLEXURAL DATA: CYLINDRICAL SPECIMENS (GA DATA)

LOT NO. RR(GL)   SPEC. DIA. ****** MM
LOG NO. 6484-82   SPEC. LENGTH 76. MM
LOG DENSITY --   MG/M**3

SPECIMEN NUMBER	ORIENT-ATION	LOCA-TION	DENSITY (MG/M**3)	YOUNGS MODULUS (GPA)	PERM-ANENT SET (PCT)	FRAC-TURE STRAIN (PCT)	TENSILE STRENGTH (MPA)
3A-M26A	AX	MLE					18.5
M28A	AX	MLE					18.4
M30A	AX	MLE					18.8
M52A	AX	MLE					18.1
M60A	AX	MLE					19.0
M62A	AX	MLE					20.4
M82A	AX	MLE					19.4
M52B	AX	MLE					18.2
M62B	AX	MLE					20.4
3A-M28B	AX	MLE					18.3
M30B	AX	MLE					16.8
M60B	AX	MLE					17.0
M82B	AX	MLE					19.8
M90A	AX	MLE					19.6
M96A	AX	MLE					16.1
M92A	AX	MLE					18.8
M100A	AX	MLE					20.3
M122A	AX	MLE					20.5
3B-M134A	AX	MLE					19.5
M142A	AX	MLE					20.5
M144A	AX	MLE					21.1
M164A	AX	MLE					16.2
M172A	AX	MLE					19.7
M174A	AX	MLE					17.0
M194A	AX	MLE					18.1
M202A	AX	MLE					19.4
M204A	AX	MLE					19.2
M222A	AX	MLE					20.1
M230A	AX	MLE					17.3
M238A	AX	MLE					15.9
3A-M90B	AX	MLE					16.5
M92B	AX	MLE					18.0
M96B	AX	MLE					19.0
M100B	AX	MLE					20.4
M122B	AX	MLE					19.8
M26B	AX	MLE					19.1
3B-M142B	AX	MLE					19.7
M144B	AX	MLE					19.8
M164B	AX	MLE					17.7
M172B	AX	MLE					17.5
M174B	AX	MLE					18.4
M194B	AX	MLE					17.4
M202B	AX	MLE					18.7
M204B	AX	MLE					18.4
M222B	AX	MLE					21.6
M230B	AX	MLE					18.3
M238B	AX	MLE					19.3
	MEAN						18.8 (2721.PSI)
	STD. DEV.						1.4 (198.PSI)

TABLE 11-7 (Continued)

LOT NO. RR(GL)　　　　SPEC. DIA. ****** MM
LOG NO. 6484-82　　　　SPEC. LENGTH 76. MM
LOG DENSITY --　　MG/M**3

SPECIMEN NUMBER	ORIENT-ATION	LOCA-TION	DENSITY (MG/M**3)	YOUNGS MODULUS (GPA)	PERM-ANENT SET (PCT)	FRAC-TURE STRAIN (PCT)	TENSILE STRENGTH (MPA)
1A-F10A	AX	EC					13.2
E20A	AX	EC					12.5
F30A	AX	EC					12.2
E40A	AX	EC					10.1
E50A	AX	EC					6.8
E60A	AX	EC					10.9
F70A	AX	EC					10.1
E80A	AX	EC					11.0
E90A	AX	EC					11.2
F100A	AX	EC					10.2
F110A	AX	EC					9.5
E120A	AX	EC					10.4
1B-F130A	AX	EC					14.7
E150A	AX	EC					13.8
F160A	AX	EC					10.5
E170A	AX	EC					13.4
E180A	AX	EC					11.9
E190A	AX	EC					11.4
F200A	AX	EC					11.8
F230A	AX	EC					11.4
E220A	AX	EC					10.3
E240A	AX	EC					11.4
E140A	AX	EC					12.7
F210A	AX	EC					12.3
1A-E20B	AX	EC					11.1
E50B	AX	EC					12.8
E60B	AX	EC					10.6
F100B	AX	EC					11.3
E110B	AX	EC					11.5
1B-F140B	AX	EC					14.4
F150B	AX	EC					12.2
E160B	AX	EC					11.3
E120B	AX	EC					8.8
1B-E170B	AX	EC					12.7
E130B	AX	EC					13.9
E190B	AX	EC					12.0
F200B	AX	EC					12.5
F210B	AX	EC					11.5
F220B	AX	EC					12.5
E230B	AX	EC					12.5
E240B	AX	EC					12.9
1A-E10B	AX	EC					12.8
E30B	AX	EC					13.1
E40B	AX	EC					13.7
E70B	AX	EC					11.0
E80B	AX	EC					10.3
E90B	AX	EC					12.1
1B-E130B	AX	EC					13.7
	MEAN						11.8 (1707.PSI)
	STD. DEV.						1.5 (218.PSI)

TABLE 11-7 (Continued)

LOT NO. RR(GL)　　　SPEC. DIA. ****** MM
LOG NO. 6484-82　　　SPEC. LENGTH 76. MM
LOG DENSITY --　　MG/M**3

SPECIMEN NUMBER	ORIENT-ATION	LOCA-TION	DENSITY (MG/M**3)	YOUNGS MODULUS (GPA)	PERM-ANENT SET (PCT)	FRAC-TURE STRAIN (PCT)	TENSILE STRENGTH (MPA)
1A- E9	RAD	EE					7.6
E19	RAD	EE					11.0
E29	RAD	EE					9.5
E39	RAD	EE					7.0
E49	RAD	EE					11.2
E59	RAD	EE					5.2
E69	RAD	EE					13.8
E79	RAD	EE					14.2
E89	RAD	EE					11.3
E99	RAD	EE					10.9
E109	RAD	EE					9.4
E119	RAD	EE					11.1
E129	RAD	EE					12.9
E139	RAD	EE					14.4
E149	RAD	EE					15.6
E159	RAD	EE					15.2
E169	RAD	EE					15.2
E179	RAD	EE					11.1
1A-E189	RAD	EE					10.1
E199	RAD	EE					11.2
E209	RAD	EE					11.2
E219	RAD	EE					14.4
E229	RAD	EE					10.8
E239	RAD	EE					8.5
E249	RAD	EE					15.9
E259	RAD	EE					16.8
	MEAN						11.8 (1706.PSI)
	STD. DEV.						3.0 (429.PSI)

TABLE 11-7 (Continued)

LOT NO. RR(GL)　　SPEC. DIA. ****** MM
LOG NO. 6484-82　　SPEC. LENGTH 76. MM
LOG DENSITY --　　MG/M**3

SPECIMEN NUMBER	ORIENT-ATION	LOCA-TION	DENSITY (MG/M**3)	YOUNGS MODULUS (GPA)	PERM-ANENT SET (PCT)	FRAC-TURE STRAIN (PCT)	TENSILE STRENGTH (MPA)
3B-M69	RAD	MLC					6.1
M79	RAD	MLC					9.1
M89	RAD	MLC					9.6
M99	RAD	MLC					11.8
M109	RAD	MLC					9.1
M119	RAD	MLC					10.0
M129	RAD	MLC					6.2
M139	RAD	MLC					5.2
M149	RAD	MLC					6.4
M159	RAD	MLC					7.6
M169	RAD	MLC					7.9
M179	RAD	MLC					8.3
3A-M189	RAD	MLC					9.0
M199	RAD	MLC					7.9
M209	RAD	MLC					9.8
M219	RAD	MLC					6.8
M229	RAD	MLC					6.3
M239	RAD	MLC					7.8
M249	RAD	MLC					12.4
M259	RAD	MLC					12.6
M269	RAD	MLC					11.2
M279	RAD	MLC					14.0
M289	RAD	MLC					13.2
M299	RAD	MLC					14.4
M309	RAD	MLC					10.8
M319	RAD	MLC					11.8
M329	RAD	MLC					11.9
M339	RAD	MLC					9.1
M349	RAD	MLC					10.7
M359	RAD	MLC					7.9
3B- M9	RAD	MLC					10.3
M19	RAD	MLC					10.7
M29	RAD	MLC					11.5
M39	RAD	MLC					10.8
M49	RAD	MLC					10.4
M59	RAD	MLC					13.1
	MEAN						9.8 (1417.PSI)
	STD. DEV.						2.4 (349.PSI)

TABLE 11-7 (Continued)

LOT NO. RR(GL) SPEC. DIA. ****** MM
LOG NO. 6484-82 SPEC. LENGTH 76. MM
LOG DENSITY -- MG/M**3

SPECIMEN NUMBER	ORIENT-ATION	LOCA-TION	DENSITY (MG/M**3)	MODULUS OF RUPTURE (MPA) (UNCORRECTED)	FLEXURAL STRENGTH (MPA) (CORRECTED)
3A-M20	AX	MLE		26.7	23.4
M46	AX	MLE		29.4	25.2
M76	AX	MLE		26.4	23.1
M22	AX	MLE		28.5	24.6
M54	AX	MLE		25.9	22.8
M84	AX	MLE		29.5	25.3
M24	AX	MLE		27.8	24.1
M56	AX	MLE		26.4	23.1
M86	AX	MLE		28.7	24.8
M116	AX	MLE		29.3	25.1
M124	AX	MLE		33.4	27.7
M120	AX	MLE		29.4	25.2
3B-M200	AX	MLE		28.5	24.6
M170	AX	MLE		28.9	24.9
M140	AX	MLE		34.2	28.2
M208	AX	MLE		30.5	25.9
M178	AX	MLE		29.5	25.3
M148	AX	MLE		30.4	25.9
M210	AX	MLE		28.2	24.4
M180	AX	MLE		29.7	25.4
M150	AX	MLE		30.5	26.0
M228	AX	MLE		27.6	24.0
M236	AX	MLE		28.9	24.9
M242	AX	MLE		30.5	26.0
	MEAN			29.1 MPA (4222. PSI)	25.0 MPA (3626. PSI)
	STD. DEV.			2.0 MPA (284. PSI)	1.3 MPA (188. PSI)

TABLE 11-7 (Continued)

LOT NO. RP(GL)　　SPEC. DIA. ****** MM
LOG NO. 6484-82　　SPEC. LENGTH 76. MM
LOG DENSITY --　　MG/M**3

SPECIMEN NUMBER	ORIENT-ATION	LOCA-TION	DENSITY (MG/M**3)	MODULUS OF RUPTURE (MPA) (UNCORRECTED)	FLEXURAL STRENGTH (MPA) (CORRECTED)
1A- E8	AX	EC		26.8	23.4
E18	AX	EC		21.5	19.4
E28	AX	EC		21.1	19.1
E38	AX	EC		18.2	16.7
E48	AX	EC		19.7	18.0
E58	AX	EC		19.6	17.9
E68	AX	EC		22.4	20.1
E78	AX	EC		19.7	18.0
E88	AX	EC		20.5	18.6
E98	AX	EC		20.1	18.3
E108	AX	EC		19.2	17.6
E118	AX	EC		21.2	19.2
1B-E128	AX	EC		21.5	19.4
E138	AX	EC		22.6	20.3
E148	AX	EC		24.1	21.4
E158	AX	EC		19.6	17.9
E168	AX	EC		19.8	18.1
E178	AX	EC		23.8	21.2
E188	AX	EC		20.6	18.7
E198	AX	EC		23.2	20.7
E208	AX	EC		21.8	19.7
E218	AX	EC		21.6	19.5
E228	AX	EC		20.7	18.8
E238	AX	EC		22.5	20.3
E248	AX	EC		19.1	17.5
	MEAN			21.2 MPA (3079. PSI)	19.2 MPA (2784. PSI)
	STD. DEV.			1.9 MPA (277. PSI)	1.5 MPA (217. PSI)

TABLE 11-7 (Continued)

LOT NO. RR(GL) SPEC. DIA. ****** MM
LOG NO. 6484-82 SPEC. LENGTH 76. MM
LOG DENSITY -- MG/M**3

SPECIMEN NUMBER	ORIENT-ATION	LOCA-TION	DENSITY (MG/M**3)	MODULUS OF RUPTURE (MPA) (UNCORRECTED)	FLEXURAL STRENGTH (MPA) (CORRECTED)
1B- E7	RAD	EE		19.1	17.1
E17	RAD	EE		20.9	18.5
E27	RAD	EE		21.0	18.6
E37	RAD	EE		20.7	18.3
E47	RAD	EE		20.0	17.8
E57	RAD	EE		20.4	18.1
E67	RAD	EE		20.9	18.5
E77	RAD	EE		24.4	20.9
E87	RAD	EE		23.9	20.6
E97	RAD	EE		24.6	21.1
E107	RAD	EE		27.4	22.9
E117	RAD	EE		28.1	23.3
E127	RAD	EE		28.2	23.4
E137	RAD	EE		24.1	20.7
E147	RAD	EE		24.2	20.8
E157	RAD	EE		27.0	22.6
E167	RAD	EE		27.1	22.7
E177	RAD	EE		28.8	23.7
1A-E187	RAD	EE		23.1	20.1
E197	RAD	EE		19.9	17.7
1A-E207	RAD	EE		21.6	19.0
E217	RAD	EE		22.9	19.9
E227	RAD	EE		23.0	20.0
E237	RAD	EE		16.2	14.8
E247	RAD	EE		30.1	24.4
E257	RAD	EE		28.1	23.3
	MEAN			23.7 MPA (3434. PSI)	20.3 MPA (2950. PSI)
	STD. DEV.			3.6 MPA (518. PSI)	2.4 MPA (353. PSI)

TABLE 11-7 (Continued)

LOT NO. RR(GL) SPEC. DIA. ****** MM
LOG NO. 6484-82 SPEC. LENGTH 76. MM
LOG DENSITY -- MG/M**3

SPECIMEN NUMBER	ORIENT-ATION	LOCA-TION	DENSITY (MG/M**3)	MODULUS OF RUPTURE (MPA) (UNCORRECTED)	FLEXURAL STRENGTH (MPA) (CORRECTED)
3B- M7	RAD	MLC		16.2	14.8
M17	RAD	MLC		20.2	18.0
M27	RAD	MLC		20.1	17.9
M37	RAD	MLC		21.4	18.8
M47	RAD	MLC		19.7	17.6
M57	RAD	MLC		17.6	16.0
M67	RAD	MLC		17.6	16.0
M77	RAD	MLC		20.7	18.3
M87	RAD	MLC		17.8	16.1
M97	RAD	MLC		20.2	18.0
M107	RAD	MLC		21.3	18.8
M117	RAD	MLC		20.5	18.2
M127	RAD	MLC		16.9	15.4
M137	RAD	MLC		19.4	17.3
M147	RAD	MLC		19.6	17.5
M157	RAD	MLC		18.4	16.6
M167	RAD	MLC		18.2	16.4
M177	RAD	MLC		19.8	17.7
3A-M187	RAD	MLC		12.8	12.0
M197	RAD	MLC		18.4	16.6
M207	RAD	MLC		16.7	15.2
M217	RAD	MLC		18.3	16.5
M227	RAD	MLC		19.7	17.5
M237	RAD	MLC		13.9	13.0
M247	RAD	MLC		20.9	18.5
M257	RAD	MLC		20.9	18.5
M267	RAD	MLC		23.8	20.6
M277	RAD	MLC		22.7	19.8
M287	RAD	MLC		23.4	20.3
M297	RAD	MLC		21.7	19.1
M307	RAD	MLC		22.0	19.2
M317	RAD	MLC		19.5	17.4
M327	RAD	MLC		23.3	20.2
M337	RAD	MLC		21.8	19.1
M347	RAD	MLC		20.3	18.1
M357	RAD	MLC		21.3	18.8
	MEAN			19.6 MPA (2848. PSI)	17.5 MPA (2537. PSI)
	STD. DEV.			2.4 MPA (355. PSI)	1.9 MPA (275. PSI)

TABLE 11-8
ROUND-ROBIN FLEXURAL DATA: CYLINDRICAL SPECIMENS (GLCC DATA)

LOT NO. 426/RR   SPEC. DIA. ****** MM
LOG NO. 6484-82   SPEC. LENGTH 76. MM
LOG DENSITY 1.73 MG/M**3

SPECIMEN NUMBER	ORIENT-ATION	LOCA-TION	DENSITY (MG/M**3)	MODULUS OF RUPTURE (MPA) (UNCORRECTED)	FLEXURAL STRENGTH (MPA) (CORRECTED)
SLAB 3 M14	AX	MLE		24.9	22.1
M40	AX	MLE		23.1	20.7
M70	AX	MLE		28.8	24.8
M48	AX	MLE		23.8	21.2
M78	AX	MLE		27.9	24.2
M18	AX	MLE		26.5	23.2
M50	AX	MLE		25.6	22.6
M80	AX	MLE		27.2	23.7
M110	AX	MLE		28.7	24.7
M118	AX	MLE		29.8	25.5
M114	AX	MLE		29.8	25.5
M206	AX	MLE		30.5	26.0
M176	AX	MLE		30.8	26.2
M146	AX	MLE		26.1	22.9
M214	AX	MLE		24.9	22.0
M184	AX	MLE		26.7	23.3
M154	AX	MLE		27.4	23.9
M216	AX	MLE		28.0	24.2
SLAB 3 M186	AX	MLE		29.8	25.5
M156	AX	MLE		28.8	24.8
M234	AX	MLE		27.4	23.8
M240	AX	MLE		28.3	24.5
M246	AX	MLE		29.0	25.0
	MEAN			27.6 MPA (3997. PSI)	23.9 MPA (3471. PSI)
	STD. DEV.			2.1 MPA (307. PSI)	1.5 MPA (217. PSI)

TABLE 11-8 (Continued)

LOT NO. 426/RR SPEC. DIA. ****** MM
LOG NO. 6484-62 SPEC. LENGTH 76. MM
LOG DENSITY 1.73 MG/M**3

SPECIMEN NUMBER	ORIENT-ATION	LOCA-TION	DENSITY (MG/M**3)	MODULUS OF RUPTURE (MPA) (UNCORRECTED)	FLEXURAL STRENGTH (MPA) (CORRECTED)
SLAB 1 E6	AX	EC		20.4	18.6
E16	AX	EC		21.7	19.6
E26	AX	EC		20.6	18.7
E36	AX	EC		18.1	16.7
E46	AX	EC		22.3	20.1
E56	AX	EC		22.3	20.0
E66	AX	EC		22.4	20.1
E76	AX	EC		20.6	18.7
E86	AX	EC		21.0	19.0
E96	AX	EC		22.2	20.0
E106	AX	EC		21.1	19.1
E116	AX	EC		23.7	21.2
E126	AX	EC		24.6	21.8
E136	AX	EC		24.9	22.0
E146	AX	EC		29.3	25.2
E156	AX	EC		22.0	19.8
E166	AX	EC		20.3	18.5
E176	AX	EC		21.2	19.2
E166	AX	EC		20.4	18.5
SLAB 1 E196	AX	EC		21.3	19.3
E206	AX	EC		20.6	18.7
E216	AX	EC		20.8	18.9
E226	AX	EC		18.6	17.1
E236	AX	EC		24.5	21.8
E246	AX	EC		22.1	19.9
	MEAN			21.9 MPA (3174. PSI)	19.7 MPA (2858. PSI)
	STD. DEV.			2.3 MPA (327. PSI)	1.7 MPA (250. PSI)

TABLE 11-8 (Continued)

LOT NO. 426/RR — SPEC. DIA. ****** MM
LOG NO. 6484-R2 — SPEC. LENGTH 76. MM
LOG DENSITY 1.73 MG/M**3

SPECIMEN NUMBER		ORIENT-ATION	LOCA-TION	DENSITY (MG/M**3)	MODULUS OF RUPTURE (MPA) (UNCORRECTED)	FLEXURAL STRENGTH (MPA) (CORRECTED)
SLAB 1	E5	RAD	EE		15.1	13.9
	E15	RAD	EE		18.1	16.3
	E25	RAD	EE		17.3	15.7
	E35	RAD	EE		18.2	16.4
	E45	RAD	EE		18.5	16.6
	E55	RAD	EE		21.6	19.0
	E65	RAD	EE		24.3	20.9
	E75	RAD	EE		19.6	17.5
	E85	RAD	EE		24.7	21.2
	E95	RAD	EE		21.9	19.2
	E105	RAD	EE		16.2	14.8
	E115	RAD	EE		26.1	22.1
	E125	RAD	EE		24.8	21.2
	E135	RAD	EE		24.9	21.3
	E145	RAD	EE		23.4	20.3
	E155	RAD	EE		25.6	21.7
	E165	RAD	EE		25.6	21.8
	E175	RAD	EE		24.1	20.8
	E185	RAD	EE		21.6	19.0
SLAB 1	E195	RAD	EE		17.8	16.1
	E205	RAD	EE		22.3	19.5
	E215	RAD	EE		17.2	15.6
	E225	RAD	EE		16.6	15.1
	E235	RAD	EE		20.2	18.0
	E245	RAD	EE		27.3	22.8
	E255	RAD	EE		28.2	23.4
		MEAN			21.6 MPA (3130. PSI)	18.8 MPA (2734. PSI)
		STD. DEV.			3.8 MPA (555. PSI)	2.8 MPA (403. PSI)

TABLE 11-8 (Continued)

LOT NO. 426/RR SPEC. DIA. ****** MM
LOG NO. 6484-82 SPEC. LENGTH 76. MM
LOG DENSITY 1.73 MG/M**3

SPECIMEN NUMBER		ORIENT- ATION	LOCA- TION	DENSITY (MG/M**3)	MODULUS OF RUPTURE (MPA) (UNCORRECTED)	FLEXURAL STRENGTH (MPA) (CORRECTED)
SLAB 3	M5	RAD	MLC		21.3	18.8
	M15	RAD	MLC		17.9	16.2
	M25	RAD	MLC		19.2	17.2
	M35	RAD	MLC		17.7	16.1
	M45	RAD	MLC		21.1	18.7
	M55	RAD	MLC		18.8	16.9
	M65	RAD	MLC		13.1	12.2
	M75	RAD	MLC		20.8	18.4
	M85	RAD	MLC		20.2	18.0
	M95	RAD	MLC		19.0	17.1
	M105	RAD	MLC		20.7	18.3
	M115	RAD	MLC		19.9	17.7
	M125	RAD	MLC		18.1	16.4
	M135	RAD	MLC		15.5	14.2
	M145	RAD	MLC		18.7	16.8
	M155	RAD	MLC		17.7	16.0
	M165	RAD	MLC		15.6	14.3
	M175	RAD	MLC		16.9	15.3
	M185	RAD	MLC		16.1	14.8
SLAB 3	M195	RAD	MLC		16.6	15.2
	M205	RAD	MLC		15.1	13.9
	M215	RAD	MLC		14.8	13.7
	M225	RAD	MLC		18.6	16.8
	M235	RAD	MLC		15.6	14.3
	M245	RAD	MLC		19.6	17.5
	M255	RAD	MLC		20.0	17.8
	M265	RAD	MLC		22.3	19.5
	M275	RAD	MLC		15.7	14.4
	M285	RAD	MLC		23.0	20.0
	M295	RAD	MLC		19.5	17.4
	M305	RAD	MLC		19.7	17.6
	M315	RAD	MLC		21.5	18.9
	M325	RAD	MLC		21.0	18.6
	M335	RAD	MLC		20.9	18.5
	M345	RAD	MLC		16.7	15.2
	M355	RAD	MLC		21.1	18.7
		MEAN			18.6 MPA (2699. PSI)	16.7 MPA (2422. PSI)
		STD. DEV.			2.4 MPA (350. PSI)	1.9 MPA (274. PSI)

TABLE 11-9
ROUND-ROBIN FLEXURAL DATA: SQUARE CROSS SECTION SPECIMENS (GA DATA)

LOT NO. RR(GL) SPEC. DIA. 6.4 MM
LOG NO. 6484-22 SPEC. LENGTH 51. MM
LOG DENSITY -- MG/M**3

SPECIMEN NUMBER	ORIENT-ATION	LOCA-TION	DENSITY (MG/M**3)	MODULUS OF RUPTURE (MPA) (UNCORRECTED)	FLEXURAL STRENGTH (MPA) (CORRECTED)
1A-144	AX	LC		17.6	15.9
148	AX	LC		24.1	20.9
152	AX	EC		28.5	23.9
156	AX	EC		25.8	22.1
160	AX	LC		24.5	21.2
164	AX	LC		23.5	20.4
168	AX	LC		16.9	15.4
172	AX	EC		25.8	22.1
176	AX	EC		19.4	17.4
180	AX	LC		21.5	19.0
184	AX	LC		23.2	20.2
188	AX	LC		22.2	19.5
192	AX	EC		20.4	18.1
196	AX	EC		21.5	18.9
200	AX	EC		25.2	21.6
204	AX	EC		22.6	19.8
208	AX	EC		24.1	20.9
1E-212	AX	EC		23.7	20.6
216	AX	LC		25.6	22.1
220	AX	EC		27.2	23.0
1E-224	AX	EC		27.6	23.2
228	AX	EC		22.5	19.7
232	AX	EC		23.4	20.4
236	AX	EC		25.0	21.5
240	AX	EC		26.0	22.2
244	AX	EC		21.0	18.6
248	AX	LC		27.1	22.9
252	AX	LC		27.1	22.9
256	AX	LC		30.8	25.2
260	AX	EC		26.6	22.6
264	AX	LC		27.8	23.3
268	AX	LC		30.1	24.8
272	AX	EC		25.6	21.9
276	AX	LC		27.7	23.3
280	AX	EC		27.8	23.4
	MEAN			24.6 MPA (3561. PSI)	21.1 MPA (3062. PSI)
	STD. DEV.			3.3 MPA (472. PSI)	2.3 MPA (335. PSI)

TABLE 11-9 (Continued)

LOT NO. RR(GL) SPEC. DIA. 6.4 MM
LOG NO. 6484-82 SPEC. LENGTH 51. MM
LOG DENSITY -- MG/M**3

SPECIMEN NUMBER	ORIENT-ATION	LOCA-TION	DENSITY (MG/M**3)	MODULUS OF RUPTURE (MPA) (UNCORRECTED)	FLEXURAL STRENGTH (MPA) (CORRECTED)
3A- 6	AX	MLE		37.2	28.5
10	AX	MLE		35.1	27.5
12	AX	MLE		34.0	27.0
16	AX	MLE		31.7	25.7
22	AX	MLE		32.5	26.2
26	AX	MLE		35.7	27.8
28	AX	MLE		31.7	25.7
32	AX	MLE		34.0	27.0
38	AX	MLE		32.1	26.0
44	AX	MLE		31.2	25.5
46	AX	MLE		35.7	27.9
50	AX	MLE		34.2	27.1
52	AX	MLE		34.5	27.2
56	AX	MLE		31.5	25.6
64	AX	MLE		32.7	26.3
66	AX	MLE		34.7	27.3
68	AX	MLE		33.6	26.8
3B- 78	AX	MLE		30.4	25.0
80	AX	MLE		30.2	24.9
82	AX	MLE		31.0	25.4
84	AX	MLE		33.8	26.9
94	AX	MLE		34.5	27.2
96	AX	MLE		33.8	26.9
98	AX	MLE		30.4	25.0
100	AX	MLE		36.6	28.2
110	AX	MLE		33.6	26.8
112	AX	MLE		26.5	22.6
114	AX	MLE		31.0	25.4
116	AX	MLE		34.2	27.1
118	AX	MLE		34.5	27.2
130	AX	MLE		35.3	27.6
132	AX	MLE		34.2	27.1
136	AX	MLE		35.5	27.7
138	AX	MLE		37.9	28.8
140	AX	MLE		30.4	25.0
	MEAN			33.3 MPA (4833. PSI)	26.6 MPA (3855. PSI)
	STD. DEV.			2.4 MPA (341. PSI)	1.3 MPA (184. PSI)

TABLE 11-9 (Continued)

LOT NO. RP(GL) SPEC. DIA. 6.4 MM
LOG NO. 6484-82 SPEC. LENGTH 51. MM
LOG DENSITY -- MG/M**3

SPECIMEN NUMBER	ORIENT-ATION	LOCA-TION	DENSITY (MG/M**3)	MODULUS OF RUPTURE (MPA) (UNCORRECTED)	FLEXURAL STRENGTH (MPA) (CORRECTED)
1B-147	RAD	EE		18.0	15.9
151	RAD	EE		23.1	19.4
155	RAD	EE		26.3	21.4
159	RAD	EE		16.3	14.6
163	RAD	EE		22.5	19.0
167	RAD	EE		23.8	19.9
171	RAD	EE		24.2	20.1
175	RAD	EE		24.0	20.0
179	RAD	EE		23.5	19.7
183	RAD	EE		27.8	22.2
187	RAD	EE		22.7	19.2
191	RAD	EE		24.6	20.4
195	RAD	EE		31.0	23.8
199	RAD	EE		27.0	21.8
203	RAD	EE		28.7	22.7
207	RAD	EE		27.0	21.8
211	RAD	EE		28.0	22.3
215	RAD	EE		33.4	24.6
1A-219	RAD	EE		28.9	22.8
223	RAD	EE		31.5	23.9
227	RAD	EE		32.5	24.3
231	RAD	EE		27.4	22.0
235	RAD	EE		25.0	20.7
239	RAD	EE		26.5	21.5
243	RAD	EE		34.2	24.9
247	RAD	EE		29.5	23.1
251	RAD	EE		26.5	21.5
255	RAD	EE		30.2	23.4
259	RAD	EE		33.2	24.6
263	RAD	EE		33.4	24.6
267	RAD	EE		30.2	23.4
271	RAD	EE		33.0	24.5
275	RAD	EE		29.8	23.2
279	RAD	EE		32.7	24.4
283	RAD	EE		32.5	24.3
287	RAD	EE		35.1	25.1
	MEAN			27.9 MPA (4045. PSI)	22.0 MPA (3187. PSI)
	STD. DEV.			4.5 MPA (657. PSI)	2.5 MPA (360. PSI)

TABLE 11-9 (Continued)

LOT NO. RP(GL) SPEC. DIA. 6.4 MM
LOG NO. 6464-82 SPEC. LENGTH 51. MM
LOG DENSITY -- MG/M**3

SPECIMEN NUMBER	ORIENT-ATION	LOCA-TION	DENSITY (MG/M**3)	MODULUS OF RUPTURE (MPA) (UNCORRECTED)	FLEXURAL STRENGTH (MPA) (CORRECTED)
3B- 3	RAD	MLC		23.1	19.4
7	RAD	MLC		14.2	12.9
11	RAD	MLC		23.5	19.7
15	RAD	MLC		18.8	16.5
19	RAD	MLC		17.6	15.5
23	RAD	MLC		25.7	21.0
27	RAD	MLC		19.5	17.0
31	RAD	MLC		16.7	14.9
35	RAD	MLC		24.0	20.0
39	RAD	MLC		18.8	16.5
43	RAD	MLC		24.0	20.0
47	RAD	MLC		21.0	18.0
51	RAD	MLC		18.6	16.3
55	RAD	MLC		19.0	16.7
59	RAD	MLC		19.9	17.3
63	RAD	MLC		20.8	17.9
67	RAD	MLC		21.6	18.5
71	RAD	MLC		22.9	19.3
3A- 75	RAD	MLC		20.3	17.6
79	RAD	MLC		16.5	14.7
83	RAD	MLC		18.4	16.2
87	RAD	MLC		20.8	17.9
91	RAD	MLC		21.2	18.2
95	RAD	MLC		23.3	19.6
99	RAD	MLC		27.6	22.1
103	RAD	MLC		18.7	16.4
107	RAD	MLC		24.8	20.5
111	RAD	MLC		27.0	21.8
115	RAD	MLC		22.9	19.3
119	RAD	MLC		23.1	19.4
123	RAD	MLC		25.0	20.7
127	RAD	MLC		23.3	19.6
131	RAD	MLC		25.7	21.0
135	RAD	MLC		23.8	19.9
139	RAD	MLC		21.4	18.3
143	RAD	MLC		24.2	20.1
	MEAN			21.6 MPA (3133. PSI)	18.4 MPA (2662. PSI)
	STD. DEV.			3.1 MPA (454. PSI)	2.1 MPA (310. PSI)

TABLE 11-10

ROUND-ROBIN FLEXURAL DATA: SQUARE CROSS SECTION SPECIMENS (GLCC DATA)

LOT NO. RR(GL) SPEC. DIA. ****** MM

LOG NO. 6484-82 SPEC. LENGTH 76. MM

LOG DENSITY -- MG/M**3

SPECIMEN NUMBER	ORIENT-ATION	LOCA-TION	DENSITY (MG/M**3)	MODULUS OF RUPTURE (MPA) (UNCORRECTED)	FLEXURAL STRENGTH (MPA) (CORRECTED)
1A- E8	AX	EC		25.2	22.3
E18	AX	EC		20.2	18.4
E28	AX	EC		19.9	18.1
E38	AX	EC		17.1	15.8
E48	AX	EC		18.5	17.0
E58	AX	EC		18.4	16.9
E68	AX	EC		21.0	19.1
E78	AX	EC		18.5	17.0
E86	AX	EC		19.3	17.6
E98	AX	EC		18.9	17.3
E108	AX	EC		18.1	16.6
E118	AX	EC		20.0	18.2
1B-E128	AX	EC		20.2	18.4
E138	AX	EC		21.3	19.3
E148	AX	EC		22.6	20.3
E158	AX	EC		18.4	17.0
E168	AX	EC		18.7	17.1
E178	AX	EC		22.4	20.1
F188	AX	EC		19.4	17.7
E198	AX	EC		21.8	19.7
E208	AX	EC		20.5	18.7
E218	AX	EC		20.3	18.5
E228	AX	EC		19.5	17.8
E238	AX	EC		21.2	19.2
E248	AX	EC		18.0	16.6
	MEAN			20.0 MPA (2897. PSI)	18.2 MPA (2639. PSI)
	STD. DEV.			1.8 MPA (261. PSI)	1.4 MPA (208. PSI)

TABLE 11-10 (Continued)

LOT NO. RR(GL) SPEC. DIA. ****** MM
LOG NO. 6484-82 SPEC. LENGTH 76. MM
LOG DENSITY -- MG/M**3

SPECIMEN NUMBER	ORIENT-ATION	LOCA-TION	DENSITY (MG/M**3)	MODULUS OF RUPTURE (MPA) (UNCORRECTED)	FLEXURAL STRENGTH (MPA) (CORRECTED)
3A-M20	AX	MLF		25.2	22.2
M46	AX	MLE		27.6	24.0
M76	AX	MLE		24.9	22.0
M22	AX	MLE		26.8	23.4
M54	AX	MLE		24.4	21.7
M84	AX	MLE		27.7	24.1
M24	AX	MLE		26.2	23.0
M56	AX	MLE		24.8	22.0
M86	AX	MLE		27.0	23.6
M116	AX	MLE		27.5	23.9
M124	AX	MLE		31.4	26.5
M120	AX	MLE		27.7	24.1
3B-M200	AX	MLE		26.8	23.4
M170	AX	MLE		27.2	23.7
M140	AX	MLF		32.1	27.0
M208	AX	MLE		28.7	24.7
M178	AX	MLE		27.8	24.1
M148	AX	MLE		28.6	24.7
M210	AX	MLE		26.6	23.2
M180	AX	MLE		27.9	24.2
M150	AX	MLF		28.7	24.8
M228	AX	MLE		26.0	22.8
M236	AX	MLF		27.2	23.7
M242	AX	MLE		28.7	24.8
	MEAN			27.4 MPA (3973. PSI)	23.8 MPA (3455. PSI)
	STD. DEV.			1.8 MPA (267. PSI)	1.3 MPA (185. PSI)

TABLE 11-10 (Continued)

LOT NO. RR(GL) SPEC. DIA. ****** MM
LOG NO. 6484-82 SPEC. LENGTH 76. MM
LOG DENSITY -- MG/M**3

SPECIMEN NUMBER	ORIENT-ATION	LOCA-TION	DENSITY (MG/M**3)	MODULUS OF RUPTURE (MPA) (UNCORRECTED)	FLEXURAL STRENGTH (MPA) (CORRECTED)
1B- E7	RAD	EE		18.0	16.2
E17	RAD	EE		19.7	17.6
E27	RAD	EE		19.7	17.6
E37	RAD	EE		19.5	17.4
E47	RAD	EE		18.8	16.9
E57	RAD	EE		19.2	17.2
E67	RAD	EE		19.6	17.5
E77	RAD	EE		23.0	20.0
E87	RAD	EE		22.5	19.6
E97	RAD	EE		23.1	20.1
E107	RAD	EE		25.8	21.9
E117	RAD	EE		26.5	22.3
E127	RAD	EE		26.6	22.4
E137	RAD	EE		22.7	19.8
E147	RAD	EE		22.8	19.8
E157	RAD	EE		25.4	21.6
E167	RAD	EE		25.5	21.7
E177	RAD	EE		27.1	22.7
1A-E187	RAD	EE		21.7	19.1
E197	RAD	EE		18.7	16.8
1A-E207	RAD	EE		20.3	18.1
E217	RAD	EE		21.5	18.9
E227	RAD	EE		21.7	19.1
E237	RAD	EE		15.3	14.0
E247	RAD	EE		28.3	23.4
E257	RAD	EE		26.5	22.3
	MEAN			22.3 MPA (3232. PSI)	19.4 MPA (2811. PSI)
	STD. DEV.			3.4 MPA (488. PSI)	2.4 MPA (346. PSI)

TABLE 11-10 (Continued)

LOT NO. RR(GL) SPEC. DIA. ****** MM
LOG NO. 6484-82 SPEC. LENGTH 76. MM
LOG DENSITY -- MG/M**3

SPECIMEN NUMBER	ORIENT-ATION	LOCA-TION	DENSITY (MG/M**3)	MODULUS OF RUPTURE (MPA) (UNCORRECTED)	FLEXURAL STRENGTH (MPA) (CORRECTED)
3B- M7	RAD	MLC		15.3	14.0
M17	RAD	MLC		19.0	17.0
M27	RAD	MLC		18.9	17.0
M37	RAD	MLC		20.1	17.9
M47	RAD	MLC		18.5	16.7
M57	RAD	MLC		16.6	15.1
M67	RAD	MLC		16.6	15.1
M77	RAD	MLC		19.5	17.4
M87	RAD	MLC		16.7	15.2
M97	RAD	MLC		19.0	17.1
M107	RAD	MLC		20.1	17.9
M117	RAD	MLC		19.3	17.3
M127	RAD	MLC		15.9	14.6
M137	RAD	MLC		18.2	16.4
M147	RAD	MLC		18.5	16.6
M157	RAD	MLC		17.3	15.7
M167	RAD	MLC		17.2	15.6
M177	RAD	MLC		18.7	16.8
3A-M187	RAD	MLC		12.0	11.3
M197	RAD	MLC		17.4	15.7
M207	RAD	MLC		15.7	14.4
M217	RAD	MLC		17.3	15.7
M227	RAD	MLC		18.5	16.7
M237	RAD	MLC		13.1	12.3
M247	RAD	MLC		19.6	17.5
M257	RAD	MLC		19.6	17.5
M267	RAD	MLC		22.4	19.6
M277	RAD	MLC		21.4	18.9
M287	RAD	MLC		22.0	19.3
M297	RAD	MLC		20.4	18.1
M307	RAD	MLC		20.7	18.3
M317	RAD	MLC		18.4	16.6
M327	RAD	MLC		21.9	19.2
M337	RAD	MLC		20.5	18.2
M347	RAD	MLC		19.1	17.1
M357	RAD	MLC		20.0	17.8
	MEAN			18.5 MPA (2680. PSI)	16.6 MPA (2408. PSI)
	STD. DEV.			2.3 MPA (334. PSI)	1.8 MPA (265. PSI)

TABLE 11-11
SUMMARY OF FLEXURAL STRENGTHS OF PGX GRAPHITE
(Log 6484-112, Lot 805-3)

	Flexural Strength (MPa)											
	Axial						Radial					
	Center		Midradius		Edge		Center		Midradius		Edge	
Slab	$\bar{x}$	σ	$\bar{x}$	σ	$\bar{x}$	σ	$\bar{x}$	σ	$\bar{x}$	σ	$\bar{x}$	σ
Top	15.8	1.2	16.1	1.0	16.0	0.9	15.1	1.8	15.5	1.8	16.6	1.2
Middle	15.3	0.9	15.9	0.8	16.8	0.8	14.3	2.2	15.7	1.5	17.1	1.6
Bottom	14.1	1.3	13.3	1.0	14.3	1.1	14.1	1.7	13.9	1.1	13.5	1.9

TABLE 11-12
FLEXURAL STRENGTH OF PGX GRAPHITE

LOT NO. 8D5-3 | SPEC. DIA. 6.4 MM
LOG NO. 6484-112 | SPEC. LENGTH 51. MM
LOG DENSITY 1.78 MG/M**3

SPECIMEN NUMBER		ORIENT-ATION	LOCA-TION	DENSITY (MG/M**3)	MODULUS OF RUPTURE (MPA) (UNCORRECTED)	FLEXURAL STRENGTH (MPA) (CORRECTED)
1AE	56A	AX	EE		19.7	16.8
	56B	AX	EE		17.5	15.3
	58A	AX	EE		16.7	14.7
	58B	AX	EE		18.0	15.6
	62A	AX	EE		17.4	15.2
	62B	AX	EE		17.1	15.0
	68A	AX	EE		18.6	16.1
	68B	AX	EE		18.3	15.9
	70A	AX	EE		17.3	15.1
	70B	AX	EE		16.8	14.8
1BE	128A	AX	EE		19.0	16.3
	128B	AX	EE		17.7	15.4
	130A	AX	EE		20.3	17.2
	130B	AX	EE		20.3	17.[illegible]
	134A	AX	EE		21.1	17.7
	134B	AX	EE		19.6	16.7
	140A	AX	EE		19.6	16.7
	140B	AX	EE		19.9	17.0
	142A	AX	EE		16.8	14.8
1BE	142B	AX	EE		18.8	16.2
		MEAN			18.5 MPA (2688. PSI)	16.0 MPA (2320. PSI)
		STD. DEV.			1.4 MPA (196. PSI)	.9 MPA (137. PSI)

TABLE 11-12 (Continued)

LOT NO. 8D5-3 SPEC. DIA. 6.4 MM
LOG NO. 6484-112 SPEC. LENGTH 51. MM
LOG DENSITY 1.78 MG/M**3

SPECIMEN NUMBER	ORIENT-ATION	LOCA-TION	DENSITY (MG/M**3)	MODULUS OF RUPTURE (MPA) (UNCORRECTED)	FLEXURAL STRENGTH (MPA) (CORRECTED)
1AY 36A	AX	EM		16.7	14.7
36B	AX	EM		22.0	18.3
38A	AX	EM		19.5	16.7
38B	AX	EM		19.4	16.6
42A	AX	EM		17.1	15.0
42B	AX	EM		16.4	14.5
48A	AX	EM		18.9	16.3
48B	AX	EM		19.2	16.5
50A	AX	EM		19.6	16.7
50B	AX	EM		19.4	16.6
1BY 108A	AX	EM		19.5	16.7
108B	AX	FM		19.8	16.9
110A	AX	EM		18.1	15.7
110B	AX	EM		18.3	15.8
114A	AX	EM		17.5	15.3
114B	AX	EM		20.7	17.5
120A	AX	EM		19.5	16.7
120B	AX	EM		17.9	15.6
1BY 122A	AX	EM		15.8	14.0
122B	AX	EM		18.0	15.6
	MEAN			18.7 MPA (2707. PSI)	16.1 MPA (2333. PSI)
	STD. DEV.			1.5 MPA (217. PSI)	1.0 MPA (152. PSI)

TABLE 11-12 (Continued)

LOT NO. 8D5-3 SPEC. DIA. 6.4 MM
LOG NO. 6484-112 SPEC. LENGTH 51. MM
LOG DENSITY 1.78 MG/M**3

SPECIMEN NUMBER	ORIENT-ATION	LOCA-TION	DENSITY (MG/M**3)	MODULUS OF RUPTURE (MPA) (UNCORRECTED)	FLEXURAL STRENGTH (MPA) (CORRECTED)
1AC	12A AX	EC		19.1	16.5
	12B AX	EC		18.6	16.1
	10A AX	EC		15.8	14.1
	10B AX	EC		19.1	16.5
	16A AX	EC		18.6	16.1
	16B AX	EC		21.1	17.8
	24A AX	EC		17.4	15.2
	24B AX	EC		16.7	14.8
	26A AX	EC		14.6	13.2
	26B AX	EC		18.7	16.2
	32A AX	EC		16.9	14.9
	32B AX	EC		18.8	16.3
1BC	88A AX	EC		16.9	14.9
	88B AX	EC		19.7	16.9
	86A AX	EC		16.9	14.9
	86B AX	EC		21.4	18.0
	80A AX	EC		17.5	15.4
1BC	80B AX	EC		16.5	14.6
	96A AX	EC		16.9	14.9
	96B AX	EC		18.8	16.3
	102A AX	EC		19.1	16.5
	102B AX	EC		20.1	17.2
	104A AX	EC		18.9	16.4
	104B AX	EC		16.8	14.8
	MEAN			18.1 MPA (2628. PSI)	15.8 MPA (2289. PSI)
	STD. DEV.			1.6 MPA (237. PSI)	1.2 MPA (172. PSI)

TABLE 11-12 (Continued)

LOT NO. 8D5-3 SPEC. DIA. 6.4 MM
LOG NO. 6484-112 SPEC. LENGTH 51. MM
LOG DENSITY 1.78 MG/M**3

SPECIMEN NUMBER		ORIENT-ATION	LOCA-TION	DENSITY (MG/M**3)	MODULUS OF RUPTURE (MPA) (UNCORRECTED)	FLEXURAL STRENGTH (MPA) (CORRECTED)
6AE	200A	AX	MLE		19.2	16.6
	200B	AX	MLE		17.6	15.5
	202A	AX	MLE		21.8	18.4
	202B	AX	MLE		18.1	15.9
	206A	AX	MLE		17.8	15.7
	206B	AX	MLE		19.0	16.5
	212A	AX	MLE		19.7	17.0
	212B	AX	MLE		19.2	16.7
	214A	AX	MLE		19.5	16.9
	214B	AX	MLE		18.6	16.2
6BE	270A	AX	MLE		20.3	17.4
	270B	AX	MLE		19.4	16.8
	272A	AX	MLE		19.1	16.6
	272B	AX	MLE		21.0	17.9
	276A	AX	MLE		19.5	16.9
	276B	AX	MLE		19.9	17.2
	280A	AX	MLE		18.4	16.1
	280B	AX	MLE		20.9	17.9
	282A	AX	MLE		20.0	17.2
6BE	282B	AX	MLE		18.9	16.4
		MEAN			19.4 MPA (2815. PSI)	16.8 MPA (2434. PSI)
		STD. DEV.			1.1 MPA (157. PSI)	.8 MPA (110. PSI)

TABLE 11-12 (Continued)

LOT NO. 8D5-3 SPEC. DIA. 6.4 MM
LOG NO. 6484-112 SPEC. LENGTH 51. MM
LOG DENSITY 1.78 MG/M**3

SPECIMEN NUMBER		ORIENT-ATION	LOCA-TION	DENSITY (MG/M**3)	MODULUS OF RUPTURE (MPA) (UNCORRECTED)	FLEXURAL STRENGTH (MPA) (CORRECTED)
6AY	180A	AX	MLM		19.8	17.0
	180B	AX	MLM		19.8	17.0
	182A	AX	MLM		19.3	16.7
	182B	AX	MLM		16.2	14.4
	186A	AX	MLM		18.8	16.3
	186B	AX	MLM		18.4	16.0
	192A	AX	MLM		18.9	16.4
	192B	AX	MLM		18.1	15.6
	194A	AX	MLM		18.6	16.2
	194B	AX	MLM		16.6	14.7
6BY	250A	AX	MLM		18.6	16.1
	250B	AX	MLM		17.6	15.4
	252A	AX	MLM		18.0	15.7
	252B	AX	MLM		16.9	14.9
	256A	AX	MLM		17.4	15.3
	256B	AX	MLM		18.7	16.2
	262A	AX	MLM		16.7	14.8
	262B	AX	MLM		18.6	16.2
6BY	264A	AX	MLM		17.7	15.5
	264B	AX	MLM		19.1	16.5
		MEAN			18.2 MPA (2639. PSI)	15.9 MPA (2300. PSI)
		STD. DEV.			1.0 MPA (152. PSI)	.8 MPA (111. PSI)

TABLE 11-12 (Continued)

LOT NO. 8D5-3 SPEC. DIA. 6.4 MM
LOG NO. 6484-112 SPEC. LENGTH 51. MM
LOG DENSITY 1.78 MG/M**3

SPECIMEN NUMBER	ORIENT- ATION	LOCA- TION	DENSITY (MG/M**3)	MODULUS OF RUPTURE (MPA) (UNCORRECTED)	FLEXURAL STRENGTH (MPA) (CORRECTED)
6AC 154A	AX	MLC		16.8	14.8
154B	AX	MLC		19.1	16.4
156A	AX	MLC		16.5	14.5
156B	AX	MLC		17.0	14.9
160A	AX	MLC		17.7	15.4
160B	AX	MLC		19.5	16.7
174A	AX	MLC		14.2	12.8
174B	AX	MLC		16.9	14.8
176A	AX	MLC		18.6	16.0
176B	AX	MLC		18.6	16.0
168A	AX	MLC		18.9	16.2
168B	AX	MLC		18.7	16.1
6BC 224A	AX	MLC		17.4	15.2
224B	AX	MLC		15.1	13.5
226A	AX	MLC		17.8	15.4
226B	AX	MLC		18.2	15.7
232A	AX	MLC		18.2	15.8
6BC 232B	AX	MLC		16.9	14.8
236A	AX	MLC		17.2	15.0
236B	AX	MLC		17.3	15.1
238A	AX	MLC		16.9	14.8
238B	AX	MLC		18.9	16.2
244A	AX	MLC		18.5	15.9
244B	AX	MLC		17.0	14.9
	MEAN			17.6 MPA (2550. PSI)	15.3 MPA (2218. PSI)
	STD. DEV.			1.3 MPA (181. PSI)	.9 MPA (133. PSI)

TABLE 11-12 (Continued)

LOT NO. 8D5-3 SPEC. DIA. 6.4 MM
LOG NO. 6484-112 SPEC. LENGTH 51. MM
LOG DENSITY 1.78 MG/M**3

SPECIMEN NUMBER		ORIENT-ATION	LOCA-TION	DENSITY (MG/M**3)	MODULUS OF RUPTURE (MPA) (UNCORRECTED)	FLEXURAL STRENGTH (MPA) (CORRECTED)
12AE	340A	AX	EE		17.4	15.1
	340B	AX	EE		14.1	12.7
	342A	AX	EE		14.1	12.7
	342B	AX	EE		15.6	13.8
	346A	AX	EE		17.4	15.1
	346B	AX	EE		16.5	14.5
	352A	AX	EE		15.7	13.9
	352B	AX	EE		14.8	13.2
	354A	AX	EE		15.3	13.6
	354B	AX	EE		18.8	16.1
12BE	412A	AX	EE		18.9	16.1
	412B	AX	EE		15.4	13.6
	414A	AX	EE		17.3	15.0
	414B	AX	EE		14.5	12.9
	418A	AX	EE		17.4	15.2
	418B	AX	EE		14.3	12.8
	424A	AX	EE		16.6	14.5
	424B	AX	EE		18.6	15.9
	426A	AX	EE		17.3	15.0
12BE	426B	AX	EE		16.7	14.6
		MEAN			16.3 MPA (2369. PSI)	14.3 MPA (2077. PSI)
		STD. DEV.			1.5 MPA (224. PSI)	1.1 MPA (165. PSI)

TABLE 11-12 (Continued)

LOT NO. 8D5-3 SPEC. DIA. 6.4 MM
LOG NO. 6484-112 SPEC. LENGTH 51. MM
LOG DENSITY 1.78 MG/M**3

SPECIMEN NUMBER		ORIENT-ATION	LOCA-TION	DENSITY (MG/M**3)	MODULUS OF RUPTURE (MPA) (UNCORRECTED)	FLEXURAL STRENGTH (MPA) (CORRECTED)
12AY	320A	AX	EM		16.2	14.2
	320B	AX	EM		13.7	12.3
	322A	AX	EM		16.3	14.3
	322B	AX	EM		15.8	13.9
	326A	AX	EM		13.6	12.2
	326B	AX	EM		14.7	13.1
	332A	AX	EM		14.2	12.7
	332B	AX	EM		15.5	13.7
	334A	AX	EM		12.9	11.7
	334B	AX	EM		13.3	12.0
12BY	392A	AX	EM		16.6	14.5
	392B	AX	EM		15.7	13.9
	394A	AX	EM		13.7	12.3
	394B	AX	EM		13.8	12.4
	398A	AX	EM		14.8	13.2
	398B	AX	EM		13.2	11.9
	404A	AX	EM		16.2	14.2
	404B	AX	EM		15.1	13.4
12BY	406A	AX	EM		17.5	15.1
	406B	AX	EM		16.1	14.2
		MEAN			14.9 MPA (2168. PSI)	13.3 MPA (1923. PSI)
		STD. DEV.			1.3 MPA (195. PSI)	1.0 MPA (148. PSI)

TABLE 11-12 (Continued)

LOT NO. 8D5-3 SPEC. DIA. 6.4 MM
LOG NO. 6484-112 SPEC. LENGTH 51. MM
LOG DENSITY 1.78 MG/M**3

SPECIMEN NUMBER		ORIENT-ATION	LOCA-TION	DENSITY (MG/M**3)	MODULUS OF RUPTURE (MPA) (UNCORRECTED)	FLEXURAL STRENGTH (MPA) (CORRECTED)
12AC	294A	AX	EC		15.0	13.3
	294B	AX	EC		15.2	13.6
	296A	AX	EC		13.6	12.3
	296B	AX	EC		17.0	14.9
	300A	AX	EC		17.4	15.2
	300B	AX	EC		15.5	13.7
	310A	AX	EC		17.4	15.2
	310B	AX	EC		17.2	15.0
	312A	AX	EC		16.0	14.1
	312B	AX	EC		13.7	12.4
	316A	AX	EC		17.1	14.9
	316P	AX	EC		15.6	13.8
12BC	368A	AX	EC		14.0	12.6
	368B	AX	EC		17.1	15.0
	366A	AX	EC		15.3	13.6
	366B	AX	EC		15.5	13.8
	372A	AX	EC		17.8	15.5
12BC	372B	AX	EC		21.3	17.8
	384A	AX	EC		15.5	13.8
	384B	AX	EC		15.4	13.7
	382A	AX	EC		14.2	12.8
	382B	AX	EC		13.1	11.9
	388A	AX	EC		17.4	15.2
	388B	AX	EC		17.7	15.4
	MEAN				16.0 MPA (2328. PSI)	14.1 MPA (2052. PSI)
	STD. DEV.				1.8 MPA (262. PSI)	1.3 MPA (193. PSI)

TABLE 11-12 (Continued)

LOT NO. 8D5-3 SPEC. DIA. 6.4 MM
LOG NO. 6484-112 SPEC. LENGTH 51. MM
LOG DENSITY 1.78 MG/M**3

SPECIMEN NUMBER	ORIENT-ATION	LOCA-TION	DENSITY (MG/M**3)	MODULUS OF RUPTURE (MPA) (UNCORRECTED)	FLEXURAL STRENGTH (MPA) (CORRECTED)
1AE 111	RAD	EE		18.0	16.0
115	RAD	EE		19.8	17.4
117	RAD	EE		16.2	14.6
121	RAD	EE		16.6	14.9
123	RAD	EE		19.0	16.8
137	RAD	EE		19.5	17.1
141	RAD	EE		18.3	16.2
143	RAD	EE		16.4	14.8
147	RAD	EE		17.6	15.7
149	RAD	EE		21.3	18.4
1BE 267	RAD	EE		21.2	18.3
271	RAD	EE		18.8	16.6
273	RAD	EE		20.5	17.9
277	RAD	EE		21.0	18.2
279	RAD	EE		19.6	17.2
293	RAD	EE		19.6	17.2
297	RAD	EE		17.9	15.9
299	RAD	EE		15.9	14.4
303	RAD	EE		19.2	16.9
1BE 305	RAD	EE		19.3	17.0
	MEAN			18.8 MPA (2726. PSI)	16.6 MPA (2404. PSI)
	STD. DEV.			1.6 MPA (239. PSI)	1.2 MPA (180. PSI)

TABLE 11-12 (Continued)

LOT NO. 8D5-3 SPEC. DIA. 6.4 MM
LOG NO. 6484-112 SPEC. LENGTH 51. MM
LOG DENSITY 1.78 MG/M**3

SPECIMEN NUMBER	ORIENT-ATION	LOCA-TION	DENSITY (MG/M**3)	MODULUS OF RUPTURE (MPA) (UNCORRECTED)	FLEXURAL STRENGTH (MPA) (CORRECTED)
1BY 215	RAD	EM		15.2	13.7
219	RAD	EM		17.7	15.6
221	RAD	EM		20.2	17.5
225	RAD	EM		19.9	17.2
227	RAD	EM		18.4	16.1
241	RAD	EM		16.7	14.9
245	RAD	EM		19.5	17.0
247	RAD	EM		19.4	16.9
251	RAD	EM		17.2	15.3
253	RAD	EM		17.4	15.4
1AY 59	RAD	EM		16.6	14.8
63	RAD	EM		16.4	14.6
65	RAD	EM		14.9	13.5
69	RAD	EM		12.4	11.4
1AY 71	RAD	EM		13.0	11.9
85	RAD	EM		19.4	16.9
89	RAD	EM		20.0	17.3
91	RAD	EM		19.8	17.2
95	RAD	EM		18.3	16.1
97	RAD	EM		18.2	16.0
	MEAN			17.5 MPA (2543. PSI)	15.5 MPA (2243. PSI)
	STD. DEV.			2.3 MPA (332. PSI)	1.8 MPA (255. PSI)

TABLE 11-12 (Continued)

LOT NO. 8D5-3 SPEC. DIA. 6.4 MM
LOG NO. 6484-112 SPEC. LENGTH 51. MM
LOG DENSITY 1.78 MG/M**3

SPECIMEN NUMBER	ORIENT-ATION	LOCA-TION	DENSITY (MG/M**3)	MODULUS OF RUPTURE (MPA) (UNCORRECTED)	FLEXURAL STRENGTH (MPA) (CORRECTED)
1BC	163 RAD	EC		15.8	14.1
	165 RAD	EC		15.8	14.1
	169 RAD	EC		17.8	15.7
	171 RAD	EC		17.2	15.2
	175 RAD	EC		11.5	10.7
	189 RAD	EC		15.4	13.8
	191 RAD	EC		19.7	17.0
	195 RAD	EC		15.7	14.1
1BC	197 RAD	EC		21.1	18.0
	201 RAD	EC		16.3	14.5
1AC	7 RAD	EC		16.8	14.9
	9 RAD	EC		15.0	13.5
	13 RAD	EC		18.8	16.4
	15 RAD	EC		18.0	15.8
	19 RAD	EC		20.3	17.5
	33 RAD	EC		21.8	18.4
	35 RAD	EC		14.4	13.0
	39 RAD	EC		16.1	14.4
	41 RAD	EC		16.6	14.8
	45 RAD	EC		17.5	15.5
	MEAN			17.1 MPA (2478. PSI)	15.1 MPA (2185. PSI)
	STD. DEV.			2.4 MPA (354. PSI)	1.8 MPA (266. PSI)

TABLE 11-12 (Continued)

LOT NO. 8D5-3 SPEC. DIA. 6.4 MM
LOG NO. 6484-112 SPEC. LENGTH 51. MM
LOG DENSITY 1.78 MG/M**3

SPECIMEN NUMBER	ORIENT-ATION	LOCA-TION	DENSITY (MG/M**3)	MODULUS OF RUPTURE (MPA) (UNCORRECTED)	FLEXURAL STRENGTH (MPA) (CORRECTED)
6AE 423	RAD	MLE		18.7	16.7
427	RAD	MLE		18.9	16.8
429	RAD	MLE		22.8	19.7
433	RAD	MLE		18.9	16.8
435	RAD	MLE		16.6	15.0
449	RAD	MLE		16.3	14.8
453	RAD	MLE		20.3	17.9
455	RAD	MLE		19.2	17.1
459	RAD	MLE		21.3	18.7
461	RAD	MLE		23.5	20.2
6BE 553	RAD	MLE		18.3	16.3
557	RAD	MLE		16.7	15.1
559	RAD	MLE		17.8	16.0
563	RAD	MLE		20.6	18.1
565	RAD	MLE		18.4	16.4
579	RAD	MLE		22.9	19.8
6BE 583	RAD	MLE		17.1	15.4
585	RAD	MLE		20.6	18.1
589	RAD	MLE		19.3	17.1
591	RAD	MLE		18.9	16.8
	MEAN			19.3 MPA (2806. PSI)	17.1 MPA (2486. PSI)
	STD. DEV.			2.1 MPA (305. PSI)	1.6 MPA (230. PSI)

TABLE 11-12 (Continued)

LOT NO. 8D5-3		SPEC. DIA.	6.4 MM
LOG NO. 6484-112		SPEC. LENGTH	51. MM
LOG DENSITY 1.78	MG/M**3		

SPECIMEN NUMBER	ORIENT-ATION	LOCA-TION	DENSITY (MG/M**3)	MODULUS OF RUPTURE (MPA) (UNCORRECTED)	FLEXURAL STRENGTH (MPA) (CORRECTED)
6AY 371	RAD	MLM		18.1	16.1
375	RAD	MLM		18.7	16.5
377	RAD	MLM		14.3	13.1
381	RAD	MLM		16.1	14.5
383	RAD	MLM		18.5	16.4
397	RAD	MLM		18.1	16.1
401	RAD	MLM		19.1	16.8
6AY 403	RAD	MLM		18.2	16.2
407	RAD	MLM		12.0	11.2
409	RAD	MLM		19.0	16.7
6BY 501	RAD	MLM		17.4	15.6
505	RAD	MLM		19.4	17.0
507	RAD	MLM		17.6	15.7
511	RAD	MLM		18.2	16.2
513	RAD	MLM		19.2	16.9
527	RAD	MLM		19.3	17.0
531	RAD	MLM		18.4	16.3
533	RAD	MLM		17.6	15.7
537	RAD	MLM		17.9	15.9
539	RAD	MLM		15.7	14.2
	MEAN			17.6 MPA (2557. PSI)	15.7 MPA (2277. PSI)
	STD. DEV.			1.8 MPA (268. PSI)	1.5 MPA (213. PSI)

TABLE 11-12 (Continued)

LOT NO. 8D5-3 SPEC. DIA. 6.4 MM
LOG NO. 6484-112 SPEC. LENGTH 51. MM
LOG DENSITY 1.78 MG/M**3

SPECIMEN NUMBER	ORIENT-ATION	LOCA-TION	DENSITY (MG/M**3)	MODULUS OF RUPTURE (MPA) (UNCORRECTED)	FLEXURAL STRENGTH (MPA) (CORRECTED)
6AC	319 RAD	MLC		13.8	12.6
	321 RAD	MLC		19.0	16.7
	325 RAD	MLC		12.4	11.5
	327 RAD	MLC		17.4	15.5
	331 RAD	MLC		17.1	15.3
	345 RAD	MLC		9.7	9.1
	347 RAD	MLC		18.6	16.4
	351 RAD	MLC		10.1	9.5
	353 RAD	MLC		17.6	15.6
	357 RAD	MLC		17.7	15.7
6BC	471 RAD	MLC		17.2	15.3
	473 RAD	MLC		14.5	13.2
	475 RAD	MLC		16.3	14.6
	477 RAD	MLC		14.2	13.0
	481 RAD	MLC		16.8	15.1
6BC	483 RAD	MLC		18.6	16.4
	485 RAD	MLC		14.4	13.1
	487 RAD	MLC		17.8	15.8
	489 RAD	MLC		17.6	15.6
	493 RAD	MLC		17.7	15.7
	MEAN			15.9 MPA (2310. PSI)	14.3 MPA (2072. PSI)
	STD. DEV.			2.7 MPA (396. PSI)	2.2 MPA (321. PSI)

TABLE 11-12 (Continued)

LOT NO. 8D5-3 SPEC. DIA. 6.4 MM
LOG NO. 6484-112 SPEC. LENGTH 51. MM
LOG DENSITY 1.78 MG/M**3

SPECIMEN NUMBER		ORIENT- ATION	LOCA- TION	DENSITY (MG/M**3)	MODULUS OF RUPTURE (MPA) (UNCORRECTED)	FLEXURAL STRENGTH (MPA) (CORRECTED)
12AE	709	RAD	EE		14.4	13.1
	713	RAD	EE		17.2	15.3
	715	RAD	EE		10.9	10.2
	719	RAD	EE		12.9	11.9
	721	RAD	EE		14.9	13.5
	735	RAD	EE		17.3	15.4
	739	RAD	EE		11.9	11.0
	741	RAD	EE		12.9	11.9
	745	RAD	EE		16.6	14.8
	747	RAD	EE		16.4	14.6
12BE	865	RAD	EE		17.7	15.7
	869	RAD	EE		14.7	13.3
	871	RAD	EE		11.6	10.8
	875	RAD	EE		14.7	13.3
12BE	877	RAD	EE		14.2	12.9
	891	RAD	EE		18.2	16.0
	895	RAD	EE		12.8	11.8
	897	RAD	EE		17.6	15.5
	901	RAD	EE		13.1	12.0
	903	RAD	EE		19.0	16.6
		MEAN			15.0 MPA (2169. PSI)	13.5 MPA (1955. PSI)
		STD. DEV.			2.4 MPA (351. PSI)	1.9 MPA (280. PSI)

TABLE 11-12 (Continued)

LOT NO. 8D5-3 SPEC. DIA. 6.4 MM
LOG NO. 6484-112 SPEC. LENGTH 51. MM
LOG DENSITY 1.78 MG/M**3

SPECIMEN NUMBER	ORIENT-ATION	LOCA-TION	DENSITY (MG/M**3)	MODULUS OF RUPTURE (MPA) (UN·ORRECTED)	FLEXURAL STRENGTH (MPA) (CORRECTED)
12AY	657 RAD	EM		14.0	12.8
	661 RAD	EM		16.3	14.6
	663 RAD	EM		14.0	12.8
	667 RAD	EM		16.6	14.8
12AY	669 RAD	EM		14.9	13.5
	683 RAD	EM		14.2	12.9
	687 RAD	EM		15.4	13.9
	689 RAD	EM		15.3	13.8
	693 RAD	EM		14.8	13.4
	695 RAD	EM		14.4	13.1
12BY	813 RAD	EM		14.2	12.9
	817 RAD	EM		17.1	15.2
	819 RAD	EM		12.8	11.8
	823 RAD	EM		15.7	14.1
	825 RAD	EM		17.4	15.5
	839 RAD	EM		15.0	13.5
	843 RAD	EM		18.8	16.5
	845 RAD	EM		14.2	13.0
	849 RAD	EM		16.1	14.5
	851 RAD	EM		16.6	14.8
	MEAN			15.4 MPA (2234. PSI)	13.9 MPA (2013. PSI)
	STD. DEV.			1.4 MPA (209. PSI)	1.1 MPA (165. PSI)

TABLE 11-12 (Continued)

LOT NO. 8D5-3 SPEC. DIA. 6.4 MM
LOG NO. 6484-112 SPEC. LENGTH 51. MM
LOG DENSITY 1.78 MG/M**3

SPECIMEN NUMBER	ORIENT-ATION	LOCA-TION	DENSITY (MG/M**3)	MODULUS OF RUPTURE (MPA) (UNCORRECTED)	FLEXURAL STRENGTH (MPA) (CORRECTED)
12AC 601	RAD	EC		14.2	13.0
605	RAD	EC		15.7	14.2
607	RAD	EC		14.2	13.0
611	RAD	EC		15.2	13.8
613	RAD	EC		17.6	15.8
627	RAD	EC		14.4	13.2
631	RAD	EC		16.8	15.1
633	RAD	EC		16.1	14.6
637	RAD	EC		18.9	16.7
639	RAD	EC		12.2	11.4
12BC 757	RAD	EC		16.6	14.9
761	RAD	EC		13.7	12.6
763	RAD	EC		15.9	14.4
767	RAD	EC		18.2	16.2
12BC 769	RAD	EC		12.8	11.9
783	RAD	EC		16.5	14.9
787	RAD	EC		18.5	16.4
789	RAD	EC		18.3	16.2
793	RAD	EC		14.1	12.9
795	RAD	EC		12.1	11.2
	MEAN			15.6 MPA (2264. PSI)	14.1 MPA (2048. PSI)
	STD. DEV.			2.1 MPA (306. PSI)	1.7 MPA (246. PSI)

TABLE 11-13

SUMMARY OF DENSITY, STRENGTH, AND ELASTIC MODULUS DATA FOR H-440N GRAPHITE, LOG 6484-81

Property	Axial						Radial					
	Top Slab			Middle Slab			Top Slab			Middle Slab		
	$\bar{x}$	σ	N[(a)]	$\bar{x}$	σ	N	$\bar{x}$	σ	N	$\bar{x}$	σ	N
Density, Mg/m^3	1.746	0.004	12	1.706	0.029	12	1.740	0.007	8	1.700	0.018	8
Tensile:												
Strength												
MPa	11.2	1.5	34	10.9	1.3	34	13.1	1.1	20	10.4	1.3	20
psi	1621	211		1579	194		1905	153		1506	182	
Modulus												
GPa	7.1	0.3	12	6.0	1.0	12	8.0	0.7	8	7.0	0.8	8
Mpsi	1.03	0.05		0.88	0.14		1.16	0.10		1.01	0.11	
Flexural strength												
MPa	20.5	1.1	42	18.5	1.8	42	21.8	1.4	20	20.1	1.6	20
psi	2976	162		2689	260		3165	197		2908	231	
Compression:												
Strength												
MPa	52.2	2.9	8	49.7	5.2	8	49.4	2.3	8	40.3	1.6	8
psi	7574	414		7168	333		7212	753		5843	237	
Modulus												
GPa	5.7	0.4	8	5.2	0.9	8	7.2	0.4	8	5.2	0.5	
Mpsi	0.83	0.05		1.04	0.05		0.76	0.13		0.75	0.07	

(a) N = number of replicates.

TABLE 11-14

TENSILE STRENGTH AND MODULUS OF ELASTICITY DATA FOR GRADE H-440N

LOT NO. SPEC. DIA. 12.8 MM
LOG NO. 6484-81 SPEC. LENGTH 70. MM
LOG DENSITY -- MG/M**3

SPECIMEN NUMBER	ORIENT-ATION	LOCA-TION	DENSITY (MG/M**3)	YOUNGS MODULUS (GPA)	PERM-ANENT SET (PCT)	FRAC-TURE STRAIN (PCT)	TENSILE STRENGTH (MPA)
SLAB1A-L- 6A	AX	END	1.747	7.4	.018	.221	12.4
- 8A	AX	END	1.752	6.5	.016	.234	11.9
-10B	AX	END	1.743	6.7	.017	.265	12.8
-14A	AX	END	1.744	7.2	.020	.245	12.9
-20A	AX	END	1.741	7.3	.020	.265	13.7
-22B	AX	END	1.737	7.1	.020	.241	12.5
- 6B	AX	END					11.3
- 8B	AX	END					11.1
-12A	AX	END					10.5
-12B	AX	END					9.9
-14B	AX	END					11.4
-18A	AX	END					7.2
-18B	AX	END					10.1
-20B	AX	END					9.3
-22A	AX	END					6.9
-24A	AX	END					9.7
-24B	AX	END					10.9
SLAB1B-L-30A	AX	END	1.748	7.6	.017	.200	11.3
-34B	AX	END	1.751	6.9	.016	.206	11.0
-36A	AX	END	1.746	6.7	.025	.241	12.2
-38A	AX	END	1.746	7.3	.017	.209	11.5
-44A	AX	END	1.750	7.1	.020	.209	11.0
-46B	AX	END	1.748	7.2	.020	.240	12.4
-30B	AX	END					12.1
-32A	AX	END					10.2
-32B	AX	END					10.5
-36B	AX	END					10.9
-38B	AX	END					10.6
SLAB1B-L-42A	AX	END					12.2
-42B	AX	END					12.6
-44B	AX	END					12.6
-46A	AX	END					11.0
-48A	AX	END					11.3
-48B	AX	END					11.7
	MEAN		1.746	7.1 (1.03 MPSI)	.019	.231	11.2 (1621.PSI)
	STD. DEV.		.004	.3 (.05 MPSI)	.003	.022	1.5 (211.PSI)

TABLE 11-14 (Continued)

LOT NO. SPEC. DIA. 12.8 MM
LOG NO. 6484-81 SPEC. LENGTH 70. MM
LOG DENSITY -- MG/M**3

SPECIMEN NUMBER	ORIENT-ATION	LOCA-TION	DENSITY (MG/M**3)	YOUNGS MODULUS (GPA)	PERM-ANENT SET (PCT)	FRAC-TURE STRAIN (PCT)	TENSILE STRENGTH (MPA)
SLAB6A-L-54A	AX	ML	1.726	6.7	.019	.176	9.4
56A	AX	ML	1.673	5.3	.035	.180	7.4
58B	AX	ML	1.676	5.6	.030	.241	10.0
SLAB6A-L-62A	AX	ML	1.737	8.3	.005	.168	11.4
68A	AX	ML	1.676	5.0	.030	.275	10.0
-L-70B	AX	ML	1.742	6.7	.022	.231	11.7
-50A	AX	ML					10.4
-50B	AX	ML					10.2
-54B	AX	ML					12.5
-56B	AX	ML					9.9
-60A	AX	ML					9.8
-60B	AX	ML					11.2
-66A	AX	ML					11.3
-66B	AX	ML					11.7
-68B	AX	ML					8.4
-70A	AX	ML					11.5
-72A	AX	ML					11.7
-72B	AX	ML					10.6
SLAB6B-L-78A	AX	ML	1.724	6.0	.019	.190	9.3
-82B	AX	ML	1.671	5.0	.030	.237	9.0
-84	AX	ML	1.676	5.2	.026	.228	9.3
-86A	AX	ML	1.718	6.1	.019	.230	11.0
-92A	AX	ML	1.735	6.5	.021	.194	9.7
-94B	AX	ML	1.725	6.3	.023	.268	12.3
-74A	AX	ML					11.6
-74B	AX	ML					12.6
-78B	AX	ML					11.2
-80A	AX	ML					11.3
-80B	AX	ML					10.7
-84B	AX	ML					10.1
-86B	AX	ML					12.7
SLAB6B-L-90A	AX	ML					12.0
-90B	AX	ML					12.6
-92B	AX	ML					10.5
-94A	AX	ML					12.0
-96A	AX	ML					13.5
-96B	AX	ML					12.1
	MEAN		1.706	6.0	.023	.218	10.9
				(.88 MPSI)			(1579.PSI)
	STD. DEV.		.029	1.0	.008	.036	1.3
				(.14 MPSI)			(194.PSI)

TABLE 11-14 (Continued)

LOT NO. SPEC. DIA. 12.8 MM
LOG NO. 6484-81 SPEC. LENGTH 70. MM
LOG DENSITY -- MG/M**3

SPECIMEN NUMBER	ORIENT-ATION	LOCA-TION	DENSITY (MG/M**3)	YOUNGS MODULUS (GPA)	PERM-ANENT SET (PCT)	FRAC-TURE STRAIN (PCT)	TENSILE STRENGTH (MPA)
SLAB1A L- 7	RAD	END	1.733	7.9	.015	.223	13.0
- 11	RAD	END	1.742	9.0	.010	.223	15.0
SLAB 1A-L-25	RAD	END	1.745	8.2	.015	.210	13.0
-29	RAD	END	1.737	8.2	.016	.213	12.8
- 5	RAD	END					12.5
- 9	RAD	END					14.1
-13	RAD	END					13.5
-23	RAD	END					11.0
-27	RAD	END					12.7
-31	RAD	END					12.3
SLAB1B-L-43	RAD	END	1.748	7.6	.019	.239	13.5
-47	RAD	END	1.749	7.9	.015	.195	11.9
-61	RAD	END	1.738	8.5	.015	.265	15.8
-65	RAD	END	1.729	6.7	.018	.251	12.4
-41	RAD	END					13.0
-45	RAD	END					13.0
-49	RAD	END					12.4
-59	RAD	END					13.1
-63	RAD	END					13.5
-67	RAD	END					14.0
	MEAN		1.740	8.0 (1.16 MPSI)	.015	.227	13.1 (1905.PSI)
	STD. DEV.		.007	.7 (.10 MPSI)	.003	.023	1.1 (153.PSI)

TABLE 11-14 (Continued)

LOT NO.   SPEC. DIA.   12.8 MM
LOG NO. 6484-81   SPEC. LENGTH   70. MM
LOG DENSITY --   MG/M**3

SPECIMEN NUMBER	ORIENT-ATION	LOCA-TION	DENSITY (MG/M**3)	YOUNGS MODULUS (GPA)	PERM-ANENT SET (PCT)	FRAC-TURE STRAIN (PCT)	TENSILE STRENGTH (MPA)
SLAB6A L-79	RAD	ML	1.720			.140	8.5
-83	RAD	ML	1.714	7.2	.016	.189	10.8
-97	RAD	ML	1.720	8.5	.015	.149	9.8
101	RAD	ML	1.713	7.2	.018	.169	9.7
SLAB6A-L-77	RAD	ML					11.8
-81	RAD	ML					12.5
-85	RAD	ML					11.9
-95	RAD	ML					13.3
-99	RAD	ML					11.2
103	RAD	ML					10.3
SLAB6B L115	RAD	ML	1.684	6.4	.019	.193	9.9
119	RAD	ML	1.678	6.2	.015	.204	10.3
133	RAD	ML	1.686	6.7	.016	.170	9.3
137	RAD	ML	1.688	6.5	.020	.218	11.0
113	RAD	ML					9.9
117	RAD	ML					8.6
121	RAD	ML					9.3
131	RAD	ML					9.3
135	RAD	ML					10.2
139	RAD	ML					10.1
	MEAN		1.700	7.0 (1.01 MPSI)	.017	.179	10.4 (1506.PSI)
	STD. DEV.		.018	.8 (.11 MPSI)	.002	.027	1.3 (182.PSI)

TABLE 11-15
FLEXURAL STRENGTH DATA FOR GRADE H-440N

LOT NO.	SPEC. DIA. 6.4 MM
LOG NO. 6484-81	SPEC. LENGTH 51. MM
LOG DENSITY -- MG/M**3	

SPECIMEN NUMBER		ORIENT-ATION	LOCA-TION	DENSITY (MG/M**3)	MODULUS OF RUPTURE (MPA) (UNCORRECTED)	FLEXURAL STRENGTH (MPA) (CORRECTED)
SLAB1A	2A	AX	END		26.5	21.7
	2B	AX	END		23.9	20.1
	4A	AX	END		26.5	21.7
	4B	AX	END		21.4	18.4
	6A	AX	END		26.4	21.7
	6B	AX	END		24.6	20.6
	10A	AX	END		24.3	20.4
	10B	AX	END		22.6	19.2
	12A	AX	END		24.3	20.4
	12B	AX	END		24.8	20.7
	14A	AX	END		23.9	20.1
	14B	AX	END		22.8	19.4
	18A	AX	END		27.2	22.1
	18B	AX	END		25.8	21.3
	20A	AX	END		26.7	21.8
	20B	AX	END		27.1	22.1
	22A	AX	END		22.9	19.4
	22B	AX	END		23.2	19.7
	30A	AX	END		28.7	22.9
SLAB1A	30B	AX	END		24.2	20.2
	32A	AX	END		26.2	21.5
	32B	AX	END		24.3	20.3
SLAB1B	34A	AX	END		25.7	21.2
	34B	AX	END		23.5	19.8
	36A	AX	END		24.0	20.1
	36B	AX	END		26.6	21.7
	40A	AX	END		23.5	19.8
	40B	AX	END		23.3	19.7
	42A	AX	END		20.7	17.9
	42B	AX	END		24.9	20.7
	44A	AX	END		23.5	19.8
	44B	AX	END		24.9	20.7
	50A	AX	END		24.6	20.6
	50B	AX	END		24.1	20.2
	52A	AX	END		23.8	20.0
	52B	AX	END		26.2	21.5
	56A	AX	END		26.8	21.8
SLAB1B	56B	AX	END		20.4	17.7
	58A	AX	END		24.1	20.2
	58B	AX	END		24.4	20.4
	60A	AX	END		25.9	21.3
	60B	AX	END		25.2	20.9
		MEAN			24.6 MPA (3572. PSI)	20.5 MPA (2976. PSI)
		STD. DEV.			1.8 MPA (256. PSI)	1.1 MPA (162. PSI)

TABLE 11-15 (Continued)

LOT NO. SPEC. DIA. 6.4 MM
LOG NO. 6484-81 SPEC. LENGTH 51. MM
LOG DENSITY -- MG/M**3

SPECIMEN NUMBER		ORIENT-ATION	LOCA-TION	DENSITY (MG/M**3)	MODULUS OF RUPTURE (MPA) (UNCORRECTED)	FLEXURAL STRENGTH (MPA) (CORRECTED)
SLAB6A	66A	AX	ML		24.5	19.6
	66B	AX	ML		24.9	19.8
	68A	AX	ML		25.0	19.8
	68B	AX	ML		24.3	19.5
	70A	AX	ML		24.3	19.5
	70B	AX	ML		26.0	20.3
	74A	AX	ML		16.8	14.7
	74B	AX	ML		19.6	16.6
	76A	AX	ML		21.8	18.0
	76B	AX	ML		18.4	15.9
	78A	AX	ML		19.0	16.2
	78B	AX	ML		18.4	15.8
	82A	AX	ML		24.5	19.6
SLAB6A	82B	AX	ML		24.3	19.5
	84A	AX	ML		24.9	19.8
	84B	AX	ML		24.4	19.5
	86A	AX	ML		27.4	20.9
	86B	AX	ML		25.1	19.9
	92A	AX	ML		27.3	20.9
	92B	AX	ML		25.1	19.9
	94A	AX	ML		28.0	21.2
	94B	AX	ML		25.9	20.3
SLAB6B	98A	AX	ML		25.5	20.1
	98B	AX	ML		25.1	19.9
	100A	AX	ML		23.5	19.0
	100B	AX	ML		21.8	18.1
	104A	AX	ML		19.5	16.6
	104B	AX	ML		17.9	15.5
	106A	AX	ML		18.6	16.0
	106B	AX	ML		18.8	16.1
	108A	AX	ML		17.9	15.5
SLAB6B	108B	AX	ML		19.3	16.4
	114A	AX	ML		24.1	19.3
	114B	AX	ML		24.0	19.3
	116A	AX	ML		26.5	20.6
	116B	AX	ML		25.7	20.2
	120A	AX	ML		23.2	18.9
	120B	AX	ML		23.1	18.8
	122A	AX	ML		21.2	17.7
	122B	AX	ML		21.6	17.9
	128A	AX	ML		20.8	17.4
	128B	AX	ML		22.9	18.7
		MEAN			22.9 MPA (3318. PSI)	18.5 MPA (2689. PSI)
		STD. DEV.			3.0 MPA (441. PSI)	1.8 MPA (260. PSI)

TABLE 11-15 (Continued)

LOT NO.		SPEC. DIA.	6.4 MM
LOG NO. 6484-81		SPEC. LENGTH	51. MM
LOG DENSITY --	MG/M**3		

SPECIMEN NUMBER	ORIENT-ATION	LOCA-TION	DENSITY (MG/M**3)	MODULUS OF RUPTURE (MPA) (UNCORRECTED)	FLEXURAL STRENGTH (MPA) (CORRECTED)
SLAB1A	7 RAD	END		25.3	21.6
	9 RAD	END		25.0	21.4
	13 RAD	END		23.0	20.0
	15 RAD	END		22.4	19.5
	19 RAD	END		25.5	21.7
	33 RAD	END		24.9	21.3
	35 RAD	END		29.1	24.0
	39 RAD	END		27.0	22.7
	41 RAD	END		22.2	19.4
	45 RAD	END		23.6	20.4
SLAB1B	59 RAD	END		24.3	20.9
	61 RAD	END		25.4	21.6
	65 RAD	END		27.2	22.8
	67 RAD	END		26.8	22.5
	71 RAD	END		29.0	23.9
	85 RAD	END		26.2	22.1
	91 RAD	END		29.4	24.2
	93 RAD	END		26.3	22.2
SLAB1B	97 RAD	END		26.0	22.0
SLAB1B	87 RAD	END		26.1	22.1
	MEAN			25.7 MPA (3733. PSI)	21.8 MPA (3165. PSI)
	STD. DEV.			2.1 MPA (297. PSI)	1.4 MPA (197. PSI)

TABLE 11-15 (Continued)

LOT NO.		SPEC. DIA.	6.4 MM
LOG NO. 6484-81		SPEC. LENGTH	51. MM
LOG DENSITY --	MG/M**3		

SPECIMEN NUMBER	ORIENT- ATION	LUCA- TION	DENSITY (MG/M**3)	MODULUS OF RUPTURE (MPA) (UNCORRECTED)	FLEXURAL STRENGTH (MPA) (CORRECTED)
SLAB6A 111	RAD	ML		24.7	20.5
113	RAD	ML		25.4	21.0
117	RAD	ML		26.7	21.7
119	RAD	ML		26.2	21.4
123	RAD	ML		25.1	20.7
137	RAD	ML		27.4	22.1
139	RAD	ML		28.1	22.5
143	RAD	ML		26.3	21.5
145	RAD	ML		25.7	21.1
149	RAD	ML		27.1	21.9
SLAB6B 163	RAD	ML		22.3	18.9
165	RAD	ML		23.4	19.7
169	RAD	ML		24.6	20.4
171	RAD	ML		21.9	18.7
175	RAD	ML		21.6	18.5
189	RAD	ML		21.1	18.1
SLAB6B 191	RAD	ML		21.2	18.2
195	RAD	ML		20.3	17.6
197	RAD	ML		21.8	18.6
201	RAD	ML		20.6	17.8
	MEAN			24.1 MPA (3493. PSI)	20.1 MPA (2908. PSI)
	STD. DEV.			2.5 MPA (368. PSI)	1.6 MPA (231. PSI)

TABLE 11-16
COMPRESSIVE STRENGTH AND MODULUS OF ELASTICITY FOR GRADE H-440N

LOT NO.
LOG NO. 6484-81
LOG DENSITY -- MG/M**3

SPEC. DIA. 12.8 MM
SPEC. LENGTH 25. MM

SPECIMEN NUMBER		ORIENT-ATION	LOCA-TION	DENSITY (MG/M**3)	YOUNGS MODULUS (GPA)	PERM-ANENT SET (PCT)	FRAC-TURE STRAIN (PCT)	COMPR. STRENGTH (MPA)
1A	L6C	AX	END		6.0	.150	2.084	47.0
	L8C	AX	END		5.2	.180	3.289	53.8
	L12C	AX	END		6.1	.110	2.176	48.7
	L14C	AX	END		6.0	.150	3.104	53.4
1B	L30C	AX	END		6.0	.180	2.850	52.4
	L32C	AX	END		5.3	.160	3.404	54.7
	L36C	AX	END		5.5	.180	3.484	54.8
	L38C	AX	END		5.5	.200	3.238	53.1
		MEAN			5.7	.164	2.953	52.2
					(.83 MPSI)			(7574.PSI)
		STD. DEV.			.4	.028	.544	2.9
					(.05 MPSI)			(414.PSI)
1A	L5B	RAD	END		6.7	.130	2.345	52.6
	L9B	RAD	END		6.9	.130	2.186	50.6
	L13B	RAD	END		7.4	.120	1.669	46.6
	L23B	RAD	END		7.2	.140	1.836	48.0
1B	L41B	RAD	END		7.9	.130	2.311	52.3
	L45B	RAD	END		7.1	.130	2.178	50.0
	L49B	RAD	END		6.9	.140	1.956	48.1
	L59B	RAD	END		7.2	.120	1.778	47.2
		MEAN			7.2	.130	2.032	49.4
					(1.04 MPSI)			(7168.PSI)
		STD. DEV.			.4	.008	.257	2.3
					(.05 MPSI)			(333.PSI)

TABLE 11-16 (Continued)

LOT NO. SPEC. DIA. 12.8 MM
LOG NO. 6484-81 SPEC. LENGTH 25. MM
LOG DENSITY -- MG/M**3

SPECIMEN NUMBER	ORIENT-ATION	LOCA-TION	DENSITY (MG/M**3)	YOUNGS MODULUS (GPA)	PERM-ANENT SET (PCT)	FRAC-TURE STRAIN (PCT)	COMPR. STRENGTH (MPA)
6A L50C	AX	ML		6.2	.160	3.221	53.6
L54C	AX	ML		5.8	.120	2.990	52.3
L56C	AX	ML		4.4	.180	2.983	43.7
L60C	AX	ML		5.8	.150	3.027	52.0
6B L74C	AX	ML		6.0	.130	3.461	55.4
L78C	AX	ML		5.6	.160	3.502	53.8
L80C	AX	ML		3.9	.129	2.999	43.1
L84C	AX	ML		4.3	.150	3.043	43.9
	MEAN			5.2	.148	3.153	49.7
				(.76 MPSI)			(7212.PSI)
	STD. DEV.			.9	.020	.217	5.2
				(.13 MPSI)			(753.PSI)
6A L77R	RAD	ML		5.6	.170	1.765	39.2
L81R	RAD	ML		5.4	.160	1.991	41.4
L85R	RAD	ML		4.5	.180	2.214	39.4
L95R	RAD	ML		6.1	.140	1.638	40.8
6B L113E	RAD	ML		5.2	.130	1.904	37.9
L117	RAD	ML		5.0	.120	2.650	42.8
L121	RAD	ML		5.2	.100	2.316	41.7
L131R	RAD	ML		4.6	.180	2.167	39.0
	MEAN			5.2	.148	2.080	40.3
				(.75 MPSI)			(5843.PSI)
	STD. DEV.			.5	.030	.325	1.6
				(.07 MPSI)			(237.PSI)

TABLE 11-17
FATIGUE TESTS ON PGX GRAPHITE

LOT NO: --　　　　　　　　LOG NO: 6484-74
ORIENTATION: AX　　　　　LOCATION: END-ONE THIRD RADIUS

STRESS RATIO, R (MIN. STRESS / MAX. STRESS): -1.0

SPECIMEN NO.	DENSITY (MG/M**3)	MAX. STRESS (MPA)	MIN. STRESS (MPA)	CYCLES TO FAILURE
34C	1.771	4.3	4.3	>121500 (RUNOUT)
10B	1.765	4.3	4.3	>119600 (RUNOUT)
28A	1.767	4.3	4.3	>100100 (RUNOUT)
18B	1.763	4.3	4.3	11000
8C	1.760	4.3	4.3	>104000 (RUNOUT)
60C	1.764	4.3	4.3	500
72B	1.765	4.3	4.3	>163590 (RUNOUT)
54A	1.757	4.3	4.3	>146900 (RUNOUT)
80A	1.760	4.3	4.3	>137800 (RUNOUT)
86C	1.770	4.3	4.3	>100500 (RUNOUT)
40B	1.761	5.4	5.4	16101
48A	1.759	5.4	5.4	1342
28C	1.760	5.4	5.4	1825
56C	1.767	5.4	5.4	55900
22A	1.778	5.4	5.4	859
14B	1.753	5.4	5.4	231
82C	1.765	5.4	5.4	16000
66B	1.767	5.4	5.4	>126800 (RUNOUT)
76A	1.769	5.4	5.4	2500
2C	1.756	5.6	5.6	474
34B	1.765	6.2	6.2	208
14A	1.766	6.3	6.3	605
24C	1.764	6.3	6.3	496
16A	1.757	6.3	6.3	23
6B	1.759	6.3	6.3	82
50C	1.775	6.3	6.3	2130
76C	1.773	6.3	6.3	646
70A	1.761	6.3	6.3	260
62B	1.760	6.3	6.3	418
88B	1.760	6.3	6.3	176
44C	1.759	6.9	6.9	17
36A	1.757	6.9	6.9	44
30B	1.768	6.9	6.9	113
18C	1.746	6.9	6.9	193
56B	1.757	6.9	6.9	16
2B	1.774	6.9	6.9	38
82B	1.768	6.9	6.9	79
12A	1.753	6.9	6.9	8
72C	1.766	6.9	6.9	36
64A	1.779	6.9	6.9	27
76B	1.759	7.4	.0	< 1 (FIRST CYCLE)
40C	1.761	7.8	.0	1
24B	1.768	7.8	7.8	18
12C	1.755	7.8	7.6	5
50B	1.768	7.8	.0	2
32A	1.765	7.8	7.8	8
6A	1.760	7.8	7.8	3
66C	1.763	7.8	7.8	12
60A	1.772	7.8	.0	1
96A	1.776	7.8	7.8	3

TABLE 11-18
UNIAXIAL FATIGUE ENDURANCE LIMITS FOR PGX GRAPHITE
(SPECIMENS FROM LOG 6484-74, END - ONE-THIRD RADIUS LOCATION)

Orientation	Stress Ratio, R $\sigma_{min}/\sigma_{max}$	Number of Cycles	Endurance Limits, Peak Stress/Mean Strength	
			50% Survival	99/95 Lower Tolerance Limit
Radial	0	100	0.92	0.71
		1,000	0.90	0.69
		10,000	0.87	0.66
		100,000	0.85	0.64
	-1	100	0.86	0.66
		1,000	0.82	0.62
		10,000	0.78	0.59
		100,000	0.74	0.56
Axial	0	100	0.85	0.70
		1,000	0.81	0.67
		10,000	0.78	0.63
		100,000	0.74	0.60
	-1	100	0.83	0.67
		1,000	0.77	0.62
		10,000	0.71	0.57
		100,000	0.66	0.52

TABLE 11-19
AVERAGE AND RANGE OF STEAM OXIDATION REACTION RATES OF STACKPOLE 2020 GRAPHITE[a]

		High (%/hr)	Average (%/hr)	Low (%/hr)	Sampling Frequency
Slab 1	Edge	0.5488	0.1268	0.0042	48
	Whole radius	0.1147	0.0350	0.0085	16
	Center	0.0483	0.0138	0.0048	14
Slab 3	Edge	0.0084	0.0049	0.0013	45
	Whole radius	0.0132	0.0083	0.0053	17
	Center	0.0084	0.0060	0.0020	17
Slab 5	Edge	0.0123	0.0078	0.0031	45
	Whole radius	0.0374	0.0173	0.0081	17
	Center	0.0159	0.0093	0.0034	17

[a] Experimental conditions: temperature = 1148 K, gas mix = 5% H_2, 3% H_2O, balance He.

TABLE 11-20
REACTION RATE AND DENSITY OF SAMPLES, GROUPED ACCORDING TO SECTION

Slab	Section	Distance from Top of Log (m)	Sample Type	Orien-tation	Sample No.[a]	Burnoff (%)	Reaction Rate (%/h)		Density x 10^{-3} (kg/m^3)	
1	A	0 - 0.076	Comp.	Radial	1 E	4.315	0.0891		--	
					4 C	4.791	0.0124		1.776	
					5 E	15.774	0.2504		1.774	
					7 E	12.195	0.1009		1.772	
					8 C	2.544	0.0120		--	
					9 E	7.767	0.0597		1.775	
				Axial	201 E	13.344	0.2756		1.783	
					203 E	5.967	0.1962		1.784	
					204 E	4.807	0.0993		1.779	
					205 E	16.695	0.5488		1.785	
					207 E	11.954	0.2468		--	
					209 E	1.157	0.0089		1.790	
					211 E	3.894	0.1512		1.779	
					213 C	0.933	0.0193		1.782	
			Tens.	Radial	1 R	6.305	0.0430		1.780	
					4 R	5.091	0.0348		1.787	
					5 R	16.541	0.1129		1.782	
					8 R	6.095	0.0416		1.781	
					9 R	16.803	0.1147		1.781	
				Axial	201 E	2.625	0.0208		1.784	
					203 E	13.223	0.1047		1.780	
					205 E	3.693	0.0292		1.786	
					207 E	25.392	0.2009		1.788	
					209 E	17.612	0.1393		1.782	
					211 E	2.474	0.0196		1.785	
					213 E	3.352	0.0365		1.787	
					215 E	5.313	0.0420	High 0.5488	1.788	High 1.790
					217 E	2.880	0.0228	Avg. 0.1053	1.787	Avg. 1.782
					219 C	3.827	0.0303	Low 0.0089	1.787	Low 1.772
	B	0.076 - 0.152	Comp.	Radial	12 C	1.167	0.0483		1.772	
					13 E	3.820	0.0058		1.773	
					16 C	0.768	0.0122		1.766	
					17 E	3.569	0.0058		1.776	

TABLE 11-20 (Continued)

Slab	Section	Distance from Top of Log (m)	Sample Type	Orien-tation	Sample No.[a]	Burnoff (%)	Reaction Rate (%/h)		Density x 10^{-3} (kg/m^3)	
(1)	(B)	(0.076 - 0.152)	(Comp.)	Axial	215 E	23.379	0.1912		1.784	
					217 E	14.496	0.2971		1.786	
					219 E	5.347	0.2707		1.783	
					221 E	7.932	0.4016		1.792	
					223 E	2.531	0.0124		1.794	
					225 E	8.650	0.4380		1.780	
					227 C	2.141	0.0101		--	
			Tens.	Radial	12 R	2.277	0.0155		1.780	
					16 R	1.950	0.0133		1.778	
					17 R	8.672	0.0592		1.776	
				Axial	221 E	0.714	0.0056		1.784	
					223 E	1.828	0.0145		1.782	
					225 E	3.834	0.0303		1.783	
					227 E	24.096	0.1906		1.780	
					229 E	10.152	0.0803		1.781	
					231 E	0.503	0.0050		1.778	
					233 E	4.499	0.0087		1.781	
					235 E	2.883	0.0042	High 0.4380	1.778	High 1.794
					237 E	0.576	0.0058	Avg. 0.0891	1.766	Avg. 1.780
					239 C	5.340	0.0118	Low 0.0042	1.779	Low 1.766
	C	0.152 - 0.229	Comp.	Radial	20 C	3.015	0.0095		1.771	
					21 E	3.399	0.0088		1.784	
					24 C	0.676	0.0057		1.775	
					25 E	4.353	0.0073		1.783	
				Axial	229 E	7.378	0.1523		--	
					230 E	9.292	0.1475		1.779	
					231 E	14.953	0.1223		1.788	
					233 E	14.386	0.2971		1.782	
					235 E	10.968	0.3606		1.789	
					237 E	5.841	0.0083		1.790	
					239 E	7.323	0.3708		1.780	
					241 C	2.577	0.0053		1.783	
			Tens.	Radial	20 R	1.747	0.119		1.778	
					21 R	5.142	0.0351	High 0.3708	1.778	High 1.790
					24 R	1.850	0.0126	Avg. 0.0984	1.781	Avg. 1.781
					25 R	2.824	0.0193	Low 0.0053	1.781	Low 1.771

TABLE 11-20 (Continued)

Slab	Section	Distance from Top of Log (m)	Sample Type	Orien- tation	Sample No.[a]	Burnoff (%)	Reaction Rate (%/h)		Density x 10^{-3} (kg/m^3)	
(1)	D	0.229 - 0.305	Comp.	Radial	28 C	1.430	0.0068		--	
					29 E	0.622	0.0052		1.780	
					30 C	4.454	0.0048		1.766	
					32 C	2.039	0.0053		1.784	
					33 E	2.394	0.0066		1.777	
			Tens.	Radial	28 R	1.873	0.0128		1.780	
					29 R	1.806	0.0123	High 0.0128	1.784	High 1.784
					32 R	1.804	0.0123	Avg. 0.0083	1.781	Avg. 1.779
					33 R	0.830	0.0085	Low 0.0048	1.781	Low 1.766
3	E	0.762 - 0.838	Comp.	Radial	36 C	1.655	0.0078		--	
					37 E	0.649	0.0055		1.775	
					40 C	2.310	0.0064		1.774	
					41 E	2.610	0.0082		1.773	
					44 C	0.749	0.0063		1.775	
				Axial	243 E	0.646	0.0052		1.782	
					245 E	3.164	0.0027		1.783	
					247 E	1.393	0.0066		--	
					249 E	1.899	0.0067		1.784	
					250 E	0.828	0.0064		1.780	
					251 E	0.875	0.0070		1.779	
					253 E	4.341	0.0047		1.782	
					255 C	3.082	0.0063		1.778	
			Tens.	Radial	36 R	2.415	0.0053		1.782	
					37 R	4.170	0.0107		1.782	
					40 R	0.753	0.0077		1.782	
					41 R	3.780	0.0073		1.783	
					44 R	2.862	0.0099		1.787	
				Axial	243 E	1.675	0.0015		1.786	
					245 E	0.506	0.0021		1.783	
					247 E	1.614	0.0015		1.783	
					249 E	1.407	0.0033		1.784	
					251 E	0.562	0.0023		1.783	
					253 E	1.930	0.0017		1.782	
					255 E	3.961	0.0061		1.782	
					257 E	1.056	0.0044	High 0.0107	1.783	High 1.787
					259 C	2.818	0.0054	Avg. 0.0055	1.783	Avg. 1.781
					261 C	3.438	0.0053	Low 0.0015	1.782	Low 1.773

TABLE 11-20 (Continued)

Slab	Section	Distance from Top of Log (m)	Sample Type	Orien-tation	Sample No.[(a)]	Burnoff (%)	Reaction Rate (%/h)		Density $\times 10^{-3}$ (kg/m^3)	
(3)	F	0.838 - 0.914	Comp.	Radial	45 E	4.362	0.0073		1.774	
					47 E	0.858	0.0031		1.766	
					48 C	1.690	0.0082		1.766	
					49 E	1.947	0.0050		1.768	
					52 C	1.254	0.0059		--	
				Axial	257 E	0.579	0.0045		1.784	
					259 E	1.025	0.0036		1.785	
					261 E	3.426	0.0039		1.786	
					263 E	1.483	0.0046		1.784	
					265 E	0.839	0.0067		1.782	
					267 E	1.222	0.0058		--	
					269 C	4.404	0.0047		1.782	
			Tens.	Radial	45 R	0.789	0.0081		1.780	
					48 R	2.944	0.0106		1.786	
					49 R	2.411	0.0053		1.776	
					52 R	0.780	0.0080		1.777	
				Axial	263 E	0.480	0.0020		1.787	
					265 E	1.462	0.0013		1.787	
					267 E	1.074	0.0021		1.787	
					269 E	2.147	0.0041		1.786	
					271 E	0.811	0.0033		1.785	
					273 E	4.197	0.0065		1.784	
					275 E	3.768	0.0058		1.786	
					277 E	1.112	0.0046	High 0.0106	1.784	High 1.787
					279 C	2.250	0.0020	Avg. 0.0052	1.784	Avg. 1.781
					281 C	4.5501	0.0071	Low 0.0013	1.781	Low 1.766
	G	0.914 - 0.991	Comp.	Radial	53 E	0.642	0.0054		1.772	
					56 C	3.264	0.0084		1.764	
					57 E	2.675	0.0084		1.775	
					60 C	2.860	0.0047		1.771	

TABLE 11-20 (Continued)

Slab	Section	Distance from Top of Log (m)	Sample Type	Orientation	Sample No.[a]	Burnoff (%)	Reaction Rate (%/h)		Density x 10^{-3} (kg/m^3)	
(3)	(G)	(0.914 - 0.991)	(Comp.)	Axial	271 E	1.565	0.0055		1.787	
					273 E	1.399	0.0066		--	
					275 E	3.004	0.0062		1.780	
					276 E	1.743	0.0084		1.754	
					277 E	0.846	0.0068		1.778	
					279 E	1.382	0.0043		1.787	
					281 E	2.023	0.0042		1.778	
					283 C	0.915	0.0073		1.783	
			Tens.	Radial	53 R	0.812	0.0083		1.774	
					56 R	4.248	0.0127	High 0.0127	1.780	High 1.787
					57 R	0.712	0.0073	Avg. 0.0068	1.777	Avg. 1.776
					60 R	2.715	0.0060	Low 0.0042	1.781	Low 1.754
	H	0.991 - 1.067	Comp.	Radial	61 E	1.588	0.0075		--	
					62 C	0.666	0.0048		1.769	
					64 C	0.684	0.0058		1.768	
					65 E	4.614	0.0077		1.782	
					68 C	1.150	0.0054		--	
			Tens.	Radial	61 R	4.377	0.0132		1.781	
					64 R	0.677	0.0068	High 0.0132	1.781	High 1.783
					65 R	3.417	0.0066	Avg. 0.0072	1.783	Avg. 1.778
					68 R	0.684	0.0070	Low 0.0048	1.783	Low 1.768
5	I	1.524 - 1.600	Comp.	Radial	69 E	1.956	0.0093		--	
					72 C	0.524	0.0083		1.787	
					73 E	2.865	0.0047		1.792	
					76 C	2.691	0.0130		1.789	
					77 E	0.920	0.0077		1.799	
					78 C	1.225	0.0100		1.790	
				Axial	285 E	4.589	0.0049		1.800	
					286 E	1.007	0.0060		1.796	
					287 E	1.977	0.0069		1.800	
					289 E	4.823	0.0053		1.792	
					291 E	0.607	0.0112		1.792	
					293 E	2.509	0.0077		1.795	
					295 E	1.627	0.0070		1.795	
					297 C	1.966	0.0093		--	

TABLE 11-20 (Continued)

Slab	Section	Distance from Top of Log (m)	Sample Type	Orien-tation	Sample No.[a]	Burnoff (%)	Reaction Rate (%/h)		Density x 10^{-3} (kg/m^3)	
(5)	(I)	(1.524 - 1.600)	Tens.	Radial	69 R	1.128	0.0177		1.796	
					72 R	4.492	0.0180		1.800	
					73 R	3.009	0.0088		1.798	
					76 R	0.876	0.0138		1.796	
					77 R	4.218	0.0081		1.797	
				Axial	283 E	1.511	0.0062		1.806	
					285 E	4.677	0.0091		1.806	
					287 E	4.764	0.0093		1.802	
					289 E	0.650	0.0065		1.804	
					291 E	3.263	0.0033		1.802	
					293 E	5.062	0.0078		1.804	
					295 E	1.401	0.0058		1.801	
					297 E	2.289	0.0054	High 0.0180	1.803	High 1.806
					299 C	5.289	0.0117	Avg. 0.0085	1.802	Avg. 1.801
					201 C	2.445	0.0035	Low 0.0033	1.802	Low 1.796
	J	1.600 - 1.676	Comp.	Radial	80 C	1.822	0.0088		1.794	
					81 E	5.209	0.0088		1.799	
					84 C	0.543	0.0086		1.800	
					85 E	2.023	0.0096		--	
				Axial	299 E	1.338	0.0107		1.792	
					301 E	4.638	0.0057		1.799	
					303 E	2.495	0.0118		--	
					305 E	2.015	0.0062		1.791	
					307 E	1.569	0.0077		1.792	
					308 E	1.183	0.0082		1.788	
					309 E	6.143	0.0079		1.790	
					311 C	0.734	0.0091		1.783	
			Tens.	Radial	80 R	4.794	--		1.802	
					81 R	2.214	0.0348		1.798	
					84 R	2.382	0.0374		1.801	
					85 R	2.561	0.0075		1.805	

TABLE 11-20 (Continued)

Slab	Section	Distance from Top of Log (m)	Sample Type	Orien-tation	Sample No.[(a)]	Burnoff (%)	Reaction Rate (%/h)		Density x 10^{-3} (kg/m^3)	
(5)	(J)	(1.600 - 1.676)	(Tens.)	Axial	303 E	0.562	0.0056		1.809	
					305 E	4.573	0.0090		1.809	
					307 E	4.736	0.0092		1.808	
					309 E	1.166	0.0048		1.808	
					311 E	3.036	0.0031		1.805	
					313 E	5.376	0.0083		1.806	
					315 E	1.617	0.0067		1.806	
					317 E	4.691	0.0092	High 0.0374	1.807	High 1.809
					319 C	3.375	0.0034	Avg. 0.0100	1.803	Avg. 1.800
					321 C	1.764	0.0073	Low 0.0031	1.802	Low 1.783
	K	1.676 - 1.753	Comp.	Radial	88 C	3.628	0.0104		1.794	
					89 E	2.022	0.0098		1.800	
					92 C	1.755	0.0083		--	
					93 E	6.563	0.0112		1.807	
				Axial	313 E	1.073	0.0046		1.799	
					315 E	2.599	0.0123		--	
					317 E	2.370	0.0073		1.795	
					319 E	2.218	0.0109		1.793	
					321 E	2.183	0.0093		1.795	
					323 E	2.326	0.0110		--	
					325 C	1.725	0.0138		1.785	
			Tens.	Radial	88 R	1.931	0.0303		1.799	
					89 R	3.943	0.0110	High 0.0303	1.803	High 1.807
					92 R	5.311	0.0117	Avg. 0.0119	1.807	Avg. 1.798
					93 R	1.098	0.0173	Low 0.0046	1.802	Low 1.785
	L	1.753 - 1.829	Comp.	Radial	96 C	2.431	0.0117		1.807	
					97 E	0.906	0.0076		1.807	
					100 C	5.060	0.0159		1.807	
					101 E	3.877	0.0110		1.815	
					102 C	1.425	0.0044		1.803	
			Tens.	Radial	96 R	4.013	0.0110		1.809	
					97 R	2.786	0.0082	High 0.0234	1.805	High 1.815
					100 R	1.490	0.0234	Avg. 0.0116	1.808	Avg. 1.808
					101 R	4.924	--	Low 0.0044	1.808	Low 1.803

[(a)] Lateral location; C = center, E = edge, and R = whole radius.

TABLE 11-21
IMPURITIES FOUND IN STACKPOLE 2020 GRAPHITE

Specimen Number	Impurity Concentration (ppm)												Position in 5.5-m Log	
	Al	Ba	B	Ca	Cu	Fe	Pb	Mg	Nb	Si	Ti	V	Distance From Top (m)	Edge or Center[a]
6799-52-11	60	20	2	200	<1	40	6	<0.5	<6	20	20	20	0.075	E
6799-52-34	20	20	2	100	<1	10	60	<0.5	<6	80	2	<0.5	0.250	C
6799-53-43	20	20	2	100	8	10	<6	1	20	40	40	20	0.85	E
6799-53-58	60	20	2	100	<1	4	<6	1	<6	60	40	20	0.95	C
6799-54-71	<1	10	2	100	<0.5	<1	<6	1	<6	60	20	10	1.5	E
6799-54-98	100	20	2	200	<1	<1	<6	1	<6	60	10	8	1.8	C
Mean	43	18	2	133	2	14	15	0.8	8	63	22	13		

[a] C = center sample obtained at depth of 44 mm or greater from surface
E = edge sample obtained within 44 mm of surface

APPENDIX
TOPICAL REPORTS PUBLISHED DURING THE QUARTER

Kovacs, W. J., "Preirradiation Report of TRISO and BISO Coated ThO_2 Particles for Irradiation Capsules HT-31 and HT-33," ERDA Report GA-A13923, General Atomic Company, November 1976.

Price, R. J., and L. A. Beavan, "Final Report on Graphite Irradiation Test OG-3," ERDA Report GA-A14211, General Atomic Company, January 1977.